Design of a soluble P-selectin biosensor for detecting platelet activation

by

Willem Adriaan Laubscher

Thesis presented in partial fulfilment of the requirements for the degree of

Master of Engineering (Electronic)

in the Faculty of Engineering at Stellenbosch University

Supervisor: Prof. W.J. Perold

December 2019

Acknowledgments

Stephan.

Declaration

By submitting this thesis electronically, I declare that the entirety of the work contained therein is my own, original work, that I am the sole author thereof (save to the extent explicitly otherwise stated), that reproduction and publication thereof by Stellenbosch University will not infringe any third party rights and that I have not previously in its entirety or in part submitted it for obtaining any qualification.

December 2019

Opsomming

Die hoof oorsake van dood is besig om te verander van oordraagbare siektes, soos Tuberkulose, na nie-oordraagbare siektes, soos kardiovaskulêre siektes. Kardiovaskulêre siektes, tesame met ander siektes, word geassosieer met kroniese inflammasie wat ook interafhanklik is met geaktiveerde bloedplaatjies. Geaktiveerde bloedplaatjies stel biomerkers vry in die bloedstroom wat gebruik kan word om siektes te diagnoseer en monitor. Huidiglik is daar geen hoogs akkurate toetse wat kroniese inflammasie kan meet nie, en konvensionele toeste is soms duur, tydrowend, en onprakties in vêrafgeleë areas. Dit is duidelik dat daar plek is vir verbetering in die diagnosering van inflammasie.

Die projek se invalshoek was om 'n biomerker te kry wat 'n goeie aanduiding is van bloedplaatjie aktivering, en wat opgereguleer is in inflammatoriese siektes. Oplosbare P-selectin was geïdentifiseer as 'n plaatjie membraan reseptor wat vrygestel word in die bloedstroom wanneer die plaatjie aktiveer.

'n Studie was gedoen oor die verskillende tipe biosensors, en 'n etiket-vrye elektrochemiese biosensor was gekies. Elektrochemiese biosensors het robuuste kenmerke en dit kan vervaardig word met lae koste materiale. Kommersïele grafiet oksied en koolstof nanovesel gedrukte elektrodes was aangekoop om die sensors te vervaardig. Die elektroplatering van 4-karboksiefeniel diazonium sout was gebruik om ondersteunende groepe te skep op die sensor sodat menslike oplosbare P-selectin teenliggaampies geheg kan word deur middel van EDC/NHS bindings chemie. Vierkantsgolf voltammetrie was geïdentifiseer as 'n baie sensitiewe diagnostiese tegniek wat gebruik kan word om elektrochemiese metings te neem. Ferrisianied/ferrosianied en ruteniumheksamien(III) chloraat was gebruik as die twee redoks probes vir die voltammetriese metings. 'n Potentiostaat toestel was ontwikkel om die vierkantsgolf potensiaal toe te pas op die sensors, en die reaksie te meet. Die draagbare toestel kon spannings toepas in die gebied van ± 1.65 V, en strome meet in die gebied van ± 244 μA.

Die projek het drie verskillende metodes probeer om die proteïen te meet oor 'n reeks van vyf volskaalse toetse. Nie een van die metodes het daarin geslaag om 'n lineêre aanwins te toon oor die konsentrasies wat getoets was nie, maar een van die metodes het wel 'n verskil in reaksie getoon tussen sP-selectin en nie-spesifieke CRP. As gevolg van probleme met die sensors aan die einde van die projek, kon die ontwikkelde potentiostaat nie gebruik word om die metings te neem nie. Die toestel het wel uitstekende resultate getoon vir die meting van verskillende konsentrasies (0.5 tot 5 mM) van die ferrisianied/ferrosianied redoks probe, en die werking van die masjien was geverifieer deur 'n konvensionele potentiostaat as 'n maatstaaf te gebruik.

Die werk wat in hierdie tesis verrig was het gewys dat, as die P-selectin biosensor geop-

timaliseer word met die benodigde toerusting en materiale, dit moontlik sou wees om die ontwikkelde potentiostaat toestel te gebruik om die konsentrasie van oplosbare P-selectin in 'n oplossing te meet.

Summary

The main causes of death are shifting from communicable disease, such as Tuberculosis, to non-communicable disease, such as cardiovascular disease. This disease, along with many other diseases, have been associated with chronic inflammation which is also interrelated with activated blood platelets. When platelets activate, they release biomolecules that can be used as biomarkers for diagnosing or monitoring diseases. Currently, there are no highly accurate tests that can measure the level of chronic inflammation and conventional tests ar either costly, time-consuming, or unpractical in remote areas. Therefore, there is room for improvement in the area of diagnostics of chronic inflammation.

This project set out to find a potential biomarker that is a good indicator of platelet activation and is upregulated in an inflammatory individual. Soluble P-selectin was identified as a platelet membrane receptor that is shed upon activation into the blood stream.

A study was conducted about the different biosensing techniques, and a label-free electrochemical biosensor approach was chosen for this work. Electrochemical biosensors have been shown to be robust and can be manufactured with relatively low-cost materials. Commercial graphene oxide and carbon nanofiber screen printed electrodes were acquired to establish a working proof of concept. The sensors were electrografted with 4-carboxyphenyl diazonium salt to create support groups for the subsequent attachment of human soluble P-selectin antibodies through EDC/NHS crosslinking chemistry. Square wave voltammetry was identified as a very sensitive diagnostic technique that can be used to quantify the concentration of biomolecules in a sample. Ferricyanide/ferrocyanide and hexaammineruthenium(III) chloride was used as the two redox probes for the voltammetry measurements. In parallel, an application specific potentiostat device was developed to apply the square wave potential and measure the sensor response. The portable device had a potential range of ± 1.65 V and a current range of ± 244 μA.

The project used three different approaches for the detection tests over a range of five full scale experiments. Even though none of the approaches were successful in realizing a linear detection range, one approach showed a difference in response between sP-selectin and non-specific CRP. Due to an unfortunate event with the sensors at the closing of the project, the home-built potentiostat could not be used to perform the final detection measurements of the immunosensor. However, it showed excellent performance against a conventional potentiostat device for detecting ferricyanide/ferrocyanide concentrations in the range of 0.5 to 5 mM.

The work done in this thesis showed that if the immunosensor was optimized with the necessary equipment and materials, it would have been possible to use the home-built potentiostat to quantify the level of soluble P-selectin in a sample.

Contents

List of Tables

List of Figures

Nomenclature

Abbreviations

NCD	Non-communicable disease
CVD	Cardiovascular disease
CD62P	P-selectin
ELISA	Enzyme-linked immunosorbent assay
GP	Glycoprotein
LTA	Light transmission aggregometr
HRP	Horseradish peroxidase
EIS	Electrochemical impedance spectroscopy
WE	Working electrode
RE	Reference electrode
CE	Counter electrode
GOx	Glucose oxidase
PBS	Phosphate buffer saline
CNF	Carbon nanofiber
SWV	Square wave voltammetry
CV	Cyclic voltammetry
SMN	Survival motor neuron
CRP	C-reactive protein
NHS	N-hydroxysuccinimide
EDC	N-(3-Dimethylaminopropyl)-N-ethylcarbodiimide hydrochloride
BSA	Bovine serum albumine
GPHOX	Graphene oxide
AC	Alternating current
ITO	Indium tin oxide
TSM	Thickness shear mode
DAC	Digital-to-analog converter
ADC	Analog-to-digital converter
MCU	Microcontroller unit
MW	Molecular weight
IC	Integrated circuit
PCB	Printed circuit board
RMS	Root mean square

USB	Universal Serial Bus
USART	Universal Synchronous/Asynchronous Receiver/Transmitter
DMA	Direct memory access
RuHex	Hexaammineruthenium(III) chloride redox probe
FeCN	Ferricyanide/ferrocyanide redox couple

Constants

π	3.141 592 654
$R =$	8.314 459 8
$F =$	96 485.332 89

Variables with units

R	Universal gas constant	$[\,\mathrm{J \cdot K^{-1} \cdot mol^{-1}}\,]$
F	Faraday's constant	$[\,\mathrm{C \cdot mol^{-1}}\,]$
V_{cell}	Cell potential	$[\,\mathrm{V}\,]$
V_w	Working electrode potential	$[\,\mathrm{V}\,]$
V_r	Reference electrode potential	$[\,\mathrm{V}\,]$
V_i	Input voltage	$[\,\mathrm{V}\,]$
I_{cell}	Cell current	$[\,\mathrm{A}\,]$
R_f	Feedback resistor	$[\,\Omega\,]$
E	Applied cell potential	$[\,\mathrm{V}\,]$
E^0	Standard potential	$[\,\mathrm{V}\,]$
T	Temperature	$[\,\mathrm{K}\,]$
E_{pa}	Anodic peak potential	$[\,\mathrm{V}\,]$
E_{pc}	Cathodic peak potential	$[\,\mathrm{V}\,]$
$E^{0,}$	Formal potential	$[\,\mathrm{V}\,]$
Δi_p	Differential peak current	$[\,\mathrm{A}\,]$
A	Working electrode surface area	$[\,\mathrm{cm^2}\,]$
C_O^*	Bulk oxidized species concentration	$[\,\mathrm{mol \cdot cm^{-3}}\,]$
D_O	Diffusion coefficient of oxidized species	$[\,\mathrm{cm^2 \cdot s^{-1}}\,]$
t_p	Pulse width	$[\,\mathrm{s}\,]$
$\Delta\Psi_p$	Dimensionless peak current	$[\,-\,]$
f	Frequency	$[\,\mathrm{Hz}\,]$
Z	Impedance	$[\,\Omega\,]$

Chapter 1

Introduction

1.1 Background

The main causes of death are continually shifting from communicable diseases, such as Tuberculosis, to non-communicable disease (NCD), like cardiovascular disease (CVD) and diabetes mellitus. Ischaemic heart disease and stroke are the two leading causes of death that claimed a combined 15.2 million lives in 2016. Diabetes came in seventh place, killing 1.6 million people in the same year. NCDs are especially prevalent in middle- and high-income countries, accounting for over 78% of the global deaths in 2016 [1].

CVD is a group of diseases that are related to the heart or blood vessels [2]. Many of these diseases are due to a process called atherosclerosis, which is the abnormal build up of plaque in the walls of arteries. This leads to the narrowing of vessels which restricts the flow of blood, eventually causing a blood clot or a rupture [2]. CVD is also closely associated with diabetes with about 70% of the diabetic population succumbing to diabetes-related cardiovascular disease [3]. Increasing amounts of people are living sedentary and unhealthy lifestyles which is why diabetes is becoming more and more prevalent.

CVD and diabetes are among many other major diseases that have been associated with abnormal levels of chronic inflammation. Inflammation is the body's automatic response to fight off invading pathogens or heal damaged cells. But chronic inflammation, on the other hand, may lead to a host of diseases, such as atherosclerosis, arthritis, obesity, and even cancer [4, 5, 6, 7, 8, 9, 10, 11]. Although chronic inflammation might not be the cause of all of these diseases, it could serve as an underlying indicator of imminent health complications. Low levels of chronic inflammation can also persist for many years without showing any symptoms until it is too late.

Activated blood platelets have been shown to be related to many of these diseases [8, 11, 12] and it is also interrelated with inflammation [12, 13, 14, 15]. Upon activation, they secrete a large number of pro-inflammatory proteins and biomolecules which could be used as potential biomarkers [16]. It is increasingly realized that platelets play a major role in inflammation and immunity, which is why its associated biomarkers can be used to predict and diagnose disease states.

There are no highly accurate tests to assess the level of chronic inflammation and it is often only diagnosed in conjunction with another medical condition. There are, how-

ever, two inexpensive blood tests that can be used to diagnose systemic inflammation, namely high-sensitivity C-reactive protein and Serum Amyloid A. Unfortunately, the former is only indicative of acute inflammation and Serum Amyloid A is poorly standardized. In general, most assays are either costly, time consuming, or unpractical in remote setups where medical care is not always easily accessible [17]. Therefore, there is room for improvement and new additions in the current diagnostic tests that are available for inflammation related biomarkers. This includes finding new potential biomarkers that could be indicative of underlying chronic inflammation and developing an inexpensive assay for screening purposes.

1.2 Motivation and approach

The World Health Organization (WHO) recognizes that NCDs, or chronic diseases, lead to premature deaths that can be controlled and prevented. The major risk factors, such as tobacco use, physical inactivity, and abuse of alcohol can all be reduced if people are properly educated about their lifestyle choices. The organization released a report in 2005 (Preventing Chronic Disease: A Vital Investment) stating that the early detection, screening and treatment of these diseases are part of the war on chronic diseases [18]. The United Nations have also listed the fight against NCDs as part of their goals in the 2030 Agenda for Sustainable Development that was released in 2015 [19]. They plan on reducing the number of premature deaths due to NCDs by one third through prevention and treatment as well as education about mental health and well-being.

It is recognized that chronic diseases is a huge problem for the economy of South Africa since it degrades the health of the working population [20]. A report released by the WHO (Non-Communicable Disease Country Profiles in 2018: South Africa) estimated that NCDs were responsible for about 51% of the deaths in the country in 2016 [21]. The South African Non-communicable Disease Alliance have outlined three major implementations in their Strategic Plan for the Prevention and Control of Non-Communicable Diseases 2013-2017 [22]:

1. Prevention of NCDs and promotion of health and wellness at population, community and individual levels;

2. Improved control of NCDs through health systems strengthening and reform;

3. Monitoring NCDs and their main risk factors and conducting innovative research on low-cost screening and intervention approaches.

Although the strategic plan ended in 2017, it is part of a larger goal that would contribute to the 2020 targets that have been set out by the South African Declaration for Prevention and Control of Non-communicable diseases. The main target is to reduced the number of deaths (under the age of 60) due to NCDs by 25% through the effective implementation of promotive, preventive, curative, rehabilitative, and palliative services.

Based on these goals, it is clear that a low-cost screening tool for detecting early signs of chronic disease could serve as a building block for a more robust health system. This project aims at developing an inexpensive *in-vitro* diagnostic device that can be used for detecting and monitoring platelet activation as a marker for inflammation.

1.3 Project scope

The scope of this project was to develop a device that would be able to detect a biomarker that is indicative of inflammation. This included finding an appropriate biomarker that is involved in the process of inflammation, and developing a platform that could be used to test for this biomarker in a physiological solution or blood plasma. The biomarker should be present in healthy individuals (at least in small concentrations), and upregulated in sick individuals. The platform includes a sensor area that contains the sample and an electronic setup that can connect to the sensor and perform measurements at the sensing area. The electronic setup should be able to measure the biomarker concentration and communicate the results to a computer. It should ideally be battery powered which would make it a more portable device that can be used in resource-limited areas.

1.4 Thesis outline

This project includes a literature study about the two main aspects of a biosensor device namely the biomarker and the design of an electronic measuring device.

The process of blood platelet activation and its relationship with inflammation is firstly reviewed to understand the different mechanisms and find a potential biomarker that would be upregulated in an inflammatory condition. The current commercial laboratory tests for platelet activation and its biomarkers are then considered to see what their advantages and limitations are. The different types of biosensing techniques are then reviewed to determine what the best approach would be for developing the sensing platform. The sensing platform includes the different components of a biosensor device and this is studied by looking at the different research-based biosensors that are available for other types of biomarkers. A biosensing technique is chosen based on this study. The benchtop, industrial grade instrument that is used to characterize the chosen type of biosensor is then researched to determine what the specifications for an electronic measurement setup will be that can substitute the larger instrument.

After this thorough literature review, the methodology that is used to develop and characterize the biosensor and the electronic measurement device is described in detail. This is followed by the presentation of the results and a discussion of the findings. Conclusions and future recommendations are then made to discuss how well the device works and to make suggestions where it can be improved.

Chapter 2

Literature Study

A literature study was done to determine what the main role of platelets are and how they are linked to chronic inflammation. This was done to assess the viability of using platelets or its secreted proteins as a marker of inflammation. Commercial platelet function tests are discussed in terms of their uses, advantages and drawbacks. Some of the current biosensing techniques are then researched to see which approach would be the best for designing a portable platelet function testing device. The discussed techniques include considering the current research-based platelet function testing biosensors that have been developed. A suitable technique is then chosen based on these findings. The measurement setup that accompanies the chosen biosensor technique is then described in more detail in terms of its design, cost, features, and portability. Finally, the proposed methodology for developing a soluble P-selectin biosensor device is given.

2.1 Blood platelets

This section describes the function of blood platelets and how they prevent and stop bleeding. It describes the changes that platelets undergo and the proteins it secretes from its membrane during activation. It also explains how platelet activation is linked to inflammation which make platelets and its secreted proteins possible biomarkers for diagnosing inflammatory conditions and cardiovascular disease.

2.1.1 Role of platelets

Blood platelets play a key role in hemostasis, which is the body's normal physiological response for the prevention and stopping of bleeding. They are 2 to 5 μm in diameter and 0.5 μm thick on average [23]. There are about 150-400$\times 10^9$ platelets per liter of blood, waiting to repair and heal any damage to the hosts blood vessels [24]. Even though this function can be beneficial to the host, it can also be dangerous and that is why it is important to understand the functioning of the cell. For example, it has only recently been discovered that platelets are involved in tumor growth and inflammation [25]. A low platelet count can lead to bleeding disorders, whereas a high platelet count or hyperactive platelets can lead to abnormal thrombotic events. These events can cause atherosclerosis, thrombosis, and chronic inflammation which are some of the leading causes of death in the Western world [12, 25, 26]. Thus, it is important to understand the platelet pathology to develop methods of maintaining its normal function.

The most important role of platelets is to maintain hemostasis [27]. The mechanism by which our body tries to repair damage to blood vessels is called the coagulation cascade. This mechanism involves blood platelet activation, adhesion to the blood vessel wall, and aggregation to other platelets to form a blood clot. This process is shown in Fig. 2.1.

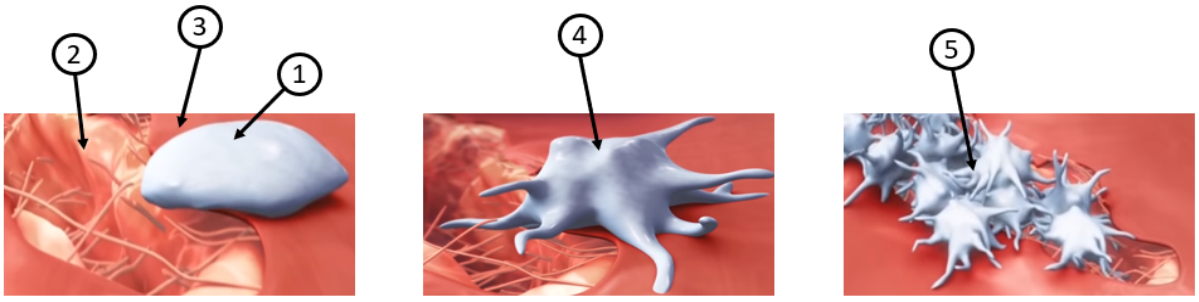

Figure 2.1: An inactive platelet ① passes the site of injury ② in the blood vessel ③. The platelet activates and adheres to the vessel wall ④ before aggregating to other platelets to form a blood clot ⑤. [28]

Platelets that are close to the site of injury undergo a conformational change when they are exposed to the underlying collagen fibers of the vessel wall. Von Willebrand factor forms a bridge between these fibers and the glycoprotein (GP) Ib-IX-V receptor on the platelet membrane to facilitate binding. The collagen also binds directly to GP Ia/IIa and GP VI receptors on the platelets [16]. This leads to the secretion of the contents of the platelet granules and the formation of the foot-like extensions shown in Fig. 2.1. Further platelet activation is stimulated by the bound secretion products which causes a snowballing effect with surrounding platelets. These prothrombotic factors activate nearby platelets leading to the upregulation of GP IIb/IIIa receptors on the platelet membrane. This receptor facilitates platelet-platelet aggregation, ultimately leading to the formation of a platelet plug as shown on the right of Fig. 2.1 [29].

Thus, platelets play an important role in preventing blood loss, but the thrombotic nature of platelets can also contribute to cardiovascular disease [30]. It is well known that platelets form aggregates at lesions of atherosclerotic plaque, resulting in atherothrombosis [14, 31]. Platelets are stimulated to activate and aggregate even though no bleeding occurs at the lesion, leading to the formation of a thrombus and an increased risk of a heart attack. Platelets also shed microparticles during activation that has been associated with the progression of type two diabetes [3, 8, 11]. It is clear that these multifunctional cells have both the ability to repair and destroy its host.

2.1.2 Platelet activation as a biomarker for inflammation

When platelets activate and undergo shape change a large number of prothrombotic and proinflammatory substances are released from their granules. These substances are inflammatory and immune modulating factors that are either released into the blood or translocated to the membrane of the activated platelets to serve as binding spots for other immune cells [16, 32]. This allows different immune cells to be “recruited” to the site of injury so that the healing process can begin.

One of the most studied markers of activation is P-selectin (also known as CD62P) which is stored in the α-granules of platelets [16]. Upon activation, platelets express large amount of P-selectin on the surface of their membrane. This adhesion molecule plays a central role in the interaction between platelets and immune cells. It is a mediator of platelet-leukocyte aggregates, thereby upregulating proinflammatory cytokines at the damaged area [15, 16]. The soluble form of P-selectin (commonly referred to as sP-selectin or sCD62P) comes from activated platelets and damaged endothelial cells, with the majority originating from activated platelets [33, 34]. Elevated levels of this marker has been found in numerous inflammatory conditions such as atherosclerosis [35, 36], unstable angina [36, 37], acute myocardial infarction [38], and insulin-dependent diabetes [39]. It has been suggested that sP-selectin can serve as a potential biomarker for *in-vivo* activation, which could possibly be used for diagnosing cardiovascular risk [16, 33, 35, 40]. Platelets can easily be activated *ex-vivo* due to blood sampling or preprocessing, which is why it is important to have a biomarker that would be resistant to this variable. P-selectin is expressed on activated platelets following activation, and then shed through cleavage. This mechanism of cleavage is resistant to *ex-vivo* activation as long as the plasma is immediately seperated from the platelets, and that is why sP-selectin is a potential marker of *in-vivo* activation [33, 41].

The circulating protein is also not completely absent in healthy individuals. Some literature reports concentrations of 123.2±38.6 ng/ml in 31 healthy subjects with ages 56.9±9.3. This study did, however, report that 114 age- and sex-matched individuals with type 2 diabetes had levels almost three to fourfold higher (303.4±141.8 ng/ml) [39]. Other literature reported levels of 15-100 ng/ml in healthy humans and wild-type mice and confirmed the fourfold upregulation in patients with CVD, making it an attractive biomarker [42]. Lastly, it is worth mentioning that elevated levels of circulating sP-selectin is a consequence rather than a cause of cardiovascular disease. This is because circulating monomeric sP-selectin must combine with other sP-selectin molecules to promote inflammation and coagulation in mice [42].

2.2 Commercial platelet function tests

It is clear that platelets are multifunctional cells that are involved in more than just host defense. Thus, numerous clinical tests have been developed to test platelet functionality. This section discusses some of the widely used platelet function assays and their advantages and drawbacks.

2.2.1 Light Transmission Aggregometry

Light transmission aggregometry (LTA) is used to detect platelet defects and diseases [25]. It is still considered to be the golden standard test for platelet function, even though it was invented in the 1960s [43]. The LTA, shown in Fig. 2.2, is a benchtop instrument that is mostly available in specialized pathology laboratories and research facilities.

Figure 2.2: A benchtop light transmission aggregometry device. [44]

The principle by which the LTA operates is illustrated in Fig. 2.3. It measures the transmitted light intensity as it is shown through a platelet rich plasma sample, while aggregation is induced through stirring and addition of a platelet activator, called an agonist. Different agonists stimulate different platelet activation pathways by binding to specific receptors on the platelet membrane. Thus, by adding different agonists to the sample one can study the different platelet activation pathways that are involved in the coagulation cascade. As the platelets activate and aggregate, more light is transmitted through the sample, giving an indication of the degree of aggregation.

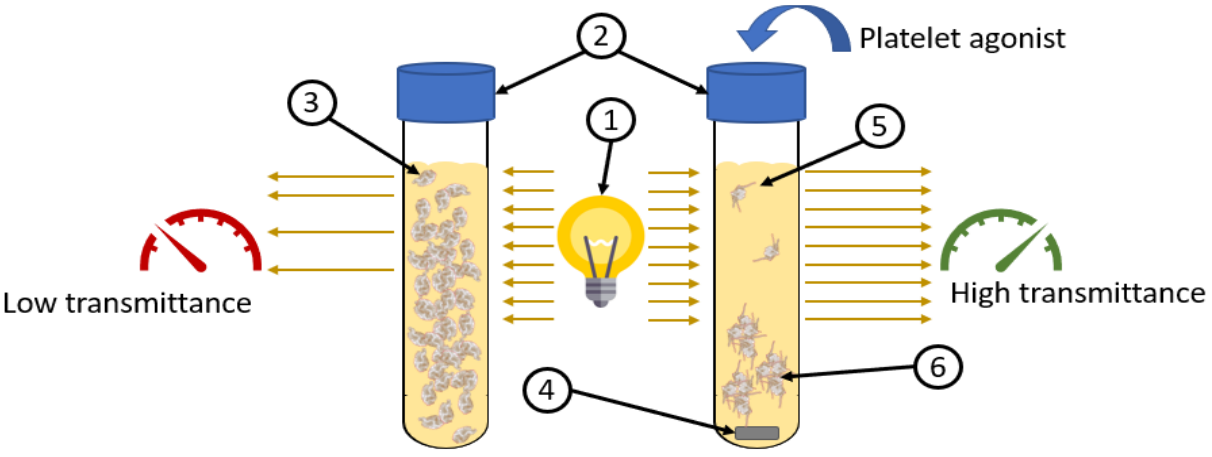

Figure 2.3: Light ① is shown through platelet rich plasma samples ②. A vial containing resting platelets ③ is set to 0% light transmission. Through magnetic stirring ④ and addition of a platelet activator (agonist), the platelets from another vial is forced to activate ⑤ and aggregate ⑥. This leads to sedimentation of the aggregates and a higher level of transmittance.

Over the last few years the system has improved with automatic setting of 100% and 0% baselines and multichannel capabilities. More sensitive versions employ laser light scattering as a way to detect small aggregates due to small agonist concentrations [45, 46, 47, 48]. Although the LTA can be used to detect a large number of platelet diseases and monitor antiplatelet therapy, it still has some disadvantages. These devices are limited to laboratory environments and require trained personnel to perform the test and interpret the results. The test lacks standardization and artifacts can be introduced due to the preprocessing of the blood - even when it is done by people with significant expertise. The

low shear stirring conditions do not accurately mimic the environment in which platelets would activate and aggregate in *in-vivo* conditions. This method is also influenced by platelet count, making it unsuitable for patients with a low number of platelets [25]. These limitations have given rise to more portable and easy-to-use systems, such as the VerifyNow device which is discussed in the next section.

2.2.2 VerifyNow system

The VerifyNow instrument, shown in Fig. 2.4, is used to monitor antiplatelet therapy such as aspirin, clopidogrel, and GP IIb/IIIa inhibitors. The device works on the principle that fibrinogen-coated polystyrene beads agglutinate in proportion to the amount of active GP IIb/IIIa receptors on the platelet membrane. These receptors can be activated by a specific agonist, which can be blocked by antiplatelet agents [25].

Figure 2.4: The point-of-care VerifyNow device. [25]

Compared to the LTA, the test is fully automated, point-of-care, and can be performed in whole blood, reducing the chance of introduction of artifacts due to pretreatment. It can be performed without the requirement of a specialized laboratory, resulting in smaller time delays and instant information. Although it has some advantages over the conventional LTA device, it is still influenced by factors such as platelet count, fibrinogen levels, and time from blood sampling to testing. The disposable cartridges are also expensive and can only be used to monitor three different classes of antiplatelet drugs, which is why this system lacks flexibility.

2.2.3 Measurement of activation markers by fluorescence

Platelets release a large number of prothrombotic molecules from their granules upon activation and shape change [16, 32]. The assessment of the level of some of these substances can provide information regarding the degree of platelet activation. These activation markers can be studied by flow cytometry analysis or enzyme-linked immunosorbent assays (ELISA).

Flow cytometry is used to study the chemical and physical properties of particles or cells in a solution by means of fluorescent labels. These particles or cell components are then excited with a laser as they pass through a channel, emitting various wavelengths that are passed through optical filters and beam splitters before hitting the relevant detector [49]. It is commonly used to study the expression of P-selectin receptors on the

platelet surface, and the active conformation of GP IIb/IIIa receptors using fluorescein isothiocyanate tagged PAC-1 antibodies. It can be used to perform a wide variety of tests in whole blood using only a small sample volume, and it is not influenced by platelet count. Some of the drawbacks include requiring a specialized operator, introduction of artifacts due to pretreatment, and the cost of operation [25].

ELISAs have also been used to study the levels of soluble platelet activation markers such as GP Ibα and sP-selectin [25]. The method, illustrated in Fig. 2.5, uses capture antibodies immobilized in the bottom of a well to target a specific protein in a solution. A secondary enzyme-linked, typically horseradish peroxidase (HRP), detection antibody is then added to the solution to bind to the opposite side of the captured protein. The added substrate then reacts with this enzyme to produce a colour or fluorescent signal which is analyzed by a fluorescent microplate reader to determine the presence and quantity of the target analyte [50].

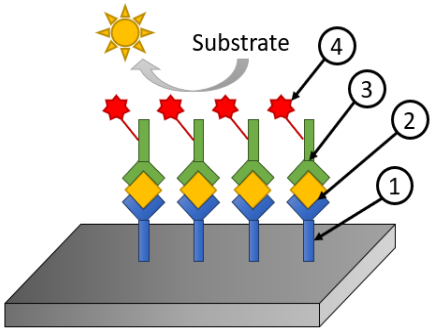

Figure 2.5: A sandwich ELISA uses an antibody ① to capture the target protein ②. A second enzyme-linked antibody ③ acts as a detection antibody. The substrate is then added to react with the enzyme ④ which is then converted into a colour or fluorescent signal.

Although the ELISA test can be specific and accurate in measuring activation markers, it is still very time consuming to conduct. It is also prone to artifact during the sample preparation and care needs to be taken not to activate platelets *ex-vivo* since this would cause large amounts of markers to be released, giving a misinterpretation of the level of *in-vivo* activation.

2.2.4 Summary

After reviewing the conventional platelet function tests it is clear that there are limitations that prevent these methods from being widely used in a clinical setup. Some of the most notable drawbacks being cost of operation, time to results, and lack of point-of-care assays. Even though the VerifyNow assay is a point-of-care system it does not provide information regarding *in-vivo* platelet activation. ELISAs and flow cytometry studies are also the only commercially available methods of detecting P-selectin and sP-selectin in blood, but these assays are time consuming and expensive. The development towards inexpensive, point-of-care, and accurate platelet function tests are thus needed to address these issues. Recent advances in biosensor technology has made this possible with more and more research-based approaches appearing in literature as will be discussed in Section 2.3.4.

2.3 Biosensors

Advances in nanotechnology has driven the scientific community toward developing biosensor technologies that could ultimately provide lab-on-a-chip analysis at the point-of-care level. These sensors would be of immense diagnostic and prognostic value in very remote areas where medical care is not always easily accessible. Thus, there is a large movement to make biosensors that are simple to operate, highly sensitive, robust, affordable, miniaturized, and have multiplex capabilities [51]. The operation of a biosensor is briefly described on a conceptual level, followed by a review of some of the current biosensor techniques found in literature. There are numerous types of techniques such as optical, mass-based, electrochemical, and piezoelectrical. But to discuss each of them in detail is not within the scope of this thesis. Only electrochemical biosensors will be described since they have been shown to be robust, affordable, sensitive, and relatively easy to fabricate [52].

2.3.1 Biosensor fundamentals

A biosensor is a device that can detect the presence of chemicals, enzymes, or proteins by using other biomolecules, called the biorecognition element, that are attached to the surface of a physiochemical transducer [53, 54]. A diagram of a basic biosensor setup is shown in Fig. 2.6.

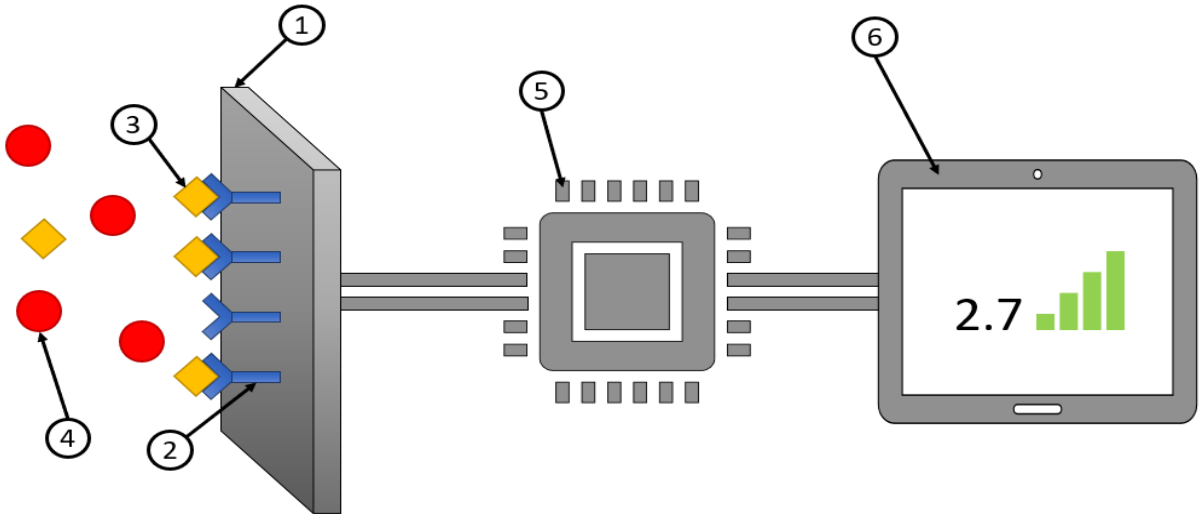

Figure 2.6: A basic biosensor setup consists of a transducer ① with an immobilized biorecognition element ②. The transducer is in contact with the target analyte ③ and the other non-specific proteins ④. The electronic setup ⑤ measures changes at the transducer and converts the electrical signal into a quantitative value ⑥.

The biorecognition element interacts with the target analyte in the solution, leading to physical, electrical, or chemical changes close to the surface of the transducer. The biorecognition element can be any bioelement that shows high affinity for binding to the target analyte, while remaining irresponsive to other interfering molecules in the solution. The transducer "senses" these changes, which are then amplified as an electrical signal by the microprocessor unit.

There is currently no standard for classifying the type of a biosensor since different

approaches are used throughout literature. Some classify biosensors according to the transduction method used, whereas other use either the type of biorecognition element or target analyte as classification method. In this writing the transduction method will be used.

2.3.2 Electrochemical biosensor

Biosensors have the complex task of converting a biological event into an electrical signal. Electrochemical biosensors are thus attractive solutions to this problem since they combine the sensitivity of electrochemical transducers with the high specificity of biological recognition processes [55]. The recognition process results in a catalytic or binding event that ultimately produces a chemical change at the transducer that is proportional to the analyte concentration. This chemical change is then converted into an electrical signal by the transducer. Electrochemical biosensors can be divided into two main categories depending on the recognition process, namely biocatalytic devices and affinity sensors. Biocatalytic devices incorporate enzymes into the sensor that release electroactive species upon recognition of the analyte. An example of such a sensor would be the widely available blood glucose monitoring device that is used by diabetic patients. Affinity sensors, on the other hand, use antibodies, nucleic acids, or receptors that are immobilized on the sensor to selectively bind with the target analyte. Affinity sensors are usually used as an alternative method since selective and sufficient enzymes are not always available for all target analytes [55].

The three main electrochemical transduction techniques that are used are voltammetric, potentiometric, and impedimetric [56]. Another technique, called field-effect, uses transistor characteristics to translate the accumulation of charge at a gate electrode into a measurable current [52, 57, 58]. All electrochemical techniques have a low limit of detection, but they have different drawbacks in terms of simplicity, ease of fabrication, and complexity of a portable measurement setup. Impedimetric biosensors are based on the principle of electrochemical impedance spectroscopy (EIS). It is used to measure the resistive and capacitive components of a material (which could be a biosensor transducer surface) that is excited by a small sinusoidal waveform [59]. This requires more complex measurement electronics that must be able to detect the in/out-of-phase current [59, 60, 61]. Potentiometric biosensors measure the potential of an electrochemical cell while negligible current is flowing. These sensors, however, suffer from slow responses and interference from other non-specific ions in the solution [56]. Voltammetric biosensors function by applying a potential and measuring the resulting current as a function of the applied potential - making this an attractive solution due to its simplicity [62]. It is also reported that voltammetric sensors are more sensitive than potentiometric devices [63, 64]. Thus, only the different voltammetric biosensors will be discussed due to it's simplicity and ease of characterization. The theory behind electrochemistry and some voltammetric techniques is discussed in Section 2.4.

2.3.2.1 Voltammetric biosensors

Electrochemical biosensors usually require three electrodes, namely a counter electrode (CE), reference electrode (RE), and a working or redox active electrode (WE) that are in contact with a solution. The working electrode (usually a redox inert conductive material) serves as the transducer where the biological detection event takes place. The reference

electrode, commonly made from silver/silver chloride (Ag/AgCl), is kept away from the reaction site to maintain a stable potential. The counter electrode (also an inert conductive material) is used to establish a connection to the solution, and allow a current to flow to and from the working electrode [55]. The type of material used for these electrodes are discussed in Section 2.3.3.2.

Voltammetric biosensors operate on the principle that an applied potential (WE versus RE) produces a redox current that is proportional to the analyte concentration [56]. The redox current originates from the reduction or oxidation of an electroactive species at the working electrode/solution interface. This requires that the applied potential is within the region of the redox potential of the species, otherwise little to no current will flow. The most widely used techniques are amperometry, cyclic voltammetry, and square wave voltammetry [62]. They all operate on the same principle of applying a potential and measuring a redox current, but they differ in the type of applied voltage waveform. The experimental results are used to plot the current versus the applied potential, which is called a voltammogram. The voltammogram is then used to make conclusions regarding the analyte concentration. Amperometry, however, does not result in a voltammogram but rather a plot of current versus time.

An amperometric biosensor measures the flow of current due to the application of a constant voltage [56]. An example of a first generation amperometric sensor is where glucose is oxidized in the presence of glucose oxidase (GOx) to produce hydrogen peroxide [65]. The resultant reaction is,

$$\text{glucose} + O_2 \xrightarrow{\text{GOx}} \text{D-gluconic acid} + H_2O_2, \tag{2.1}$$

where the analyte is glucose, the substrate is O_2, and the product is H_2O_2. The amount of oxygen that is consumed, or hydrogen peroxide that is produced, is directly proportional to the unknown amount of glucose in the sample. The oxidation of the hydrogen peroxide at the surface of the electrode produces the current as shown in Fig. 2.7.

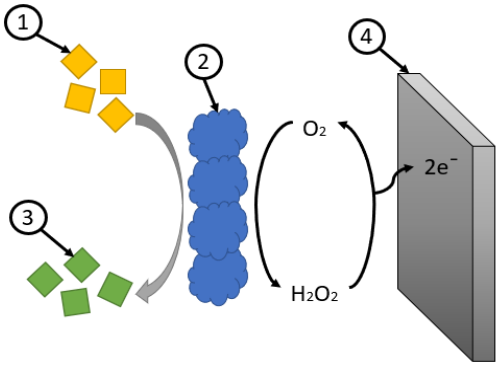

Figure 2.7: Operation of a first generation glucose biosensor based on amperometry. Glucose ① reacts with glucose oxidase ② to produce D-gluconic acid ③ and H_2O_2. The H_2O_2 is then oxidized at the electode ④ to produce a current.

Redox mediators and enzyme-polymer interactions can also be used to enhance the electron transfer and lower the high oxidation and reduction potentials that are needed in first generation amperometric biosensors [56]. Kuek Lawrence *et al.* developed a paper based glucose amperometric biosensor by using a ferrocene monocarboxylic acid mediator [66].

The ferrocene mediator is used to carry the electron from the GOx to the surface of the electrode. Ferrocene is thus reduced, instead of hydrogen peroxide, and then reoxidized at the electrode providing an electrical signal and regenerating the oxidized form of the mediator [67]. The fabrication method is shown in Fig. 2.8.

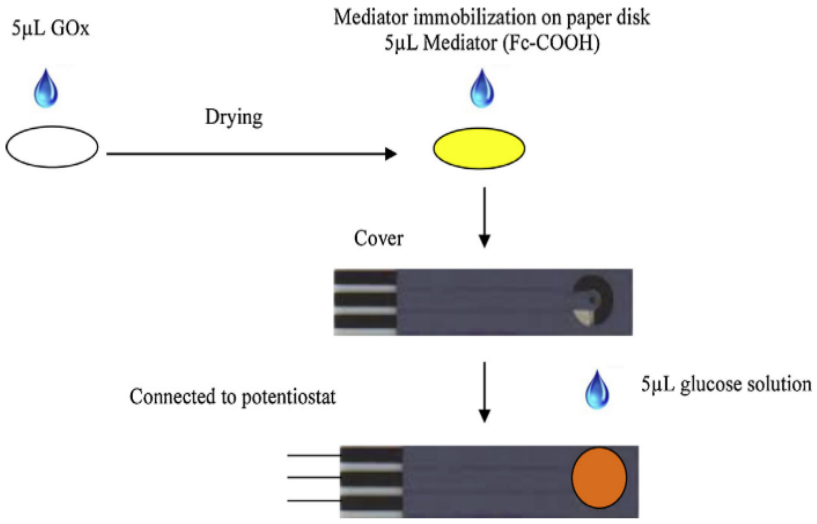

Figure 2.8: Stepwise fabrication method of a glucose biosensor with ferrocene monocarboxylic acid as a mediator. [66]

GOx was adsorbed onto cellulose papers by a dropcasting step and left to dry. The mediator was then added to this paper and placed on top of a disposable screen printed carbon electrode. To optimize the sensor sensitivity, Kuek Lawrence *et al.* performed experiments to determine the optimal pH and redox potential. The biosensor was operated at potentials between 0 and 0.5 V and the current was measured to find the voltage that would result in the largest oxidation current. They also identified a pH of 7.0 as the optimal environment for the biomolecules and the redox behavior of the mediator. Thus, all amperometric experiments were performed at 0.25 V in a 0.1 M phosphate buffer saline (PBS) solution (pH 7.0). The device exhibited a linear calibration curve in the range of 1 to 5 mM glucose ($r^2 = 0.971$) with a detection limit of 0.18 mM. Shelf life tests showed that the sensor only had a 2% degradation in response after 4 months, and it could detect glucose concentrations in soda beverages with results comparable to that of commercial standard tests. This demonstrates that this simple and low-cost sensor shows promising prospects for food processing control.

Cyclic voltammetry (CV) is used to obtain information about the electrochemical reaction rates and the potential where the redox reaction takes place [52]. The applied potential is swept between two values at a fixed rate, but when the voltage reaches the second potential it is swept back to the starting potential. Although cyclic voltammetry can be used for sensing purposes, it is most often used to monitor the process of electrode modification [52]. For example, Kuek Lawrence *et al.* used cyclic voltammetry to monitor the change in peak redox currents as they go through the modification steps of the screen printed electrodes. The resulting voltammograms are shown in Fig. 2.9. The tests were performed at the different stages of the modification process with a scan rate of 25 $mV.s^{-1}$. The black line shows that PBS does not contribute to any redox peaks in the scanned range. The red voltammogram shows that there is some redox reactions present

due to the mediator that is added. The blue line shows that catalytic oxidation is upregulated significantly, which is characteristic of the enzyme dependent oxidation of glucose as mediated by the ferrocene mono-carboxylic acid mediator [68]. Cyclic voltammetry can thus be used as a qualitative and quantitative measure of the modification steps that are followed throughout the fabrication process.

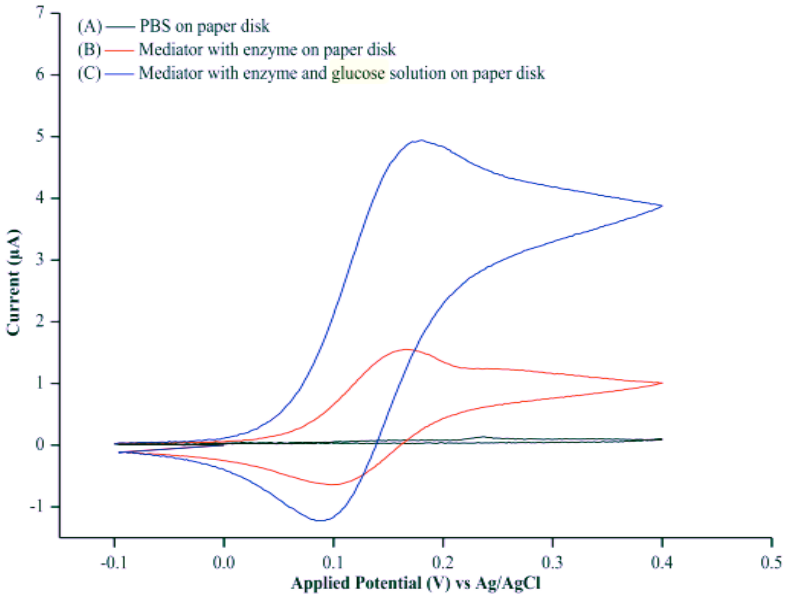

Figure 2.9: Cyclic voltammogram of the immobilized GOx on the paper disk. (A) 0.1 M PBS (pH 7.0). (B) A + GOx with 10 mM ferrocene mono-carboxylic acid. (C) B + 5 mM glucose at a scan rate of 25 $mV.s^{-1}$. [66]

Not only can cyclic voltammetry be used as a tool for monitoring the physical and chemical properties of an electrode or solution, but it can also be used as a way to modify the working electrode. For example, Eissa *et al.* showed how the electroreduction of diazonium salt can be used to create carboxylic acid moieties on the surface of various electrodes [69]. Different carbon based screen printed electrodes (from DropSens, Spain) were subjected to cyclic voltammetry in a carboxyphenyl diazonium salt solution. The electrografting was done using scans from 0.2 to -0.6 V at a scan rate of 100 $mV.s^{-1}$. The voltammogram for a carbon nanofiber (CNF) modified carbon electrode is shown in Fig. 2.10.

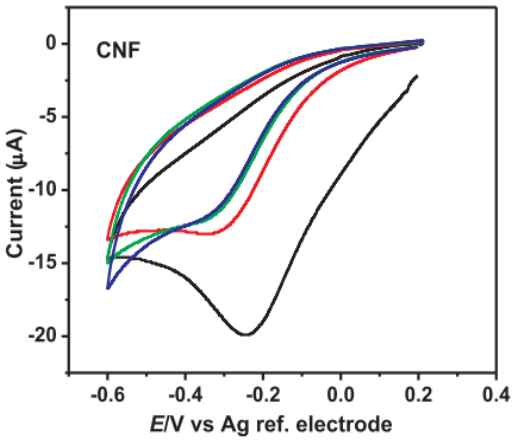

Figure 2.10: Sucessive CV scans of carboxphenyl diazonium salt on a CNF modified electrode. The black line represents the first cycle and the coloured lines represent the subsequent cycles. [69]

The graph shows a strong irreversible reduction current peak at -0.25 V for the first cycle, which then gradually diminishes for subsequent cycles. The peak is generated due to the one electron transfer process between the diazonium salt and the CNF working electrode. The subsequent cycles have smaller intensities because of the increasing number of grafted carboxyl groups, and thus a decrease in the electron transfer efficiency between the salt and the remaining electrode area. They further developed a biosensor for the detection of survival motor neuron (SMN) protein by using square wave voltammetry as a detection technique.

Square wave voltammetry (SWV) has been widely adopted as a sensitive and selective technique of detecting disease-related biomarkers and harmful chemicals. The number of papers that reported using SWV has doubled from 2003 to 2012, which shows that it is increasing in popularity [70]. Briefly put, the method uses a symmetrical square wave superimposed on a stair case resulting in the waveform shown in Fig. 2.11. The current is sampled twice at *S1* and *S2* and the difference current is calculated (*S1* - *S2*) to obtain the voltammogram.

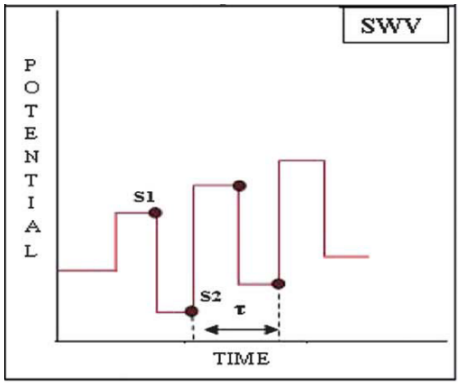

Figure 2.11: Potential waveform used in SWV. [70]

Eissa *et al.* concluded that the CNF electrode was the most responsive platform for detecting SMN protein due to its high surface area and high degree of selectivity against other non-specific proteins. After the electrografting step shown in Fig. 2.10, N-(3-Dimethylaminopropyl)-N-ethylcarbodiimide hydrochloride (EDC) and N-hydroxysuccinimide

(NHS) were used to activate the carboxyl groups for subsequent attachment of the anti-SMN antibody. The detection experiments were performed with SWV in a 5 mM potassium ferricyanide/ferrocyanide ($[Fe(CN)_6]^{3-/4-}$) redox solution prepared in 10 mM PBS (pH 7.4). The scan range was 0.3 to -0.4 V at 125 $mV.s^{-1}$, the frequency was 25 Hz, the pulse amplitude was 20 mV, and the step potential was 5 mV. The voltammograms for different concentrations of the SMN protein are shown on the left of Fig. 2.12 and the calibration curve on the right. The detection was determined by measuring the change in the reduction peak current before and after binding of the SMN protein. They attributed the increase of the reduction peak current to the isoelectric point of the SMN protein. Since the experiments were performed at a pH of 7.4, the SMN protein would be positively charged due to its isoelectric point of 8. The bound SMN proteins thus attract the negatively charge redox anions closer to the surface, leading to an enhanced electron transfer efficiency. The sensor exhibited a linear response from 1.0 pg/ml to 100 ng/ml with a detection limit of 0.75 pg/ml. The biosensor's application in the clinical setup was also tested. Whole blood samples from healthy individuals were diluted in a lysing buffer and spiked with standard SMN solutions of known concentrations. The tests showed that between 91% and 95% of the SMN protein could be recovered, suggesting that the sensor can be applied for testing SMN proteins in whole blood.

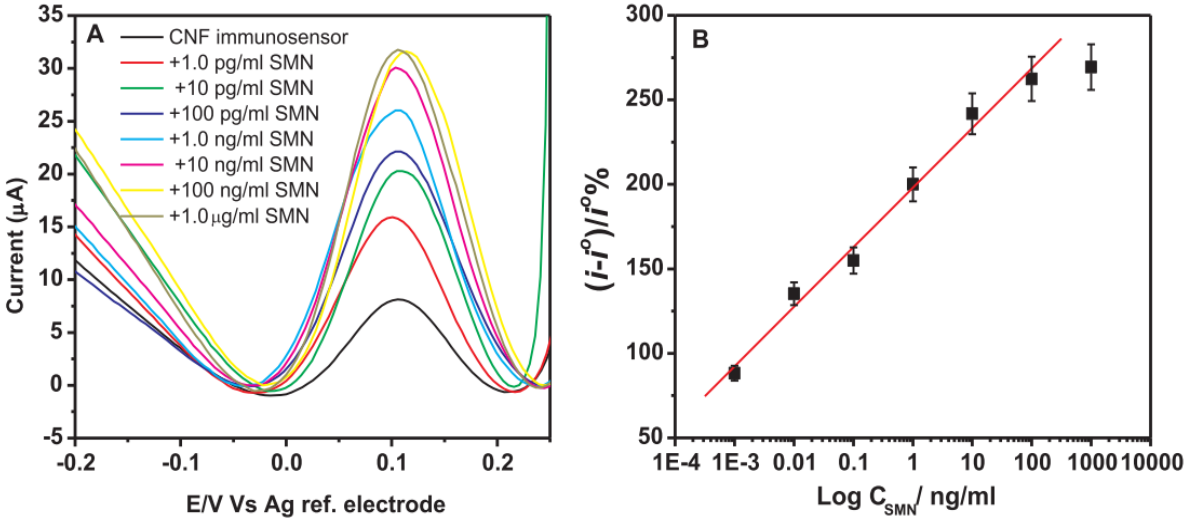

Figure 2.12: Square wave voltammetry results of the CNF sensor for the detection of survival motor neuron disease. A) Voltammograms for different concentrations, and B) the percentage change in redox current peaks for each concentration. [69]

The blocking effect by the analyte can also be used to retard the electron transfer ability as demonstrated by Li *et al.* [71]. They developed a label-free angiogenin biosensor that uses an anti-angiogenin-aptamer capture molecule immobilized on a gold working electrode. The term "label-free" refers to the fact that the captured angiogenin does not need to have a label (fluorescent or amplification) attached to the protein in order for the biosensor to work. The mechanism by which the aptasensor operates is shown on the left of Fig. 2.13. The aptamer modified gold electrode blocks some of the redox anions due to its negatively charged phosphate backbones. This was also verified using electrochemical impedance spectroscopy that indicated that the charge transfer resistance increased significantly after this modification. The addition of increasing concentrations

of angiogenin further suppresses the redox peak current as shown on the right of Fig. 2.13.

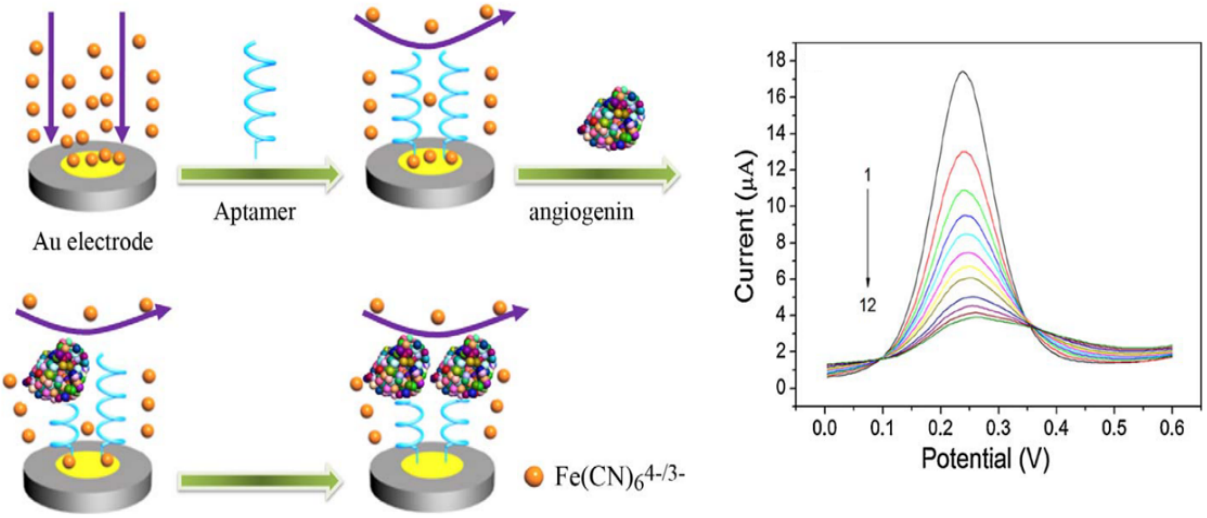

Figure 2.13: Mechanism of operation of the angiogenin aptasensor on the left, and the voltammograms of the different angiogenin concentrations on the right. The concentration increases from curve 1 to 12. [71]

Li *et al.* also compared the sensor response with other electrochemical methods such as CV and EIS. Interestingly, they concluded that SWV was the most repeatable, sensitive and rapid way for detecting angiogenin in a sample. The sensor had a linear detection range from 0.01 nM to 30 nM with a limit of detection of 1 pM. Serum samples of lung cancer patients were tested using the sensor and a commercial Human Angiogenin Immunoassay. The percentage accuracy of the biosensor was calculated as the ratio between the biosensor's measured concentration, and that of the immunoassay. The accuracy varied between 92% and 104%, which shows that the aptasensor is able to work with complex biological samples that are usually prone to non-specific bindings. One drawback that was noted is that the aptamer is not a very stable molecule since it can degrade by nucleases.

It is clear that biosensors based on voltammetric techniques are simple to fabricate, easy to characterize, and show robust performance even with biological samples. But the different voltammetric techniques each have their own advantages and drawbacks. The application of a constant voltage (amperometry) leads to negligible charging currents, which results in smaller background signals and thus lower limits of detection [55]. The amperometric biosensors are thus simple and robust, but unfortunately not all target proteins have associated enzymes that can undergo redox reactions. Most amperometric biosensors focus on testing glucose due its market value, but the technology surrounding the redox enzyme has improved significantly according to an in-depth review done by Bollela *et al.* [72]. Cyclic voltammetry is a good tool for many things, such as modifying the working electrode, monitoring changes at the working electrode, and performing characterization of the biosensor. Its main drawbacks, however, include the charging currents that are generated due to the sweeping potential and longer analysis times when compared to SWV or amperometry. SWV is a technique that reduces that charging currents because the current is sampled at the end of the applied potential pulses. It's high sensitivity,

reliability, and ability to be operated at a high frequency, makes it an attractive technique [70].

2.3.3 Biosensor components

This section looks at the different components that a typical affinity based biosensor device consists of. Recognition element immobilization strategies are discussed as well as the different nanomaterials that can be used to fabricate the electrochemical transducer element.

2.3.3.1 Biorecognition element and immobilization strategies

A biological marker, or biomarker for short, is a naturally occurring molecule, protein, gene, cell, or characteristic that is associated with a specific biological process or disease, and that can be measured reproducibly and accurately [73]. The presence of the biomarker in blood/saliva/urine could indicate that an underlying biological process or disease is active, and the concentration of the marker could give an indication of the degree of activation. A biosensor measures the presence and concentration of a biomarker by using a biorecognition element that is attached to the surface of the transducer. The biorecognition element can be an enzyme, antibody, nucleic acid, or whole cell [52].

Nucleic acids (also referred to as aptamers) are folded single stranded deoxyribonucleic acid (DNA) or ribonucleic acid (RNA) sequences that are highly stable, sensitive, and specific [74]. Aptamers can be synthesized at a low cost and can easily be modified with chemical tags without influencing their ability to bind with a target - which is highly desirable for biosensor fabrication. Aptamers have been used for the detection of cancer biomarkers [71, 75, 76, 77, 78] and numerous foodborne pathogens [74]. Enzymes are also widely used for electrochemical detection techniques for their biocatalytic activity and specificity. They consist of amino acids that catalyze biochemical reactions. These biosensors are simple, inexpensive, reusable, and provide rapid results. They do, however, need to be regenerated periodically since the enzyme layer loses activity. Redox permeable membranes sometimes need to be employed to limit the interference from unwanted electroactive species that undergo redox reactions within the same detection potential. Despite these drawbacks, they are still the most widely available and studied biosensors due to their applications for glucose monitoring for the diabetic population [55]. Enzyme-based biosensors have been used for the detection of glucose [55, 66, 72, 79, 80], l-lactate [81], and cholesterol [82, 83]. Whole-cell based biosensors use live cell lines and cultured cells that are immobilized on a transducer. The transducer detects electrochemical/biochemical changes that these cells undergo as they grow or respond to external stimuli in physiological conditions. Compared to conventional immunoassays, these biosensors provide more complex functional data that is associated with certain signaling pathways. Since cells are extremely sensitive to environmental conditions, such as pH, temperature, and humidity, these sensors are still confined to laboratories that provide control of these factors. Whole-cell based biosensors have been used to study cells using organic electrochemical transistors [57, 58, 84].

Antibodies are of particular importance for the use of affinity based biosensors. They show high specificity for biomarkers due to the molecular recognition between the binding sites on the antibody and the antigen on the biomarker. They make the transducer

sensitive, but that also depends on the immobilization method, immobilization orientation, and low non-specific adsorption to the solid support. The structure of an antibody is shown in Fig. 2.14. It consists of two light chains and two heavy chains that both have constant and variable regions. The antigen binding fragment is denoted by the "Fab" region and the non-antigen binding fragment as "Fc" [85].

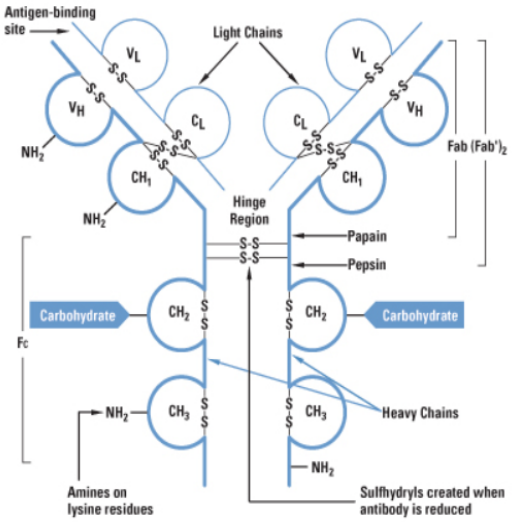

Figure 2.14: Diagram of an antibody showing the various functional groups that can be used for crosslinking. [86]

The antibody must be carefully immobilized so that the antigen binding site is open to interact with the target analyte, and so that its ability to bind with the antigen is not compromised. The orientation can usually be controlled by the interaction between various reactive groups on the solid surface and the antibody molecule. Care must also be taken not to saturate the transducer with antibodies since this can lead to steric hindrance and the formation of multiple layers. Different immobilization strategies are commonly used, such as biotin-streptavidin linkages, adsorption to a conductive surface, and covalent binding [55, 85]. The adsorption method makes use of electrostatic forces, ionic bonds, hydrophobic interactions, and van der Waals forces to functionalize the surface with antibodies. Although this is the simplest method, it leads to random orientation of the antibodies since various functional groups interact with each other [55, 87]. The biotin-streptavidin linkages are part of affinity immobilization methods. When a metallic or functionalized polymeric surface is immobilized with a streptavidin molecule, it provides a surface that shows high affinity for biotinylated biomolecules. The biotin molecule is typically attached to the "Fc" region of the antibody which allows for the uniform and proper orientation of capture antibodies on streptavidin functionalized surfaces. Although this is a relatively simple process, it still requires a specific surface and an antibody that has a biotin tag. These type of antibodies are not always widely available and they can be expensive.

Covalent immobilization involves modifying the surface with a functional group that can form a covalent bond with a functional group on the antibody. It has been studied extensively for its ability to facilitate long-term storage and reusability of sensors. This can be achieved through amine coupling, thiol coupling, or glycomoiety coupling, as shown in Fig. 2.15. Glycomoiety coupling requires creating active diol groups on the "Fc" region

of antibodies and linking them with amine groups that are present on the sensor. This method requires the use of highly reactive chemicals that might reduce the antibody's binding capacity or even result in the loss of some antibodies. The procedure also requires numerous tedious steps resulting in time delays [87]. Thiol coupling requires the binding between a thiol group present on an antibody and an active disulphide group on a surface, or vice versa. The method requires the reduction of the disulphide groups (−S−S−) present on the antibody, shown in Fig. 2.14, to form sulfhydryl-reactive groups (−SH). If the sulfhydryl-reactive group comes into contact with an active disulphide group on the sensor it would form a thiol-disulphide exchange. This method allows more control over the orientation of the antibodies since there are only a few sulfhydryl groups available on the protein [87, 88].

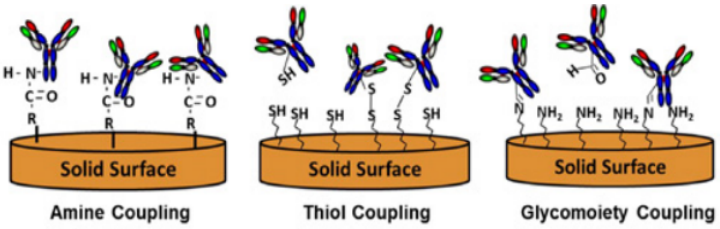

Figure 2.15: Covalent immobilization techniques. [87]

The amine groups present on the lysine chains of the "Fc" fragment (shown in Fig. 2.14) are easily accessible which is why amine coupling is mostly used in literature. These primary amines can be coupled with carboxyl groups (if it is present on the solid surface) that are activated through EDC and NHS crosslinking chemistry. The reaction scheme is shown in Fig. 2.16. EDC reacts with the carboxylic acid group (-COOH) to form an unstable intermediate called o-Acylisourea. This group then couples with the NHS (or sulfo-NHS) to form a more stable amine-reactive ester that improves the reaction efficiency. When the ester comes into contact with a primary amine group, such as that found on antibodies, it forms a stable amide bond.

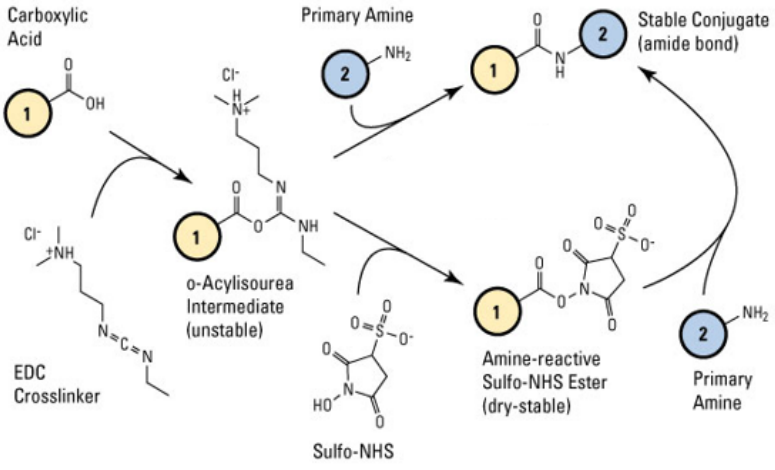

Figure 2.16: The carboxylic acid group is coupled to a primary amine using EDC/NHS crosslinking chemistry. [89]

EDC/NHS crosslinking chemistry has been used extensively in literature for the functionalization of graphene oxide (GPHOX) [90, 91, 92], terminal carboxylated thiol groups on gold [93, 94], and carboxyphenyl diazonium salts [60, 61]. Compared to the thiol and glycomoiety coupling, this method does not require the activation of any groups present on the antibody. It only requires that the carboxyl groups present on the transducer are activated. It does, however, suffer from randomly orientated antibodies since there are so many different primary amine groups on the molecule. Some low-cost materials, such as graphene oxide (discussed in Section 2.3.3.2), already contains carboxyl groups, which makes it an attractive transducer that is increasingly being used for biosensing applications [95, 96]. However, most polymer or metallic surfaces do not have carboxyl groups present and thus it should be introduced through chemical or physical modification of the material. Some of these modifications processes are described below.

One approach is that of Eissa *et al.* described in Section 2.3.2.1 [69]. They used the electroreduction of carboxyphenyl diazonium salts to create functional groups on different carbon-based materials. They compared screen-printed electrodes with a carbon counter electrode, a silver reference electrode, and different working electrodes (graphene, graphene oxide, carbon nanofiber, single-walled carbon nanotubes, multi-walled carbon nanotubes, and carbon). The modification scheme is shown in Fig. 2.17. 4-carboxyphenyl diazonium salt was prepared by mixing sodium nitrite and 4-aminobenzoic acid in hydrochloric acid, and subjecting it to CV on screen-printed electrodes. The diazonium salt molecules close to the working electrode are reduced which leads to the elimination of the nitrogen molecule and the formation of an aryl radical that can be grafted on the electrode. The grafted carboxyl groups were then activated by EDC/NHS crosslinking chemistry and the anti-SMN antibody was attached. One drawback of this method is that multiple organic layers can be formed during the electrografting step [97]. This would make the lower layers unusable and it can possibly result in a less sensitive transducer.

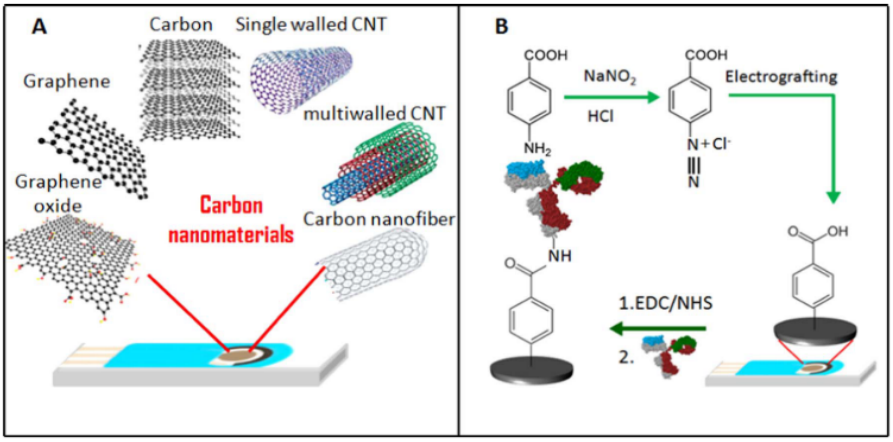

Figure 2.17: A) shows the different working electrode materials that were used, and B) shows the electrografting scheme with the attachment of the antibodies. [69]

Baraket *et al.* used a similar method to immobilize antibodies to the surface of gold electrodes [98]. Interestingly, they firstly attached the antibody to an aryl diazonium salt and then grafted the whole molecule using an electroaddressing step. The 4-carboxymethyl aryl diazonium salt was incubated with monoclonal antibodies and EDC/NHS was used to form an amide bond. This solution was then diazotated in hydrochloric acid and sodium

nitrite. The carboxymethyl-modified antibody was then grafted onto the gold working electrodes using five CV scans from 0.3 to -1.4 V at a scan rate of 100 mV/s.$^{-1}$. The modification scheme is shown in Fig. 2.18.

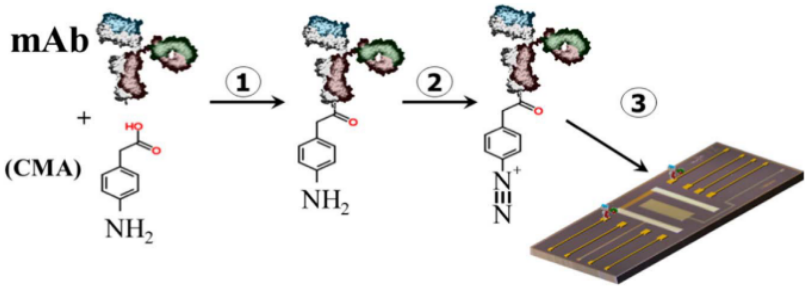

Figure 2.18: ① The antibody is modified with the diazonium salt using EDC/NHS crosslinking chemistry. The modified antibody is then diazotated ② and grafted to the surface of the gold electrode using CV ③. [98]

The performance of a biosensor is directly influenced by three factors: 1) it needs to have a functioning biorecognition element attached to the transducer; 2) the recognition element needs to be able to bind with a target analyte; and 3) the surface should exhibit low non-specific adsorption [52, 87]. The latter can lead to false signals that are not related to the target analyte, but are rather due to random proteins that are adsorbed to the transducer. This can be circumvented by using a surface site blocker such as bovine serum albumine (BSA). After the capture element is incubated on the sensor a washing step is usually performed to remove the unbound capture proteins. Then BSA is incubated on the sensor to block the free surface sites that were not utilized by the capture proteins.

It is clear that there are numerous different immobilization strategies - each with their own advantages and limitations. The chosen method will be determined by many factors, such as the type of capture protein, the availability of the capture protein or a tagged version, and most importantly the transducer material.

2.3.3.2 Transducer

The type of transducer material that is used will depend on the type of biosensor that is designed. Common materials include gold-coated glass for optical biosensors based on surface plasmon resonance [94, 99, 100, 101], poly(3,4-ethylenedioxythiophene) polystyrene sulfonate for organic electrochemical transistors [57, 58, 102, 103], and gold for quartz crystal microbalance sensors [93, 104, 105]. Hybrid transducers are also used to enhance the performance of the biosensing platform, such as graphene oxide and gold for surface plasmon resonance biosensors [92] and gold-nanoparticle modified graphene for impedance sensors [106]. Theoretically, any type of metal or conductive polymer can be used for biosensors based on electrochemistry, but certain materials are preferred due to their properties. The material is typically chosen based on criteria such as biocompatibility, conductivity, stability in an aqueous environment, surface-to-volume ratio, cost, and the presence of functional groups for crosslinking.

Graphene oxide is a single atomic layer material that has various oxygen containing groups on the basal planes and edges of the flakes, as shown in Fig. 2.19. These functional groups

and the large surface area of graphene oxide makes it an ideal platform for protein immobilization [90]. Specifically, the carboxyl groups (−COOH) on the edges of the flakes can be used to immobilize antibodies using EDC/NHS crosslinking chemistry.

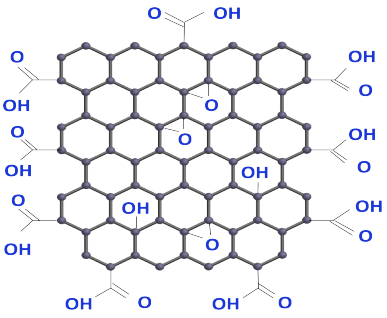

Figure 2.19: Chemical structure of a graphene oxide flake showing the reactive groups present on the basal plane and outer edges. [107]

Graphene oxide is commonly used to modify a standard glassy carbon electrode so that it has a lower charge transfer resistance. This is desired since smaller changes at the electrode/solution interface can be measured, ultimately leading to a more sensitive biosensor. Current literature utilizes this technique of modifying a glassy carbon electrode with colloidal graphene oxide by using a dropcasting step [75, 90, 108, 109].

Carbon nanofibers, another novel carbon based nanomaterial, have also been used to create an enhanced electrochemical biosensor platform. These fibers are composed of graphene layers that are folded into cylindrical nanostructures, and stacked as cones and cups [110]. Commercial techniques such as catalytic chemical vapor deposition are commonly used to fabricate these fibers. It involves the decomposition of gas-phase molecules at high temperatures, followed by the subsequent growth of the fibers on a substrate around metal catalyst particles. Some of the individual strands, shown in Fig. 2.20, can be grown up to a few micrometers long, and between single nanometers and a few hundred nanometers wide.

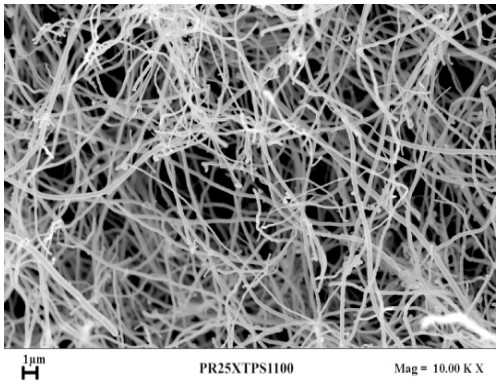

Figure 2.20: Electron microscopy photo of carbon nanofibers. [110]

The outer walls of the fibers have edge plane defects that can facilitate the electron transfer of an electroactive species in a solution. The whole surface of the fiber can also be activated to produce a wide range of oxygen containing groups without degrading the structural integrity. This, along with the fact that it has a very large surface-to-volume

ratio, is why it is an ideal immobilization matrix for biomolecules.

Various companies (such as DropSens, Spain) have started manufacturing carbon-based screen-printed electrodes as shown in Fig. 2.21. The strip consists of a ceramic substrate ($3.4 \times 1.0 \times 0.05$ cm) with a carbon counter electrode, a silver reference electrode, and various working electrode materials. The strip also has silver connections that can be connected to any potentiostat device with the proper connection cable. It is a relatively low-cost (≈R100) and disposable platform that can be used for electrochemistry experiments and research purposes, making it ideal for establishing a working proof-of-concept. It provides numerous advantages, such as being premodified with a biocompatible material, it contains all the needed electrodes in a small area, and it can be used with small sample volumes (≈ 50 μl).

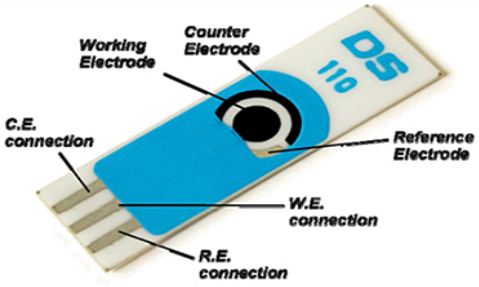

Figure 2.21: A commercial screen-printed electrode from DropSens, Spain. [111]

2.3.4 Research-based platelet function biosensors

Platelet function testing is needed to understand the pathology of these multitalented cells and to aid in diagnostics and prognostics of diseases and abnormalities. This, accompanied by the limitations of conventional platelet function tests, has spurred the development of new technologies to assess platelet function. This section discusses some of these research-based devices that are used to test platelet activation and coagulation abilities.

Kailashiya *et al.* have developed a graphene oxide-based biosensor for the detection of platelet-derived microparticles [112]. These particles are a major risk factor for thrombus formation that could ultimately lead to strokes and acute myocardial infarction [8, 16, 113]. A modified glassy carbon electrode, shown in Fig. 2.22, was used as the working electrode for this sensor. Graphene oxide was dropcasted onto the glassy carbon electrode to create functional carboxyl groups. EDC and NHS was added to the surface to activate the carboxyl groups for the attachment of antibodies. Thereafter, 5 μl of PAC-1 antibody was dropcasted onto the sensor and incubated for 1 hour. PAC-1 antibodies bind to the active conformation of GP IIb/IIIa receptors that are expressed on the platelet-derived microparticles [114]. This makes the biosensor specific for activated platelet microparticles and not circulating microparticles derived from other cells. A blocking step was performed with BSA to deactivated the remaining active carboxyl binding sites. Electrochemical impedance spectroscopy was performed on an Autolab PGStat 302NFRA2 (from Metrohm, The Netherlands) using a platinum wire counter electrode, Ag/AgCl reference electrode, and the modified glassy carbon electrode as working electrode. 15 μl of the microparticle suspension (in platelet poor plasma) was dropped on

the modified electrode and left to incubate for 15 minutes before a final washing step to remove the unbound particles. The experiments were carried out in 5 mM potassium ferricyanide ($K_3Fe(CN)_6$) in the range of 0.1 - 10 000 Hz at 0.2 V with a 10 mV alternating current (AC) signal.

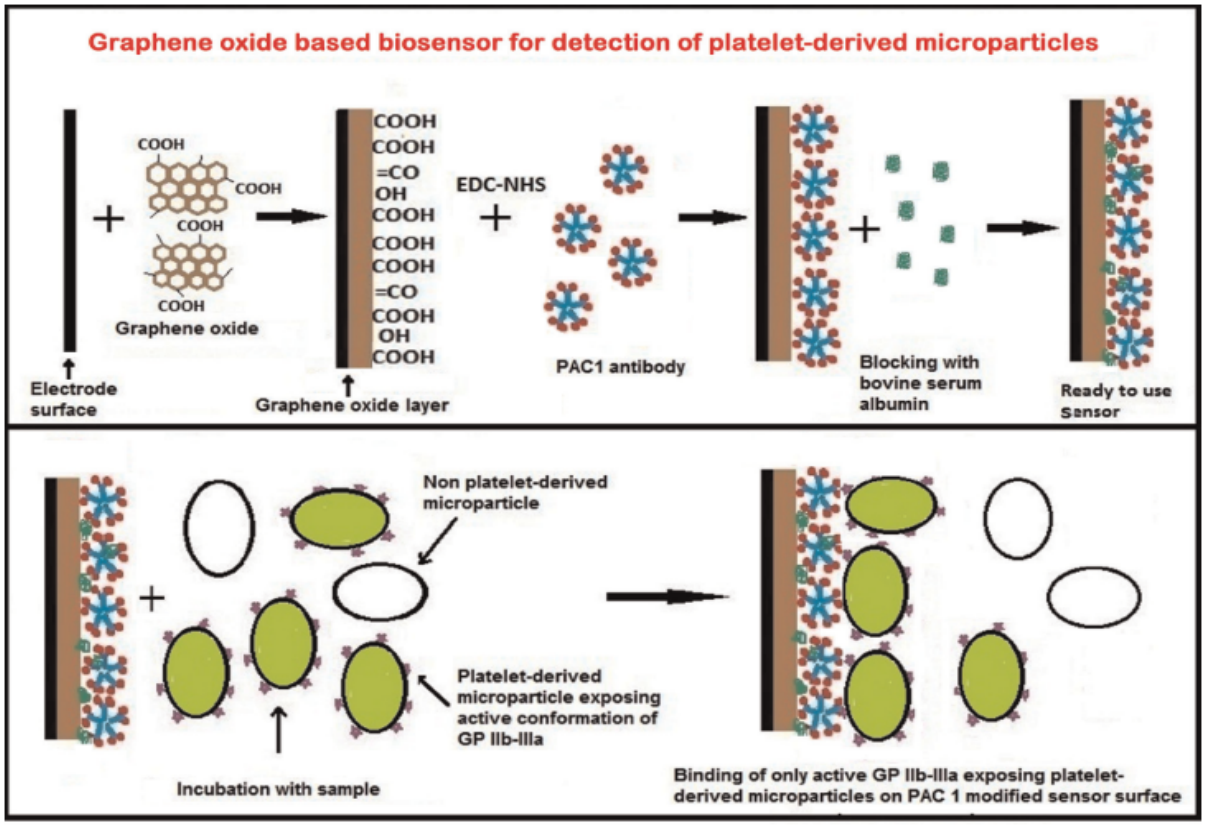

Figure 2.22: Schematic design of the graphene oxide biosensor for the detection of platelet derived microparticles. The diagram shows the stepwise immobilization of graphene oxide, PAC-1 capture antibody, and BSA onto a glassy carbon electrode. [112]

The nyquist plots, shown in Fig. 2.23, showed a progressive rise in the impedance due to increasing number of platelet microparticles. The sensor obtained a linear relationship from 100 to 7000 microparticles per μl and an r^2 value of 0.942. Control experiments were also conducted to test the sensor specificity for platelet microparticles. It was reported that platelet poor plasma without microparticles showed hardly any change, whereas platelet poor plasma with microparticles showed a significant increase in impedance. The sensor was also tested for clinical application by comparing patients that have been diagnosed with acute myocardial infarction and matched healthy individuals. Both flow cytometry and the biosensor showed a significantly higher number of circulating platelet microparticles in the diagnosed individuals. In fact, it was reported that the biosensor was more sensitive and specific for platelet microparticles compared to flow cytometry - obviating the need for such a time consuming and expensive test.

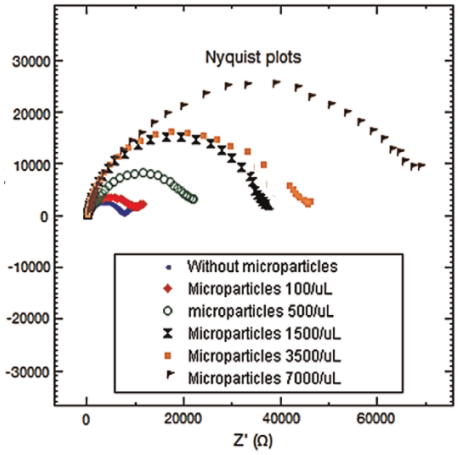

Figure 2.23: Nyquist plots of the experiments showing a rise in the impedance due to increasing number of platelet microparticles. [112]

The same group has since improved this sensor by using a novel nanosilica approach to detect platelet microparticles in blood [115]. Chronoamperometry and cyclic voltammetry were utilized for the electrochemical deposition of thionine doped silica nanoparticles onto indium tin oxide (ITO) glass. The nanosilica acts as a large surface area for the attachment of biomolecules and the thionine acts as an electron transfer mediator which enhances the sensitivity of these sensors [116]. PAC-1 antibodies were then immobilized onto the silica nanoparticles using glutaraldehyde as a crosslinking agent. HRP entrapped amine functionalized mesoporous silica nanoparticles were functionalized with P-selectin antibodies to act as a secondary detection antibody in a sandwich type assay. The modification scheme is shown on the left of Fig. 2.24. The experiments were performed with an Autolab PGStat 101 (from Metrohm, The Netherlands) using a platinum wire counter electrode, Ag/AgCl reference electrode, and the modified ITO glass as working electrode. Experiments were repeated 3 to 5 times to confirm the results.

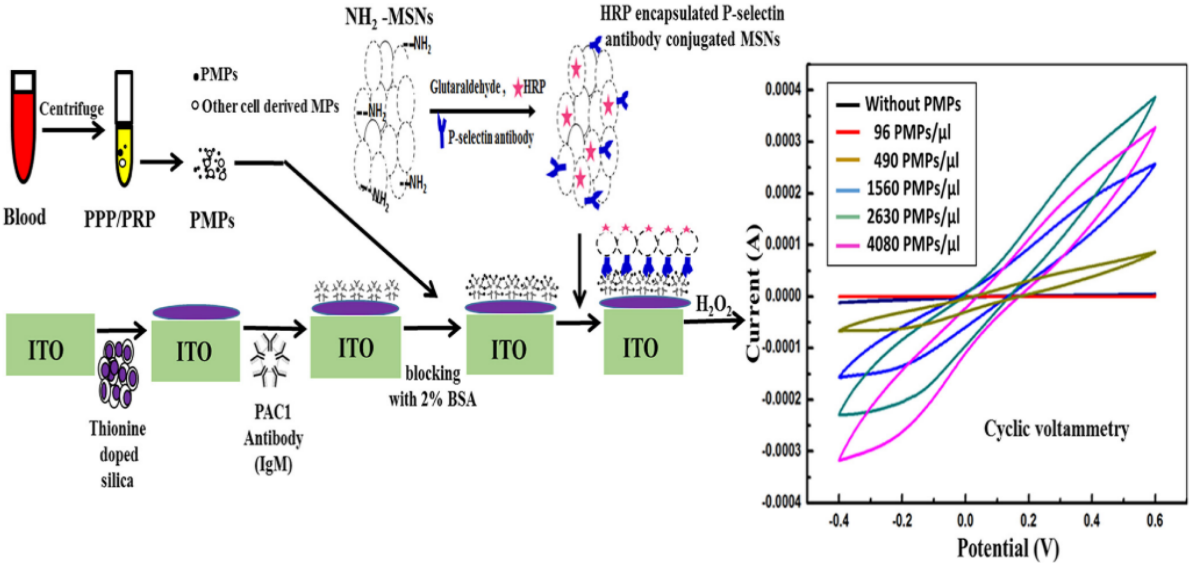

Figure 2.24: Schematic illustrating the modification process of an ITO glass electrode on the left, and the experimental results on the right. [115]

When a fixed concentration of H_2O_2 is immobilized onto the sensor it is reduced by the HRP encapsulated in the mesoporous silica nanoparticles on the working electrode. The cyclic voltammetry graphs, shown on the right of Fig. 2.24, shows that the reduction peak current increases with a higher number of microparticles. This confirms that there is a direct correlation between the number of HRP molecules and the number of microparticles in the sample. The sensor had a linear response between 490 and 4080 microparticles per μl and the detection limit was 96 microparticles per μl. This sensor has detection limits that are comparable to flow cytometry, and can thus be used as a biosensor for the detection of platelet microparticles within the relevant range (100 to 4000 per μl) in blood plasma [117]. It was also reported that the sensor maintained its stability with only a 5% reduction in electrochemical response after 1 month. This promising sensor has been patented and the group is aiming to develop a miniaturized sensing platform based on this work.

The development of micro- and nanofluidics have opened up possiblities of measuring thrombus formation using whole blood at defined shear rates. When parallel-plate flow chambers are combined with microscopic imaging techniques, it can give valuable information regarding the thrombogenic potential of blood. Different parameters can be controlled, such as shear rate, chamber surface coatings, and chamber temperature to closely simulate the *in-vivo* characteristics in which platelets aggregate [118]. There is, however, very little widespread use of microfluidic devices for monitoring thrombus formation in the clinical setup. This is mostly due to the difficulty of converting complex microscopic techniques into simple devices which provide quick results. There is one commercially available device that uses a finger-prick sample of blood to measure high-shear thrombus formation. It functions by oscillating blood through a narrow channel with a spring to hold the thrombus [25, 119]. The device measures the time to occlusion of the channel, which gives information regarding the time it takes for the platelets to form a clot.

Ergenzen *et al.* have developed an electromechanical sensor to monitor platelet adhesion and aggregation to collagen fibers in real-time [120]. The thickness shear mode (TSM) sensor is a piezoelectric-based sensor that functions by applying an AC voltage to produce a mechanical shear strain and vice versa. The excitation signal produces standing acoustic waves on the sensor, shown in Fig. 2.25, which can be used to monitor a deposited mass. This resonator can also be operated at odd harmonics, instead of the fundamental harmonic, to assess the properties of the deposited mass at various depths. Loading of the sensor with a biological medium will result in magnitude changes of the resonant frequency which can be correlated with the mechanical properties at the surface/medium interface. The sensor consisted of a quartz crystal with bonded gold electrodes on either side. It was coated with insoluble fibrillar collagen type I to mimic the site of injury within a blood vessel. The sensor was placed in the bottom of a static cell while the magnitude and frequency response was continuously monitored as 200 μl samples of either water, PBS, platelet poor plasma, or platelet rich plasma were added to the cell.

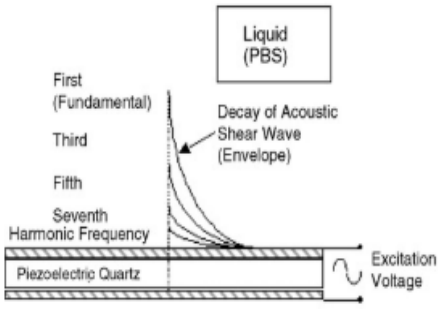

Figure 2.25: Penetration depth of the fundamental and harmonic resonant frequencies of the TSM sensor. [120]

They showed that the sensor was sensitive to the different phases of platelet adhesion, activation, and aggregation on collagen-coated gold surfaces. The technique could also detect molecular mechanisms that are involved in the process of hemostasis, proving that this could be a useful assay for monitoring platelet disorders or antiplatelet therapy. These sensors have also been used to study nanoparticle-induced platelet aggregation [121], and for monitoring antiplatelet therapy as an alternative to using the conventional LTA [104].

2.4 Electrochemistry

Electrochemistry is the study of chemical reactions and the flow of electrons between different chemical compounds. It describes how electrons would flow due to certain chemical reactions and, vice versa, how the flow of electrons would have a certain chemical reaction as an outcome. This section looks more closely at the electrochemistry behind electrochemical biosensors by considering the mathematical model of the electrochemical cell and describing the electron transfer kinetics. It also describes the methods of cyclic voltammetry and square wave voltammetry in more detail.

2.4.1 The electrochemical cell

The electrochemical cell consists of the three electrodes that are immersed in an electrochemical solution. The electrochemical solution typically consists of a supporting electrolyte and an electroactive species that can undergo redox reactions in response to changes in the cell potential. The supporting electrolyte is typically a salt that is dissolved in a solvent to decrease the solution resistance. By varying the cell potential in different ways, one can measure different characteristics of the electrochemical cell. Electrochemical impedance spectroscopy is commonly used to build a model of the cell by applying an AC potential and measuring the resulting AC current [55]. This provides useful information about phenomenon that takes place at the electrode/solution interface, such as charge transfer resistance and solution resistance [65]. The different electrical components of the model can then be used to determine what changes have been made to the cell due to the binding of biomolecules on the working electrode surface. The Randle's equivalent circuit, shown in Fig. 2.26, is frequently used to model the cell characteristics.

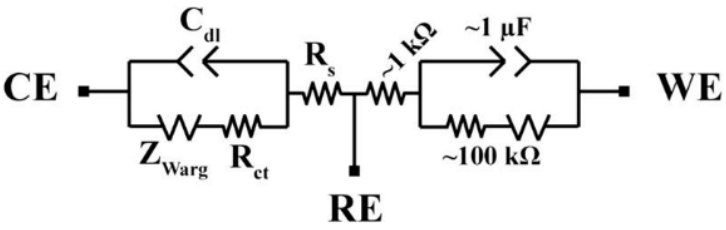

Figure 2.26: The Randle's equivalent circuit of an electrochemical cell. C_{dl} is the double layer capacitance, R_{ct} is the charge transfer resistance, Z_{Warg} is the Warburg impedance, and R_s is the solution resistance. [122]

The double layer capacitance (C_{dl}) is due to the distribution of ions close to the charged electrode and the electrode capacitance itself. Therefore, it's value depends on the concentration of the ions in the solution and the voltage of the electrode since this would influence the electrostatic forces between the ions and the electrode. This capacitance is responsible for the background current (sometimes called non-faradaic current) that flows regardless of whether the redox active species is present [123]. It is directly proportional to the scan rate that is used for cyclic voltammetry, which is why this technique is not always sensitive enough for characterizing biosensors. Since electrochemical biosensors are primarily concerned with the faradaic current (redox current), it is desirable to minimize the non-faradaic current to be able to detect small changes. The charge transfer resistance (R_{ct}) is a measure of the ability of the electrode to transfer electrons to and from the solution due to redox reactions. The value can be infinite if no redox active species are present, but in faradaic experiments it depends on the concentration of the redox molecule and the electrode material and voltage. The Warburg impedance (Z_{Warg}) models the movement of the redox molecules to and from the electrode surface. The solution resistance (R_s) is a characteristic that models the drifting of the ions in the bulk of the solution (i.e. far away from the electrode), and thus acts as a solution conductivity measurement.

The type of supporting electrolyte that is used plays a major role in electrochemical experiments since it needs to balance the charge of the cell. A good supporting electrolyte has to have the following characteristics [123]:

- It needs to be a liquid at the experimental temperatures;
- It needs to be redox stable in the potential range of the experiment. In other words, it cannot undergo redox reactions in the same potential range as the electroactive species that are studied;
- It needs to provide a suitable environment for biomolecules;
- The salt concentrations need to be as high as possible to increase the solution conductivity so that it is easier to balance charge in the cell;
- The salt concentrations need to be as high as possible to limit the analyte migration.

The last characteristic that was mentioned above is worth examining in detail. The electroactive species can be transported to the working electrode through the electrochemical cell by three methods: convection, migration, and diffusion. Convection is a mode of transport that requires stirring of the solution through mechanical means. Migration is

the movement of the electroactive species due to an electrical field (such as attraction due to electrode charge). Both of these modes are not considered since it simplifies the theoretical predictions and modeling of the cell behavior. Convection is excluded because the solution is not stirred, and the migration of the electroactive species is limited by using high salt concentrations for the supporting electrolyte. The latter causes the salt ions to migrate to balance charge instead of the ions of the electroactive species [123]. Diffusion due to a concentration grading is thus the only mass transport mode that is considered when the cell behavior is predicted.

2.4.2 Electron transfer kinetics

The current that flows between the counter and working electrode is due to two processes. Firstly, at the electrode/solution interface it is due to the redox reactions that transfer electrons between electroactive species and the electrode. This can be described as,

$$\mathrm{Ox} + \mathrm{e}^- \rightleftharpoons \mathrm{Red}, \tag{2.2}$$

where Ox is the oxidized form of the species, and Red is the reduced form. And secondly, in the bulk solution it is due to the migration of ions that is similar to the movement of charge carriers. Consider for example the reduction reaction in Fig. 2.27. An oxidized form of the electroactive species receives an electron from the working electrode and is reduced. This reduced form of the molecule then diffuses away from the electrode to the bulk solution due to the concentration gradient that exists. Oxidized species in the bulk solution also experience a concentration gradient and thus they tend to migrate to the working electrode.

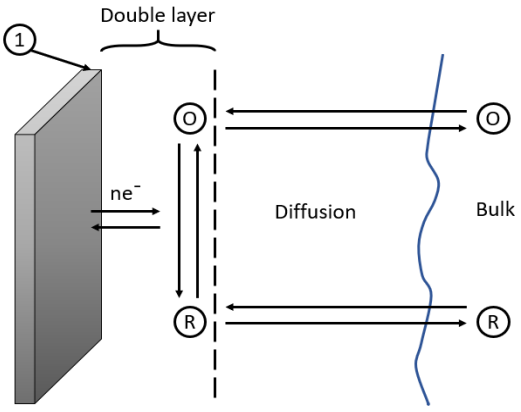

Figure 2.27: The electroactive species undergo redox reactions at the electrode (1) and diffuse between the bulk solution if a concentration gradient exists.

This is referred to as the heterogeneous transfer of electrons. The driving force behind this transfer is the difference in the energy of the electrons in the electrode and the energy of the lowest unoccupied molecular orbital of the oxidized form of the species. If the electrons in the electrode has more energy than that of the lowest unoccupied molecular orbital of the oxidized species, an electron will be transferred from the electrode to the molecule [123].

When a reduction reaction occurs at the working electrode an oxidation reaction occurs at the counter electrode, and vice versa. Although the reaction at the counter electrode

is not the main concern of electrochemical experiments, it is important that the electron transfer kinetics at this electrode do not inhibit the flow of current. Therefore, the counter electrode usually has a larger surface area than the working electrode and it is made of a redox inert material [123].

2.4.3 The Nernst equation

The description of the Nernst equation and cyclic voltammetry is adopted from an excellent practical guide on voltammetry written by Elgrishi *et al.* [123], and an electrochemistry textbook written by Belding *et al.* [124]. The section on square wave voltammetry is based on a book about electrochemical methods written by *Bard & Faulkner* [125].

Electrochemical biosensors are mainly concerned with measuring the faradaic current instead of the non-faradaic current. Usually, the conditions, such as scan rate, are chosen so that the capacitive current is minimized compared to the current from electron transfer. The faradaic current due to the electron transfer kinetics and electroactive species diffusion rate can then be described using the Nernst equation,

$$E = E^0 + \frac{RT}{nF} \ln \frac{[Ox]}{[Red]}, \tag{2.3}$$

where E is the electrochemical cell potential, E^0 is the standard potential of the oxidized and reduced forms at equilibrium, R is the universal gas constant, T is the temperature, n is the number of electrons, F is Faraday's constant, $[Ox]$ is the concentration of the oxidized form, and $[Red]$ is the concentration of the reduced form. For the simple one electron transfer reaction the standard potential is replaced with the formal potential, $E^{0,}$, and n is replaced by 1 so that,

$$\begin{aligned} E &= E^{0,} + \frac{RT}{F} \ln \frac{[Ox]}{[Red]} \\ E - E^{0,} &= \frac{RT}{F} \ln \frac{[Ox]}{[Red]} \end{aligned} \tag{2.4}$$

where the formal potential can usually be determined experimentally to be halfway between the peak reduction and oxidation potential values. This is only true for a reversible redox couple. A redox couple is said to be reversible if it can be reduced and oxidized at the working electrode. The formal potential can be calculated as,

$$E^{0,} = \frac{E_{pa} + E_{pc}}{2}, \tag{2.5}$$

where E_{pa} is the potential at the peak anodic current (due to the oxidation reaction), and E_{pc} is the potential at the peak cathodic current (due to the reduction reaction). Note that Eq. 2.3 and Eq. 2.4 are only valid for the concentrations of the electroactive species in the immediate vicinity of the working electrode. Eq. 2.4 can be used as a tool to predict how the concentrations of the redox couple would change due to a change in the applied cell potential, and vice versa. For example, consider the case where only the oxidized form of the species is present in the solution at the start of the experiment. If the applied voltage is smaller than the formal potential ($E < E^{0,}$), then by Eq. 2.4 it would lead to the reduction of the oxidized species. If the voltage is then made greater than the formal potential ($E > E^{0,}$), it would lead to the oxidation of the reduced species.

If $E = E^{0,}$ is applied, the equation predicts that the concentrations would be the same. The reactions are easier to visualize by considering the cyclic voltammetry graphs that are shown in Fig. 2.28.

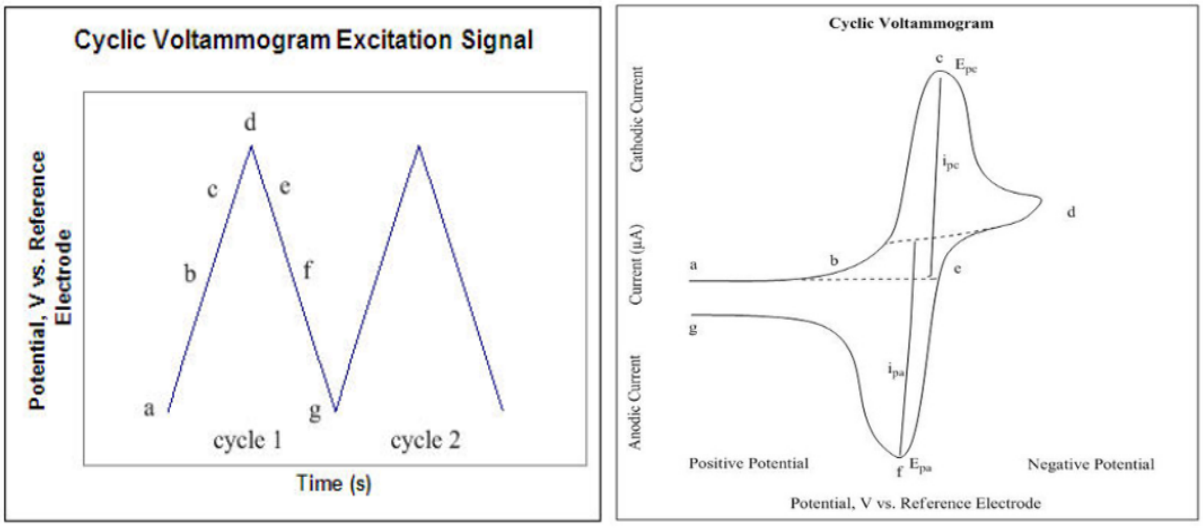

Figure 2.28: Potential sweep of a cyclic voltammetry experiment (left) and the resulting voltammogram (right). [126]

The triangular waveform is applied to the working electrode to sweep the cell potential from a positive (a) to a more negative potential (d). This is referred to as the cathodic scan. Eq. 2.4 predicts that the cathodic scan will lead to the reduction of the electroactive species, and thus the resulting current is referred to as the reduction or cathodic current. This current reaches it's peak value at E_{pc} (c) and it has a value of i_{pc} (called the peak cathodic current). The reverse scan (from (d) to (g)) scans from a negative to a more positive cell potential which is called the anodic scan. Eq. 2.4 predicts that this scan would lead to the oxidation of the species that were just reduced, and thus this current is called the anodic current. It reaches it's maximum value at E_{pa} (f) and it has a value of i_{pa} (called the peak anodic current). There are a few things that are worth mentioning when analyzing a voltammogram.

Firstly, the peak currents are not measured from zero, but relative to baseline currents. The baseline currents are indicated by the dotted lines in the voltammogram and they can be the result of the background capacitive current or other electroactive species that have redox potentials in the vicinity of the scanned potential. The residual current for the reverse scan ((d) to (g)) is also affected by the switching potential value at (d). The baseline currents can be reduced by using a smaller scan rate or using a perfectly reversible redox couple that fully satisfies the Nernst equation. Luckily, most potentiostat devices come equipped with software that can accurately determine the baseline currents.

Secondly, it is not necessarily true that an experiment has to start with the cathodic scan. The starting potential and scan direction largely depend on the form of the electroactive species at the start of the experiment. If only the oxidized form of the species are present, the first potential is usually chosen to start far positive of the reduction potential and then scan to a more negative potential in order to reduce the species. If only the reduced form of the species are present, the potential would start at a negative value and

then scan to a more positive value in order to oxidize the species. Some systems start an experiment with both the oxidized an reduced form of redox couple in the solution at an equal concentration. Thus, it does not matter which way is scanned first since a current will be observed in both scan directions.

Thirdly, the faradaic current does not increase past the peak reduction or oxidation potential due to the current becoming diffusion limited. For example, as the potential is scanned more negatively it leads to the reduction of the species at the working electrode. This leads to the build up of the reduced form in the immediate vicinity of the electrode, which retards the diffusion of the oxidized species from the bulk solution to the surface. Thus, upon scanning to more negative potentials, the rate of diffusion becomes slower which results in the decreasing current from (c) to (d).

And then lastly, there are two conventions, as shown in Fig. 2.29, that are used when representing the data on a voltammogram. The two conventions are just mirror images of each other but they convey the same information. The IUPAC convention will be used in this project.

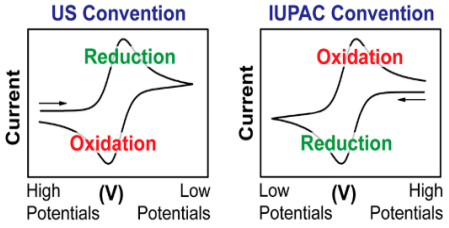

Figure 2.29: The different conventions that are used when representing a voltammogram. [123]

The experimental results are influenced by many factors and it is often wise to do numerous iterations to perfect the system before using it as a biosensing technique. The electrochemical potential window, that is dependent on the type of electrode and supporting electrolyte, should be determined for the system. This must be done to make sure that the electrode and supporting electrolyte are redox inert in the scanned window. The electrodes should also be cleaned of possible contaminants and stirred before each experiment to make sure no bubbles are present on the surface. A background scan should also be done without the redox active species to quantify the capacitive current. Although cyclic voltammetry is a good method for studying the redox couple, more sensitive methods are employed for biosensing, such as square wave voltammetry.

Square wave voltammetry is part of a collection of techniques called pulse voltammetry. It changes the cell potential by pulsing between potential values instead of linearly sweeping between them, such as in cyclic voltammetry. It involves the application of a symmetrical square wave superimposed on a staircase potential as shown in Fig. 2.30.

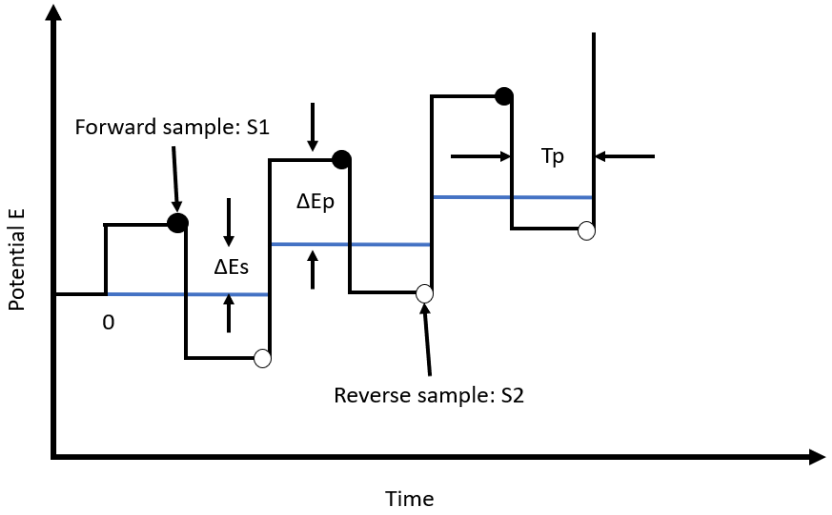

Figure 2.30: Square wave voltammetry waveform.

The square wave amplitude is denoted as ΔE_p, the step height as ΔE_s, the pulse width as t_p, and the forward and reverse current samples as S_1 and S_2, respectively. The current response is calculated as $S_1 - S_2$ and plotted against the staircase waveform. Since the diffusion layer close to the electrode is not renewed at the beginning of each measurement cycle, it is inherently more complex to calculate the theoretical peak current response. The conditions for each pulse cycle is a complex function of all the previous cycles and the kinetics and mechanisms of the chemistry linked to the electrode process [125]. If it is assumed that only the oxidized form of the species is available in the bulk solution, the peak current can be calculated as,

$$\Delta i_p = \frac{nFA\sqrt{D_O}C_O^*}{\sqrt{\pi t_p}}\Delta\Psi_p, \tag{2.6}$$

where Δi_p is the differential peak current, F is Faraday's constant, A is the working electrode surface area, D_O is the diffusivity of the oxidized species, C_O^* is the concentration of the oxidized species in the bulk solution, t_p is the pulse width, and $\Delta\Psi_p$ is a dimensionless value related to the number of transferred electrons and the SWV parameters. The main advantage of SWV is that the charging (non-faradaic) current is excluded which makes this technique more sensitive than cyclic voltammetry. The charging current decays at an exponential rate, whereas the faradaic current decays at a rate that is inversely proportional to the square root of time. Sampling the current at the end of each pulse therefore results in a negligible charging current compared to the faradaic current. The technique can be operated at high frequencies which means that quick results can be obtained and electroactive species can be conserved [70].

2.5 Potentiostat devices

A potentiostat is a device that uses three electrodes to perform electroanalytical experiments in an electrochemical cell. The potentiostats that are used to characterize electrochemical biosensors are mostly benchtop devices that are confined to specialized laboratories. This equipment is often very expensive and have a lot of functionality that are not useful for developing and testing electrochemical biosensors. Recently, more

portable and affordable potentiostats have been developed to circumvent these problems. This section serves as a review and comparison of the current commercial and research-based potentiostats that are used for electrochemistry. The commercial devices that will be reviewed are from companies that specialize in electrochemical instrumentation. The devices are the Gamry Interface 1010T (Gamry Instruments, United States of America), 910 PStat Mini (Metrohm, The Netherlands), and PalmSens 4 (PalmSens, The Netherlands). The research-based potentiostats that will be discussed is the DStat [127], a dual-microprocessor potentiostat [128], and the Universal Wireless Electrochemical Detector [129]. The principle of operation is firstly examined.

2.5.1 Principle of operation

The main function of a potentiostatic circuit is to control the potential at a working electrode so that the current can be measured at a known and constant potential. Two electrode configurations achieve this by using the setup shown in Fig. 2.31A. The potential is measured between the counter and the working electrode, while the current flowing through the working electrode is monitored. This configuration measures the potential drop across the whole electrochemical cell instead of the potential drop across the half-cell reaction of interest that occurs at the working electrode [130]. It is also very difficult for the counter electrode to maintain a constant interfacial potential while current is passed through the electrode [125]. This fact, along with the uncompensated voltage drop across the whole solution, leads to poor control of the interfacial potential at the working electrode.

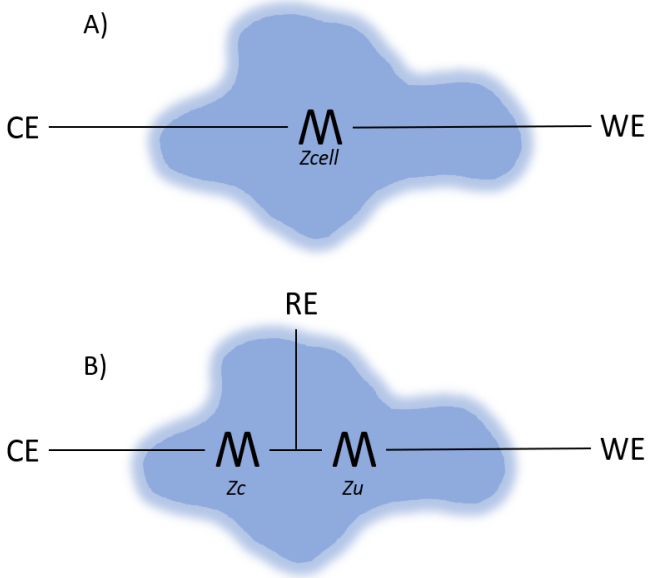

Figure 2.31: A simplified model of the electrochemical cell in the case of 2- and 3-electrode configurations. A) Shows the 2-electrode configuration that consist of the counter (CE) and working electrode (WE) separated by the cell impedance, Z_{cell}. B) Shows the 3-electrode setup that consists of a third reference electrode (RE) that separates the cell into a compensated, Z_c, and uncompensated impedance (Z_u).

Therefore, the counter electrode is separated into two electrodes (shown in Fig. 2.31B) to form a new electrode, called the reference electrode. This electrode is used to maintain a stable potential while the current is passed through the counter electrode. In this

configuration, the working electrode is also kept at a stable and know potential. The potential difference between the working and reference electrodes are controlled at all times by the amount of current that flows between the counter and working electrode. The potentiostat instrument applies the necessary potential to the counter electrode so that the potential difference between the working and reference electrode is equal to that specified by the user [130]. The reference electrode is designed so that no current flows through it, causing only a small uncompensated potential drop across Z_u between the reference electrode and the working electrode [131]. This configuration also allows the counter electrode to supply enough current to compensate for the potential drop of the half-cell reaction occurring at the electrode and the potential drop of the solution resistance, which are modeled together as Z_c. The electronic circuit that is used to achieve this operation is shown in Fig. 2.32. The electrochemical cell potential is usually reported as the potential of the working electrode versus the reference electrode as can be noticed in some of the published voltammograms (for example Fig. 2.28). Therefore, the same convention is used throughout this thesis. For the calculations in this work, the current is also chosen to flow into the working electrode.

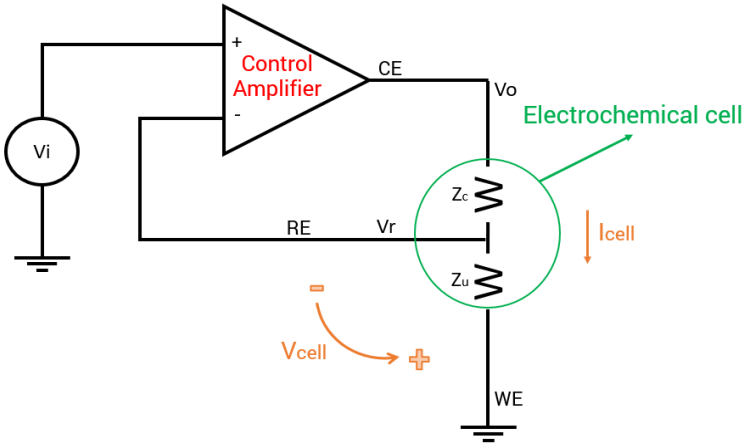

Figure 2.32: A simplified schematic of the potentiostatic circuit that is used to control the 3-electrode configuration.

The role of the amplifier is to amplify the difference of the two input terminals according to,

$$\begin{aligned} V_o &= A(V_+ - V_-) \\ &= A(V_i - V_r), \end{aligned} \tag{2.7}$$

where V_o is the output of the amplifier, and A is the open-loop gain of the amplifier. Furthermore, it is assumed that negligible current flows through the reference electrode since it is connected to a high input impedance path. The cell current can then be described according to,

$$I_{cell} = \frac{V_o}{Z_c + Z_u}, \tag{2.8}$$

and,

$$I_{cell} = \frac{V_r}{Z_u}, \tag{2.9}$$

where I_{cell} is the cell current, Z_c is the compensated impedance, and Z_u is the uncompensated impedance. The combination of Eq. 2.8 and Eq. 2.9 then gives,

$$\begin{aligned} \frac{V_o}{Z_c + Z_u} &= \frac{V_r}{Z_u} \\ V_r &= \frac{Z_u}{Z_u + Z_c} V_o \\ V_r &= \beta V_o \end{aligned} \tag{2.10}$$

where β is the portion of the output voltage used in the feedback path. The combination of Eq. 2.7 and Eq. 2.10 then leads to the following equation,

$$\begin{aligned} V_r &= \beta A(V_i - V_r) \\ &= \beta A V_i - \beta A V_r \\ \frac{V_r}{V_i} &= \frac{\beta A}{1 + \beta A} \\ &= \frac{1}{\frac{1}{\beta A} + 1}. \end{aligned} \tag{2.11}$$

The βA factor is usually much larger than 1 and thus Eq. 2.11 reduces to,

$$V_r = V_i, \tag{2.12}$$

which proves that the amplifier functions by maintaining the potential between the reference and working electrodes to be equal to the input voltage, V_i.

A slightly more complicated circuit is shown in Fig. 2.33. The I-V converter amplifier keeps the working electrode biased at ground potential while the current is converted to a voltage using the feedback resistor, R_f. This amplifier keeps the working electrode at ground potential so that,

$$\begin{aligned} V_{cell} &= V_w - V_r \\ &= 0 - V_i \\ &= -V_i, \end{aligned} \tag{2.13}$$

where V_{cell} is the cell voltage, V_w is the working electrode potential, V_r is the reference electrode potential, and V_i is the applied potential. The resulting current can then be measured as,

$$\begin{aligned} V_{out} &= -I_{cell} \times R_f \\ \therefore I_{cell} &= -\frac{V_{out}}{R_f} \end{aligned} \tag{2.14}$$

where V_{out} is the output voltage of the I-V converter, R_f is the feedback resistor, and I_{cell} is the cell current.

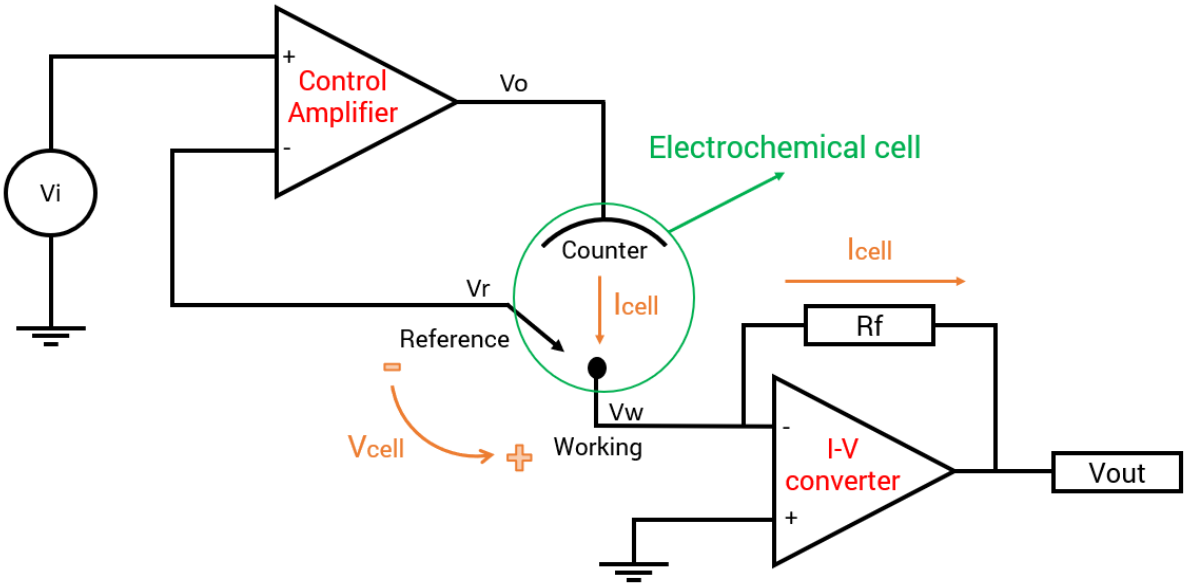

Figure 2.33: A basic potentiostat using simple operational amplifier circuit.

Since there are different ways to control the voltage between two electrodes, there are also different ways to build a potentiostatic circuit. Each setup has varying parameters, requirements, or advantages, but they all measure different aspects of the same phenomenon. Every potentiostat functions by moving and displacing charge at the interface between the working electrode and an electrolytic solution within an electrochemical cell. The electrochemical cell typically contains a salt solution with an electroactive species present in this solution. By controlling the cell voltage, V_{cell}, one can force the electroactive species to undergo redox reactions at the working electrode, resulting in the transfer of electrons at the interface of the solution and the electrode.

2.5.2 Commercial potentiostat devices

This section reviews some of the commercially available potentiostats. The entry level devices are discussed for each of the companies listed. This is because the lower range commercial potentiostats have all the needed features for performing electrochemical experiments for biosensor applications. The drive towards lab-on-a-chip analysis also considers affordability to be a factor when designing these systems, which further motivates the discussion of only the entry level devices. Table 2.1 gives a summary of the main technical specifications of the three devices.

Table 2.1: Summary of the specifications of entry level commercial potentiostats.

	PalmSens4 (PS4.F0.05)	**Gamry Interface 1010T**	**910 PSTAT mini**
Potential specifications			
Range	±5 V	±5 V	±2 V
Resolution	75 μV	200 μV, 50 μV, 12.5 μV/bit	1 mV
Accuracy	$\leq$ 0.1%, ±1 mV offset	±1 mV, ±0.2% of setting	not provided
Current specifications			
Range	9 ranges (± 100 pA to ± 10 mA)	6 ranges (±1 μA to ±100 mA)	6 ranges (±2 nA to ±200 μA)
Resolution	0.006% of current range (5 fA on 100 pA range)	0.0035% full-scale/bit	0.1% for ranges ±10 nA to ±100 μA, 10 pA in the smallest range
Accuracy	$\leq$ 0.1%, at full scale range	±5 pA, ±0.3% of range	not provided

PalmSens' flagship product, the PalmSens4, is a handheld potentiostat, galvanostat, and impedance analyzer that is USB or battery powered. It can be extended with a frequency response analyzer to perform very sensitive experiments such as electrochemical impedance spectroscopy. It is also the lightest device between the three, weighing only 500 g. The battery can last for 4 hours at maximum cell current, which makes it ideal for use in resource-limited areas. Apart from having more current ranges than the competitors, it also has the smallest current range between the three devices. It's high accuracy and resolution make it an attractive option, but it comes in at a hefty price of R100 000.

Gamry Instruments' entry level device is the Interface 1010T. It is designed for undergraduate and teaching laboratories and it comes equipped with impedance measurements up to 20 kHz. The instrument needs to be operated with specialized software and powered with an AC wall socket, making this device unsuitable for remote areas. It is a large and heavy device, making it more suitable for benchtop experiments in a laboratory setup.

The 910 PSTAT mini from Metrohm is a small and compact potentiostat that can be controlled using a PC. It can perform all the necessary electrochemical techniques such as cyclic voltammetry, square wave voltammetry, differential pulse voltammetry, and amperometric detection. Even though it is a portable device, it still requires power from a USB cable and connection to a PC to be operated. One merit of note for this potentiostat is that the upper limit of the current range is only ±200 μA, which is substantially lower than the other two devices. If experiments are performed with a high concentration of electroactive species it would result in saturation of the measured current and thus artifacts will be introduced in the data. The user can thus either use a lower concentration or smaller electrodes which might come at the cost of a lower signal-to-noise ratio. The device costs about R49 000.

All of the listed potentiostats have the necessary requirements to characterize biosensors, but there are still some drawbacks. Most notably the portability and affordability are the limiting factors for using these devices at the point-of-care level. Nonetheless,

they can still aid in the development of an electrochemical biosensor. Research-based potentiostats often test their own operation and accuracy by using the commercial devices as benchmarks. If very specific specifications are needed for an electrochemical biosensor it would be a good idea to first determine the requirements using a more robust benchtop device. Thereafter, a more specialized and portable potentiostat with only the needed techniques can be fabricated at a fraction of the cost.

2.5.3 Research-based potentiostat devices

The drive towards more portable electrochemical biosensors have fueled the development of miniaturized electronics that can perform specific experiments at the point-of-care level [60, 61]. The ideal device should be portable, affordable, miniaturized, easy to use, battery powered, and capable of performing accurate measurements. There will always be a tradeoff between performance and cost when designing these devices. As the sensors get smaller, so does the electrode area. This requires sensitive, low-noise, and accurate measuring electronics incorporated into more robust designs which can get quite expensive. Literature thus contain simple solutions such as an Arduino based potentiostat [132] to more complex designs using complementary metal-oxide-semiconductor technologies [133].

2.5.3.1 DStat

One of the entry level devices, known as CheapStat, was designed as an open-source solution that can be used for educational purposes [134]. It costs less than $80 and has a wide range of applications from food- and drug-quality testing to environmental monitoring and rapid DNA detection. Another open-source design that outperforms the CheapStat and is comparable to benchtop equipment, is called the DStat ($120 per unit) [127]. It was developed as a general-purpose potentiostat that can easily be integrated with other instruments, making it more versatile than conventional equipment.

The DStat has a voltage range of ± 1.5 V and utilizes a high resolution 16-bit digital-to-analog converter (DAC) to apply potentials with a resolution of 46 μV at a maximum sampling rate of 100 kHz. The DAC also employs a 4th order low pass reconstruction filter with a cutoff frequency of 35 kHz to reduce the effect of aliasing. The sinewave outputs for CheapStat and DStat are compared in Fig. 2.34 to show the effects of aliasing. The CheapStat does not employ a reconstruction filter and has a low sampling frequency of 2 kHz, resulting in the jumps seen on the blue waveform. These jumps will result in transient spikes in the non-faradaic current at the working electrode, leading to erroneous readings [127].

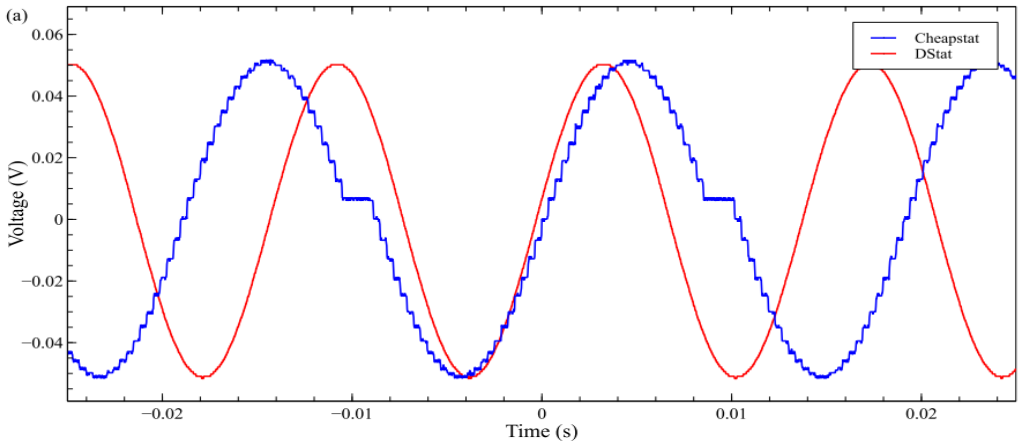

Figure 2.34: Sinewave output comparison between the CheapStat (blue) and the DStat (red), showing the effect of aliasing.

To aid in the selection of a sufficient analog-to-digital converter the current measurement circuit was simulated and the input referred noise was calculated. The size of the analog-to-digital converter (ADC) step was identified as the limiting factor in overall resolution (rather than the analogue noise) for all ADC resolutions less than 16-bits. The DStat thus employs a 24-bit ADC for accurate measurements. The device also makes use of an ATxmega256A3U microcontroller unit (MCU), which serves as a balance between cost and performance. It is used to control all the digital components and communicate with a personal computer (PC) using the onboard USB port. It makes use of the LMP7702 op-amp for controlling the cell voltage and a LMP7721 op-amp for measuring the cell current. These op-amps were chosen due to their high input impedance, low input bias voltages, low input bias currents, low input referred voltage noise densities, and high unity gain bandwidth. As a comparison with the CheapStat and a commercial EmStat from PalmSens, a cyclic voltammetry experiment was conducted in 10 mM potassium hexacyanoferrate (III) using commercial screen printed electrodes. The resulting voltammograms are shown in Fig. 2.35.

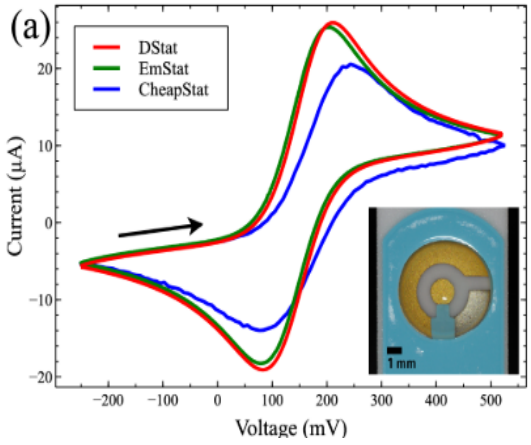

Figure 2.35: Comparison between DStat (red), CheapStat (blue) and EmStat (green) using screen printed electrodes in 10 mM potassium hexacyanoferrate (III). [127]

It is clear that the DStat outperformed the CheapStat in showing results similar to that of a commercial potentiostat.

2.5.3.2 Dual microprocessor potentiostat

Another design utilized dual microprocessors for the control and signal processing of electrochemical biosensors [128]. The motivation behind the design is the timing mismatch that exists when only one processor is used to generate the waveform and measure the resulting current. The design, shown in Fig. 2.36, utilized MCU1 to generate the waveform, and MCU2 to measure the current and communicate with the PC. The auto-range current-to-voltage converter uses different resistor values with the transimpedance amplifier to change the measured current range and resolution. The potentiostat's technical specifications were given as ±1.6 V voltage range under the resolution of 1 mV, a minimum programmable scan rate of 5 mV/s, and a current range of ±16 mA in the resolution of 8 μA to ±160 nA in the resolution of 80 pA. The device uses two C8051F005 processors with 12-bit onboard DACs and ADCs. It was compared to a commercial potentiostat (CH Instrument Model: CHI1221) and the results were almost the same.

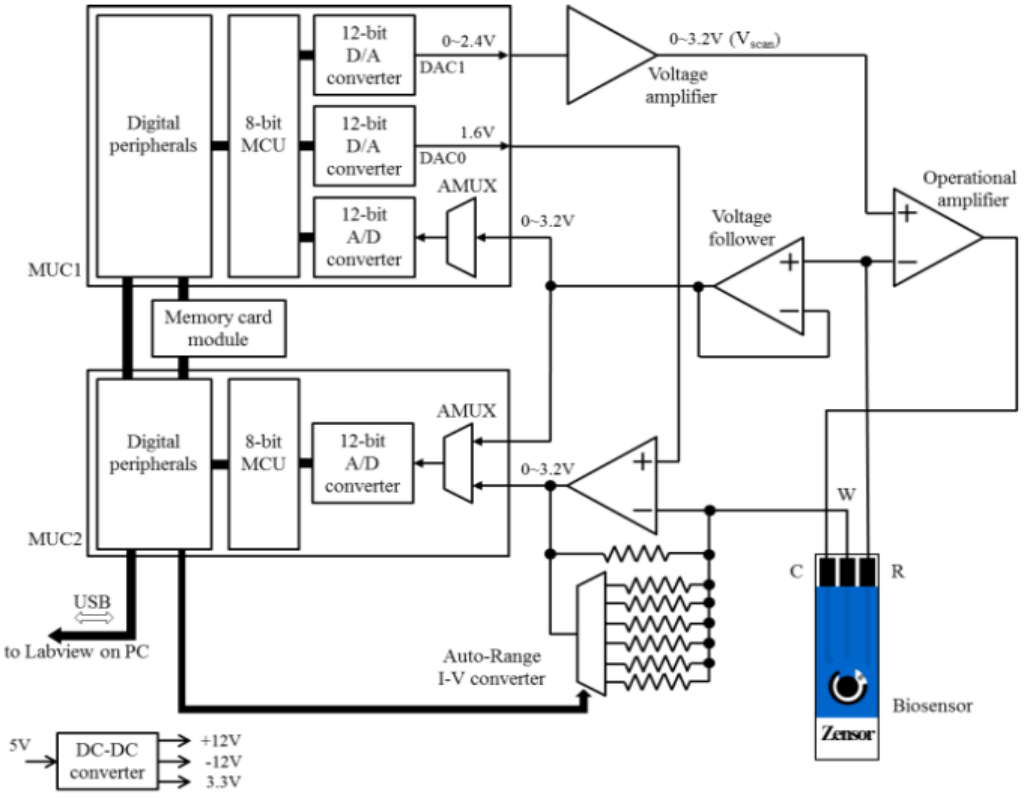

Figure 2.36: The circuit diagram of a potentiostat design using two microprocessors. [128]

2.5.3.3 Universal Wireless Electrochemical Detector

The Universal Wireless Electrochemical Detector (UWED) is a matchbox sized, battery powered, wireless potentiostat device that is capable of performing four different electroanalytical techniques [129]. It uses Bluetooth Low Energy (BLE) to communicate with a smartphone device that provides the user with an interface to perform experiments and receive results in real time. The smartphone application (App) can be used to store, process, and transmit the data to the cloud. The device is simple, compact, and affordable to construct making it ideal for use in resource-limited areas where no high-end electronics are available. It is reported that a single unit costs $61.50, but if components are ordered

in bulk it would cost as little as $15 per unit. The device and the App is shown in Fig. 2.37.

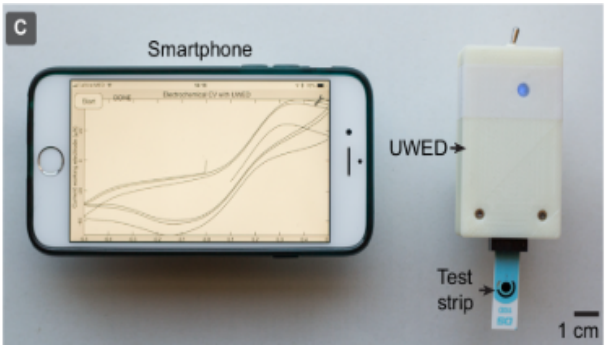

Figure 2.37: The Universal Wireless Electrochemical Detector (right) with the smartphone App (left). [129]

The device was developed to be complementary to the Universal Mobile Electrochemical Detector (UMED) which was designed by the same group [135]. The main limitation of the UMED was that each electroanalytic protocol had to be "flashed" to the device before the experiment could be performed. The UWED addresses this issue by allowing the user to change the experimental protocol without needing to change any hardware or firmware of the device. The UWED employs an RFduino microcontroller unit that contains peripheral components, such as BLE for communication, I^2C for interfacing with an external DAC, and a 10-bit ADC for performing measurements. A 3.7 V lithium ion battery is used to supply power to the electronics at 3.3 V which allows experiments to be performed within the range of ± 1.5 V. The battery could also last for 40-60 hours at full operation. The current range was reported to be ± 180 μA. The device had more noise when compared to a commercial potentiostat, but this could be decreased if the sampled current was averaged, or if an external higher resolution ADC was used.

2.5.3.4 Summary

Following the discussion it is clear that there are many ways to design a potentiostat device. All of the discussed devices utilized different electronic components to achieve the same goal, but only with different technical specifications. The DStat design showed that it is better to have high resolution ADCs and DACs to achieve low noise in the system. The dual microprocessors system showed that having multiple processors to generate the waveform and measure the current simultaneously, is beneficial to reduce timing errors. Although the UWED had more noise than conventional potentiostats, it is a fully portable and wireless solution that can be used with a smartphone App.

2.6 Project objectives and proposed methodology

There are two main goals to this project: firstly to prove the principle of operation of an electrochemical immunosensor that would be able to detect sP-selectin proteins, and secondly to develop a device that can interface with the sensor to perform measurements and ultimately determine the concentration of sP-selectin in a sample. The proposed methods for each of these goals are described below:

Sensor proof of concept

1. Graphene oxide and carbon nanofiber modified screen printed electrodes from DropSens will be used to establish the proof of concept;
2. The working electrode will be electrografted using diazonium salt to created carboxyl supports for antibody immobilization;
3. The carboxyl groups will be activated using EDC/NHS carbodiimide crosslinking chemistry to attach sP-selectin antibodies;
4. Electrochemical experiments will be performed on the prepared immunosensors using a Gamry Interface 1000E instrument, and square wave voltammetry as the diagnostic technique;
5. Data analysis will be performed to accurately extract the peak currents from the voltammograms.

Portable potentiostat device

1. The necessary technical specifications for a portable potentiostat device will be acquired by using the results from the experiments on the Gamry device. The results include the necessary potential range to produce a redox peak, and also the magnitude of the current for common electrochemical measurements on the sensors;
2. A potentiostatic circuit will be designed and components will be acquired;
3. The circuit will be analyzed in LTSpice in terms of a DC analysis, AC analysis, and noise analysis;
4. A printed circuit board layout will be built and characterized;
5. A communication protocol will be developed to allow the device to communicate data back to a computer;
6. The operation of the device will be compared by using the Gamry Interface 1000E as the benchmark potentiostat;
7. Ultimately, the portable potentiostat will be used to perform detection experiments with the sP-selectin immunosensor.

Chapter 3

Methodology

This chapter begins by describing the method that was used to develop an immunosensor for detecting proteins in a physiological buffer sample. A commercially available screen printed electrode sensor was modified in a stepwise manner to ultimately function as a biosensor that can detect soluble P-selectin proteins. This is followed by the design and characterization of a more portable potentiostat device that was used to perform square wave voltammetry on the immunosensors as a diagnostic technique. The final electrochemical measurements were first performed on the commercial potentiostat device, and then the home-built device was used. Lastly, a data analysis algorithm was developed to accurately analyze the electrochemical measurements that are performed on the sensors.

3.1 Biosensor development process

This section describes the experimental process that was followed to characterize the unmodified commercial sensors, and ultimately modify them to function as a biosensor. The process was divided into different steps, namely: determining the electrochemical potential window of the unmodified sensors, characterization with square wave voltammetry, reproducibility studies of the unmodified sensors, electrografting of the working electrode using diazonium salt reduction, activation of the working electrode through crosslinking chemistry, and ultimately the attachment of the soluble P-selectin antibody to the working electrode. Table 3.1 shows the materials and products that were acquired for this project.

Table 3.1: Materials and products acquired.

Product	**Company**	**Cost**
EDC, N-(3-Dimethylaminopropyl)-N'-ethylcarbodiimide hydrochloride, E7750-1g	Sigma Aldrich	R410
Sulfo-NHS, N-Hydroxysulfosuccinimide sodium salt, 56485-250mg	Sigma Aldrich	R1 571
Potassium ferricyanide(III), $K_3Fe(CN)_6$, 702587-50g	Sigma Aldrich	R563

Table 3.1 continued from previous page

Product	Company	Cost
Potassium hexacyanoferrate(II) trihydrate, $K_4Fe(CN)_6 \cdot H_2O$, P9387-100g	Sigma Aldrich	R312
Phosphate buffer saline, PBS(1X, pH 7.4), 10010056, 500 mL bottle	Thermo Fisher Scientific	R250
MES buffer, 2-(N-Morpholino)ethanesulfonic acid, 69889-50g	Sigma Aldrich	R2 057
Sodium chloride, NaCl	Borrowed from Stellenbosch University, Physiological Science Department	-
Distilled water	Borrowed from Stellenbosch University, Physiological Science Department	-
Hydrochloric acid, HCl	In stock	-
Sodium hydroxide, NaOH	Borrowed from Stellenbosch Univeristy, Physiological Science Department	-
4-aminobenzoic acid	In stock	-
Sodium nitrite, $NaNO_2$	In stock	-
DRP-110GPHOX sensors, 100 units	DropSens	R9 740
DRP-110CNF sensors, 100 units	DropSens	R9 192
Recombinant human sP-selectin, ADP3-050μg	Whitehead Scientific	R4 867
Human P-selectin Monoclonal Antibody, BBA30-200μg	Whitehead Scientific	R6 821
DRP-CAC, Connection cable for screen-printed electrodes	In stock	-
Hexaammineruthenium(III) chloride, $Ru(NH_3)_6Cl_3$, 262005-250mg	Sigma Aldrich	R766

All electrochemical measurements for the sensors were done on a Gamry Interface 1000E potentiostat from the Department of Process Engineering at Stellenbosch University, unless stated otherwise. SWV electrochemical measurements were conducted in 100 μl of

the appropriate solution using the following parameters: 5 mV step size, 20 mV pulse size, 25 Hz, and a 2 second equilibrium time. Different potential ranges were used depending on the nature of the experiment, but the remaining parameters were chosen to be the same as reported in literature for similar immunosensors [69, 71]. The potential ranges are stated in the text. The equilibrium time is the time the electrochemical cell spends at the initial potential before the scan starts. This is done to allow the migration of ions and reactions in the cell to equilibrate after the initial potential is applied. The ferricyanide/-ferrocyanide redox couple consisted of 5 mM $Fe(CN)_6^{3-/4-}$ in PBS(1X, pH 7.4) in equal molar ratios. In some instances the pH of this solution was changed, but this is explicitly stated in the text. Throughout the rest of the text the ferricyanide/ferrocyanide redox couple will be abbreviated as FeCN to distinguish it from the hexaammineruthenium(III) chloride redox probe, which will be abbreviated as RuHex. This probe was also used as 5 mM $Ru(CN)_6^{3+}$ in PBS(1X, pH 7.4). PBS(1X, pH 7.4) will also simply be referred to as PBS. A brief overview of the modification process is shown in Fig. 3.1.

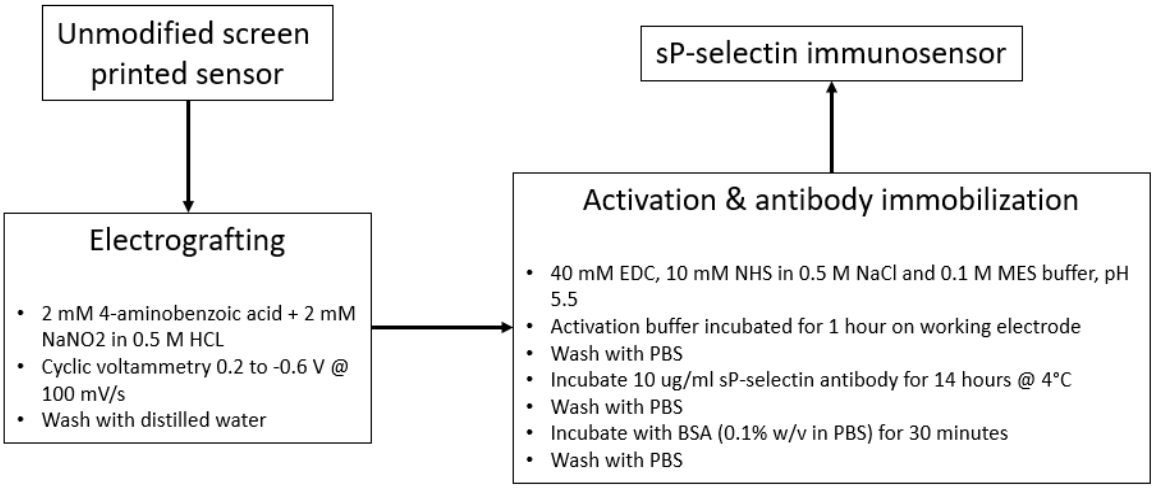

Figure 3.1: Brief overview of the modification process that was followed to turn the commercial screen printed sensor into an sP-selectin immunosensor.

The unmodified sensors were electrografted in the diazonium salt solution using cyclic voltammetry. This creates more carboxyl support groups on the surface of the working electrode. These functional groups are then activated using the EDC/NHS crosslinking chemistry. After the activation procedure the sP-selectin antibodies are incubated on the working electrode overnight in 4°C so that the antibodies can attach to the activated carboxyl groups. After a quick blocking step was performed with BSA, the immunosensors were finished. Below follows a more detailed description, but as a start the unmodified sensors were first characterized.

3.1.1 Characterization of the electrochemical window

The electrochemical window of the unmodified sensors was studied to determine three different aspects of the experimental setup, namely: 1) to make sure that the electrochemical window of the supporting electrolyte is large enough to accommodate the redox couple, 2) to determine the formal potential of the redox couple, which is also more or less the potential where the redox peak is located in a SWV experiment, and 3) to confirm

that no other redox process, other than the FeCN redox process, is present within the scanned potential window. To avoid contamination and performing redundant tests, only two sensors of each type (GPHOX and CNF) were used for this experiment.

A fresh batch of the FeCN redox couple was prepared as described in Appendix B.1. Before any experiments were done on the sensors, the surface of the electrodes were wet three times with the same solution it needed to be tested in. This was done by adding a few drops of the solution onto the area using a plastic pipette. The solution was then removed by tilting the electrode so that the drop runs off. The wetting step was done to remove any small bubbles that might have formed on the electrodes, and to wash off any impurities that might interfere with the experiment. Any references that are made to a wetting procedure throughout the rest of the text refers to the process described above.

The electrochemical window of PBS was determined by doing a CV sweep from 1 V to -0.6 V at a scan rate of 100 $mV.s^{-1}$. The limits were chosen to be well positive and negative of the oxidation and reduction potentials of the FeCN couple that are reported in literature [71, 128, 136]. Then, a CV scan of the FeCN couple was done by doing a sweep from 0.7 V to -0.5 V at a scan rate of 100 $mV.s^{-1}$. Again, the limits were chosen to be just outside the oxidation and reduction potentials that are reported in literature. The potential window of the PBS was then qualitatively determined through the voltammogram, and compared to the potentials where the FeCN couple showed oxidation and reduction. The method is shown diagrammatically in Fig. 3.2.

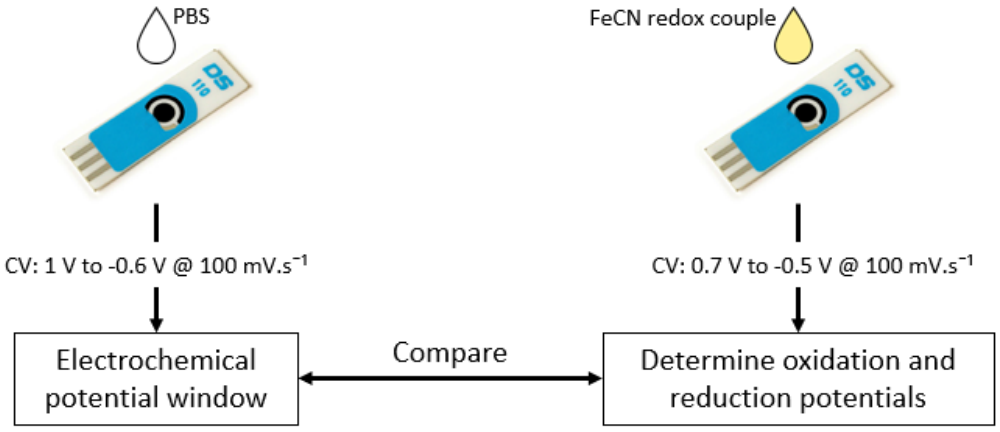

Figure 3.2: Method that was used to determine the electrochemical potential window of the PBS, as well as the oxidation and reduction potentials of the FeCN redox couple.

The reduction and oxidation potentials of the FeCN couple were then used to determine the formal potential for the setup using Eq. 2.5.

3.1.2 Characterization of unmodified sensor through square wave voltammetry

A sufficient potential range for the FeCN redox couple experiments was determined so that a well defined redox peak is achieved in the voltammograms. New, unmodified GPHOX and CNF sensors were used for the purpose of this method. The scanned range was 1 V to -1 V, which was chosen to be well positive and negative of the formal potential of the

FeCN couple that was identified in the CV scan described in Section 3.1.1. Again, only three sensors of each type were used to perform these tests to avoid contamination of the whole purchased batch.

The first experiment was performed in distilled water which is the solvent used in PBS. This was done to see if the solvent produced any redox peaks within the scanned range. Thereafter, a new sensor was used to test the contribution of PBS to the measured current. This could serve as a background scan that can be subtracted from the FeCN couple scan for the purpose of data analysis, as will be discussed in Section 3.6.1. A final SWV experiment was done in the FeCN couple to confirm that a well defined peak is present close to the formal potential that was identified in the CV scan of Section 3.1.1. The method is shown diagrammatically in Fig. 3.3.

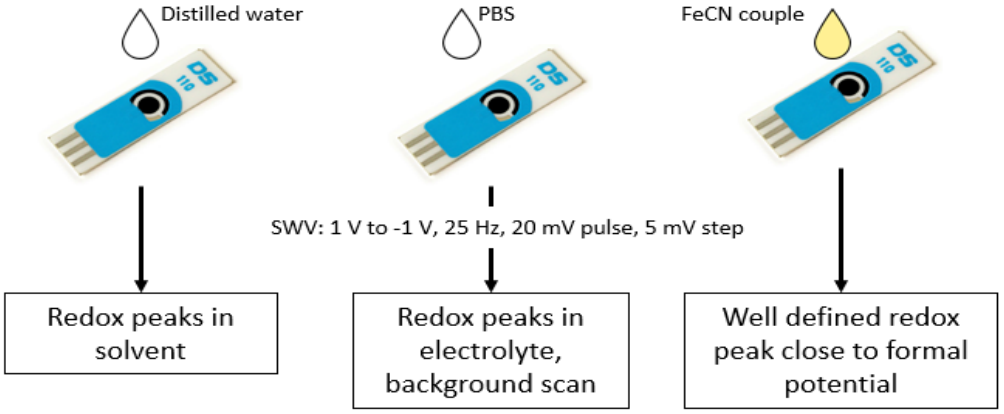

Figure 3.3: Method that was used to determine the required range of a SWV experiment.

The potential at which the peak redox current appeared was then used as a guideline for choosing an appropriate range for subsequent SWV experiments. A well defined redox peak was required so that the data analysis algorithm, described in Section 3.6, can be used to successfully extract the peak current.

3.1.3 Reproducibility of the unmodified sensors

The reproducibility of the unmodified sensors were studied to determine the best approach for comparing the different steps throughout the modification process. If the unmodified sensors are reproducible (i.e. they produce similar peak currents under the same experimental conditions) it means that all modification steps can be compared to a single baseline peak current that was acquired before the modification step took place. Therefore, it is not necessary to compare each sensor to its own baseline, but rather to a baseline that is shared with all sensors and that was determined by only using one sensor.

On the other hand, if the sensors are not reproducible it means that each sensor would have a different peak current response. Therefore, each sensor would need to be compared to its own baseline to obtain a relative change after each modification step. But this approach could be non-ideal since it could lead to degradation or contamination of the disposable electrodes that now have to be tested more than once. If this is the case, degradation could be avoided by modifying and testing the sensors in as short a time as

possible, and contamination can be reduced by properly cleaning the sensor surface after each modification step.

The inter-reproducibility was assessed by performing SWV of three new, unmodified CNF and GPHOX sensors in a freshly prepared batch of the FeCN couple. The same electrode wetting procedure was used as described previously. Experiments were performed with the default parameters and the scanned range was chosen as 0.6 to -0.4 V. The reproducibility of multiple scans on the same sensor was also tested by performing SWV in the redox couple using the same experimental parameters that are described above. Twenty scans were done on one sensor of each type without removing the electrochemical solution between tests. The time between sequential scans were minimized by immediately performing the next sweep as soon as the previous one was done and the peak currents were determined using the methods described in Section 3.6.

After analyzing the results, it was decided that all the CNF and GPHOX sensors would be compared against its own baseline that is obtained prior to any modification step. Degradation and contamination was minimized by performing the modifications and measurements over short periods of time and properly cleaning the surface between experiments.

3.1.4 Electrochemical reduction of diazonium salt on unmodified sensors

This modification step grafts 4-aminobenzoic acid diazonium salt molecules to the working electrode to create carboxyl moieties on the surface. These functional groups serve as a supporting platform for the sP-selectin antibodies. The electrografting was done using an *in-situ* prepared batch of diazonium salt. The salt solution was prepared using the protocol that is described in Appendix B.5. The preparation of the hydrochloric acid solution that was used in this protocol is described in Appendix B.4. The final diazonium salt solution had a concentration of 2 mM 4-aminobenzoic acid and 2 mM $NaNO_2$ in 0.5 M HCl, which is the same as that used by Eissa *et al* [69]. A fresh batch of the FeCN couple was also prepared for these experiments.

To determine the number of cycles that were needed to sufficiently cover the working electrode area, three new, unmodified GPHOX and CNF sensors were grafted for 1, 4, and 8 cycles, respectively. A single cycle is defined as a CV sweep from 0.2 to -0.6 V, and then back to 0.2 V. The number of cycles were arbitrarily chosen, but the range was chosen to be the same as that reported in literature [69]. In theory, more cycles would create more carboxyl moieties, but it could also lead to the formation of multi-layers which could reduce sensitivity [97]. The organic layer is formed on the surface of the working electrode, which then hinders the electron transfer process of any redox molecule, effectively reducing the peak redox current. The carboxyl groups dissociate in a solution by releasing the H atom from the hydroxyl group as a free proton (H^+). This causes the remaining oxygen atom to have a negative charge, which would cause any other negatively charged molecule in the vicinity to be repelled [137]. The negatively charged FeCN molecules can therefore be used to assess the degree to which the layers were formed. If more negatively charged carboxylic acid groups are present on the electrode, it would lead to a greater repulsion of the FeCN probe. The method that was followed is illustrated in Fig. 3.4.

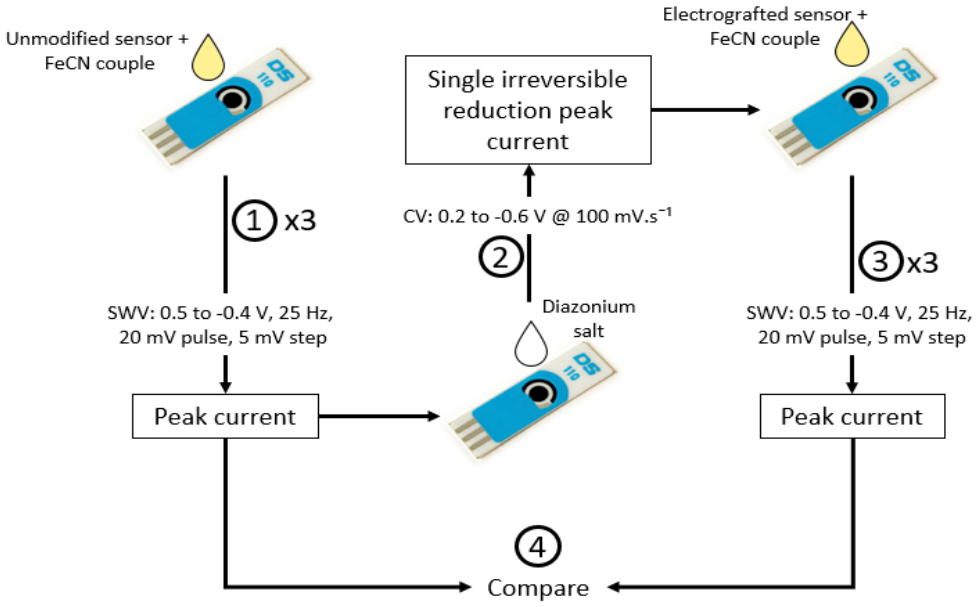

Figure 3.4: The method that was used to modify the working electrodes with diazonium salt molecules. ① The unmodified sensors were first scanned using three SWV sweeps to get an average peak current before modification. ② The same sensors were then subjected to 1,4, and 8 electrografting sweeps, respectively. ③ Three more SWV scans were done in the FeCN couple to get the peak current after modification. ④ The peak currents before and after grafting were then compared.

To compare the effect of the grafting process, each sensor was compared to its own baseline peak current prior to the electrografting step. Therefore, each sensor was first scanned three times in the redox couple using SWV to determine the mean peak current before modification. After being thoroughly washed with distilled water, it was air dried at room temperature. The washing procedure was done by adding a drop of distilled water onto the sensor using a plastic pipette, and allowing the liquid to run off of the sensor. After the sensors were dried out, a 100 μl drop of diazonium salt solution was pipetted onto the electrode area. Then, CV scans were done between 0.2 V to -0.6 V at a scan rate of 100 mV.s^{-1} in the diazonium salt mixture. The diazonium salt solution was not changed for the sensors that underwent multiple scans. After washing the sensors with a copious amount of distilled water, it was air dried at room temperature. Finally, three more SWV scans were done to determine the new mean peak current after the electrografting step. The difference in the peak currents before and after grafting were compared for each sensor to assess the effect of the number of cycles on the peak redox current. The number of cycles that would be used for modifying the sensors for full scale testing were chosen based on these results. Fig. 3.5 shows the modified working electrode after the electrografting step.

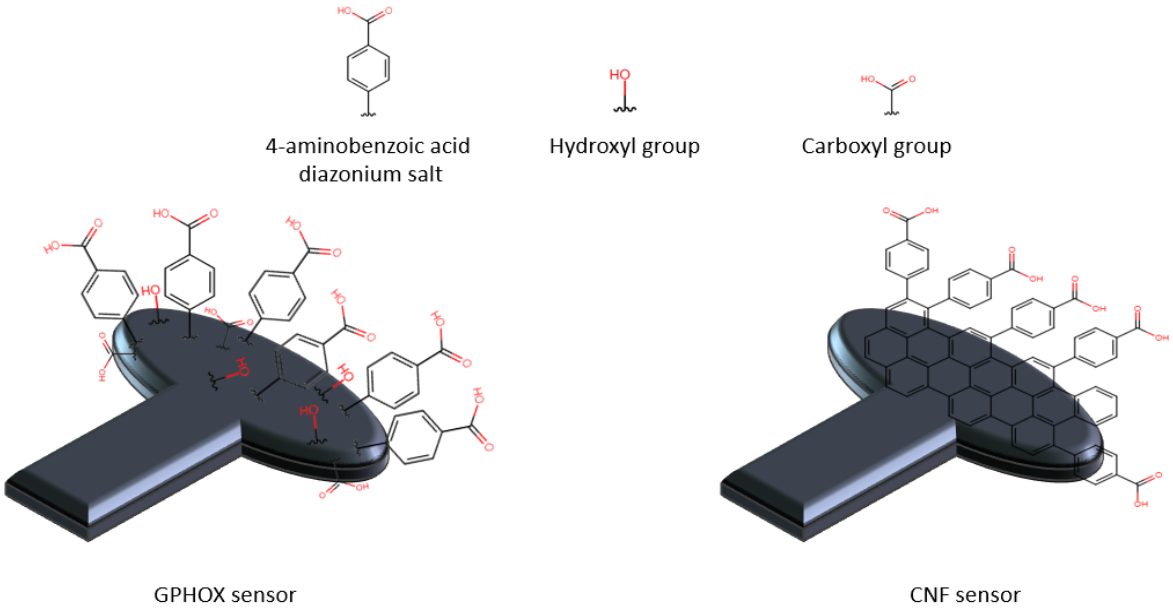

Figure 3.5: Diagram of the sensors after grafting with 4-aminobenzoic acid diazonium salt showing the carboxyl supports on the surface of the working electrode.

The underlying GPHOX sheets have hydroxyl and carboxyl groups which are now surrounded by the diazonium salt molecules, and the CNF sensors also have the diazonium salt molecules that are protruding from the carbon based fibers. After the grafting procedure, the sensors were washed with distilled water and dried at room temperature.

3.1.5 Antibody crosslinking

The attachment of the antibodies to the surface of the carboxyl grafted working electrode is what makes the sensor an immunosensor. In this step the antibodies are covalently bound to the surface using EDC/NHS crosslinking chemistry to make the electrode specific for detecting sP-selectin proteins in a physiological solution.

Two important decision regarding the antibody incubation needed to be made, namely the concentration to be used and the duration of incubation. ELISA kits commonly use concentrations of 2 μg/ml, but the concentrations used in literature vary considerably between 100 ng/ml and 100 μg/ml [69, 90, 136]. Eissa *et al.* used a concentration of 10 μg/ml on the same GPHOX and CNF sensors for the development of a survival motor neuron disease immunosensor [69]. This concentration is also close to that of an ELISA kit, which could be useful if the immunosensor had to be compared to that standard. Therefore, the same concentration was chosen for this project. The incubation time also varies from 30 minutes to overnight for similar immunosensors [69, 136, 138, 139]. It is important that enough time is allowed for the antibodies to attach to the surface and thus it was decided that the antibodies would be incubated overnight. The stock concentration was made by reconstituting 200 μg of the antibody in 400 μl PBS to get a final concentration of 500 μg/ml. This solution was divided into different eppendorf vials to avoid repeated freeze/thaw cycles of the same solution. 16 μl was added to four vials each, while 56 μl was stored in six vials each. All of these vials were stored in -20°C when not in use. Appendix B.7 shows a thorough illustration of the procedure that was followed to reconstitute the antibody. When needed, 784 μl PBS was added to a 16 μl

vial to obtain a 800 μl solution at a final concentration of 10 μg/ml. The EDC/NHS was prepared according to the protocol described in Appendix B.6 to get a final solution of 40 mM EDC and 10 mM sulfo-NHS in 0.1 M MES buffer with 0.5 M NaCl. The concentrations were chosen to be around the same order of magnitude as that reported in literature [61, 69, 75, 112]. The final solution volume was 7.5 ml which was more than enough to incubate the chosen amount of sensors. The pH of the solution (from now on called the activation buffer) was chosen to be 5.5 since the activation reaction is most efficient at a pH of 5 to 6 according to the crosslinking protocol [140].

For this thesis, five sets of full scale tests were performed, and the antibody and EDC/NHS solutions were made *in-situ* (at the time of incubation) for each set. The results of each set were used to adjust some of the variables of the next set, so as to try and improve the immunosensor response for subsequent sets. A full scale test consists of the whole process from modifying the commercial sensor, to the final electrochemical measurements after sP-selectin protein immobilization. The antibody immobilization strategy for each set are described below in the order that the full scale experiments were performed. The final immunosensor measurement procedure is described at the end of the methodology chapter in Section 3.4.

For the first set, it was decided that 32 GPHOX sensors would be used for the full scale testing of the immunosensor with different concentrations of the sP-selectin proteins. These sensors were electrografted for two cycles as described in Section 3.1.4. To avoid contamination and degradation of the sensors, the peak current before and after grafting was not compared for these sensors. After the grafting step, the sensors were washed with distilled water and air dried. For activation of the carboxyl moieties, 13.5 μl of the activation buffer was incubated on the working electrode of each sensor for 1 hour at room temperature. A water saturated environment was created for this reaction by putting the sensors in an acrylic box with a layer of water in the bottom of the container. This allows the water to evaporate before the activation buffer has a chance to dry out. Fig. 3.6 shows how the carboxyl groups have been activated to form amine-reactive sulfo-NHS esters on the surface of the GPHOX working electrode. The EDC molecule first couples with the carboxyl group to form an unstable intermediate, called o-Acylisourea. The sulfo-NHS then couples to this group to improve the reaction efficiency and provide dry-stable amine-reactive esters that can be coupled with primary amine groups.

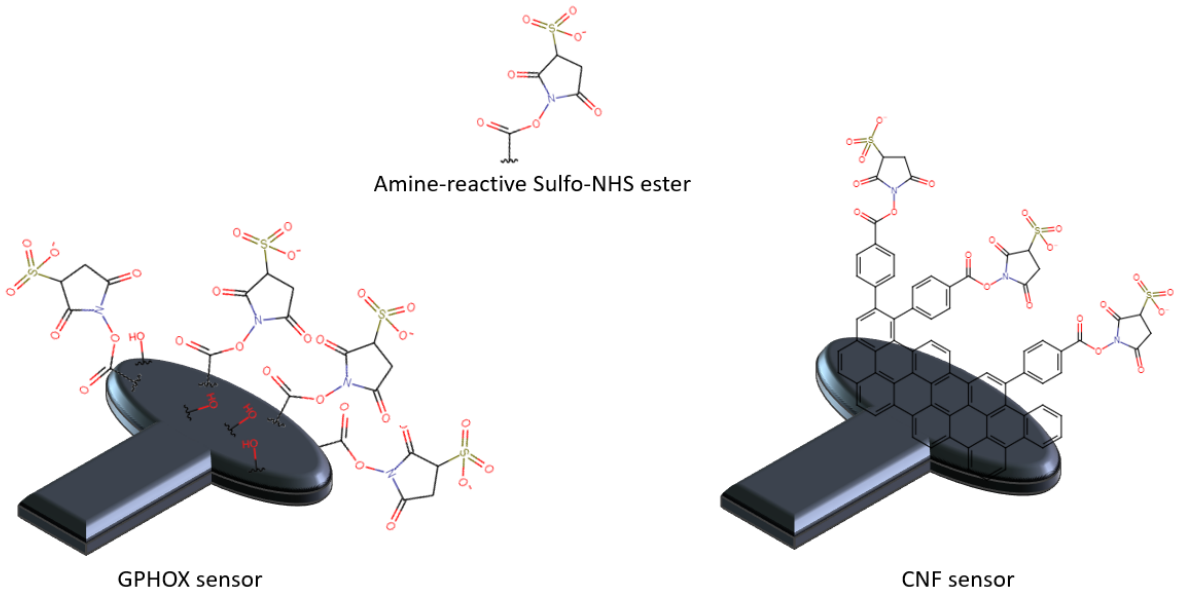

Figure 3.6: Diagram of the amine-reactive sulfo-NHS ester that is created on the working electrode after the activation buffer has been added.

The crosslinking protocol requires that the environment of the amine-reactive sulfo-NHS ester be raised to a pH of between 7.2 to 7.5 immediately before the reaction with the antibody. Therefore, the sensors were washed three times with PBS to remove the activation buffer and also raise the pH of the working electrode environment to a value of 7.4. 13.5 μl of the 10 μg/ml antibody solution was then incubated on the working electrode in a water saturated environment for 14 hours at 4°C. Afterwards, the sensors were carefully rinsed with PBS three times to remove any unbound antibodies. A blocking step was performed to block the remainder of the amine-reactive esters that did not bind with any antibodies. This step reduces non-specific adsorption of proteins onto the working electrode, which leads to an immunosensor with higher specificity. 13.5 μl BSA (0.1% w/v in PBS) was incubated on the working electrode in a water saturated environment for 30 minutes at room temperature. A last PBS washing step was performed to remove the unbound BSA, after which the sensors were stored on ice before the electrochemical measurements. Fig. 3.7 shows an illustration of the completed GPHOX immunosensor that was used for the experiments. The primary amine groups on the lysine residues of the sP-selectin antibody have formed a covalent bond with the carboxyl groups, and the BSA has blocked the remaining active sites.

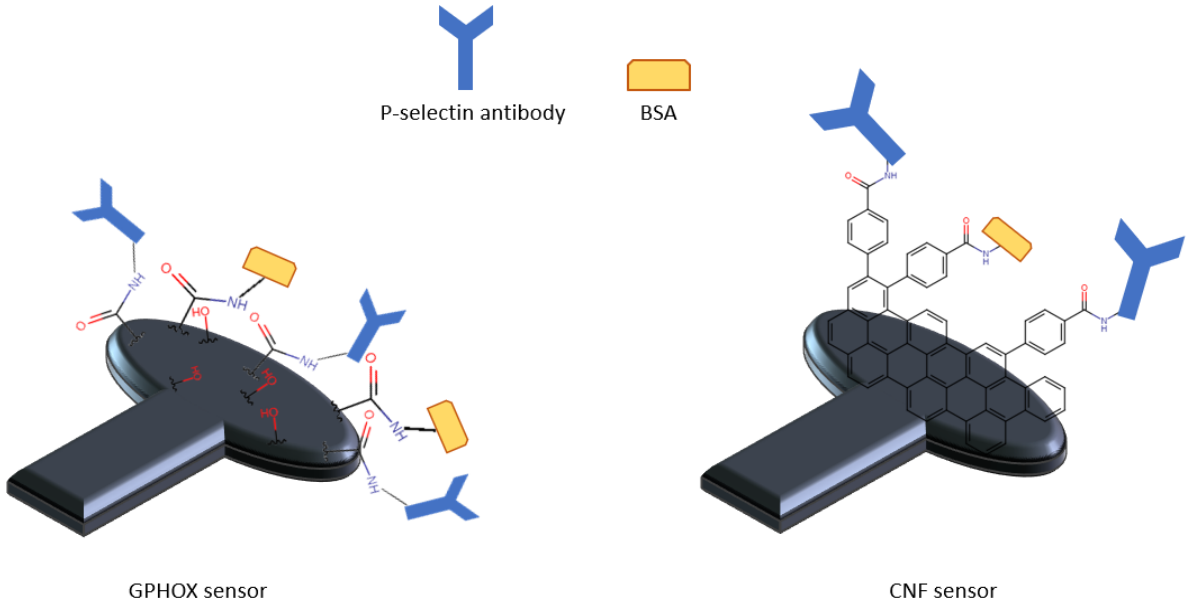

Figure 3.7: Diagram of the completed immunosensor with protruding sP-selectin antibodies and BSA blocking proteins.

For the second set, 21 CNF sensors were modified with a similar approach as described above. These sensors were electrografted for four cycles to create carboxyl groups on the surface of the carbon nanofiber working electrode. After being washed in distilled water and air dried, 13.5 μl of the activation buffer was incubated on the sensor to form the amine-reactive sulfo-NHS esters that are shown on the right of Fig. 3.6. The solution was then washed off with PBS and 32 μl of 10 μg/ml antibodies in a PBS solution of pH 7 was incubated on the working electrode for 14 hours at 4°C. The pH was adjusted to a lower value using HCl so that the antibodies would be more positively charged in the solution, and thus more sufficiently attracted to the negatively charged sulfo-NHS ester groups [141]. The isoelectric point of the antibody was reported to be around 7 which means it is more positively charged at pH values lower than 7 [142]. Briefly put, the isoelectric point of a protein is the pH at which the molecule has no net electrical charge. If the pH of the environment is higher than the isoelectric point of the antibody it is negatively charged, and vice versa. The crosslinking protocol, however, states that the binding between the antibody and the sulfo-NHS esters are most efficient at a pH of 7-8, which is why the pH of the antibody solution was not chosen lower than that. To make sure the entire working electrode was covered for the incubation period, the antibody solution volume was also increased from 13.5 to 32 μl in case some of the liquid runs off of the working electrode. Afterwards, the sensors were washed with the PBS solution and 32 μl BSA (0.1% w/v in PBS) was incubated on the sensors for 30 minutes at room temperature. A last PBS washing step was performed to remove the unbound BSA and the finished CNF immunosensors were stored on ice before the electrochemical measurements were taken. In order to keep the biological material on the sensors in a physiological environment, a 100 μl drop of PBS was added to the working electrode area. The final immunosensors are illustrated on the right in Fig. 3.7.

The antibody crosslinking step was done in the same way for the third, fourth, and fifth set of experiments. The third set used 15 CNF immunosensors, and the fourth and fifth set both used 18 CNF immunosensors. The sensors were electrografted with diazonium

salt using four CV cycles. After being washed in distilled water and air dried, 13.5 μl of the activation buffer was incubated on the working electrode for 1 hour at room temperature to activate the carboxyl groups. The solution was washed off using PBS (pH 7) and 100 μl of 10 μg/ml antibodies in PBS (pH 7) was incubated on the working electrode for 14 hours at 4°C. After being washed off with PBS, the blocking step was performed with 100 μl of BSA (0.1% w/v in PBS) for 30 minutes at room temperature. A last PBS washing step was performed to remove the unbound BSA and the immunosensors were kept on ice with a 100 μl drop of PBS during the electrochemical measurements.

3.1.6 Fluorescent study of the carbon nanofiber immunosensor

A fluorescent study was conducted for the CNF immunosensors after the second full scale test was conducted. The goal of the study was twofold: firstly to confirm that the sP-selectin antibodies are present on the surface, and secondly to confirm that a baseline SWV scan in the FeCN couple does not wash off the antibodies. A secondary fluorescent goat anti-mouse IgG Alexa Fluor®488 antibody was used for this experiment. This antibody can be bound to a primary mouse monoclonal antibody, such as the sP-selectin antibody, that is immobilized on the surface of the immunosensor.

Two unmodified CNF sensors were both electrografted for four cycles using the same method that was described previously. The same antibody attachment procedure that was used for the second set of full scale tests, were used for these two sensors. After the blocking step, a 100 μl of PBS was added on the sensors and they were kept on ice. The one sensor was subjected to 3 SWV scans in a freshly prepared batch of the FeCN couple as it would have been during a baseline peak current test. The parameters were: 20 mV pulse size, 5 mV step size, 25 Hz, and a range of 0.5 to -0.4 V. After the redox couple was washed off of this sensor, both sensors were incubated with the secondary fluorescent antibody. The secondary antibody was made in goat serum using a 1:500 dilution of the stock antibody solution. 100 μl of this solution was incubated on the sensors in a dark room for 1 hour to allow the secondary antibody to bind to the primary antibody. The secondary antibody was then washed away using PBS and the cover slips were attached to the sensor using a mounting medium.

Two unmodified CNF sensors were also used as control tests. The one sensor was studied under the confocal microscope without any treatment to look for possible autofluorescence, and the other sensor was only treated with the secondary antibody without undergoing electrografting or primary antibody attachment. This sensor was used to show the lack of fluorescence in the absence of the primary sP-selectin antibody.

Fluorescent studies were done using a Carl Zeiss LSM 780 confocal microscope using a 488 nm laser and a bandpass filter of 493 to 630 nm. Due to a shortage of sensors, the fluorescent confirmation step was not conducted for the GPHOX immunosensor.

3.1.7 Characterization of the hexaammineruthenium(III) chloride redox probe

After the third full scale CNF immunosensor test results were analyzed, it was decided that a new positively charged redox probe, called hexaammineruthenium(III) chloride (RuHex), would be tested. This was done to test the CNF immunosensor response with

an oppositely charged redox probe. The compatibility of the new probe with the electrochemical setup (PBS supporting electrolyte and CNF working electrode material) was, therefore, tested in the same manner that was described in Sections 3.1.1 and 3.1.3. These experiments were only conducted with the CNF sensors and are briefly discussed here.

As previously described in Section 3.1.1, the redox active range of the RuHex probe was determined by performing CV. A fresh batch of 5 mM $Ru(NH_3)_6$ in PBS(1X, pH 7.4) was prepared for this test as described in Appendix B.2. One unmodified CNF sensor was scanned in the PBS supporting electrolyte from 1 to -0.6 V at a rate of 100 mV/s, and another sensor in the RuHex probe from 0.3 to -0.5 V at a scan rate of 100 mV/s. The RuHex range was chosen to be the same as described for other screen printed electrodes [143]. The voltammograms of the two sensors were then compared and the formal potential of the RuHex probe was determined using Eq. 2.5. This was used as a guideline for choosing a sufficient SWV scan range that would realize a well-defined redox peak.

The reproducibility of the RuHex probe with three unmodified CNF sensors were assessed in the same manner that was described in Section 3.1.3. SWV scans were conducted from 0.4 to -0.6 V at a rate of 25 Hz, pulse size of 20 mV, step size of 5 mV, and equilibrium time of 2 seconds. The range was chosen to be well positive and negative of the formal potential that was identified in the CV scan. The reproducibility of twenty consecutive scans on the same CNF sensor was also assessed.

3.1.8 Commercial sensor methodological assumptions

One of the major assumptions that were made throughout the methodology is that each sensor would behave in a similar manner if the same tests or modifications were performed under the same experimental conditions. It was not assumed that each sensor would have exactly the same change in peak current after a specific modification process, but rather that the sensors would exhibit the same trend if they had to undergo the same modification. This assumption was necessary since repeated tests on each sensor could result in contamination or degradation of the electrodes. To make this assumption reasonable, the trend of a modification was verified for a few sensors to see if they behaved in a similar manner.

3.2 Potentiostat development process

This section describes the design, simulation, and practical measurements of the portable potentiostat. A high-level design is briefly given followed by a more in-depth discussion of each hardware component, such as the power supply, control and transimpedance amplifiers, and the Bessel filter. The software that controls the potentiostat is divided into two parts, namely a description of how the applied signal was determined and a detailed discussion of how the MCU peripherals were used to apply the signal. The USART communication protocol between the Nucleo board and the host PC is also briefly explained. Fig. 3.8 shows a picture of the potentiostat that was developed in this work. The different stages of the potentiostatic circuit are indicated by the coloured boxes.

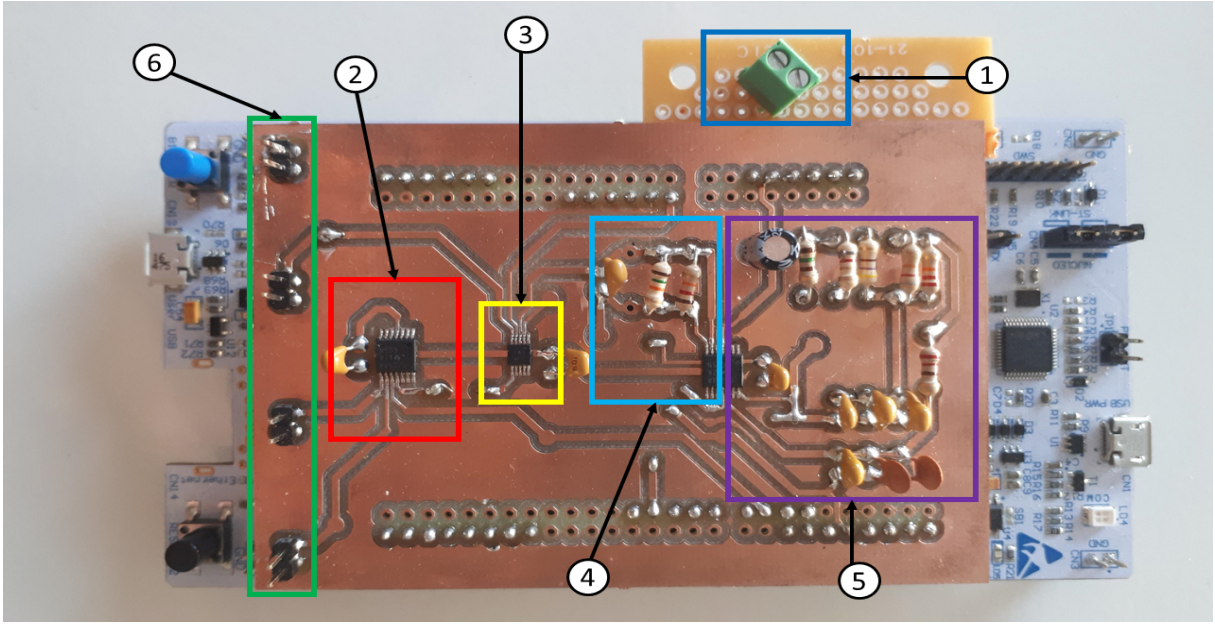

Figure 3.8: Portable developed potentiostat. A 9 V battery can be connected to the socket at ①. The control amplifier ② applies the signal to the electrochemical cell. The switch ③ connects the working electrode to the cell, while the transimpedance amplifier ④ converts the current to a voltage. The Bessel filter ⑤ reduces the noise in the circuit. The crocodile clips of the DRP-CAC cable are clamped to the connectors at ⑥.

3.2.1 Hardware

An STM32F446ZE Nucleo development board was chosen as the MCU for the design due to its attractive characteristics that are summarized in Table 3.2. The direct memory access (DMA) controller is of particular interest in the design of the potentiostat. This functionality allows tasks to be completed in the background, thereby reducing processor loading and overheads. It can, for example, transfer values sequentially from memory to a peripheral, or vice versa, without the need of any user written code to handle each transfer. A debugger/programmer board is also attached to the Nucleo board as a breakout header that can be removed if the development board is deployed in an end-user application. Atollic's TrueStudio integrated development environment (IDE) also provides numerous features, such as the STM32CubeMX code generator, that support the rapid prototyping of embedded software applications. The code generator can be used to set up the peripherals and control clock speeds using a user-friendly interface that can deploy the code directly into the IDE.

Table 3.2: STM32F446ZE Nucleo development board specifications and features.

General features	
Feature	**Value**
Core speed	Up to 180 MHz
Number of GPIO pins	114
Direct Memory Access	-
On-board ST-LINK/V2-1 debugger/programmer with serial wire debugger	-
Number of communication channels	20, including SPI, USART, and I^2C

Number of timers	17, 12 x 16-bit timers, and 2 x 32-bit timers
ADC characteristics	
Characteristic	**Value**
Number of channels	24
Number of ADCs	3
Resolution	12 bits
Speed of each ADC	2.4 MSPS
DAC characteristics	
Characteristic	**Value**
Number of channels	2
Number of DACs	2
Resolution	12 bits

A high-level design of the potentiostatic circuit is given in Fig. 3.9. The external circuit is power supplied with the 5V-pin from the Nucleo development board. The onboard 12-bit DAC applies a potential to the control amplifier in the range of 0 to 3.3 V with a resolution of 805.66 μV. The control amplifier interfaces with the electrochemical cell through the reference and counter electrodes. It applies a potential of 0 to 3.3 V to the reference electrode while the transimpedance amplifier keeps the working electrode biased at 1.65 V. This value was chosen to be in the middle of the ADC's conversion range and it allows electrochemical experiments to be performed in the range of $\pm$1.65 V, which is sufficient for the developed immunosensor. The transimpedance amplifier converts the cell current to a voltage representation before being filtered by a 2nd order Bessel filter with a cutoff frequency of 5 kHz. The onboard 12-bit ADC of the Nucleo board measures the potential in steps of 805.66 μV, and transfers the data to the host PC through the USB communication. The combination of the transimpedance amplifier gain and the potential range of the ADC allows the potentiostat to measure currents in the range of $\pm$250 μA with a resolution of 122.07 nA.

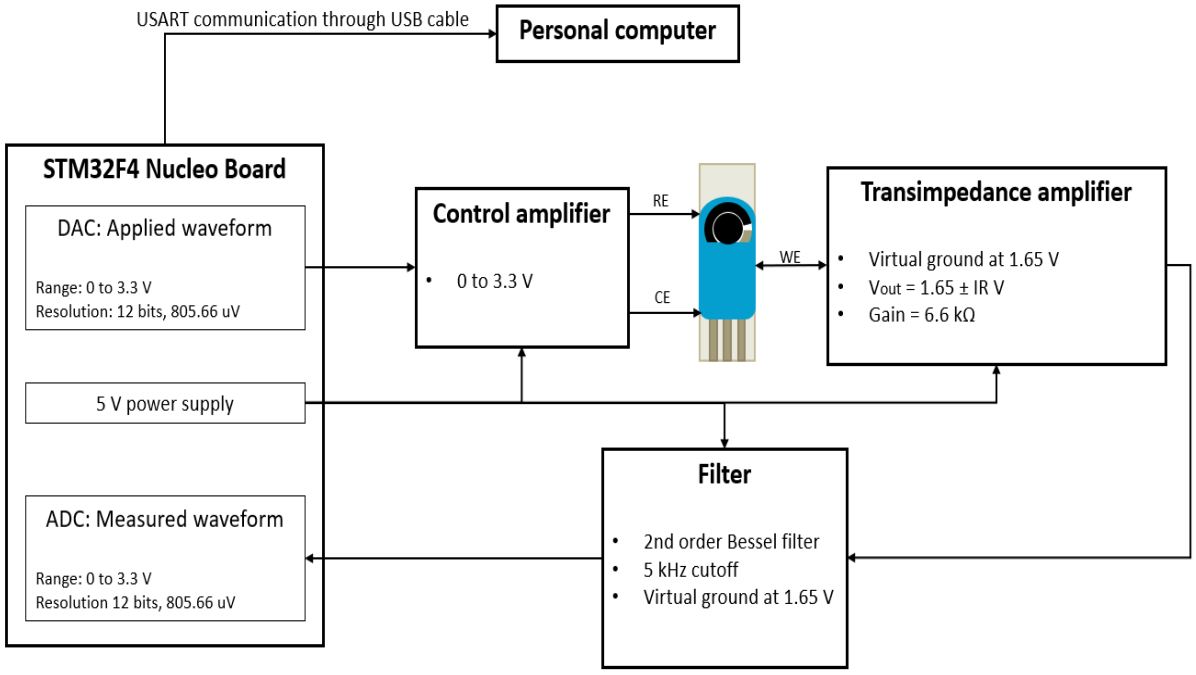

Figure 3.9: High-level design of the external potentiostatic circuit.

The simulation software, LTSpice, was used to simulate each functional component during the design process. The program contains models for resistors, capacitors, operational amplifiers, voltage sources, and many other circuit components that can be used for general circuit simulation such as DC analysis, AC analysis, and noise analysis.

3.2.1.1 Accuracy of measured voltages

Before the design of the potentiostat is described, it should first be stated how the measurements were taken throughout the process. A Tektronix TBS 1052B-Edu oscilloscope was used to measure the voltages with a 1X voltage probe. The ground lead and cap of the probe were removed to reduce the environmental noise that can couple on these loops. A much shorter wire was twisted around the ground node to reduce the length of the loop as shown in Fig. 3.10.

Figure 3.10: Probe that was used for measurements.

Matlab's Instrument Control Toolbox was used to acquire the waveforms from the oscilloscope so that it could be analyzed. Before a waveform was read, the voltage divisions on the oscilloscope display were set to be as small as possible to improve the accuracy of the measured signal, but not too small so that the signal does not appear in the viewing window. This was done since only the visible data points can be acquired in Matlab, and if the waveform fell outside the viewing window information would be lost. The accuracy of voltages was assessed by looking at their DC values and the root mean square (RMS) of the voltage noise. DC measurements were taken with the oscilloscope set to DC coupling, and RMS voltage noise values were measured with the oscilloscope set on AC coupling. The lowest possible values that can be measured using the oscilloscope were determined by shorting the measurement probe. This resulted in a small DC offset of 230.9 μV and an RMS noise voltage of 225.18 μV. It was noted that the AC measurement still contained a very small DC offset value of 28.96 μV. Therefore, all the noise measurements were calculated by first subtracting this small DC offset from the measured AC signal, and then calculating the RMS value in Matlab. The smallest RMS signal, measured by shorting the probe, was thus calculated as 223.31 μV. It should be noted that these values are not the absolute lowest values that can be measured and they are also dependent on the surrounding environmental noise that can change from time to time.

3.2.1.2 Power supply considerations

The portability of the potentiostat is mainly influenced by the power supply aspects of the device. High power applications require the use of an AC power socket or benchtop power supply unit to supply the necessary voltage and current. Low power applications, such as the Nucleo board, are often more portable since they can get the necessary supply from a computer or even batteries. The development board can be powered in four different ways: 1) by the host PC through the universal serial bus (USB) cable, 2) V_{IN} (7-12 V), 3) E5V (5 V), or 4) with a 3.3 V source. The latter option was automatically excluded from the choices since the ST-LINK is not powered in this case, and thus no communication is possible through the virtual com port interface. The designed potentiostatic circuit also requires a 5 V power rail to operate successfully, which eliminates the 3.3 V source as a possibility. Therefore, the two most portable options (host USB and V_{IN} powered) were chosen and compared in terms of the amount of noise that is caused on the 5V- and AVDD-pin of the board.

The 5V-pin will ultimately be used to power an external printed circuit board (PCB) that fits on the Zio headers of the Nucleo board. Any noise on this rail will permeate into the circuit which is why this node should be as noiseless as possible. The analog supply voltage, AVDD, should also be as noiseless as possible to improve the accuracy of the ADC and DAC peripherals. In the case that the USB is used, the Nucleo board is powered using the 5 V from the host PC, and thus the same 5 V appears on the 5V-pin of the Nucleo. On the other hand, V_{IN} uses a 5 V low-dropout voltage regulator to power the Nucleo board which should make it superior due to less noise. For portability reasons, a 9 V alkaline Energizer battery was used to power the board on the V_{IN} pin instead of using a benchtop power supply.

Table 3.3 shows how jumper pin 3 (JP3) was configured to select the appropriate power mode. The V_{IN} measurements were also taken with the USB plugged in to see what the effect would be. Even though the USB was not used to power the Nucleo board in this

case, it was still tested since the Universal Synchronous/Asynchronous Receiver/Transmitter (USART) communication requires the USB cable to be plugged in, and therefore it could have an effect on the amount of noise on the power supply pin.

Table 3.3: Power jumper state for the comparison of the RMS noise voltage on the 5V and AVDD power rails.

	JP3 state
USB powered	3-4
V_{IN} powered, USB plugged out	5-6
V_{IN} powered, USB plugged in	5-6

The measurements were performed by soldering the components shown in Fig. 3.11 onto a 16-pin PCB board, and connecting it to the 5V-pin of the Nucleo board. This was used to simulate the effects that the external PCB would have on the power rail. R1 is used to allow current to flow from the rail, C2 acts as a charge storage pool to filter out low frequency noise, and C1 would typically be used as bypass capacitors next to integrated circuits (ICs) for filtering high frequency noise.

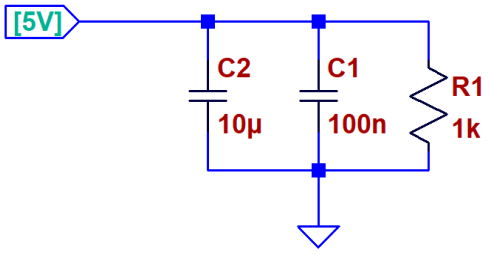

Figure 3.11: Circuit that was used as a substitute for the external potentiostatic circuit while measuring the power rail noise.

Based on these results it was decided that the V_{IN} powered option would be used for the design.

3.2.1.3 Control and transimpedance amplifier

A TLC2264 operational amplifier (op-amp) was chosen for the design of the potentiostatic circuit. The op-amps were chosen based on their low offset voltages, low bias currents, low voltage noise densities, and high input impedance. The specifications of the amplifiers are summarized in Table 3.4. A single package contains four op-amps which reduces the number of components that are required on the PCB. The output can also swing very close to the rails which allows a larger voltage range to be used when considering an op-amp that would interface with an ADC. A high input impedance is also desired so that a negligibly small current flows through the reference electrode.

Table 3.4: TLC2264AI operational amplifier specifications.

	Value	**Unit**
Input offset voltage	300 → 950	μV
Input offset current	0.5	pA
Input bias current	1	pA

Table 3.4 continued from previous page

	Value	Unit
Input impedance	1	TΩ
Equivalent input noise voltage	12	$nV/\sqrt{Hz}$
Gain bandwidth product	710	kHz

Fig. 3.12 shows the schematic of the potentiostatic circuit that was used in the design. The potential waveform is applied to the non-inverting terminal of the control amplifier using DAC1. The same waveform appears on the reference electrode which is connected through the negative feedback loop of the control amplifier. The transimpedance amplifier is biased at 1.65 V using DAC2, which was chosen to be in the middle of the ADC potential range of 3.3 V. The working electrode is connected to the inverting terminal of the transimpedance amplifier through an ultra-low resistance dual SPDT analog switch (NLAS4684 from On Semiconductor). The normally closed pathway was used since it had a very low on-resistance of 0.5 Ω (modeled as R_{ON}) that is much lower than the cell resistance, and would thus not have a large impact on the measured current. By controlling the switch with the MCU using a GPIO pin, the working electrode can be connected to the circuit allowing current to flow through the electrochemical cell. R1 was chosen as 6.6 kΩ which allowed the maximum and minimum currents of the immunosensor (as identified in some of the experiments done on the Gamry instrument) to be measured before the ADC reading is saturated.

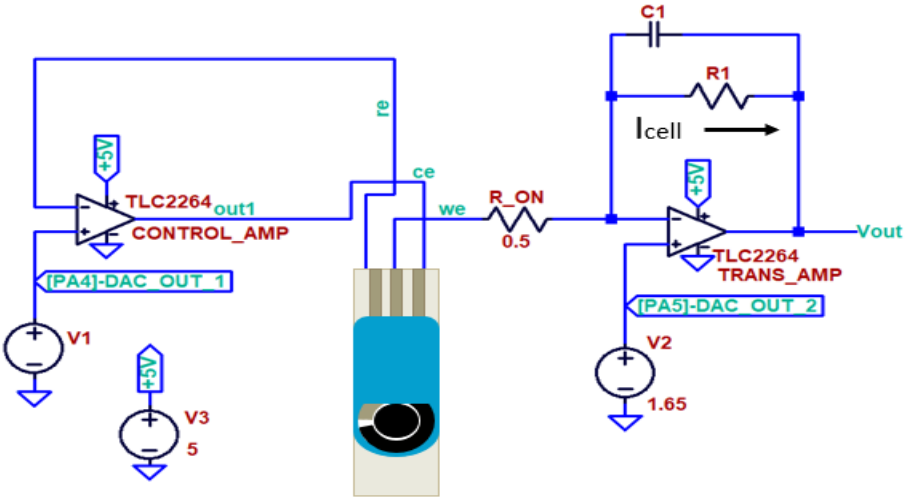

Figure 3.12: Design of the control and transimpedance amplifiers.

Since the reference electrode can be set to a minimum value of 0 V and a maximum of 3.3 V, the potential range of the potentiostat can be calculated as:

$$\begin{aligned} V_{wr(max)} &= V_w - V_{r(min)} \\ &= 1.65 - 0 \\ &= 1.65 \text{ V}, \end{aligned} \tag{3.1}$$

and,

$$\begin{aligned} V_{wr(min)} &= V_w - V_{r(max)} \\ &= 1.65 - 3.3 \\ &= -1.65 \text{ V}, \end{aligned} \tag{3.2}$$

where V_{wr} is the potential of the working electrode relative to the reference electrode, V_w is the potential of the working electrode, and V_r is the reference electrode potential. The cell current (I_{cell}) can then be calculated as,

$$\begin{aligned} I_{cell} &= \frac{V_w - V_{out}}{R5} \\ &= \frac{1.65 - V_{out}}{6.6 \text{ k}\Omega} \end{aligned} \tag{3.3}$$

where V_{out} is the output voltage of the transimpedance amplifier. Considering the fact the the ADC can only convert values in the range of 0 to 3.3 V, the maximum and minimum cell currents can be calculated from Eq. 3.3 as,

$$\begin{aligned} I_{cell(max)} &= \frac{1.65 - 0}{6.6 \text{ k}\Omega} \\ &= 250 \ \mu\text{A}, \end{aligned} \tag{3.4}$$

and,

$$\begin{aligned} I_{cell(min)} &= \frac{1.65 - 3.3}{6.6 \text{ k}\Omega} \\ &= -250 \ \mu\text{A}, \end{aligned} \tag{3.5}$$

in the resolution of,

$$\begin{aligned} I_{res} &= \frac{ADC_{step}}{R5} \\ &= \frac{805.66 \ \mu\text{V}}{6.6 \text{ k}\Omega} \\ &= 122.07 \text{ nA}. \end{aligned} \tag{3.6}$$

The resistance of the SPDT switch was not included in the equations since it is negligibly small compared to the resistance of the electrochemical cell.

A ceramic capacitor, C1, was included in the feedback path of the transimpedance amplifier to improve its stability. Any high frequency noise signal, no matter how small, could cause an unstable circuit to go into oscillation and thus this capacitor was necessary. The optimal value of the capacitor is dependent on the op-amp input capacitance and the capacitance of the electrochemical cell, and since the latter is not known, the best value could not be determined analytically. Therefore, the design approach was to put the pole due to the feedback network at a frequency much higher than the frequency of the input signal. The transfer function of the transimpedance amplifier can be calculated as,

$$\begin{aligned} V_{out} &= -I_{cell} \cdot Z_f \\ &= -I_{cell} \cdot \frac{R1}{1 + j \cdot 2 \cdot \pi \cdot f \cdot R1 \cdot C1} \end{aligned} \tag{3.7}$$

where Z_f is the impedance of the feedback network. This puts the pole frequency, f_p, at:

$$f_p = \frac{1}{2 \cdot \pi \cdot R1 \cdot C1} \tag{3.8}$$

It was decided that a value of 1 nF would be sufficient to place the pole at a much higher frequency than the 25 Hz input signal and most of its odd harmonics. This frequency was located at more or less 24.114 kHz according to Eq. 3.8.

The simulation and practical measurements for the control and transimpedance amplifier stage were not done separately, but rather included in the overall simulation and practical measurements of the final circuit that are described in Section 3.2.1.5 and 3.2.1.6. While this circuit is the core that is required to control the electrochemical cell potential, it is just as important to be able to measure the sensor's response with high accuracy and low noise. A filter stage was thus designed to filter the output of the transimpedance amplifier before measurements are taken on the ADC of the Nucleo board.

3.2.1.4 Bessel filter design

The goal of this stage was to filter out unwanted noise that is not within the bandwidth of the signal to be measured, and thus improve the signal-to-noise ratio. This stage is located after the transimpedance amplifier so that the signal noise can be reduced before it is sampled on the ADC. A few important aspects that needed to be considered is the type of filter, the phase response, the gain of the filter, the cutoff frequency, and the stopband attenuation.

The type of filter was chosen based on the type of signal that is applied to the electrochemical cell and the amount of this signal that needs to appear at the input of the ADC to still make an accurate measurement. The filter was thus designed in such a way that a square wave signal applied at its input is still reproduced at its output, while attenuating any signals at higher frequencies. Since a 25 Hz square wave is applied to the cell, the filter must be able to pass a sufficient amount of the harmonics without distorting them so that the waveform can be constructed at the ADC input to some extent. The frequency spectrum of the applied signal is shown in Fig. 3.13.

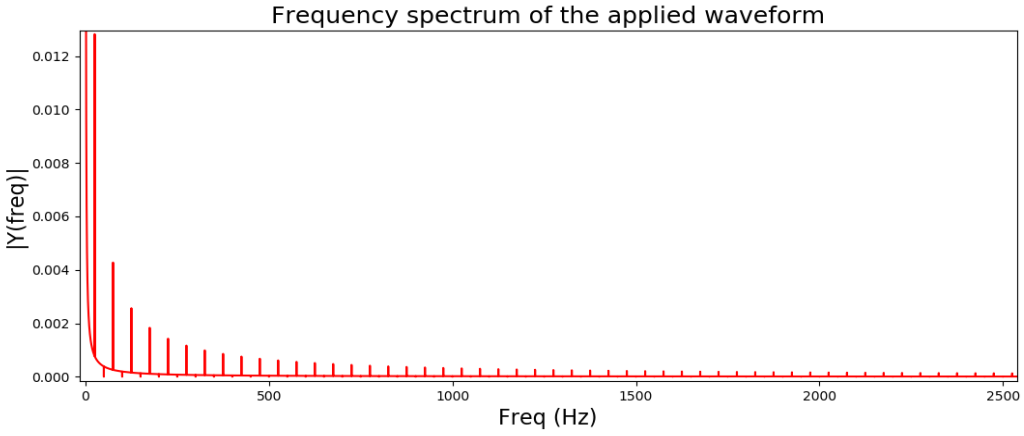

Figure 3.13: Frequency spectrum of the applied signal showing the large DC offset, a fundamental frequency of 25 Hz, and the odd harmonics at multiples of 25 Hz.

The graph shows that the applied signal has a large DC component that is due to the staircase potential. Another large component is observed at 25 Hz that is due to the fundamental frequency of the square wave potential. Smaller harmonics of this square

wave appear at the odd frequency multiples of the fundamental frequency (that is 75 Hz, 125 Hz, 175 Hz etc.). Distortion in this case can be due to attenuation of the square wave harmonics or a non-linear modification to the phase of each harmonic. A Bessel filter has the characteristic that it preserves the wave shape in the passband due to its linear phase response. Therefore, a low-pass Bessel filter was chosen as the starting point for the filter stage design.

When choosing the cutoff frequency there exists a trade-off between the amount of noise that is passed and the degree to which the signal is distorted. A lower cutoff frequency would result in less noise being passed through the filter at the expense of a more distorted signal since the phase and amplitude of the harmonics are modified. A higher cutoff frequency would lead to an output that provides a better representation of the input, but with more high frequency noise added to the signal. To illustrate this principle, two different filters were designed using Analog's Filter Wizard tool. For consistency, only first order unity gain filters were compared and the stopband frequency was always chosen to be a decade higher than the cutoff frequency. A schematic of the first order filter is shown in Fig. 3.14 and the values that were used are shown in Table. 3.5. Filter 1 had a cutoff frequency at 150 Hz and a stopband frequency of -20 dB a decade higher at 1.5 kHz. Filter 2 had a cutoff frequency at 10 kHz and a stopband frequency of -20 dB at 100 kHz. The op-amp was also biased at 1.65 V just as it would be in the final design. A voltage noise source (B1) was added to the square wave signal in the form of a relatively large white noise signal with an RMS value of 2.58 mV, a peak-to-peak value of about 12.31 mV, and a bandwidth of 500 kHz (chosen to be much higher than the bandwidth of the filter). The noise source RMS value was arbitrarily chosen, since it is only used for illustration purposes. An AC analysis was done to confirm that the filters had the correct cutoff and stopband frequencies, and then a transient analysis was done with the square wave and the noise source inputs to qualitatively assess the cutoff frequency trade-off. For the purpose of this simulation, no noise was added to the 5 V rail or the 1.65 V biasing source.

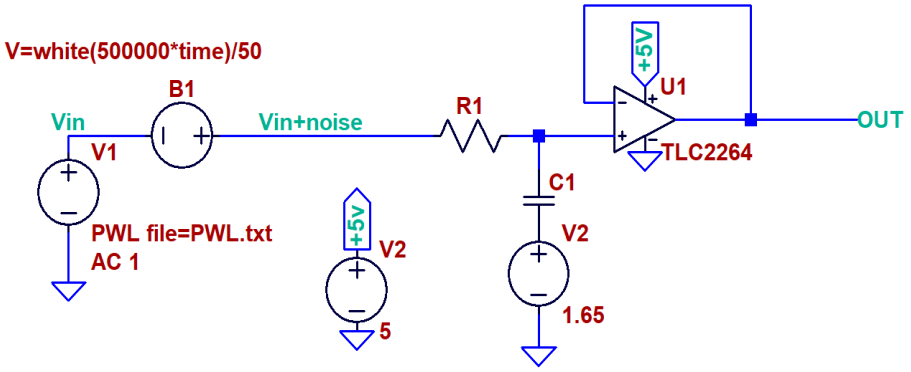

Figure 3.14: 1st order Bessel filter design.

Table 3.5: 1st order Bessel filters that are used to illustrate the cutoff frequency tradeoff.

	R1	C1	Cutoff	Stopband
Filter 1	9.62 kΩ	110 nF	-3 dB at 150 Hz	-20 dB at 1.5 kHz
Filter 2	992 Ω	16 nF	-3 dB at 10 kHz	-20 dB at 100 kHz

After analyzing the results (shown in Section 4.2.1.2) it was decided that a cutoff frequency of 5 kHz would be used. This frequency would start attenuating noise above 5 kHz, while preserving the wave shape due to a sufficient amount of harmonics that are located in the passband.

The order of the filter determines at what rate the signals are attenuated above the cutoff frequency. Higher order filters have a sharper roll-off at the cost of more components and filter stages, whereas lower order filters have a slower attenuation rate, but require less components. Thus, a second order unity gain Bessel filter was chosen for the filter stage of the potentiostat. This provided better performance than a first order filter, while still requiring a single operational amplifier and only two extra low-cost components. A unity gain was also appropriate since no voltage amplification was required after the transimpedance amplifier stage. Analog Filter Wizard was used to choose the lowest possible stopband frequency (for a filter with a 5 kHz cutoff) that would be able to realize a second order filter. The filter is shown in Fig. 3.15 and it's characteristics are summarized in Table. 3.6. The general rule is to bias capacitor C1 at the same noiseless virtual ground that the input signal is referenced to, which in this case is the 1.65 V that is used to bias the transimpedance amplifier.

Table 3.6: 2nd order Bessel filter stage components and characteristics.

	R1	C1	R2	C2	Cutoff	Stopband
2nd order Bessel filter	17.4 kΩ	2.4 nF	622 Ω	24 nF	-3 dB at 5 kHz	-20 dB at 20 kHz

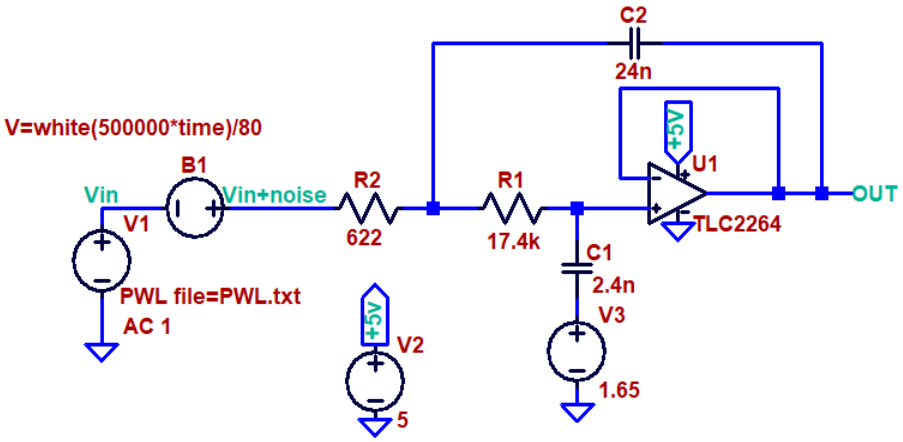

Figure 3.15: 2nd order Bessel filter stage that was used in the potentiostat design.

In general, Bessel filters have a slower roll off when compared to other filters such as a Butterworth filter. Thus, a -40 dB stopband attenuation at 50 kHz would have resulted in a 3rd order filter and not a 2nd order filter as expected. That is why the tool was selected to have a constant 5 kHz cutoff frequency and a -20 dB stopband attenuation. The stopband (-20 dB point) was just shifted from 50 kHz to lower frequencies, up until the point where it changes from a 2nd order filter to a 3rd order filter, which in this case was 20 kHz.

An AC analysis was done to confirm the bandwidth characteristics of the designed filter, followed by a transient analysis with a noisy square wave potential applied at its input.

The white noise source (B1 in Fig. 3.15) had an RMS value of 2.95 mV, a peak-to-peak value of 12.43 mV, and a bandwidth of 500 kHz. The RMS value of the noise source was chosen arbitrarily, since the source is simply used for illustration purposes. For the purpose of the transient simulation, no noise was added to the 5 V rail or 1.65 V bias.

3.2.1.5 LTSpice simulation of the potentiostatic circuit

After the theoretical design of the functional parts described above, the potentiostatic circuit was characterized as a whole system. This was done in terms of output linearity, bandwidth, and a noise analysis in the time and frequency domain that are all described in detail in this section. A full schematic of the final circuit that was simulated in LTSpice is shown in Fig. 3.16.

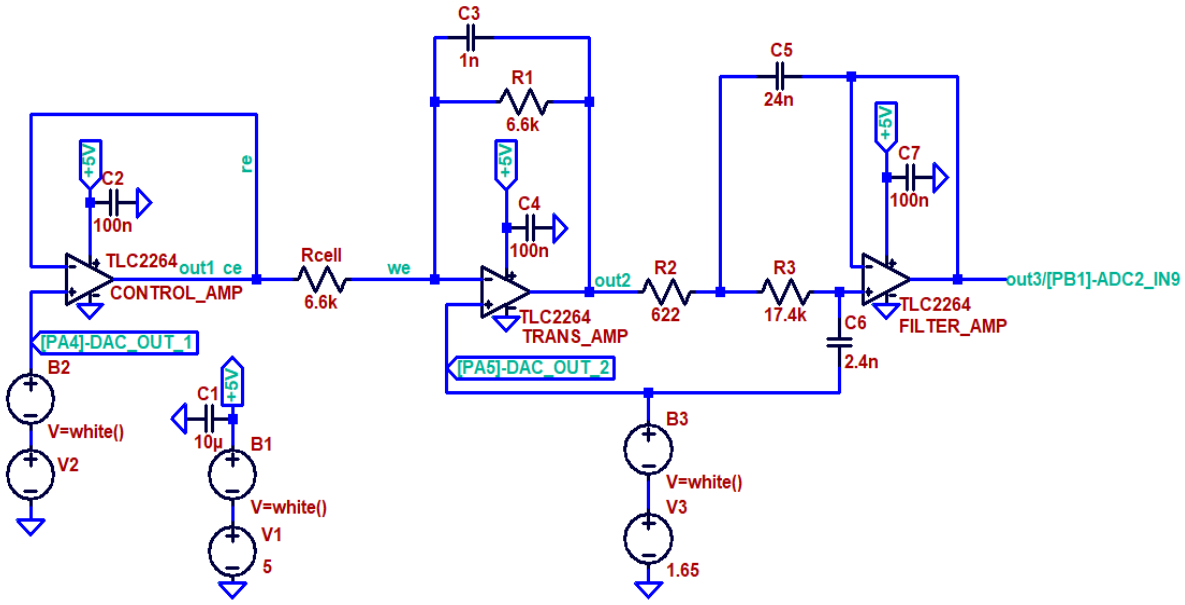

Figure 3.16: Full scale potentiostatic circuit that was used for the simulation in LTSpice.

The electrochemical cell was modeled as a 6.6 kΩ resistor and the reference and counter electrodes were shorted together so that the control amplifier acts as a buffer for DAC1. The idea behind this approach is to test the capabilities of the electronic circuit without the influence of any electrochemical experiments that might cause noise or unknown behaviour. This decision was supported by literature that followed similar procedures for the characterization step of a developed potentiostat [129, 132]. Arbitrary behavioural voltage sources B1, B2, and B3 were used in the transient noise analysis of the simulation to model white noise that is injected into the circuit from the MCU pins. The characteristics of these noise sources were measured using the procedure described in Section 3.2.1.1 and modeled as closely as possible in the software. V1 represents the [5V] power supply pin from the Nucleo board, and V2 and V3 were used to model the output of DAC1 and DAC2, respectively. The ultra-low resistance switch was excluded from the simulation since its on-resistance was negligibly small compared to the cell model resistance. A 10 μF electrolytic capacitor was placed on the 5 V power rail to act as a charge reservoir, and 100 nF ceramic capacitors were placed on the rails of each op-amp to provide a low-impedance path close to the IC. All component names and node symbols that are used in this section is in reference to Fig. 3.16.

The first step was to identify the linear working range of the circuit, and what the maximum attainable voltage range is that can be expected at the input of ADC2. This is an important step in the design procedure since the cell current (Eq. 3.3) is linearly dependent on the output voltage, V_{out}, of the transimpedance amplifier. Since the op-amps have a rail-to-rail output it was expected that the voltage at node *out3* would be able swing close to 0 and 3.3 V. Voltage source V2 was linearly swept from 0 to 3.299194 V (since this is the highest achievable DAC value that corresponds to a digital word of 4095) over a period of 5 seconds, and V3 was kept constant at 1.65 V. The output voltages on nodes *out1, out2* and *out3* were plotted to determine the linear working range of the potentiostatic circuit according to LTSpice. The voltage noise sources were not included in this analysis so that the working range can be determined under ideal noiseless conditions.

The bandwidth of the whole system was quantitatively determined by doing an AC analysis with the AC amplitude of source V2 set to 1. V2 was also biased at 1.65 V so that the AC analysis could be done at the correct DC operating region. A qualitative AC analysis was done by comparing the waveshape of the ideal output waveform to the simulated output waveform with a square wave input. A square wave signal superimposed on a staircase potential was applied at V2, and the output at *out3* was plotted against the ideal output waveform that would have resulted without the non-idealities and limited bandwidth of the various op-amp stages. This gave an indication as to how well the harmonics are passed through the system. The noise sources were excluded for this simulation so that the waveshape could be assessed under ideal noiseless conditions.

A time domain transient noise analysis was done to determine the effect of added input noise on the output of the system. Higher noise levels could lead to erroneous measurements on the ADC that would influence the accuracy of the measured current. The noise sources that were considered for this analysis is that of the power supply rail and the DAC outputs. The noise measurements were taken according to the method described in Section 3.2.1.1 with the Nucleo board powered using V_{IN} and the USB plugged in. The RMS values were determined and the sources were modeled in LTSpice as white noise signals that are added to the 5 V rail and the DAC outputs. A summary of the noise sources that were added to the simulation is shown in Table 3.7. The DAC outputs of the Nucleo board were set to 1.65 V before the noise measurements were taken and the noise results from Section 4.2.1.1 was used to model the power rail noise.

Table 3.7: White noise sources that were used in the transient noise analysis in LTSpice.

	RMS	**Peak-Peak**	**Bandwidth**
B1 (Rail)	384.86 μV	1.848 mV	500 kHz
B2 (DAC1)	389.19 μV	1.862 mV	500 kHz
B3 (DAC2)	400 μV	1.92 mV	500 kHz
	Noise source combinations		
Influence of power rail	B1 added, B2 and B3 removed		
Influence of DAC1	B2 added, B1 and B3 removed		
Influence of DAC2	B3 added, B1 and B2 removed		
Influence of all sources	B1 - B3 added		

The transient analysis was done with the four different noise source combinations that

are summarized in Table 3.7. V1 and V2 were set to a DC value of 1.65 V and the noise sources were added as described. The peak-to-peak, average, and RMS value (after subtracting the average value) of *out3* was calculated to determine the contribution of the sources to the output. A 120 ms period was used for the simulations. The simulation showed that the superimposed output noise could lead to erroneous ADC readings, especially if only one sample is taken. It was decided that the final design would circumvent this issue in the software by sampling multiple times and averaging out the zero mean white noise signal to get the underlying DC value of interest. This procedure will be explained in Section 3.2.2.2.

Lastly a frequency domain noise analysis was done to compute the noise due to Johnson, shot and flicker noise. During the noise analysis solver, LTSpice finds noise sources in the individual components of the circuit; in other words, no noise sources need to be defined in the schematic such as with the time domain noise analysis. Johnson noise, also called thermal noise, is the electronic noise that is caused by the thermal agitation of electrons inside any conductive component. This type of noise is present in any electronic circuit regardless of any applied voltage. Shot noise arises from the random fluctuation of the amount of discrete charge carriers in an electronic circuit, but this is often minuscule compared to other noise sources. Flicker noise, also called 1/f noise, is also present in most electronic devices and is often associated with transistors. Therefore, this type of noise is commonly found in electronic circuits that contain operational amplifiers. The time domain noise sources were removed from the circuit and source V2 was biased at a DC potential of 1.65 V. The electrochemical cell was modeled as a "noiseless" 6.6 kΩ resistor so that the simulation only calculated the noise contribution from the remaining components. Source V2 was set as the noiseless input signal and the output noise was calculated at nodes *out1, out2* and *out3* over the frequency range of 10 mHz to 710 kHz. The bandwidth was chosen to be the same as the gain-bandwidth-product of the op-amps since they would not work as expected at higher frequencies. The output noise at each node was compared to see what the contribution of each amplifier stage is to the noise, and the contribution of each resistor at *out3* was calculated to see which resistor had the highest contribution to thermal noise. LTSpice was used to report the noise in terms of their RMS values. The RMS values are calculated as the square root of the integral of the power spectral density over the frequency band of interest.

After the simulation results were deemed satisfactory, a schematic was drawn in Eagle CAD and a PCB was printed. The design files are shown in Appendix D and the interface between the Nucleo board peripherals and the external PCB is given in Table. 3.8.

Table 3.8: Peripheral and pin interface definitions for the external PCB.

Peripheral name	**Pin & header on Zio connectors**	**Functionality**
DAC1	PA4 on CN7	Applies square wave signal to non-inverting pin of control op-amp.
DAC2	PA5 on CN7	Applies 1.65 V bias to transimpedance and filter op-amps.

Table 3.8 continued from previous page

Peripheral name	Pin & header on Zio connectors	Functionality
GPIO pin for working electrode switch	PD7 on CN9	Switches the working electrode in and out of potentiostatic circuit.
ADC2_IN9	PB1 on CN10	Measure voltage output of filter stage.
5 V power rail	5V on CN8	Power rail for external PCB
GND pins	GND on CN9, GND on CN10	Ground rail for external PCB

The PCB was a double sided board with a large ground plane at the bottom that was connected to multiple ground pins on the Zio headers. The large ground plane reduces the resistance of the return path thereby reducing noise that is caused by variations in the return current. It is used to get a more uniform ground voltage since the ground track now has a smaller resistance and thus return currents cause smaller variations between separated parts of the ground net. Long ground tracks and loops were also avoided by using vias directly from the components to the ground plane so that magnetic coupling and interference on these tracks can be avoided. The tracks on the PCB were made as wide as possible so that the track resistance can be made smaller. 100 nF bypass capacitors were connected to each power supply pin of the IC components to create a low impedance path for high frequency noise. Four straight pin headers were used as clamping points for the screen printed electrode connection cable (DRP-CAC).

3.2.1.6 Practical measurements of the potentiostatic circuit

The practical measurements were taken with the external PCB mounted on the Zio headers of the Nucleo board just like it would be used in the final application. The whole board was powered with a 9 V battery on the V_{IN} pin and the USB was also connected to the host PC. The circuit was characterized in terms of the noise on the 5 V power rail and ADC2 input, the linear range of operation as measured on ADC2, and the bandwidth of the whole system. As in the case of the LTSpice simulation of the circuit, the electrochemical cell was modeled using a 6.6 kΩ resistor that was connected between the working electrode and the counter and reference electrodes that are shorted together.

The rail and output (node at V_{out3}) noise voltage waveforms were acquired on the oscilloscope while the DAC1 and DAC2 values were set to 1.65 V. The linear operating region was determined by sweeping DAC1 from 0 to 4095, while keeping DAC2 constant at 1.65 V, and measuring the output on ADC2. This was achieved by using the timers as interrupts. TIM6 was used to trigger DAC1 to output a value every 10 ms, and TIM3 was used to start an ADC sampling interval 5 ms after DAC1 was updated. The ADC was set to take 64 samples at a rate of 50 kHz (20 μs), after which the values are averaged and stored.

The system bandwidth was determined by removing the external PCB from the Nucleo board and connecting the inputs to the benchtop power supply and signal generator. The power supply was used to generate the 5 V rail for the board as well as the 1.65 V biasing voltage for the transimpedance and filter amplifier stages. The signal generator was used to apply a 200 mV peak-to-peak sine wave with a 1.65 V offset at the input of

the control amplifier. The bandwidth was determined by increasing the signal frequency until the peak-to-peak value at the filter output reached a value of 141 mV (which is -3 dB of gain at the corner frequency).

The results of the practical measurements were compared to that of the designed and simulated values to assess how well the circuit performed.

3.2.2 Software

The goal of the software is to apply the square wave potential to the reference electrode and measure the voltage representation of the current that flows through the working electrode. The most important task that was needed to complete this goal was to find a way to sample the current at very specific intervals in comparison to the applied waveform. This was achieved by using timer interrupts to output values at specific intervals and to invoke ADC sampling periods in relation to those intervals. A high-level description of this task is given by the control flow diagram in Fig. 3.17.

When the user button is pressed, the working electrode is switched into the potentiostatic circuit, and TIM6 is started to interrupt at a rate of 50 Hz. At each interrupt the DAC1 value is changed accordingly and TIM3 is started to interrupt after 18.6 ms. Once this interrupt fires, ADC2 is started in DMA mode and TIM2 is set to trigger 64 ADC conversions at a rate of 50 kHz. Once the DMA has transferred 64 ADC samples to memory, the values are averaged and stored before the whole process is started again. When the last pulse has been applied, the peripherals are stopped and the working electrode is removed from the circuit so that no current can flow through the electrochemical cell. A protocol then loads the collected data into an 8-bit array and sends it through USART communication to the host PC.

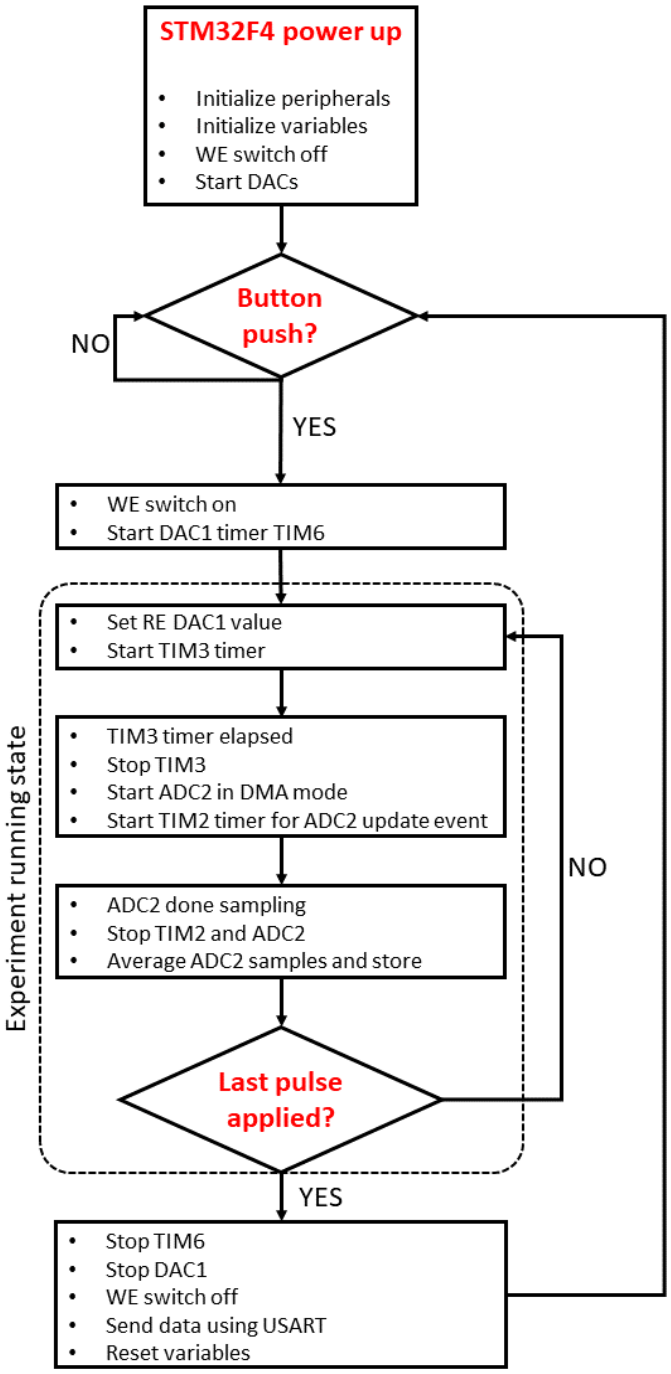

Figure 3.17: High-level description of the software that controls the potentiostat.

The MCU was programmed to apply the waveform with the following parameters:

- $V_{wr(step)} = 5$ mV;
- $V_{wr(pulse)} = 20$ mV;

- $f = 25$ Hz;
- Scan rate $= f \times V_{wr(step)} = 125$ mV.s^{-1}.

The initial and final potential could be set by initializing the variables in the code. Therefore, the Nucleo board had to be reprogrammed every time the potentials were changed.

3.2.2.1 Calculation of the square wave potential waveform

SWV requires that a square wave potential is superimposed on a staircase potential such as that shown in Fig. 3.18. The blue waveform represents the staircase potential against which the current samples are plotted in the voltammogram, and the red waveform is a square wave that is superimposed on the staircase.

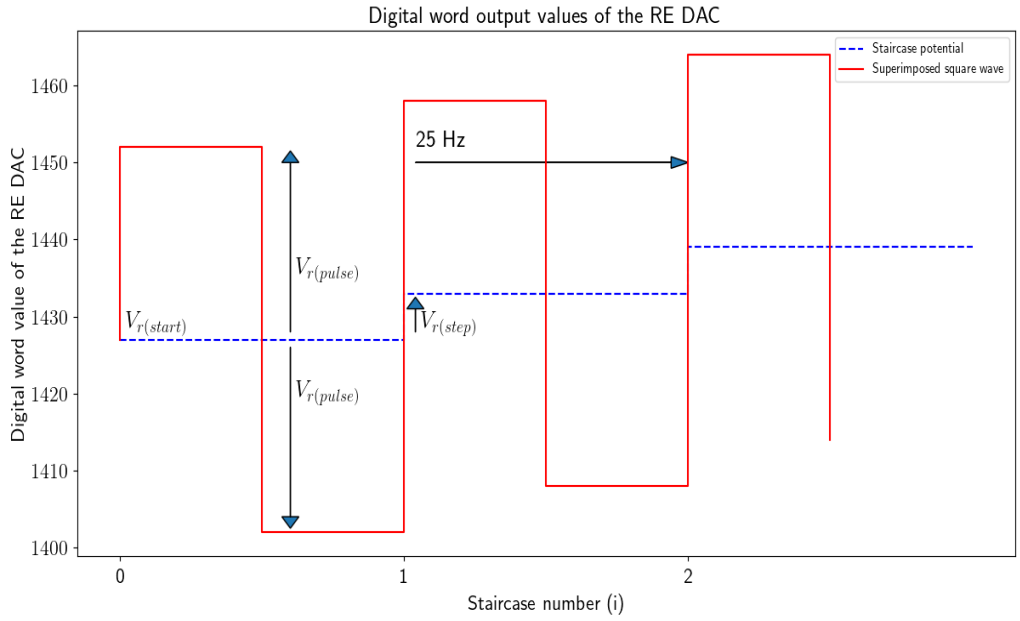

Figure 3.18: Potential waveform that is applied using DAC1 showing how the experimental parameters are used to construct the signal.

Since the experimental parameters are defined in terms of working vs reference, the values of the reference electrode first had to be calculated. To aid in the explanation of the algorithm that was used to calculated the waveform that needed to be applied, assume that the cell voltage had to be swept from 0.5 to -0.4 V for a certain SWV experiment. Since the working electrode is biased at 1.65 V, the reference electrode had to start at,

$$\begin{aligned} V_{r(start)} &= V_w - V_{wr(start)} \\ &= 1.65 - 0.5 \\ &= 1.15 \text{ V}, \end{aligned}$$

and end at,

$$\begin{aligned} V_{r(end)} &= V_w - V_{wr(end)} \\ &= 1.65 - (-0.4) \\ &= 2.05 \text{ V}. \end{aligned}$$

The step and pulse potential values of the reference electrode, however, remain 5 mV and 20 mV, respectively. The experimental parameters were then converted to digital words using the following conversion equation for a 12-bit resolution DAC,

$$Word = round\Big(\frac{voltage}{3.3} \times 2^{12}\Big),$$

where *Word* is the digital word, and *voltage* is the desired voltage. The *round* function converts the floating point value to the nearest integer value, which would result in a DAC value that is as close as possible to the desired voltage. To keep track of the number of pulses that need to be applied, the number of staircase steps were first calculated according to,

$$\begin{aligned} N_s &= round\Big(\frac{V_{r(end),word} - V_{r(start),word}}{V_{r(step),word}} + 1\Big) \\ &= round\Big(\frac{2544 - 1427}{6} + 1\Big) \\ &= 187, \end{aligned} \tag{3.9}$$

where N_s is the number of staircase steps, and $V_{r(end),word}$, $V_{r(start),word}$, and $V_{r(step),word}$ are the digital word representations of the reference electrode parameters that were calculated. The +1 term is added to account for the first potential staircase value of 1427. Since there are two pulses per staircase step, the number of pulses were, $N_p = N_s \times 2 = 374$. The digital word versions of the parameters were then used to create an array of DAC values that would be applied to the reference electrode using the following equations:

$$RE_{DAC}[i \times 2] = (V_{r(start),word} + V_{r(step),word} \times i) + V_{r(pulse),word}, \tag{3.10}$$

and,

$$RE_{DAC}[i \times 2 + 1] = (V_{r(start),word} + V_{r(step),word} \times i) - V_{r(pulse),word}, \tag{3.11}$$

where,

$$i \in N_0, i < N_s.$$

Eq. 3.10 is used to calculate the values of the forward pulses, and Eq. 3.11 is used to calculate the values of the reverse pulses. The forward pulse is defined as the pulse that applies a potential in the direction of the scanned potential, and the reverse pulse is defined as the potential that pulses back to the starting potential. Since the sweep goes from positive to negative, the forward pulse is the pulse that applies a more negative cell potential, and the reverse pulse is the pulse that applies a more positive cell potential. After calculating the digital word values and the DAC array values, the experimental parameters were then recalculated to test the accuracy of applied waveform using the following equation,

$$Voltage = \frac{word}{2^{12}} \times 3.3.$$

These accuracy results are summarized in Section 4.2.2.1.

3.2.2.2 Detailed software control flow

The main program loop of the MCU applies the potential waveform and measures the resulting current according to the time frame that is shown in Fig. 3.19. A single time

frame starts when DAC1 updates the output using TIM6 and ends when the next TIM6 update event is fired. Note that the time values and interrupt locations are not drawn exactly according to scale.

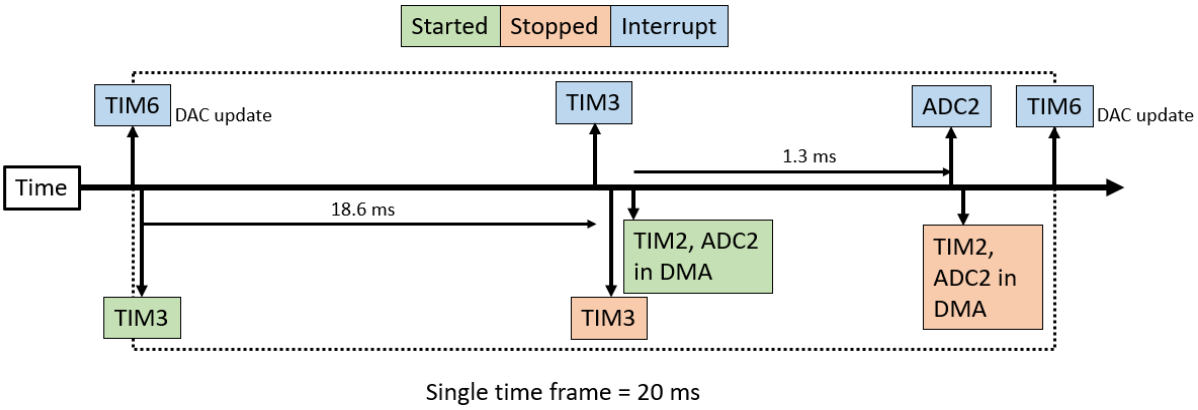

Figure 3.19: Diagram of the timers and peripherals that are used to control the ADC sampling periods and the DAC output rate.

The experimental parameters required that the staircase waveform have a frequency of 25 Hz. Since there are two pulses per staircase potential, the DAC had to be update twice as fast. Thus, TIM6 was used to fire an update event at a rate of 50 Hz (20 ms). When the interrupt routine is called, the DAC output value is manually set using each value that is stored in the reference electrode DAC array as calculated in Section 3.2.2.1. TIM3 was used to signal the start of an ADC sampling interval by setting the timer to fire an interrupt event after a period of 18.6 ms has elapsed. This timer was started immediately after the DAC output value was set. When TIM3's interrupt event fired, it was stopped and TIM2 was started together with ADC2 in DMA mode. TIM2's update event was set to a rate of 50 kHz (20 μs) and the interrupt line was internally linked to ADC2 in DMA mode. This mode allows the ADC to perform conversions, transfer the value from the peripheral, and store it directly in memory at the rate defined by TIM2, without affecting the MCU processor loading. The mode was set to sample for 1.3 ms after which the DMA calls the ADC2 conversion complete callback at about 18.6 + 1.3 = 19.9 ms after the DAC value has been set. TIM2 and ADC2 are then stopped before the next TIM6 update event is fired, and the time frame is repeated again.

Three important aspects that needed to be considered are when the ADC starts sampling, the sampling duration, and the sampling rate. The main requirement was that the current is measured as close as possible to the end of the forward and reverse pulses. There is, however, no guideline as to what the sampling parameters of the Gamry instrument is, and thus the values were chosen according to good engineering practice. In order to reduce noise it was decided that 64 samples would be taken and averaged by bit shifting the sum with 6 places. The sampling rate also needed to be high enough so that all 64 samples could be taken before the end of the pulse. The Nyquist theorem that states that the sampling rate should be at least twice as high as the highest frequency of the signal that is sampled, was also taken into account. Since the signal is essentially measured at DC and the Bessel filter was designed to have a cutoff of 5 kHz, the sampling rate was

chosen to be much higher at 50 kHz. At this rate the sampling time is,

$$\begin{aligned}\tau_s &= 64 \times 20\ \mu\text{s} + 20\ \mu\text{s} \\ &= 1.3\ \text{ms},\end{aligned}$$

if the initial 20 μs quiet time of TIM2 is also taken into account. Since a single pulse duration was 20 ms, it was decided that the ADC would start sampling after 18.6 ms, which theoretically leaves about 100 μs at the end of the pulse that is not sampled. But the MCU overhead was taken into account and thus it was decided that the parameters would not be changed to try and minimize the remaining time.

After the last pulse was measured all the peripherals were stopped, the working electrode was removed from the circuit, and the data was sent to the host PC using USART communication. The working of the detailed control flow was assessed by toggling two GPIO pins on the Nucleo board to confirm the timing characteristics using an oscilloscope. This was done to confirm that the timers are started and stopped at the correct intervals, as well as to make sure that the ADC samples in the correct interval.

3.2.2.3 USART communication

The data was only sent to the host PC after the experiment was performed since the MCU had enough memory to store the data as it was collected. Continuous communication was thus not necessary which also removes the possibility of added noise as experiments are performed. USART3 is by default connected to the ST-LINK programmer to be used as a virtual com port interface, and thus this channel was set up with a baud rate of 9600, 8N1.

The transmitted values and their number of bytes are summarized in Table 3.9. The first three values were mainly used for debugging purposes and to see if the timing parameters were chosen correctly. The staircase value, applied potential, and measured value were sent as digital words that were converted to voltage values on the host PC.

Table 3.9: Number of bytes used for the USART protocol.

Order	Value	Number of bytes used
1.	Pulse number	2
2.	Pulse type (0x0 or 0x1)	1
3.	Pulse time applied (ms)	4
4.	Staircase value	2
5.	Applied potential RE (DAC1)	2
6.	Measured current value (ADC2)	2
	Total per pulse	13 bytes

A Python script was used to establish serial communication with the Nucleo board, collect the data, and store it in text files in raw bytes and converted format. The digital words were converted to voltages and the cell current was calculated using Eq. 3.3. The data analysis algorithm was then used to extract the peak current from a curve.

3.2.3 Potentiostat methodological assumptions

Throughout the development of the potentiostat device it was assumed that the analog reference voltage of the Nucleo board is exactly 3.3 V. The calculations in this chapter were, therefore, made with this assumption since the actual value could not be determined with the equipment at hand.

The values of the resistors and capacitors were also assumed to be exact in the calculations. Since 5% tolerance resistors were used, the actual values that were used for the potentiostat differ slightly from the theoretical values. The actual values that were used on the PCB were measured using a UNI-T UT30C digital multimeter. The device itself has an accuracy of $\pm(0.8\% + 2)$ of the range. The capacitor values were measured using a Hewlett Packard 4285A precision LCR meter that has a basic accuracy of 0.1%. The values are summarized and the effects are discussed in Section 5.3.1.

3.3 Comparison of the developed potentiostat with the Gamry instrument

The developed potentiostat was verified using the Gamry 1000E instrument as a benchmark. SWV experiments were conducted with different concentrations of the FeCN redox probe. Since the SWV peak current is linearly dependent on the redox species concentration (see Eq. 2.6), it was used to verify that the device can distinguish between different redox probe concentrations [144]. Two unmodified CNF sensors were used for these tests and the FeCN dilutions were made *in-situ* as described in Appendix B.3. 5 mM, 4 mM, 3 mM, 2 mM, 1 mM, and 0.5 mM concentrations were used. The first sensor was tested on the Gamry instrument and the second sensor was tested on the developed potentiostat. The experimental parameters for the sensor tested on the Gamry instrument were: 0.5 to -0.4 V scan range, 25 Hz, 5 mV step size, and 20 mV pulse size. And the parameters of the home-built device were: 0.5 to -0.4 V scan range, 25 Hz, 4.834 mV step size, and 20.14 mV pulse size. This was slightly different from the Gamry instrument since the DAC of the Nucleo board only had a 12-bit resolution for applying potentials.

An important decision that had to be made was the concentration range that was tested. If the concentrations were too high, it would cause a large current to flow which would saturate the ADC readings of the home-built device. Since it was designed to work within a range of ± 250 μA, the maximum concentration should not produce currents higher than that. The forward and reverse current samples did not exceed ± 210 μA in any of the previous 5 mM FeCN experiments that were conducted on the Gamry instrument. Therefore, 5 mM was chosen as the highest concentration to be used and the remaining five concentrations were diluted from this. This choice was also beneficial to verify the operation of the device since subsequent sP-selectin detection measurements will be conducted in 5 mM concentrations of the redox probe.

As proof of the forward and reverse current magnitude, a typical voltammogram of an unmodified CNF sensor that was used in the reproducibility studies is included in the results (Section 4.3) of these comparison tests.

3.4 Electrochemical measurements of immunosensor with Gamry instrument

In this section the protein immobilization strategy and final electrochemical measurements of each full scale test are described. Fig. 3.20 shows a brief diagram of the protocol that was followed.

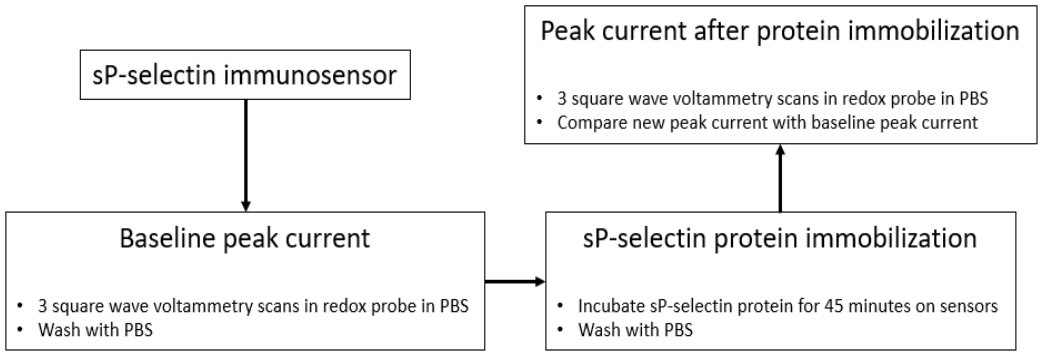

Figure 3.20: Brief overview of the process that was followed to perform the electrochemical measurements.

The antibody immobilized, sP-selectin immunosensors were first scanned in the appropriate redox probe to get a baseline peak current. Three SWV scans were used to see if the sensor had a stable response before using one of the scans for a baseline peak current. After a PBS washing step, the sensors were incubated with the sP-selectin proteins for 45 minutes on ice. A last SWV scan was done in the redox probe to get the new peak current after the proteins have bound to the immobilized antibodies. Fig. 3.21 shows a photo of the measurement setup in the lab, and an inset of the DropSens immunosensor that is connected to the Gamry 1000E instrument through the DRP-CAC cable.

Figure 3.21: Photo of the measurement setup for the immunosensor in the lab. ① shows the Gamry 1000E instrument that was used, and ② shows the the DropSens sensor connected to the DRP-CAC cable.

3.4.1 Measurements with FeCN redox couple

The immunosensor response was tested over a range of sP-selectin protein concentrations to determine the linear range of the sensor, and to get a calibration curve in this operating region. An important aspect that needed to be considered is the incubation time of the proteins. The duration used in literature varies considerably with 15 minutes [90, 138], 30 minutes [71, 136, 145], and 1 hour [115] reported for other immunosensors. Eissa *et al.* used an interesting approach to optimize the incubation time of the SMN protein [69]. A protein solution was incubated for 10, 15, 20, 25, 30, 45, and 50 minutes on the immunosensor to test which duration would lead to the biggest change in peak current. The response was maximized with an incubation time of 45 minutes, and therefore all SMN protein concentrations were incubated for that time. Due to a shortage of sensors, similar experiments could not be conducted for this project, and thus the proteins were also incubated for 45 minutes.

For the first set of GPHOX immunosensors a total of 32 sensors were tested over 8 different concentrations by grouping them into batches of 4 per category. This was done to get a statistical mean and variation of the immunosensor response. The recombinant sP-selectin protein was diluted to 8 different concentrations ranging from 100 μg/ml to 10 pg/ml in factors of 10. The stock solution was created by reconstituting 50 μg of the protein in 50 μl of PBS to get a concentration of 1 mg/ml. 16 μl was taken from this solution and added to a new vial containing 144 μl of PBS to get the highest experimental concentration of 100 μg/ml. This process was followed 8 times to dilute each previous vial by a factor of 10 until the 8^{th} vial which had a concentration of 10 pg/ml. The dilution process is illustrated in Appendix B.8 and these vials were stored in -20°C when not in use. Table 3.10 gives a summary of the experimental setup that was used for the GPHOX sensors. After the antibody attachment procedure described in Section 3.1.5 was followed, the immunosensors were numbered according to this table and kept on ice for

the duration of the electrochemical measurements. SWV experiments were conducted in a fresh batch of the redox couple solution using the following parameters: 0.5 to -0.2 V, 25 Hz, 20 mV pulse size, 5 mV step size, and 2 seconds equilibrium time.

Table 3.10: Experimental setup for first full scale test using the GPHOX immunosensors.

Sensor number	Category number	sP-selectin concentration
1 - 4	1.1	100 μg/ml
5 - 8	1.2	10 μg/ml
9 - 12	1.3	1 μg/ml
13 - 16	1.4	100 ng/ml
17 - 20	1.5	10 ng/ml
21 - 24	1.6	1 ng/ml
25 - 28	1.7	100 pg/ml
29 - 32	1.8	10 pg/ml

Each immunosensor was first subjected to three consecutive SWV scans (without removing the redox couple solution) to get a baseline peak current before the sP-selectin proteins were immobilized. The redox solution was then removed by performing three washing steps in PBS. 13.5 μl of the appropriate protein concentration was incubated on the working electrodes for 45 minutes while the sensors were kept on ice. The solution was gently washed off using PBS to remove the unbound proteins, and the sensors were again kept on ice while the next range of measurements were performed. Fig. 3.22 shows a diagram of the immunosensor after the sP-selectin proteins were incubated on the surface of the working electrode.

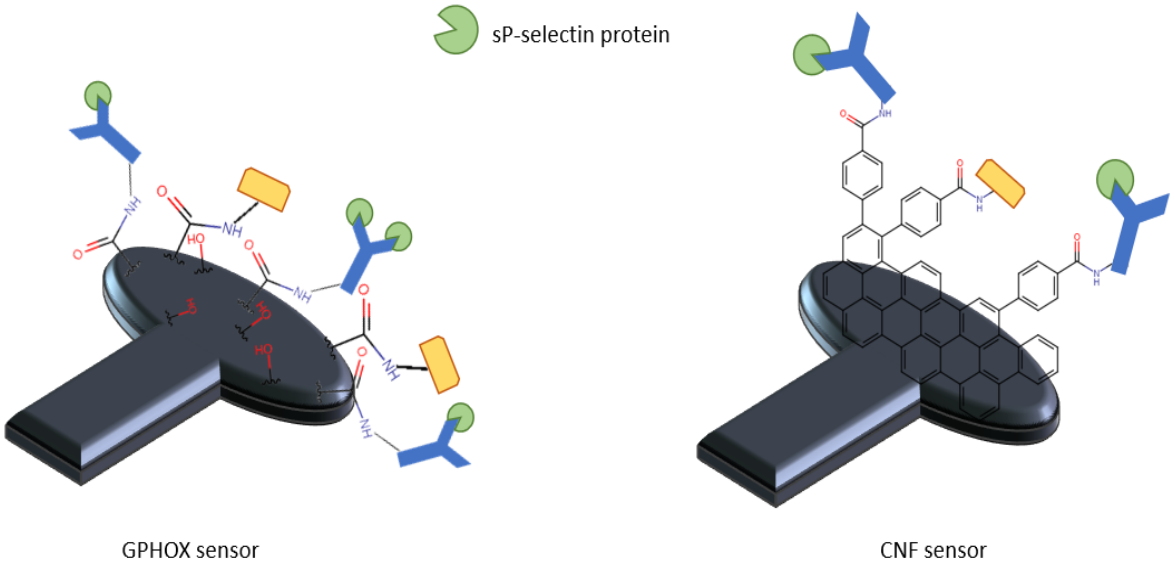

Figure 3.22: Diagram of the GPHOX and CNF immunosensors after immobilizing sP-selectin proteins.

Thereafter, each sensor was subjected to three consecutive SWV scans to get the peak redox current after the sP-selectin proteins were immobilized. For this set of tests, the measurements were performed sequentially, i.e. starting at sensor 1 and ending at sensor 32. The peak redox current of the third SWV scan taken before sP-selectin immobilization and the third SWV scan taken after immobilization was compared for each sensor

to get a relative change in peak current. Out of the three consecutive scans, it was noted that the first scan was not as reproducible as the last two which is why the third one was used for the comparison tests. The mean relative change of each category was calculated and plotted versus the concentration of sP-selectin protein. The maximum and minimum deviation from the mean was plotted as error bars on the same graph to assess the variation of the sensor response.

The second full scale test using the 21 CNF sensors was conducted after the first full scale test results were analyzed. Table 3.11 provides a summary of the experimental setup that was used for this test and Appendix B.9 illustrates how each protein dilution was made. 1 ml C-reactive protein (CRP) at a concentration of 1 μg/ml in PBS was also acquired to perform non-specific tests of the CNF immunosensors. A fresh batch of the FeCN redox couple solution was prepared for the electrochemical measurements.

Table 3.11: Experimental setup for the second full scale test using the CNF immunosensors.

Sensor number	Category number	Protein concentration
1-3	2.1	1 μg/ml sP-selectin
4-6	2.2	500 ng/ml sP-selectin
7-9	2.3	100 ng/ml sP-selectin
10-12	2.4	10 ng/ml sP-selectin
13-15	2.5	5 ng/ml sP-selectin
16-18	2.6	1 ng/ml sP-selectin
19-21	2.7	1 μg/ml CRP

A similar procedure that was used for the GPHOX immunosensors was used for the CNF sensors, except for a few minor changes that are described here. The sensors were first divided into their category and numbered accordingly before the experiments were started. The antibody attachment procedure that is described in Section 3.1.5 was used to modify the working electrode of the sensors. To obtain the baseline response, each immunosensor was then scanned with three consecutive SWV scans using the following parameters: 25 Hz, 20 mV pulse size, 5 mV step size, 2 s equilibrium time, and a range of 0.5 to -0.4 V. After being washed three times with PBS, the sP-selectin and CRP proteins were added onto the working electrode of the immunosensors. 32 μl of the appropriate concentration was incubated for a period of 45 minutes while the sensors were kept on ice. A higher volume (compared to the first set of GPHOX sensors) was used to account for any liquid that might run off the working electrode surface. The proteins were then washed off using PBS and kept wet during the last round of SWV measurements by adding a 100 μl drop of PBS. In order to exclude the time of measurement or any bias towards measuring one category earlier than another, the immunosensors were tested at random. Three more SWV scans were done using the same experimental parameters that are described above. The third SWV scan was used in the analysis to obtain a relative change in the peak current before and after protein immobilization. The mean percentage change and deviations from the mean were calculated for each category and plotted against the protein concentration.

Before the third set of experiments were conducted, a fluorescent study was done on four CNF immunosensors. The reason for this was to make sure the antibody attachment procedure worked as expected, and that the first baseline SWV scan does not wash off any antibodies. The fluorescent crosslinking procedure that was followed was described

in Section 3.1.6. The experimental setup for the third full scale test is shown in Table 3.12 and the protein dilution steps are shown in Appendix B.10.

Table 3.12: Experimental setup for the third full scale test using the CNF immunosensors.

Sensor number	Category number	Protein concentration
1-3	3.1	1 μg/ml
4-6	3.2	500 ng/ml
7-9	3.3	100 ng/ml
10-12	3.4	10 ng/ml
13-15	3.5	1 μg/ml CRP

The antibody attachment procedure that is described in Section 3.1.5 was followed to prepare these immunosensors. A fresh batch of the redox couple was made to perform electrochemical measurements, but this time the pH of the solution was adjusted from 7.4 to 5.5 using a 0.5 M HCl solution. This was done so that the pH of the testing solution would be below the isoelectric point of the sP-selectin proteins. The theoretical isoelectric point of the recombinant sP-selectin protein was calculated using the the amino acid sequence that is provided on the UniProt database [146]. The database is a central hub for the collection of structural and functional information for a large number of proteins. The sequence was entered into an online calculator, and the isoelectric point was calculated as 5.83 [147]. Therefore, the protein would be positively charged in the redox solution with a pH of 5.5. It was expected that the extra positively charged layer would attracted the negatively charged redox anions closer to the surface of the electrode thereby increasing the peak current. As with the previous tests, a baseline SWV scan was first done in the pH adjusted redox solution. After washing the immunosensors with PBS, a 100 μl of the appropriate protein concentration was incubated on the sensors for 45 minutes. The proteins were washed off using PBS and another SWV scan was done using the same pH adjusted redox solution. The scan parameters were: 20 mV pulse size, 5 mV step size, 25 Hz, 0.5 to -0.4 V scan range, and 2 seconds equilibrium time. The mean and deviation from the mean was calculated for each category and the results were plotted against the protein concentration.

3.4.2 Measurements with RuHex probe

Table 3.13 gives the experimental setup for the fourth full scale test with the RuHex probe. 18 sensors were used for this test over the concentration range of 10 ng/ml to 1 μg/ml. Non-specific tests were also done with 1 μg/ml of CRP. The immunosensors were prepared as described in Section 3.1.5. A fresh batch of 5 mM RuHex in PBS was prepared as described in Appendix B.2. The protein dilution procedure is described in Appendix B.11.

Table 3.13: Experimental setup for the fourth full scale test using the CNF immunosensors and the RuHex probe.

Sensor number	Category number	Protein concentration
1-3	4.1	1 μg/ml
4-6	4.2	500 ng/ml
7-9	4.3	100 ng/ml
10-12	4.4	50 ng/ml

Table 3.13 continued from previous page

Sensor number	Category number	Protein concentration
13-15	4.5	10 ng/ml
16-18	4.6	1 μg/ml CRP

As previously described, the immunosensors were subjected to three SWV scans to get a baseline peak current. Then, the proteins were incubated for 45 minutes while the sensors were kept on ice, followed by another three SWV scans to get the new peak current. The scan parameters were 5 mV step size, 25 Hz, 20 mV pulse size, 0.2 to -0.75 V, 2 second equilibrium time. It was noted that the first scans produced a better redox peak, and therefore the first curve was used for the data analysis step. The means and deviations were plotted against the concentration to get the calibration curve.

3.5 Electrochemical measurements of immunosensor with developed potentiostat

After the developed potentiostat was deemed functional, it was used to perform the electrochemical measurements for the fifth full scale test using the FeCN redox couple. This redox probe was chosen based on full scale test two that produced the best results. The same procedure that is described in Fig. 3.20 was used to characterize the sensors with the developed potentiostat. This time a higher sP-selectin protein concentration was used to test the immunosensor response to an abundance of proteins. A range of 1 ng/ml to 80 μg/ml was tested as shown in Table 3.14. The dilutions were made according to Appendix B.12. 10 μg/ml of CRP was used for the non-specific test for this experiment.

Table 3.14: Experimental setup for the fifth full scale test using the CNF immunosensors and the FeCN probe.

Sensor number	Category	Protein concentration
1-3	5.1	80 μg/ml
4-6	5.2	10 μg/ml
7-9	5.3	1 μg/ml
10-12	5.4	100 ng/ml
13-15	5.5	1 ng/ml
16-18	5.6	10 μg/ml CRP

As previously described, the sensors were subjected to a baseline scan, followed by incubation of the proteins, and then finally another scan to get the new peak current. The scan parameters were 20.14 mV pulse size, 25 hz, 4.834 mV step size, and a range of 0.5 to -0.7 V. The parameters were slightly different from the Gamry device due to the finite resolution of the developed potentiostat DAC. A picture of the experimental setup is shown in Fig. 3.23.

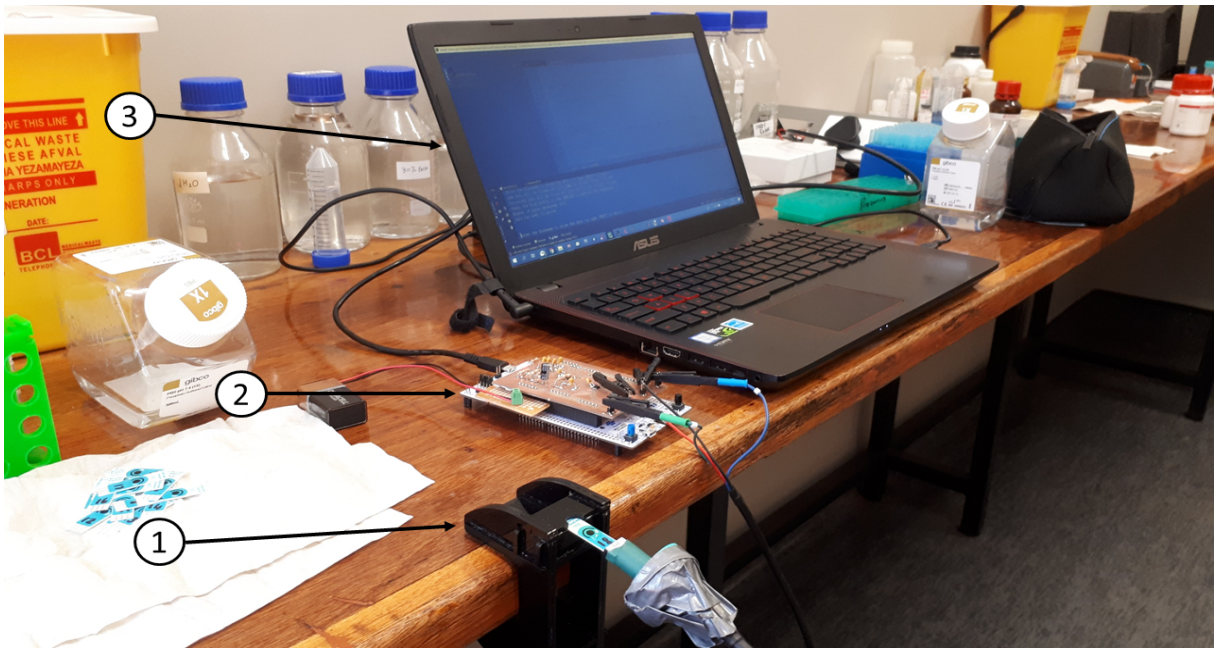

Figure 3.23: Photo of the measurement setup used for the CNF immunosensors with the developed potentiostat. The sensor ① is connected to the developed potentiostat ② through the DRP-CAC cable. The data is collected from the potentiostat on the host PC ③.

3.6 Method of analysis

The square wave voltammograms needed to be analyzed to accurately extract the peak redox current while preserving the tendency of the signal. The peak redox current contains information regarding changes at the surface of the working electrode, and thus the method should not modify the shape of the data in such a way that information is lost. Common techniques that are used include subtracting a background data scan, leading edge baseline analysis, and inflection point baseline analysis. The implementation of these techniques are described here. Thereafter, it is briefly explained how these peak currents are used to monitor the sensor modification process and ultimately test for binding of proteins.

3.6.1 Background scan subtraction

Subtracting a background scan is often done to remove unwanted redox peaks from the data so that only the peaks of interest are present in the voltammogram. A background scan that was done in 100 μl PBS without the redox active couple showed that there is no contribution to the measured current from the buffer solution. Fig. 3.24 shows that subtracting this background scan (green) from the FeCN redox couple scan (red) made almost no difference to the peak current. Both of these tests were done using the same unmodified GPHOX sensor.

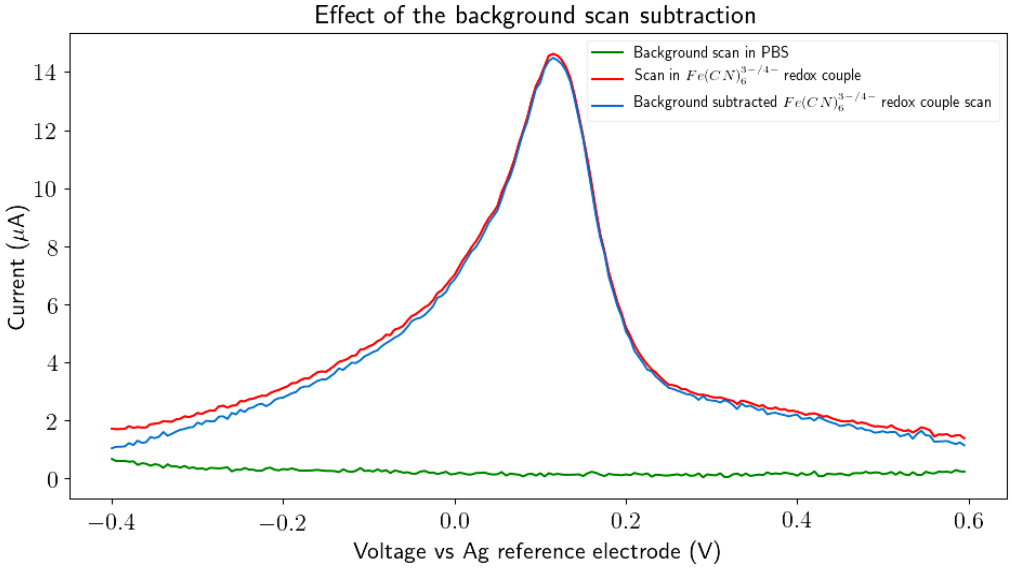

Figure 3.24: Effect of subtracting the PBS background scan from a scan done using the $Fe(CN)_6^{3-/4-}$ redox couple.

It should be noted that this behaviour is dependent on the supporting electrolyte solution that is used, and since every sensor is tested in exactly the same solution it was safely assumed that each sensor would behave in a similar manner. Since the background scan had no redox peaks, and its subtraction had no significant effect on the peak current, it was seen as a redundant step and thus not used in data analysis.

3.6.2 Baseline analysis methods

The first step of the two baseline analysis techniques was to filter the data using a Savitzky-Golay smoothing filter. This filter is commonly used for electrochemical experiments that show non-ideal data since it increases the precision of the data without distorting the signal. The low-pass filter keeps the accuracy of the peak data points by approximating the underlying function with a polynomial. It uses two parameters: 1) the order of the polynomial to fit, and 2) the window length, which is the number of points used to fit the polynomial. Gamry EchemAnalyst (the software package used by Gamry for analyzing electrochemical experiments) uses a default option of a 4th order filter with 16 data points, which is sufficient for most experiments. The same filter parameters were thus used for analyzing the data in Python using the *savgol_filter* function from the *scipy* package. The effect of this filter is shown in Fig. 3.25. The scan was done in the FeCN redox couple after a GPHOX sensor was electrografted 8 times and it was chosen because it provides a good visual representation of the effect of the filter.

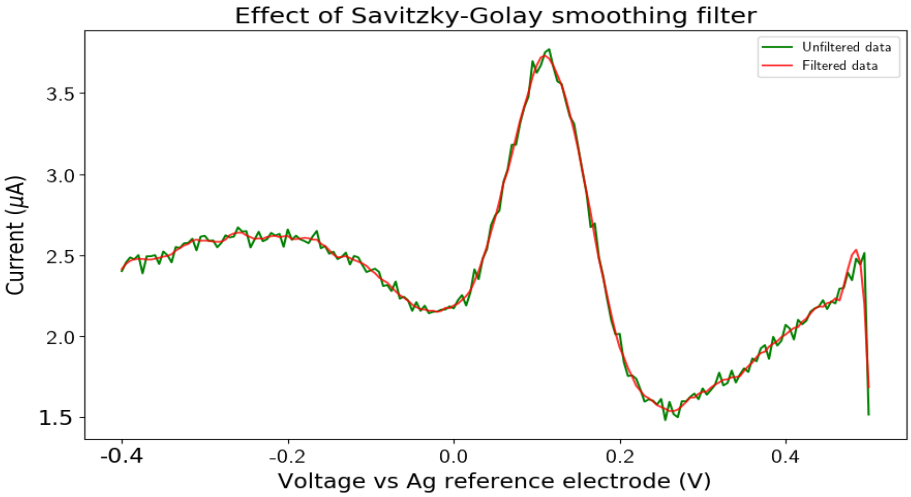

Figure 3.25: Effect of the 4^{th} order Savitzky-Golay smoothing filter using 16 data points.

Fig. 3.25 also shows that the first data point at 0.5 V started at a low current value that is irrelevant to the data in general. This outlier was noted at the starting value of all the curves and thus it was excluded from the data before any baseline analysis method was applied.

3.6.2.1 Leading edge baseline analysis method

Leading edge baseline analysis (from now on also called Method 1) is a method in which a line is extended from the flat leading edge of the scan (i.e. from the positive voltage side) to form a new baseline from which the peak redox current can be measured. Fig. 3.26 shows a scan of an unmodified GPHOX sensor in the redox couple after it was filtered using the Savitzky-Golay filter. The first 50 data points (shown in black circles) were used in linear regression analysis to get the slope and intercept of the new baseline (shown as the black dashed line). The new peak current was calculated as the vertical line distance from the maximum to the baseline (shown as the red dashed line).

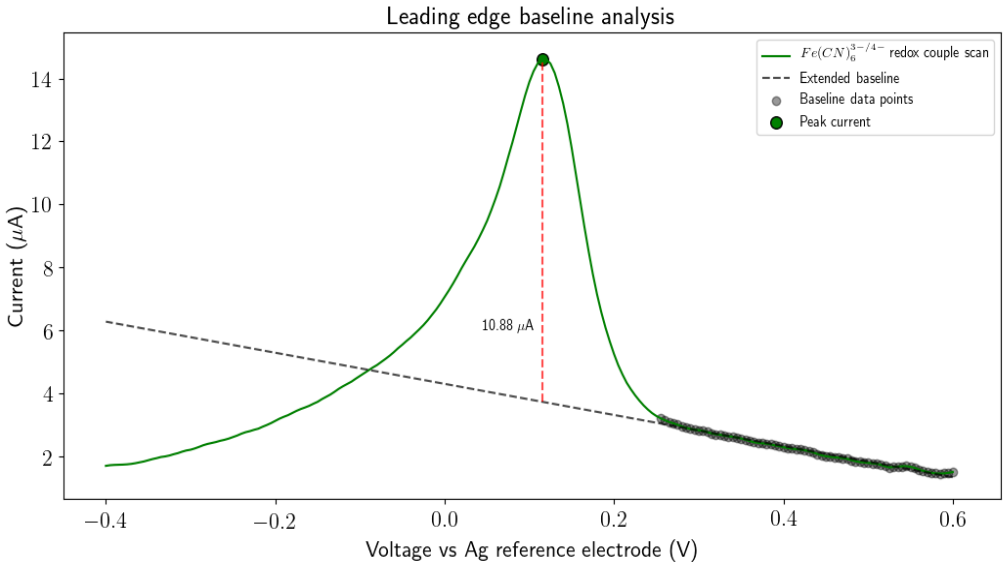

Figure 3.26: The graph shows how the leading edge was used to construct a baseline for measuring the peak current.

This method is useful if the curve did not have an inflection point on the left side of the peak, which was the case with some of the unmodified sensor experiments. It does, however, require the user to select how many data points will be used for the linear regression step which allows human error to be included in the result. When a sensor was analyzed using Method 1, the voltammogram was assessed visually to select the appropriate number of points to use for the regression analysis.

3.6.2.2 Inflection point baseline analysis method

A more suitable method of analyzing the data is the inflection point baseline analysis (also called Method 2 from hereon). The first step in this method was to filter the data using the Savitzky-Golay smoothing filter. The new data was then used to find the inflection points (i.e. turning points) of the signal on the right and left side of the peak, as shown in Fig. 3.27. This was done by first finding the peak current (shown as the red dot) in the 0 to 0.2 V range. The algorithm then "walks" from this point to the right hand side and computes the slope between adjacent points. The inflection point (green dot) is then selected to be the first point that has a positive slope. And vice versa, the algorithm "walks" to the left of the peak current to look for the first negative slope between adjacent points (yellow dot). The baseline (shown as the black dashed line) is then chosen as the line that connects the two inflection points.

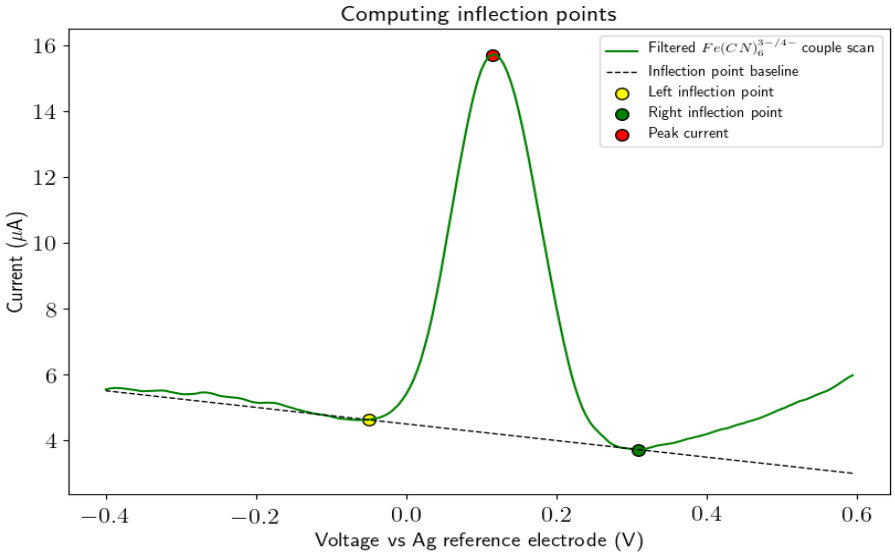

Figure 3.27: Computing the location of the inflection points to the right and left of the peak redox current.

Thereafter, the baseline is subtracted from the original filtered data so that the inflection points are located on the x-axis, as shown in Fig. 3.28. The maximum current is then simply taken as the peak current between the 0 and 0.2 V range (green dot).

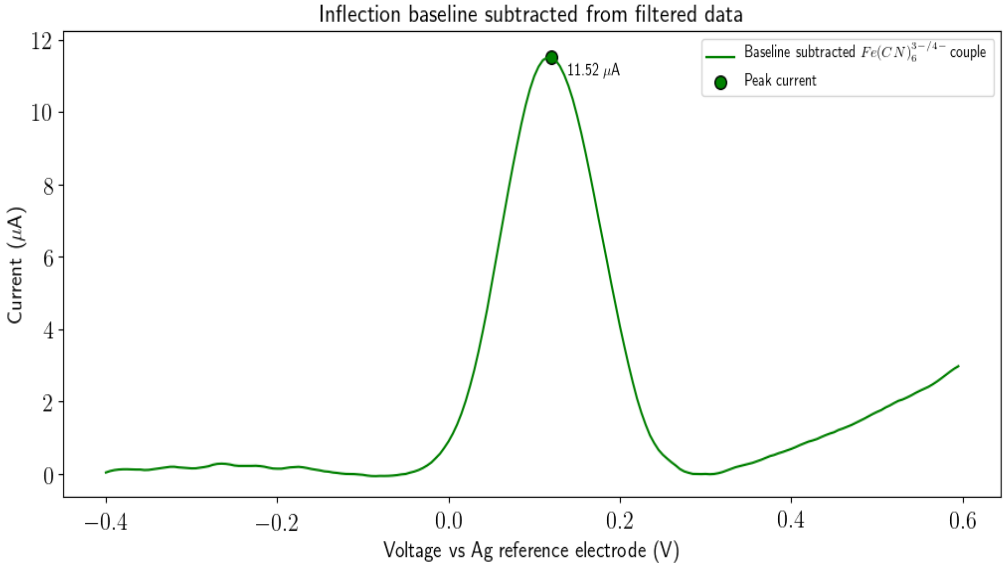

Figure 3.28: Voltammogram of the curve after the inflection point baseline was subtracted.

This method was the preferred method of analysis since it can be done without the intervention of the user. Only the potential range, where the peak current was located, had to be changed between the two redox probes. The method only required that two inflection points are present within the curve, which meant that the scanned range should be large enough to realize two points.

3.6.3 Data analysis algorithm flow chart

When analyzing the data it is important to work consistently with which method is used to extract the peak currents. Therefore, a data analysis algorithm was developed that would analyze the curve of a specific immunosensor based on what requirements the curve satisfied. In other words, if the voltammogram prior to a modification step did not have two inflection points, the voltammogram before and after the modification step was analyzed using Method 1 even if the modified voltammogram had two inflection points. This was mostly the case after the electrografting step since not all unmodified sensors had an inflection point on the left of their voltammograms, as shown in Fig. 3.26. The electrografting step, however, conveniently introduced an inflection point to the left of most of the peaks which allowed the subsequent experiments to be analyzed using the preferred Method 2. The high-level flow chart of the algorithm is shown in Fig. 3.29.

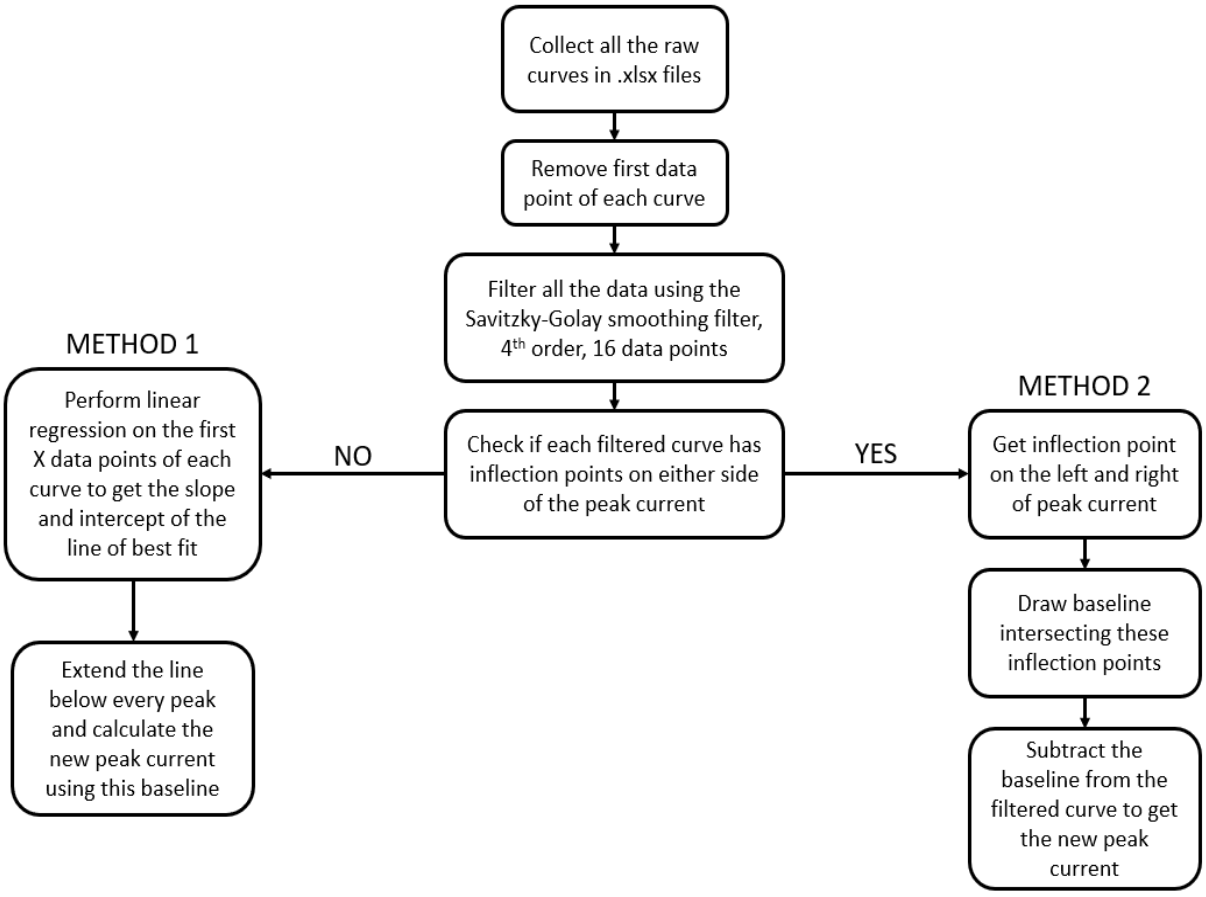

Figure 3.29: High-level flow chart of the method of data analysis that was used.

Throughout the sensor preparation process it is important to monitor each modification step by looking at the peak redox current in the voltammograms. Thus, the algorithm was used to extract the peak currents before and after the modification step to see what the relative change is. The change was then related to literature to confirm that the modification step worked. The final experimental step (i.e. the step that tested for

binding of different concentrations of sP-selectin proteins onto the antibody immobilized sensors) was analyzed according to,

$$C = \frac{r - r^0}{r^0} \times 100, \tag{3.12}$$

where C is the percentage change, r is the peak current after the binding of a specific sP-selectin protein concentration, and r^0 is the peak current before binding of sP-selectin proteins.

Chapter 4

Results

This chapter gives the findings of the development process that was used to create the sP-selectin immunosensor, followed by the results developed potentiostat. The results of the comparison between the developed potentiostat and the Gamry instrument are then given. Finally, the response of the immunosensor to different concentrations of proteins are given.

4.1 Commercial sensor results

The commercial sensor was characterized in terms of its electrochemical potential window, the voltage range required for a square wave voltammetry experiment, and the reproducibility of the sensors. This section starts by giving the findings of these characteristics. The findings of the modification process is then given in terms of the effect of the number of electrografting cycles, the fluorescent study of the primary immobilized antibodies, and finally the calibration curve of the immunosensor response.

4.1.1 Electrochemical potential window of unmodified sensors

Fig. 4.1 shows the voltammograms of PBS and the redox couple that were used to determine the electrochemical window of the GPHOX sensor setup. The PBS curve (red) showed minimal contribution to the current over the scanned range, and oxidative and reductive behaviour only appeared at about 1 V and -0.6 V. This indicated that the potential window for the supporting electrolyte is more or less 1.6 V. The redox couple (blue) showed full oxidative and reductive behaviour within the scanned range of 0.7 and -0.5 V as expected. The reduction peak current appeared at more or less -0.15 V and the oxidation potential was at 0.4 V, which puts the formal potential at the average value of 0.125 V. The results indicated that PBS could be used as the supporting electrolyte since it did not interfere with the reduction and oxidation of the redox couple. The similar peak currents also indicated that the setup can be considered as a reversible system. The slight difference could possibly be due to weight measurement errors that were made when the redox solution was made.

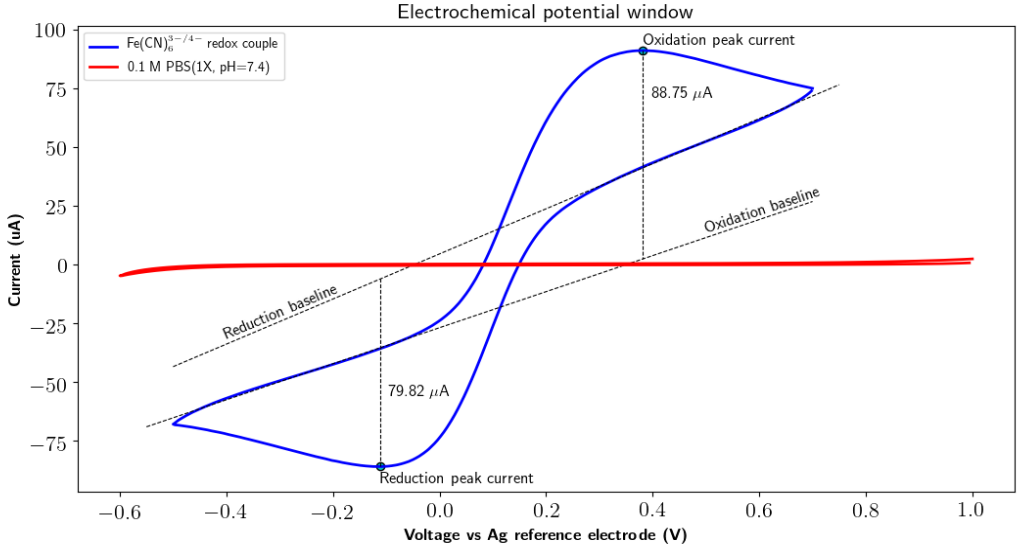

Figure 4.1: CV scan of the unmodified GPHOX sensors in PBS and the redox couple. The red curve showed that there is no contribution to any redox currents from the PBS solution. The blue curve indicated that the redox couple has reversible redox behaviour within a range of 0.7 to -0.5 V.

Fig. 4.2 shows the cyclic voltammograms of the unmodified CNF sensors. The PBS (red curve) only made a significant contribution to the current at potentials lower than -0.6 V and higher than 1 V. From the graph it can be identified that the window was about 1.2 V wide (from -0.4 to 0.8 V). The redox couple (blue) underwent full reduction and oxidation within the scanned range, and it showed almost perfectly reversible behaviour as indicated by the similar peak currents. The reduction peak was located at -14 mV and the oxidation peak was located at 254 mV, giving a formal potential of 0.12 V.

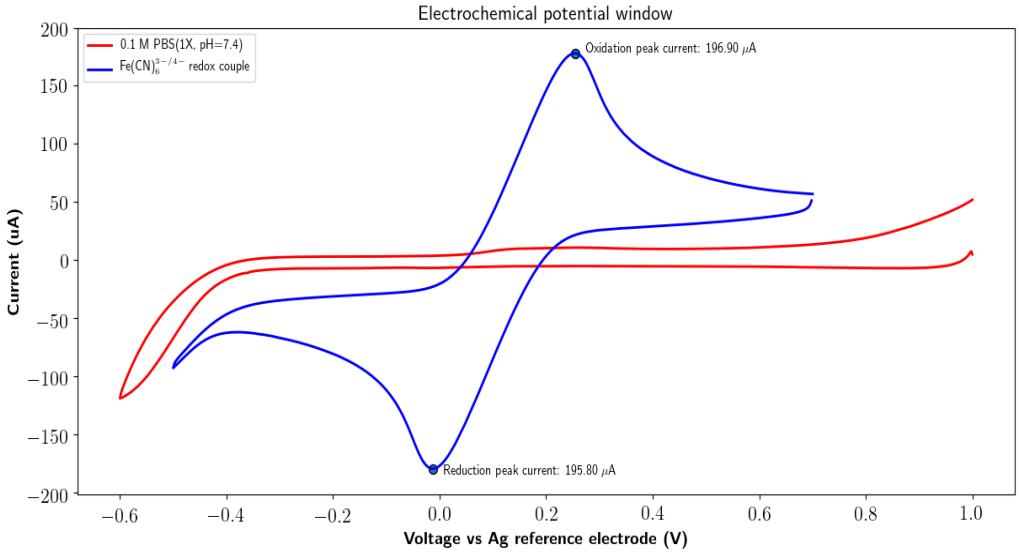

Figure 4.2: CV scan of the unmodified CNF sensors in PBS and the redox couple. The red curve showed that there is minimal contribution to the current from the PBS solution. The blue curve indicated that the redox couple underwent full redox behaviour within a range of 0.7 to -0.5 V.

4.1.2 Square wave voltammetry characteristics

Fig. 4.3 shows the square wave voltammograms that were obtained by scanning three different unmodified GPHOX sensors in distilled water, PBS, and the redox couple. The distilled water (green) showed no contribution to any current within the scanned range, indicating that distilled water would not interfere with the redox couple system. A sensor that was tested in PBS (red) showed no contribution within a large portion of the scanned range, but a peak started to appear at potentials lower than -0.25 V. The sensor that was tested in the redox couple solution (blue) showed a very large peak current at more or less 0.105 V, and a rising current at potentials lower than -0.4 V. The rising peak at the lower potential was likely due to the PBS supporting electrolyte that started undergoing a reduction reaction. The same PBS reduction behaviour was noted in the cyclic voltammogram of the sensor as shown in the previous section. The peak potential of the redox couple was very close to the formal potential that was identified in the cyclic voltammetry scans of the GPHOX sensors.

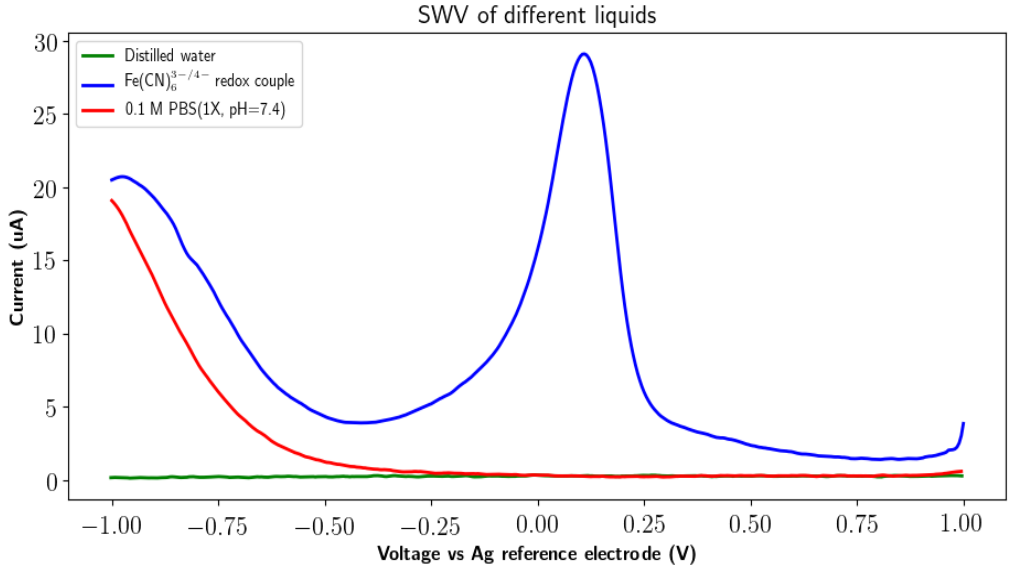

Figure 4.3: SWV scans done in distilled water, PBS, and the redox couple using the unmodified GPHOX sensors.. Distilled water (green) did not contribute to any current in the scanned range. PBS (red) only had redox behaviour at potentials smaller than -0.25 V, and the redox couple solution (blue) showed a well defined redox peak at more or less 0.105 V. The scan parameters are: 25 Hz, 5 mV step size, 20 mV pulse size, starting potential of 1 V, final potential of -1 V, equilibrium time of 2 s.

The unmodified CNF sensors had responses similar to that of the GPHOX sensors. Fig. 4.4 shows that the distilled water (green) made no contribution to the current in the scanned range. A sensor that was scanned in the PBS solution (red) showed that the supporting electrolyte had a background current. Even though the background current was non-negligible it did not have any well defined peaks in the scanned range, indicating that there are no redox reactions present. Also, the background current was only noted for the CNF sensors that were scanned from 1 V to -1 V in the PBS solution. The next section shows that the CNF sensors that were scanned in the redox solution from 0.6 to -0.4 V, was not superimposed on a background current such as the blue curve in Fig. 4.4. Therefore, it was not necessary to perform a background current subtraction for these sensors during the data analysis step. The sensor that was scanned in the redox couple

(blue) showed that a single well defined peak was present at more or less 0 V, which is close to the formal potential that was identified in the CV scan of the redox system.

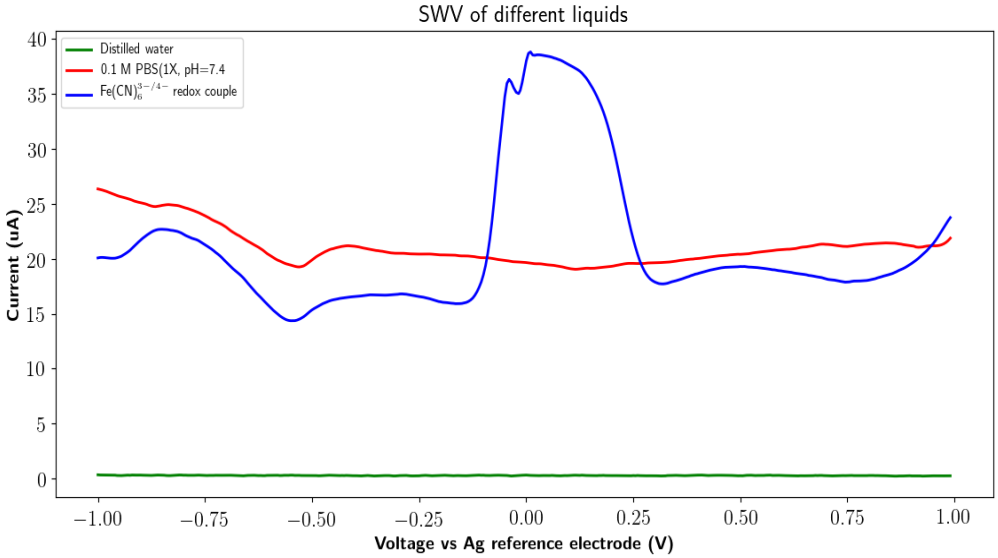

Figure 4.4: SWV scans done in distilled water, PBS, and the redox couple using the unmodified CNF sensors. Distilled water (green) did not contribute to any current in the scanned range. PBS (red) had a non-negligible background current, but it was not necessary to subtract this during the data analysis step since no redox peaks interfered with the redox couple. The redox couple solution (blue) showed a well defined redox peak at more or less 11 mV. The scan parameters are: 25 Hz, 5 mV step size, 20 mV pulse size, starting potential of 1 V, final potential of -1 V, equilibrium time of 2 s.

The GPHOX and CNF sensors had a well defined redox peak within the scanned range, and thus subsequent square wave measurements were done with smaller ranges.

4.1.3 Reproducibility of unmodified sensors

The square wave voltammograms of the unmodified GPHOX sensors that were used for the reproducibility tests are shown in Fig. 4.5. The three sensors were scanned in the redox couple solution and the peak current was analyzed using Method 1. The leading edge baselines are shown as the dashed black lines. The mean peak current was 9.59 μA and the standard deviation was 1.41 μA. The graph showed that the sensors have different peak shapes and magnitudes even under the same experimental conditions.

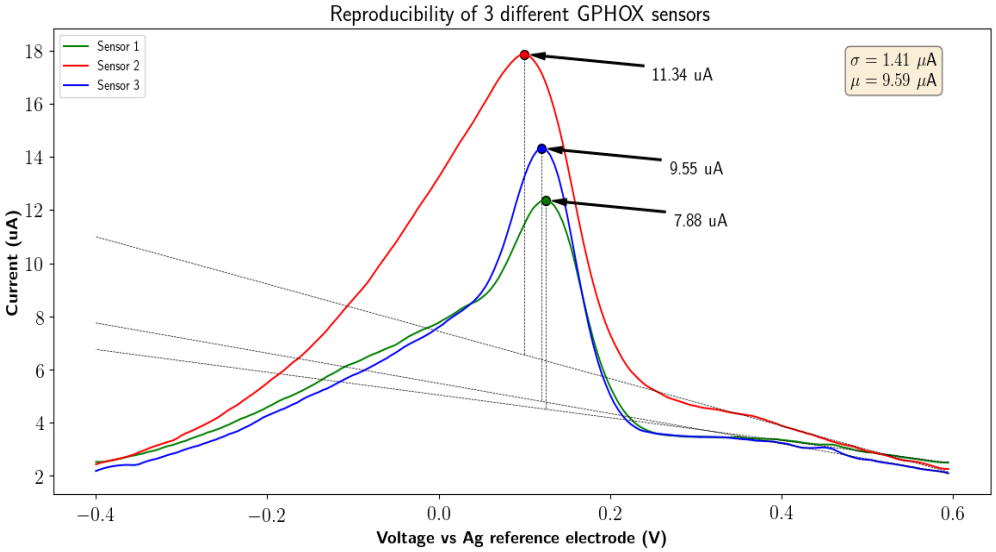

Figure 4.5: Reproducibility of three unmodified GPHOX sensors scanned in the redox couple solution.

The CNF sensors had a much better reproducibility when compared to the GPHOX sensors, as shown by Fig. 4.6. The mean sensor peak current was calculated as 37.27 μA and the standard deviation was 0.71 μA.

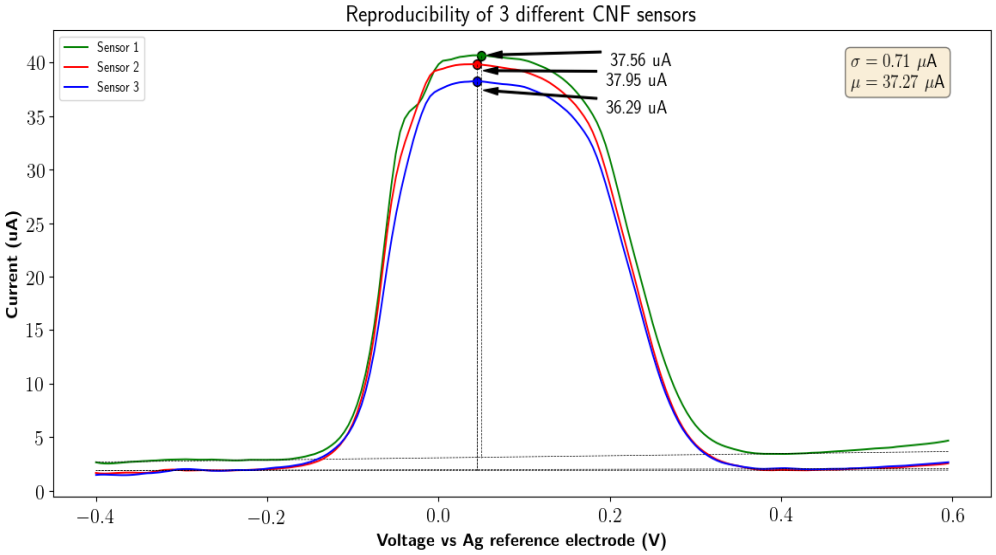

Figure 4.6: Reproducibility of three unmodified CNF sensors scanned in the redox couple solution.

The multiple scans experiment also showed that the CNF sensors are more stable than the GPHOX sensors when subjected to twenty consecutive scans. Table 4.1 summarizes the results that were obtained from this experiment. The minimum, maximum, mean, standard deviation, and co-efficient of variation were calculated for the twenty scans. The CNF sensor had a co-efficient of variation of 0.024, whereas the GPHOX sensor had a co-efficient of variation of 0.045.

Table 4.1: Reproducibility of multiple scans on the same sensor

	Min	Max	Mean	Standard deviation	Co-efficient of variation
GPHOX	7.951 μA	9.685 μA	8.947 μA	0.406 μA	0.045
CNF	35.889 μA	38.873 μA	36.884 μA	0.871 μA	0.024

These results proved that the CNF sensors are more stable and reproducible in the redox couple than the GPHOX sensors.

4.1.4 Electrochemical reduction of diazonium salt

The electrografting step creates carboxyl support groups on the working electrode by doing cyclic voltammetry in the 4-carboxyphenyl diazonium salt solution. The diazonium molecule get reduced at the working electrode which forms an aryl radical that attaches to the surface. Fig. 4.7 shows the voltammograms of a GPHOX sensor that was grafted for 8 cycles in the potential range of 0.2 and -0.6 V at a scan rate of 100 mV/s. The first dark green cycle shows a large reduction peak current at more or less -0.35 V that greatly diminishes for each subsequent cycle. This behaviour was expected since the grafted layer grows larger for each cycle, thereby reducing the available grafting space and thus decreasing the electron transfer efficiency. The reduction peak almost completely vanished after the first cycle, which indicates that the largest number of molecules were grafted during the first cycle.

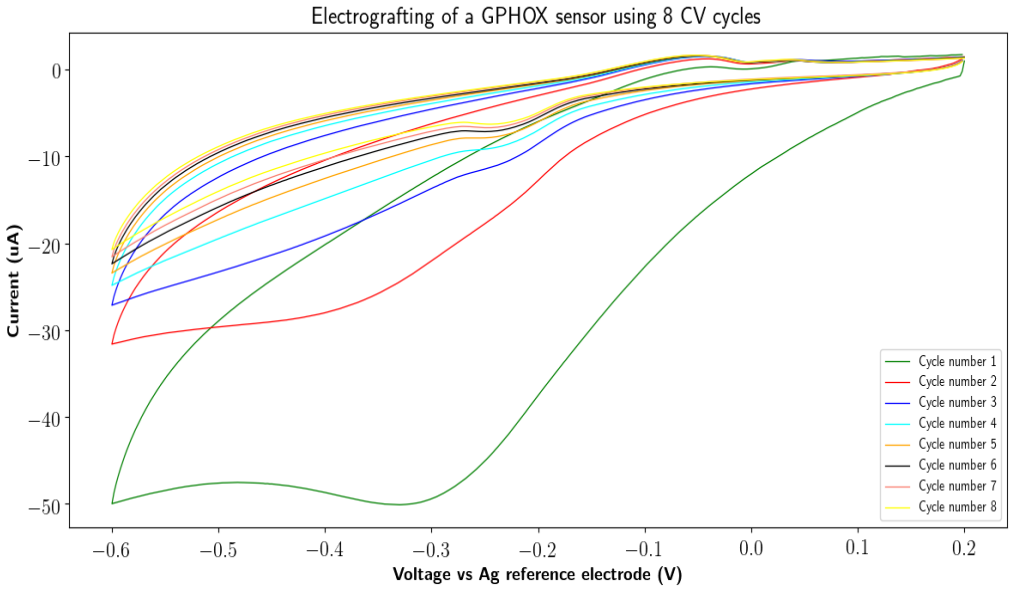

Figure 4.7: CV scans showing the 8 electrografting cycles of a GPHOX sensor.

The same behaviour was noted for a CNF sensor that was electrografted for 8 cycles. Fig. 4.10 shows that this sensor also had a large reduction peak current at more or less -0.17 V that greatly diminishes for subsequent cycles. This peak does not disappear after the first cycle which is characteristic of the large surface area provided by the CNFs. The larger surface area requires more grafting cycles to fully cover the working electrode in the diazonium molecules, which is why the peak can still be identified even after the last cycle.

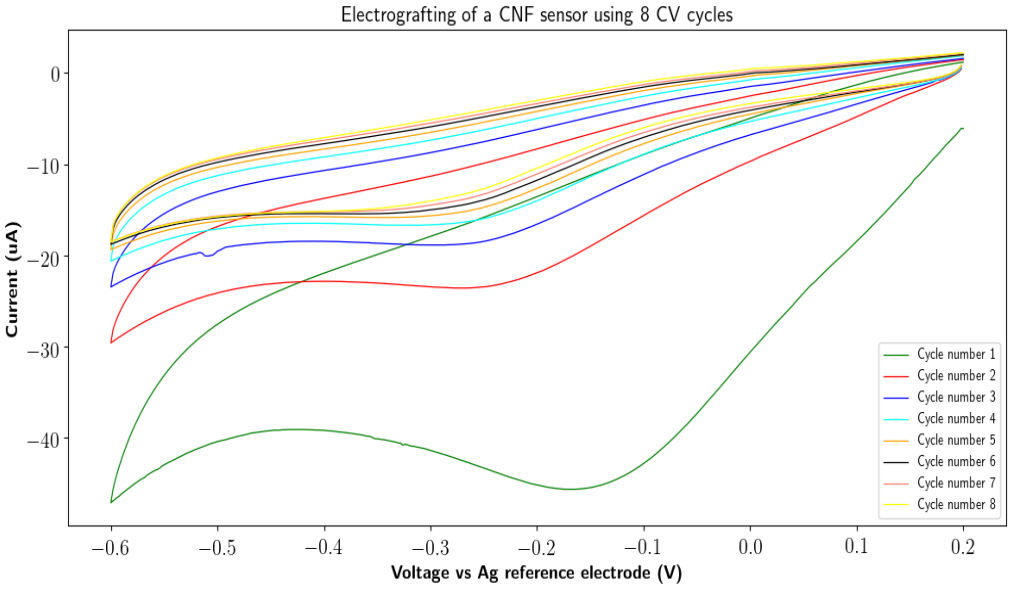

Figure 4.8: CV scans showing the 8 electrografting cycles of a CNF sensor.

The blocking effect of the carboxyphenyl layer was verified by doing square wave voltammetry of the grafted sensors in the redox couple solution. If more carboxyl groups are present on the working electrode surface it would lead to the repulsion of the redox molecule and thus a smaller peak current. Fig. 4.9 shows the square wave voltammogram of the same GPHOX sensor before and after electrografting it for 8 cycles. The green curves show three consecutive voltammograms taken before the grafting procedure, and the red curve shows the voltammograms taken after electrografting. The peak current reduced from 10.179 μA to 0.742 μA, which shows that surface was almost completely passivized. The peak current of this sensor was extracted using Method 2 of the data analysis algorithm.

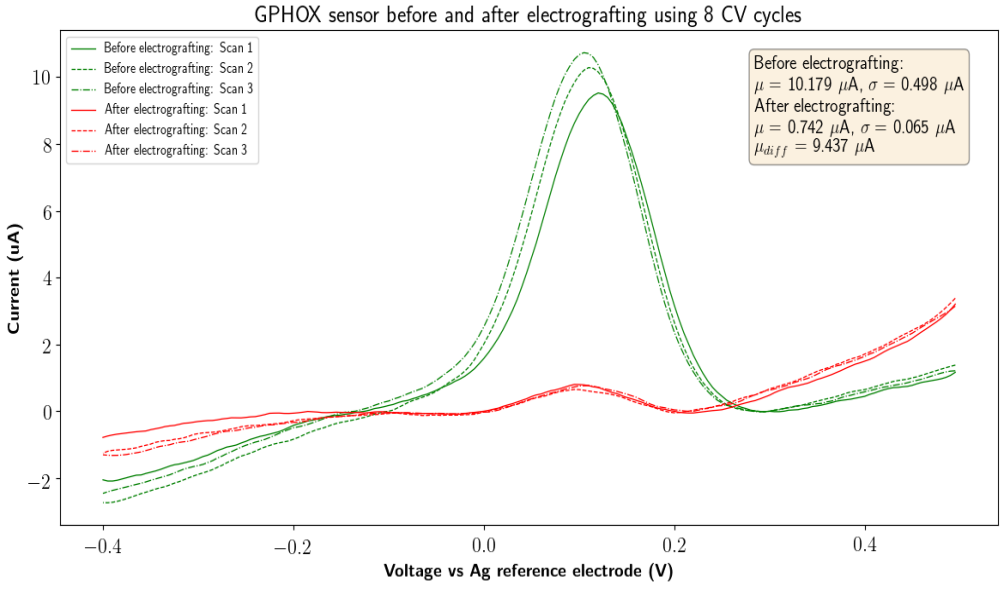

Figure 4.9: Peak current reduction after 8 electrografting cylces for GHPOX sensor.

Fig. 4.10 shows the square wave voltammogram of the CNF sensor that was grafted for 8 cycles. The final peak current was an order of magnitude larger than the GPHOX sensor (5.411 μA vs 0.742 μA) after the same number of grafting cycles were used to passivate the working electrode. This is indicative of the large surface area of the CNFs compared to the GPHOX layer.

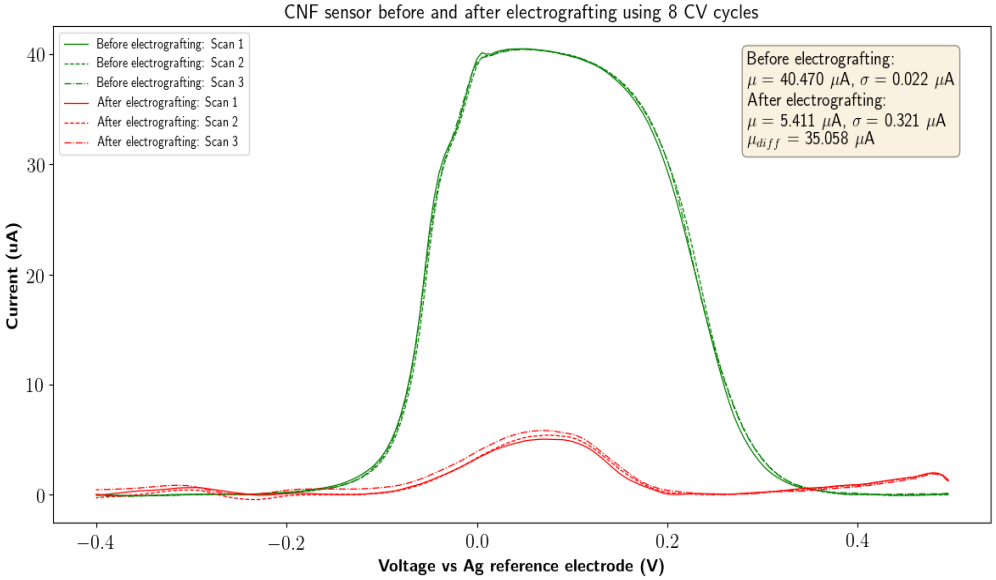

Figure 4.10: Peak current reduction after 8 electrografting cylces for CNF sensor.

Fig. 4.10 and 4.9 are only provided as a visual representation of what happens to the peak current after the electrografting procedure. The bar graph in Fig. 4.11 provides a more thorough summary of the effect of using a different number of electrografting cycles. The blue and green bars, show the magnitude of the peak redox current before the sensors were electrografted. The unmodified CNF sensors (green) all had similar peak currents of about 40 μA, whereas the unmodified GPHOX sensors had peak currents of about 10 μA and 4 μA. This, again, indicates that the unmodified GPHOX sensors were not as reproducible as the CNF sensors. The effect of grafting the same sensors for 1, 4, and 8 cycles is indicated by the orange and red bar graphs.

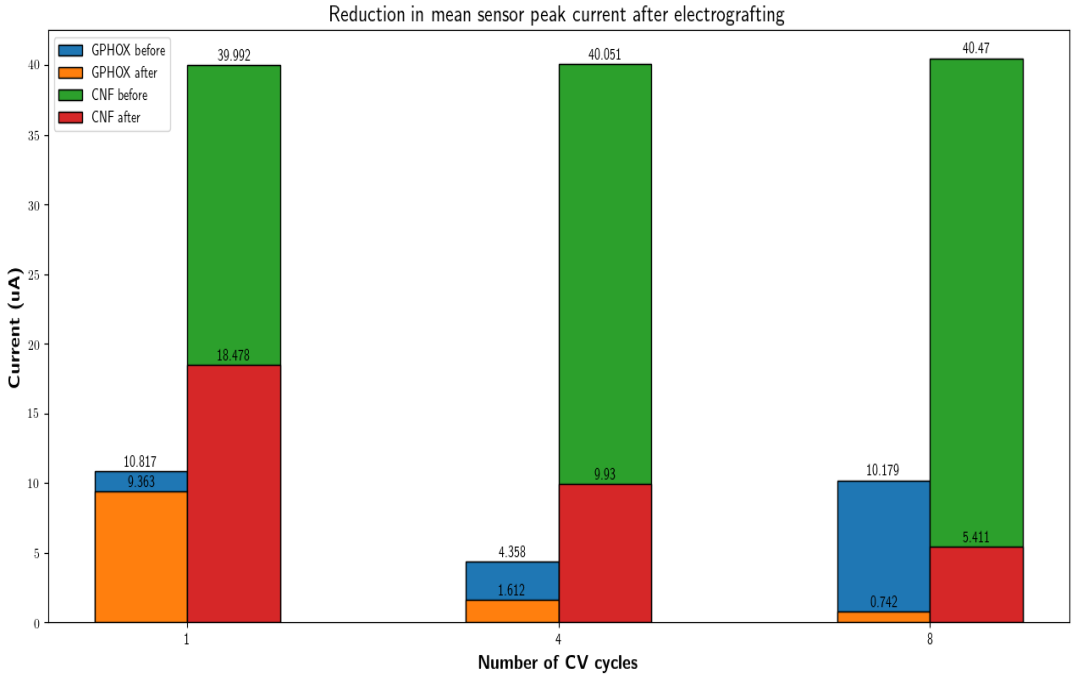

Figure 4.11: Effect on the peak redox current of the GPHOX and CNF sensors after electrografting with a different number of cycles.

The general trend was that more cycles would lead to a lower peak redox current, which is due to the negatively charged redox molecules that are repelled by the negatively charged carboxyl moieties to a greater extent. The first CNF sensor was reduced to about 50% of its peak value after one grafting cycle. The second CNF sensor was reduced by about 75% of its peak current after four cycles, and the last CNF sensor was reduced by about 86% of its peak current after eight cycles. The first GPHOX sensor peak current was reduced by about 13%, the second was reduced by 63%, and the last by about 93%. This shows that the reduction in peak current is a non-linear function of the number of cycles and it also differs for each type of electrode.

4.1.5 Antibody crosslinking and fluorescent study of the carbon nanofiber immunosensor

The fluorescent study was used to confirm that the sP-selectin antibody was successfully immobilized on the surface of the CNF sensor, and that it does not wash off after the first square wave voltammetry baseline measurement. If the antibody was successfully bound on the surface of the sensor it also means that the carboxyl groups were created by the electrografting procedure. Fig. 4.12 shows the fluorescent photos of the CNF sensors with immobilized primary and secondary antibodies. Fig. 4.12A shows a photo of the sensor that was used as the auto-fluorescence control test, and Fig. 4.12B shows a photo of the sensor that was only immobilized with secondary antibodies. There was no auto-fluorescence from the first sensor, and the fluorescence of the second sensor is mostly due to clumping of the secondary antibodies that were not washed off completely.

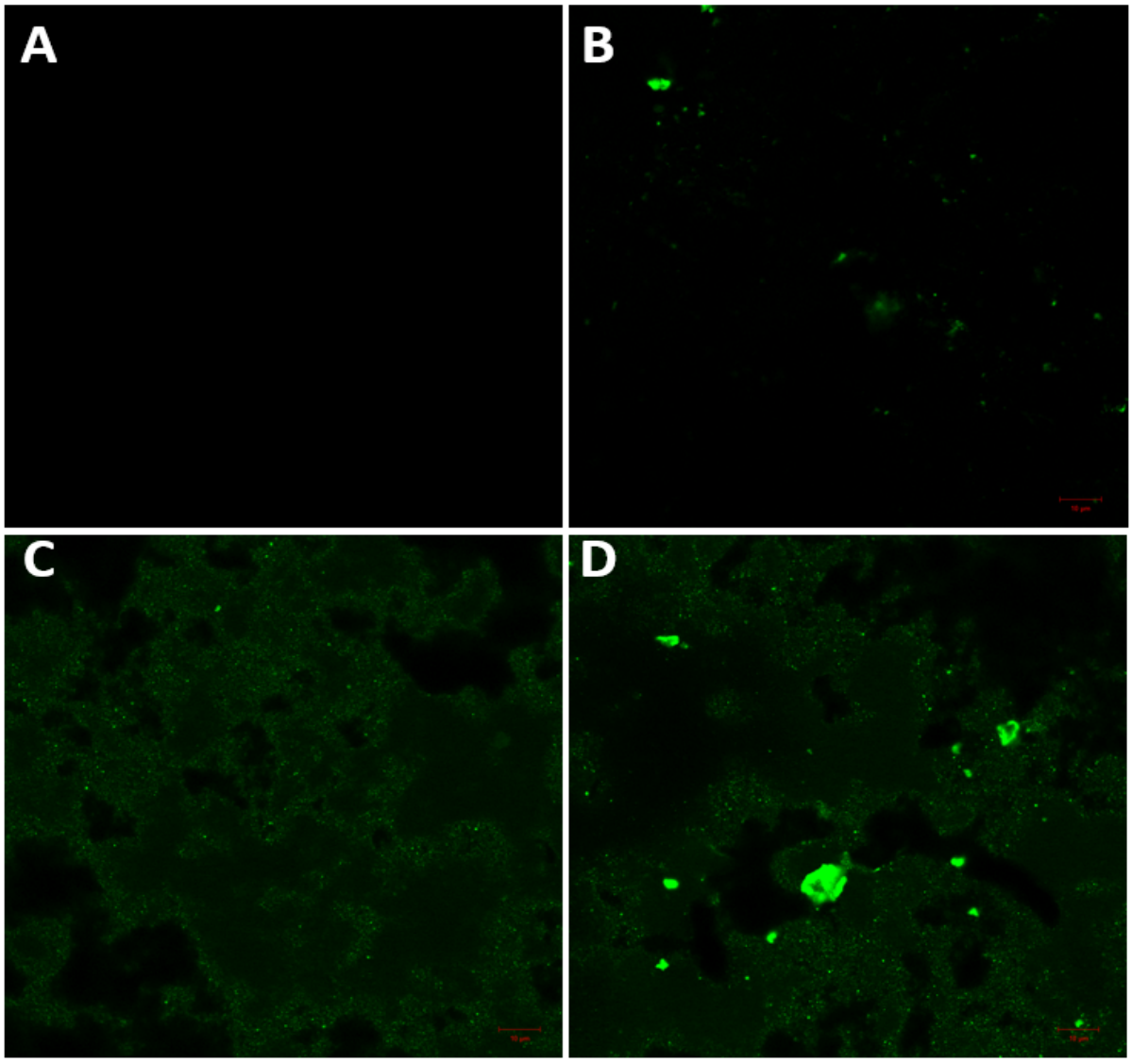

Figure 4.12: Fluorescent study of the CNF immunosensor. A) shows the auto-fluorescence of the CNF sensor, B) shows the sensor with only secondary antibodies immobilized, C) shows the sensor with primary sP-selectin antibodies, that was subjected to the baseline measurement, and then immobilized with the secondary antibody, and D) shows the sensor that was immobilized with primary and secondary antibodies without undergoing a baseline measurement.

Fig. 4.12C shows a photo of the sensor that was immobilized with primary antibodies and subjected to three SWV baseline measurements in the FeCN probe. A very strong green signal was observed across the working electrode, which shows that the primary antibodies are still safely immobilized to the surface. Fig 4.12D shows a photo of the sensor that was immobilized with the primary and secondary antibody, without undergoing a baseline measurement in the FeCN probe. The green fluorescence indicated that there were primary antibodies on the surface, and the bright green spots might be due to clumping that was also observed in Fig. 4.12B. The strong correlation between Fig. 4.12C and D suggests that the primary sP-selectin antibodies were successfully immobilized, and that the baseline measurement did not wash off the primary.

4.1.6 Electrochemical parameters of the RuHex redox probe

Fig. 4.13 shows the cyclic voltammograms of two CNF sensors that were scanned in PBS (red) and the RuHex probe (blue). The PBS showed large offscale waves at potentials lower than -0.4 V and higher than 1 V, whereas the RuHex probe showed complete reduction and oxidation behaviour within the range of -0.5 and 0.3 V. The peak reduction current was 69.57 μA and the peak oxidation current was 57.55 μA. From this graph the formal potential was calculated as -230.85 mV. The results showed that the PBS had a large enough electrochemical window to accommodate the RuHex probe.

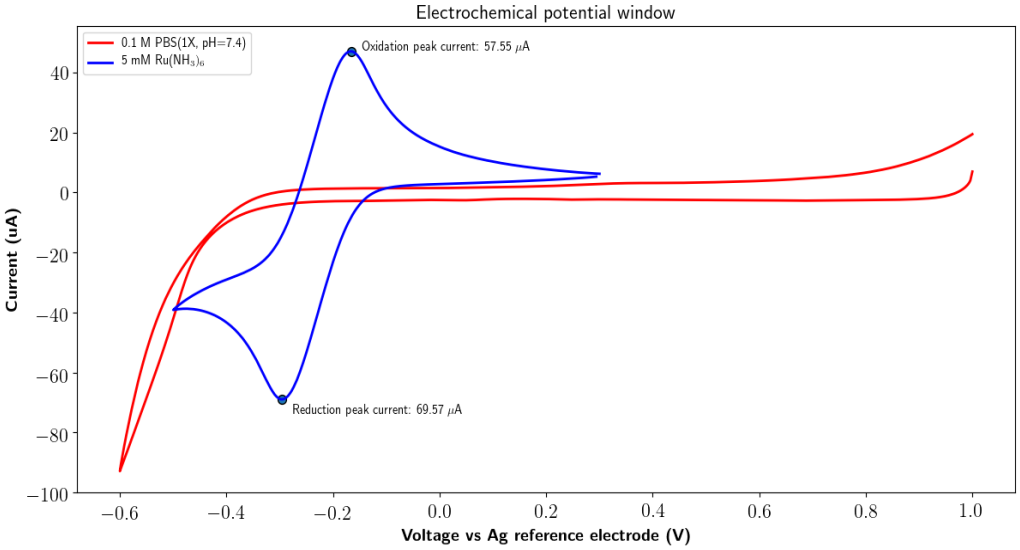

Figure 4.13: CV scans of the unmodified CNF sensors in PBS and the RuHex probe. The red curve showed that there is minimal contribution from the PBS in the redox active range of the RuHex probe. The RuHex probe (blue curve) showed full oxidation and reduction with a range of -0.5 and 0.3 V.

Reproducibility scans of the unmodified CNF sensors in the RuHex probe showed that the setup was highly reproducible. Three different sensors had a mean current of 43.38 μA and a standard deviation of 0.44 μA. Fig. 4.14 showed that the sensors had very similar responses, and the chosen scan range of 0.4 to -0.6 V was enough to produce a redox peak with two inflection points on either side of the peak. The reproducibility was similar to that of the CNF sensors with the FeCN redox couple shown in Fig. 4.6.

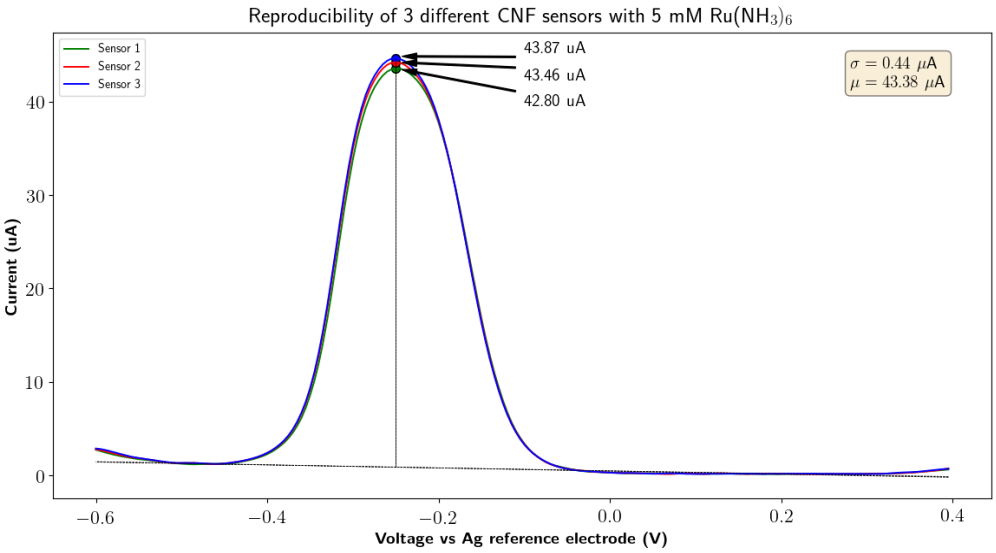

Figure 4.14: Reproducibility of three unmodified CNF sensors scanned in the RuHex probe solution.

The results from twenty consecutive scans of an unmodified CNF sensor in the RuHex probe showed highly reproducible and stable results. Table. 4.2 summarizes the results of the twenty scans. The standard deviation and co-efficient of variation from the mean was much lower for the CNF sensor scanned in the RuHex probe compared to the CNF sensor scanned in the FeCN probe for this experiment.

Table 4.2: Reproducibility of multiple scans on the same sensor: RuHex

	Min	Max	Mean	Standard deviation	Co-efficient of variation
CNF with Ru(NH_3)$_6$	43.31 μA	44.11 μA	43.78 μA	0.231 μA	0.005

4.2 Potentiostat development results

The potentiostat development results are divided into the different components of the hardware and software.

4.2.1 Hardware

The hardware findings are discussed in terms of the power supply characteristics, the filter stage design, the LTSpice simulation of the potentiostat, and finally the practical measurements of the whole application.

4.2.1.1 Power supply noise

Table 4.3 summarizes the RMS voltage noise measurements of the [5V] and [AVDD] power rails on the Nucleo board. When the USB was used to power the Nucleo board it produced a relatively large 1.9 mV RMS noise signal on the [5V] pin compared to the V_{IN} powered options that only produced an RMS value of about 380 μV. The V_{IN} powered approach showed the least amount of noise on both power rails when the USB was plugged out. Slightly higher noise measurements were noted when the USB was plugged in, even though it was not used to power the Nucleo board in this case.

Table 4.3: Measured RMS voltage noise of the [5V] and [AVDD] power rails.

	USB powered		V_{IN} powered, USB plugged out		V_{IN} powered, USB plugged in	
	5V	AVDD	5V	AVDD	5V	AVDD
RMS voltage noise	1.9 mV	353.56 μV	380.30 μV	310.13 μV	384.86 μV	354.19 μV

The USB powered approach also showed highly variable results that could have been due to inconsistent loading or processes on the host PC. The best option would, therefore, be to power the board using a 9 V battery that is connected to V_{IN} pin.

4.2.1.2 LTSpice simulation of the filters

The frequency response of the two first order Bessel filters that were used to illustrate the cutoff frequency and noise trade-off are shown in Fig. 4.15. Filter 1 had a cutoff frequency of 150 Hz and a stopband attenuation of -20 dB at 1.5 kHz, whereas Filter 2 had a cutoff frequency of 10 kHz and a -20 dB stopband at 100 kHz. Filter 1 would thus reduce the amount of noise that is passed, but also distort the square wave signal, whereas Filter 2 would cause less distortion but more noise to be passed.

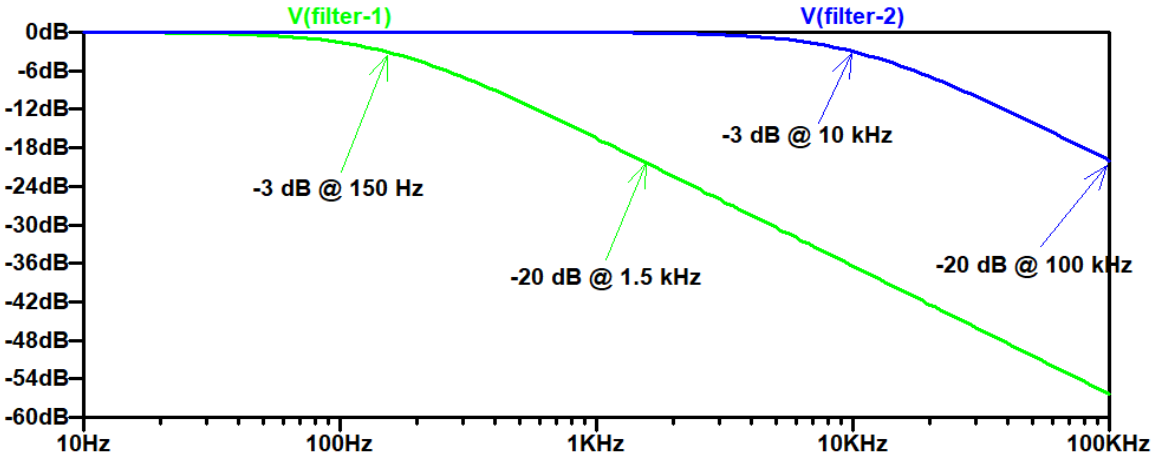

Figure 4.15: Frequency response of the two first order Bessel filters that were used to illustrate the cutoff frequency and noise trade-off. Filter 1 is shown in green, and Filter 2 is shown in blue.

A transient analysis was done of both filters with a white noise signal superimposed on a 25 Hz square wave signal. White noise with an RMS value of 2.58 mV, a peak-to-peak value of 12.31 mV, and a bandwidth of 500 kHz was chosen for this simulation. Fig. 4.16 shows the resulting filter outputs that are plotted with the input square wave signal shown in red. Filter 1 (green) showed a significant reduction in the amount of noise, but it had much slower rise and fall times when compared to the square wave signal. This is due to the higher frequency square wave harmonics that are distorted by the filter. Filter 2 (blue) showed more noise on the output but the waveshape closely resembled that of the square wave signal. This is evident from the overlapping rise and fall edges of the two waveforms at the 20 and 40 ms marks. The RMS and peak-to-peak values of the output noise was also calculated in the 0 to 20 ms region of the output waveforms. Filter 1 showed an RMS value of 237 μV and a peak-to-peak value of 525 μV, and Filter 2 had a significantly higher noise values of 901 μV RMS and 5.54 mV peak-to-peak.

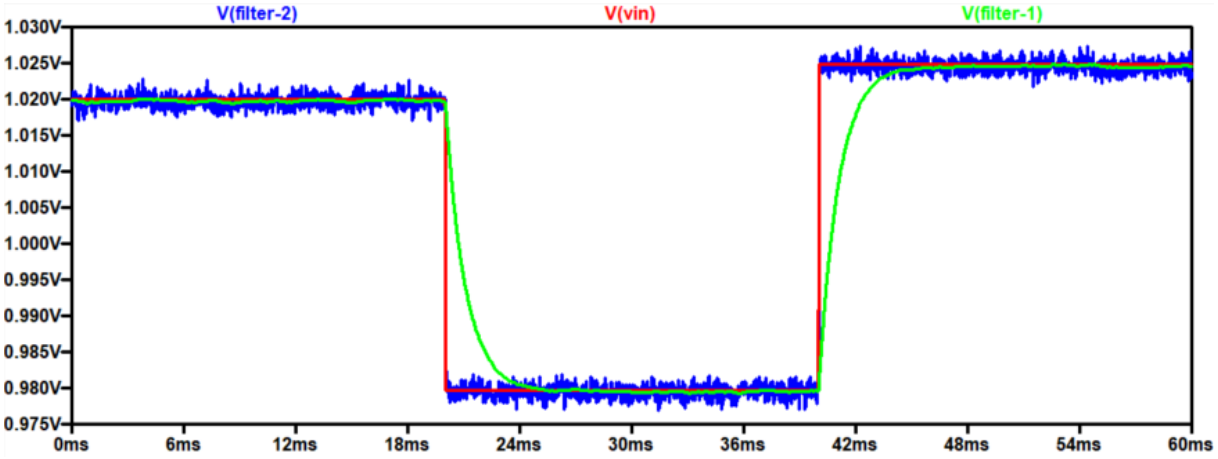

Figure 4.16: Transient analysis result of the two first order Bessel filters that were used to illustrate the cutoff frequency and noise trade-off. The input square wave is shown in red, and the outputs of Filter 1 and 2 are shown in green and blue, respectively.

Based on these results a cutoff frequency of 5 kHz was chosen for the filter design. This was arbitrarily chosen to be at the meeting point of the two designed filters. It allowed more harmonics to be passed than filter 1, resulting in a better waveshape, and also less noise to be passed compared to filter 2. The amount of noise was decreased even further by increasing the order of the filter to a second order unity gain Bessel filter. The cutoff frequency and the stopband frequency are illustrated in the AC analysis of the filter shown in Fig. 4.17. It also shows that the filter has a maximally flat group delay in the passband of about 43 μs that rolls off to 36 μs at the corner frequency.

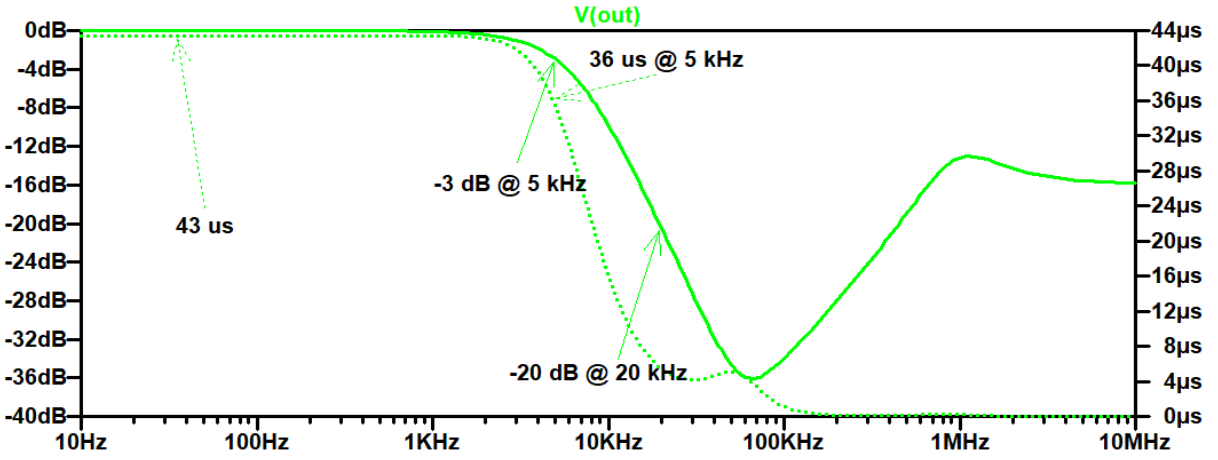

Figure 4.17: AC analysis of the second order Bessel filter stage showing the frequency characteristics and the maximally flat group delay in the passband.

A transient analysis of the filter was also done. The effect of the second order Bessel filter on a very noisy square wave signal is shown in Fig. 4.18. The green waveform shows the input signal that consists of a white noise signal superimposed on the red square wave signal. A relatively large white noise signal with a peak-to-peak amplitude of 12.43 mV, an RMS value of 2.95 mV, and a bandwidth of 500 kHz was used for this simulation. The transient analysis showed that the filter output (blue) had overlapping rising and falling edges at the 20 and 40 ms marks that are evident of a low amount of distortion of the

square wave harmonics. The input noise was also severely attenuated to a peak-to-peak value of 3.45 mV and an RMS value of 582 μV.

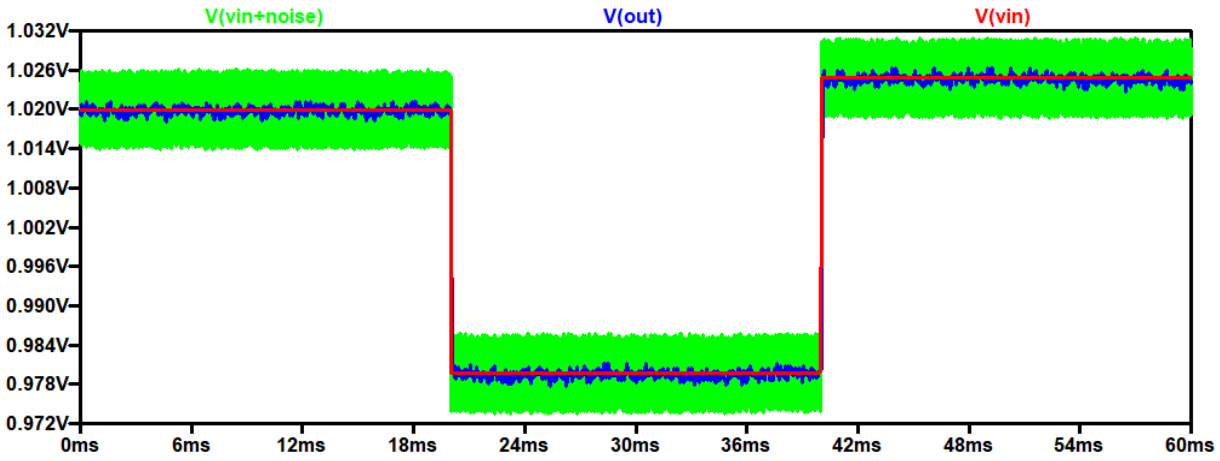

Figure 4.18: Transient analysis that shows the effect of the second order Bessel filter on a noisy square wave input signal.

These results showed that the designed filter stage preserved the waveshape and reduced the noise, which would improve the accuracy of the measured voltages.

4.2.1.3 LTSpice simulation of the potentiostatic circuit

This section gives the simulation results of the potentiostatic circuit in terms of its output linearity, bandwidth, and noise analysis in the time and frequency domain. All of the voltage nodes that are plotted in this section are in reference to Fig. 3.16.

The linear output range of the potentiostatic circuit was identified by sweeping the control amplifier input signal from 0 to 3.299194 V while keeping the working electrode biased at 1.65 V using the transimpedance amplifier. The input and output waveforms of various parts on the circuit are shown in Fig. 4.19.

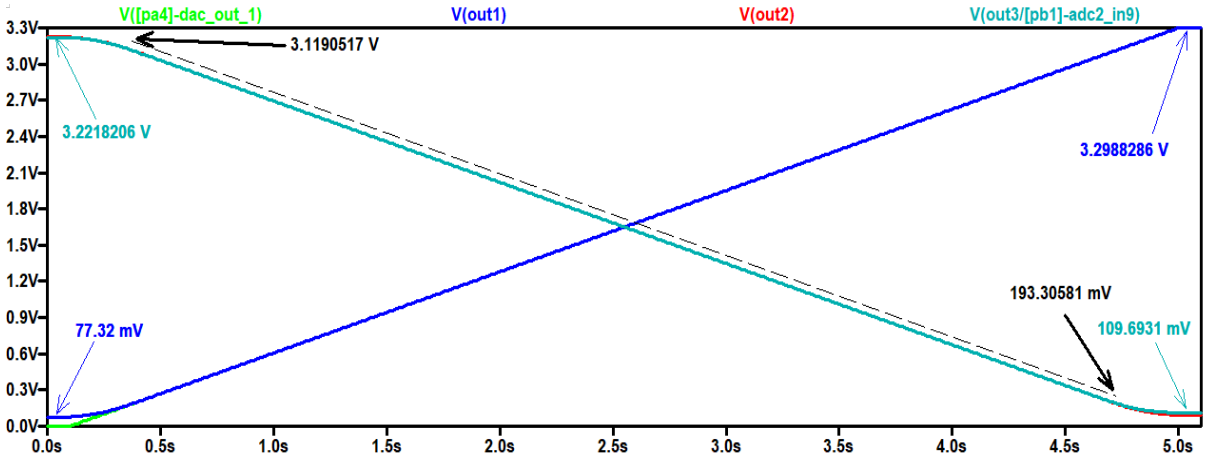

Figure 4.19: Linear output range of the potentiostatic circuit. The input and output of the control amplifier are shown in green and blue respectively. The output of the transimpedance amplifier is shown in red, and the output of the filter stage is shown in turquoise.

The input signal (shown in green) was first held constant at 0 V for the first 100 ms. The output of the control amplifier (shown in blue) was constant at 77.32 mV during this time, which showed that the op-amp output cannot swing lower than that value. This is due to the negative rail being at ground potential. The highest control amplifier output that could be achieved was 3.2988286 V, which is about 365 μV lower than the highest control amplifier input signal. Since the positive rail was much higher at 5 V, the difference is most probably due to the offset voltage of the op-amp. The difference between the input and output of the control amplifier was on average 250 μV over the linear range, which is close to the offset voltage of the TLC2264 op-amp. The output of the filter (shown in turquoise) reaches its maximum when the output of the control amplifier is at a minimum. According to LTSpice this value is 3.2218206 V. The filter also reaches its lowest value of 109.6931 mV when the output of the control amplifier is at a maximum. In order to make reliable measurements on the ADC, the filter output voltage must be linear so that Eq. 3.3 can be used to determine the cell current. Since the output of the filter stage showed saturation behaviour at 109.6931 mV and 3.2218206 V, the linear range was roughly determined to be between 193.3 mV and 3.119 V as indicated by the dashed black line. The overlapping nature of the transimpedance amplifier output (red) and the filter output, showed that the filter stage has unity gain as expected.

Fig. 4.20 shows the frequency response of the whole system at various nodes when the input to the control amplifier was set as the AC voltage source. *Out1* (red) shows the frequency response of the control amplifier stage. It has a unity gain in the passband up until around 300 kHz where the gain starts to increase before rapidly decreasing at 1 MHz. This behaviour is expected for op-amps that have a gain bandwidth product of 710 kHz, because it will already stop working as expected at frequencies as low as 300 kHz. *Out2* (green) shows that the transimpedance amplifier stage acts as a low-pass filter that reduces the bandwidth of the system to about 23.6 kHz. This was very close to the designed value of about 24.114 kHz. The filter stage (blue) further reduces the bandwidth to about 4.86 kHz and the -20 dB stopband frequency to about 17.4 kHz. It differs slightly from the values shown in Fig. 4.17 since this simulation considered the system as a whole and not the filter as a separate stage.

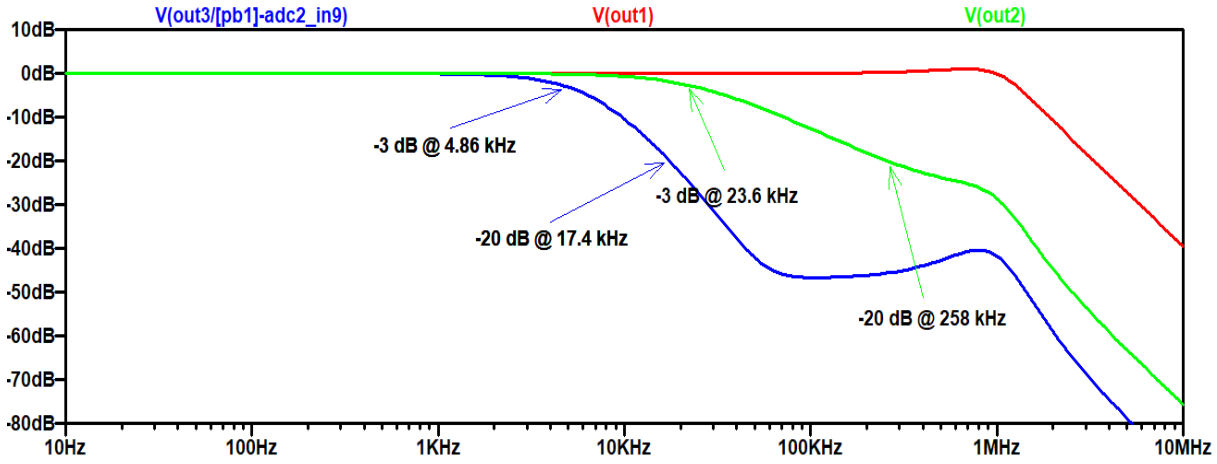

Figure 4.20: Bandwidth characteristics of the potentiostat.

The group delay of the whole system (shown in Fig. 4.21) was about 50 μs in the passband and 43 μs at the cutoff frequency. Even though these values are different from

those identified in Fig. 4.17, it still shows that the system has a maximally flat group delay in the passband that is characteristic of a Bessel filter.

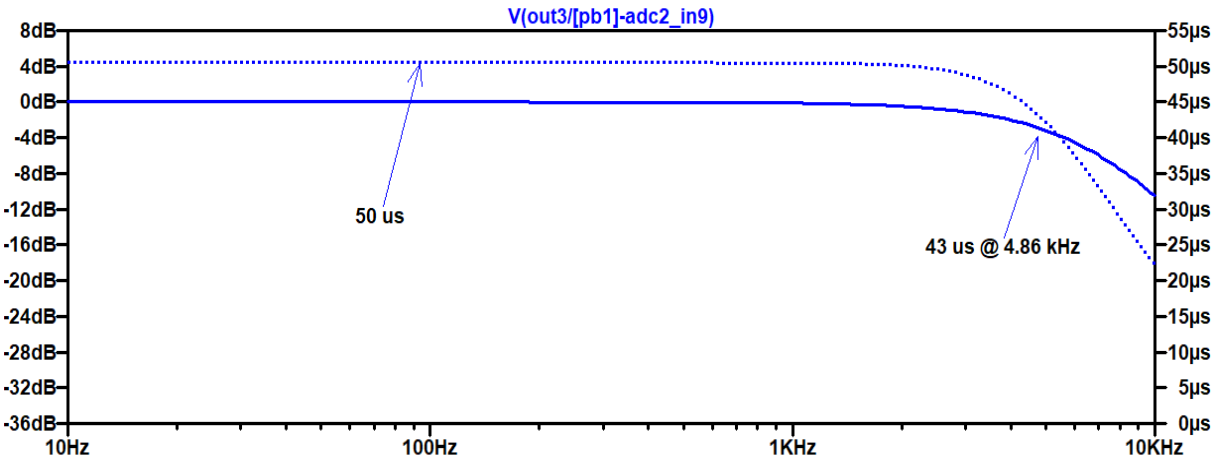

Figure 4.21: Maximally flat group delay in the passband of the potentiostatic circuit.

A transient analysis was done with a 25 Hz square wave at the input of the control amplifier. The filter output was plotted against an inverted form of the input waveform to compare the waveshape and assess to what extent the output mimics a square wave. Fig. 4.22a shows that the output (blue) closely mimics an ideal square wave signal (green), which indicates that enough harmonics are passed through the system to recreate the square wave signal. The rising and falling edges, shown in Fig. 4.22b, are about 140 μs delayed when compared to the square wave. Even though the response is delayed it is sufficiently short considering the fact that the pulse length is 20 ms.

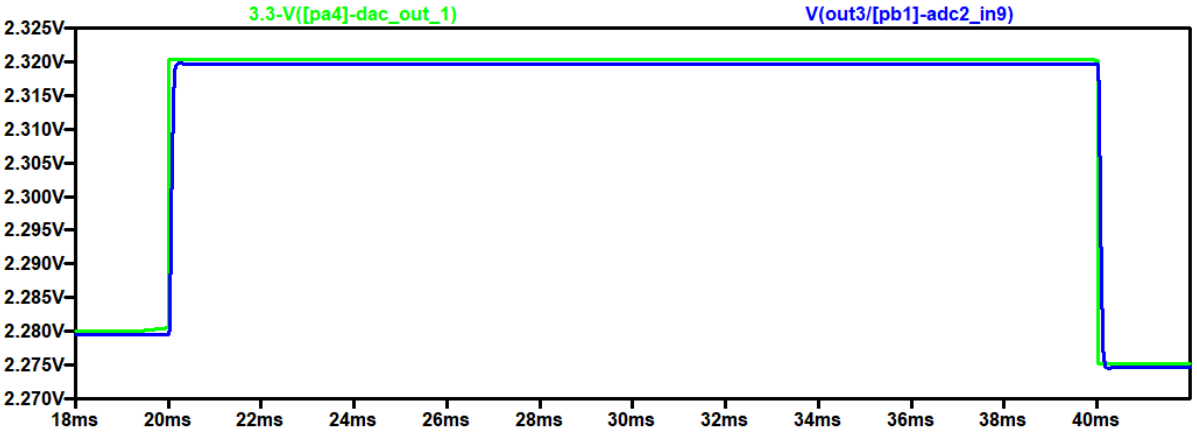

(a) Full output waveform.

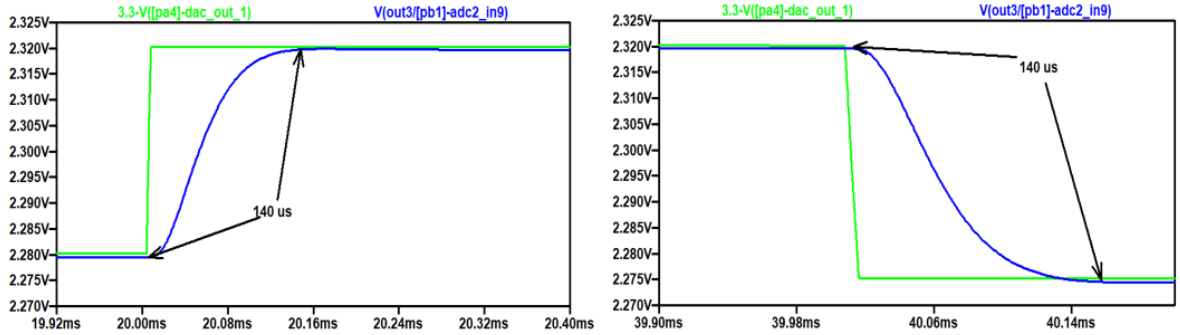

(b) Rise and fall time of the output waveform.

Figure 4.22: Comparison of the simulated output signal and an ideal square wave signal. a) Full width graph of the output waveform. b) Rise and fall time of the output waveform. The ideal square wave is shown in green and the simulated output is shown in blue

A transient analysis was done with combinations of the various noise sources to see what effect it has on the output noise. The DACs were biased at 1.65 V for these simulations. The RMS, peak-to-peak, and average values of the output for the different combinations are summarized in Table 4.4. RMS values of the input noise sources are also repeated in this table.

Table 4.4: Output noise values as determined in LTSpice.

Input noise sources			
	Rail noise source	**DAC1 noise source**	**DAC2 noise source**
RMS value	384.86 μV	389.19 μV	400 μV
Output noise			
	RMS	**Peak-to-Peak**	**Average**
Influence of rail noise	26.07 μV	251.3 μV	1.64952 V
Influence of DAC1 noise	79.3 μV	456.8 μV	1.64952 V
Influence of DAC2 noise	470.5 μV	2.25 mV	1.64952 V
Influence of all noise sources	438.19 μV	1.947 mV	1.64952 V

The simulation showed that the rail noise source made the smallest contribution to the output noise. Even though DAC1 had a relatively large noise signal, it made the second smallest contribution to the output noise. This is because the noise is added at the start of the circuit and thus it is attenuated by the transimpedance amplifier and filter stage. DAC2 made the largest contribution to the overall noise. An important result to notice is that the average output voltage in all cases was only about 480 μV lower than the ideal value of 1.65 V. This is because the op-amps have non-idealities such as offset voltages that are inherent to each op-amp and cause small DC errors in the expected outputs. According to LTSpice, the small DC offset error could cause 1 least significant bit error on the ADC reading. The effect of the output noise can be reduced by sampling the output signal multiple times and averaging out the zero mean white noise.

The frequency domain noise analysis results are summarized in Table 4.5. The control amplifier stage made the largest contribution at 22.175 μV of RMS noise. The transimpedance stage increased this noise slightly to 22.485 μV, and the filter stage reduced the total output noise to 21.681 μV. This is because the filter stage reduces the bandwidth of the whole system. There was very little thermal noise contribution to the system that is evident from the low RMS noise values of the resistors.

Table 4.5: Contribution of each node and component to the output noise.

Stage	**Node**	**RMS noise**
Control stage	*out1*	22.175 μV
Control + transimpedance stage	*out2*	22.485 μV
Control + transimpedance + filter stage	*out3*	21.685 μV, R1 = 777 nV, R2 = 343 nV, R3 = 1.507 μV

4.2.1.4 Practical measurements and comparison with designed characteristics

Fig. 4.23 shows the linearity curve that was measured using the ADC. The valid digital word range that could be measured on the ADC was identified as 42 to 4032. This corresponds to voltages of 33.846 mV and 3.2484 V. Since the filter stage has a unity gain in the signal bandwidth, Eq. 3.3 can be used to calculate the maximum and minimum cell current that can be measured accurately. The maximum positive cell current can then be calculated as,

$$\begin{aligned} I_{cell(max)} &= \frac{1.65 - 0.033846 \text{ V}}{6.6 \text{ k}\Omega} \\ &= 244.87 \ \mu\text{A}, \end{aligned} \tag{4.1}$$

and the minimum cell current as,

$$\begin{aligned} I_{cell(min)} &= \frac{1.65 - 3.2484 \text{ V}}{6.6 \text{ k}\Omega} \\ &= -242.18 \ \mu\text{A} \end{aligned} \tag{4.2}$$

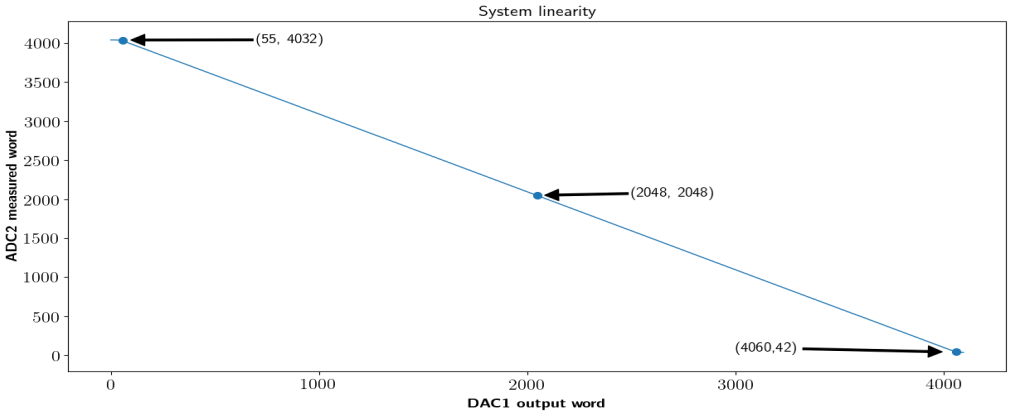

Figure 4.23: Linear voltage range that can be measured on ADC2.

Fig. 4.23 also showed that the potentiostatic circuit was biased in the center point of the ADC. When DAC1 was set to the same value as DAC2 (which is 2048 or 1.65 V) no current flows through the cell resistance because both sides of the resistor are biased at the same potential. Since no current flows through the feedback resistor of the transimpedance amplifier, the output voltage is equal to the biasing voltage of 1.65 V, which corresponds to a digital word of 2048. Table 4.6 provides a summary and comparison of all the potentiostat characteristics.

Table 4.6: Summary of the potentiostat characteristics.

Current & voltage characteristics			
	Designed	**Simulated**	**Measured**
ADC middlepoint	2048, 1.65 V	1.6495 V	2048, 1.65 V
ADC max	4095, 3.229919 V	3.1190517 V	4032, 3.2484 V
ADC min	0	109.6391 mV	42, 33.846 mV
Maximum current	250 μA	233.39 μA	244.87 μA
Minimum current	-250 μA	-222.58 μA	-242.18 μA
Noise characteristics			
	Simulated		**Measured**
Output RMS noise	438.19 μV		284 μV
Rail RMS noise	384.86 μV added to simulation		460.57 μV
Bandwidth characteristics			
	Designed	**Simulated**	**Measured**
-3 dB corner frequency	5 kHz	4.86 kHz	4.4 kHz

The measurements showed that the ADC can reliably measure voltages that correspond to digital values between 42 and 4032. Any values outside of these digital words should be discarded since the op-amp outputs are most likely saturated. These digital words corresponded to currents between -242.18 μA and 244.87 μA, and it is a larger current window than LTSpice predicted (-222.58 μA to 233.39 μA).

The measured output RMS noise (284 μV) was in the same order of magnitude as lowest possible noise measurement that could be taken by shorting the probe to ground (223.31 μV). This was also much lower than LTSpice predicted (438.19 μV). The measured rail noise (460.57 μV) was only slightly higher than the rail noise that was added to the

simulation and that was measured in Section 4.2.1.1 (384.86 μV). Overall, the noise measurements were in the same order of magnitude as the lowest possible noise measurement that was acquired by shorting the probe to ground, and therefore the system had low noise.

The actual system bandwidth was measured as 4.9 kHz, which was 100 Hz lower than the designed value. This was because of the influence of the transimpedance amplifier feedback network that acts as an extra low pass filter in the system.

4.2.2 Software

The software findings are described in terms of the accuracy of the applied waveform and the timing characteristics of the control flow algorithm.

4.2.2.1 Accuracy of the applied waveform

The accuracy of the applied square wave signal is summarized in Table 4.7. Since the initial and final potentials are arbitrarily be chosen by the user, it was not included in the accuracy results. Due to the finite resolution of the DAC of the Nucleo board, the initial and final potential might be slightly off, but it would not lead to any significant errors in the experiments. Even though the step size was still very accurate, it had the largest deviation of 3.32% from the ideal value. Since the step amplitude was smaller than 5 mV, it caused the square wave signal to have more staircase potential values within a single sweep, compared to the Gamry device.

Table 4.7: Accuracy of the experimental waveform that is applied using the developed potentiostat.

	Value	**Accuracy**
$V_{wr(step)}$	4.834 mV	3.32%
$V_{wr(pulse)}$	20.14 mV	0.708%
Scan rate	120.85 mV.s^{-1}	3.32%

4.2.2.2 Control flow and DAC timing characteristics

Fig. 4.24 gives an illustration of the timing characteristics that were determined on the oscilloscope. The full time frame, labeled TIM6, represents a single time frame in the case of a running experiment. A single time frame was verified to be 20 ms in duration as expected. TIM3 was started 2.66 μs after the DAC1 value was updated in the TIM6 interrupt callback. After 18.6 ms the TIM3 interrupt was fired and 53.2 μs later ADC2 and TIM2 were started. The ADC2 peripheral then sampled for a duration of 1.3 ms before stopping about 44.2 μs before the start of the next time frame. The results supported the choice of timing parameters since the MCU overhead left about 44 μs of processing time before the start of the next time frame.

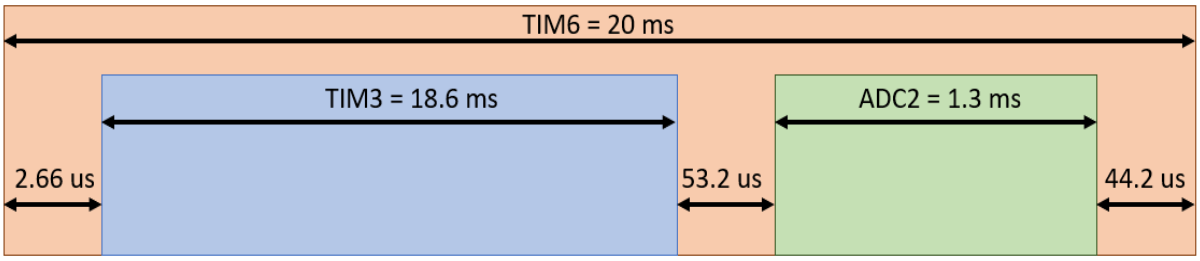

Figure 4.24: Illustration of the timing characteristics of the peripherals that were determined using the oscilloscope and GPIO pins that were toggled.

Another important timing characteristic is that of the DAC output value. Ideally, it should be able to change between values instantaneously but in reality there is a finite settling time. Fig. 4.25 shows an oscilloscope timing diagram of the DAC output at the moment that it switches between two pulse values. The orange waveform is that of a GPIO pin that is toggled at the instant that the DAC value is updated, and the blue signal is that of the DAC output. The image on the left shows that the DAC takes about 5 μs to switch between two pulse values which is very short in comparison to the pulse length of 20 ms. The DAC also has a ringing effect that lasts about 300 ns as shown on the right of the figure. The first oscillation had the biggest amplitude of about 75.2 mV which then greatly diminishes for each subsequent oscillation.

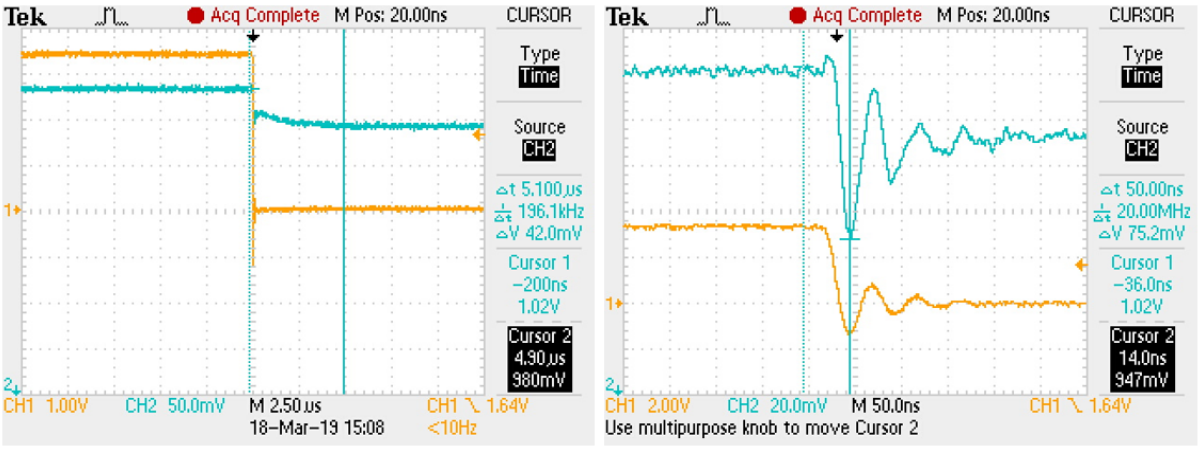

Figure 4.25: Oscilloscope data of the DAC timing characteristics.

4.3 Comparison of developed potentiostat with Gamry instrument

Fig. 4.26 shows the forward and reverse current samples of an unmodified CNF sensor that was used in the previous reproducibility studies. This is a data curve collected from the sensor that underwent twenty consecutive scans in 5 mM of the FeCN redox couple. The raw data was collected from Gamry EchemAnalyst. It showed that the lowest measured current was -208 μA, which justified the concentration range that was used for the Gamry and developed potentiostat comparison experiments.

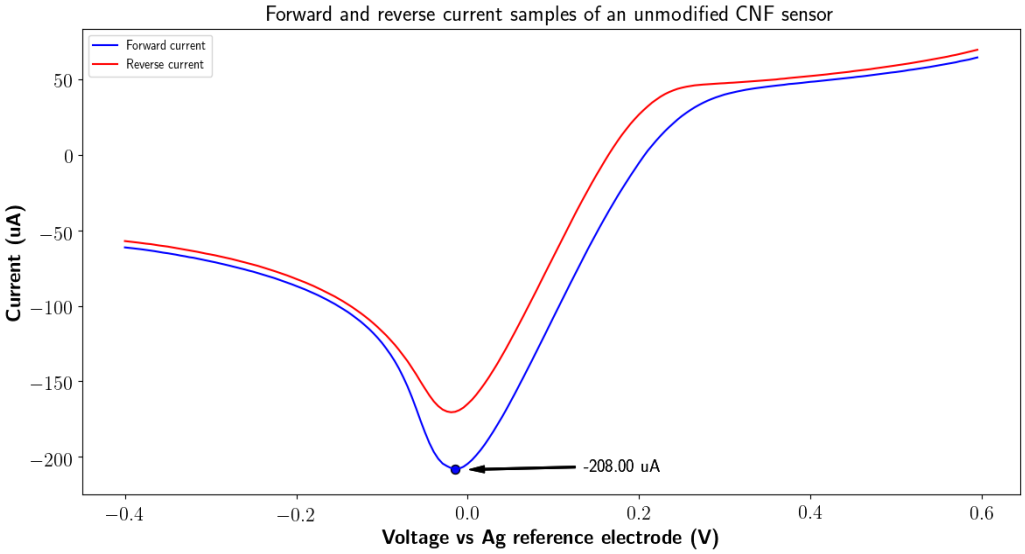

Figure 4.26: Raw data curves of the forward and reverse current samples of the unmodified CNF sensor that was used in the multiple scans reproducibility study. The data was collected from the Gamry device.

Fig. 4.27 shows the unfiltered and unprocessed voltammograms that were acquired from the Gamry instrument and the developed potentiostat. The solid lines are from the Gamry device and the dotted lines are from the developed potentiostat. The curves with the same color are from the same concentrations, but only differ in the device that was used. In all the cases the developed potentiostat measured a higher current than the Gamry device. The developed potentiostat also had a very sharp rise at the starting potential of 0.5 V, whereas the Gamry device had a very flat initial response. The maximum redox current of each curve appeared in the potential range of 65.1-105.2 mV for the Gamry device, and 64.8-98.7 mV for the developed potentiostat.

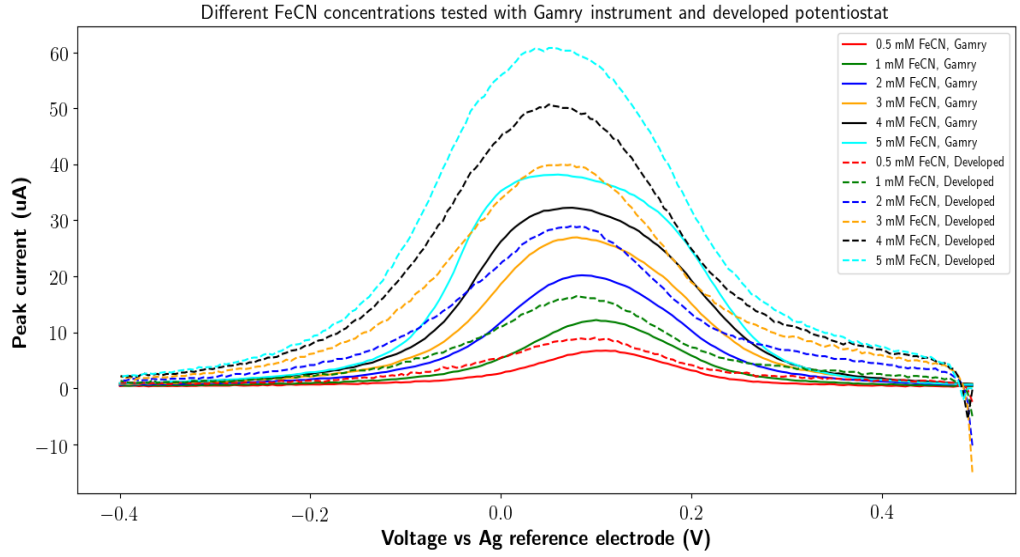

Figure 4.27: Raw data curves acquired for the tests with different FeCN concentrations on the Gamry instrument and the developed potentiostat.

None of the curves had inflection points on the left and right hand side of the redox peak, and therefore the leading edge baseline analysis (Method 1) was used to extract the peak current. The first 35 samples were used for the regression analysis step, and the first 6 samples of the developed potentiostat curves were excluded so that only the initial flat response is used. The peak current of each curve is plotted in Fig. 4.28 along with the calibration curve. The Gamry device had a calibration curve of, $y_1 = 5.59x + 3.87$ μA, where x is the concentration in mM. The developed potentiostat had a calibration curve of $y_2 = 7.01x + 2.85$ μA. Both devices exhibited excellent r^2 values, and could easily distinguish between the different concentrations. The developed potentiostat and the Gamry device had similar peak currents at the lower concentrations, and only started to diverge around 2 mM.

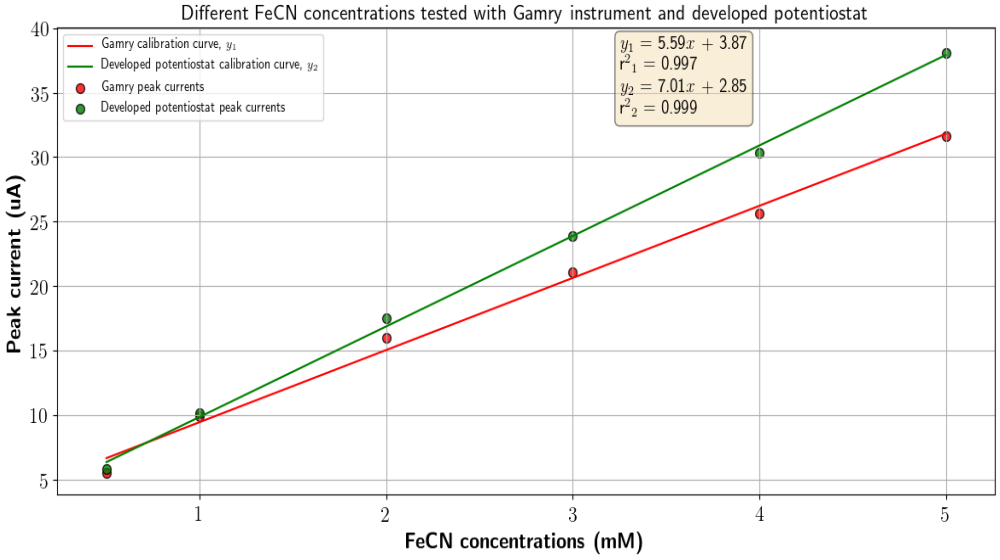

Figure 4.28: Calibration curves acquired by testing different FeCN concentrations on the Gamry instrument and the developed potentiostat.

The results confirmed the operation of the home-built device and they were comparable to the benchmark Gamry instrument for this particular application.

4.4 sP-selectin immunosensor response measured with Gamry instrument

This section gives the findings of the full scale tests that were conducted with the Gamry instrument. The immunosensor response with the FeCN redox probe is given, followed by the RuHex probe.

4.4.1 Immunosensor measured with the FeCN redox couple

Fig. 4.29 shows the calibration curve of the first full scale test using the GPHOX sensors. All of the peak currents were extracted using Method 2 of the data analysis algorithm. The calibration curve is a plot of the mean change in peak current before and after sP-selectin protein immobilization for each concentration category. The maximum and minimum

deviation from this mean is also plotted as the error bars. The curve showed that there is no linear detection range and all the means are centered around a 0% change in peak current. The deviations of each category are also overlapping which means that different concentrations cannot be distinguished from one another. The GPHOX immunosensors could therefore not detect the presence of any sP-selectin proteins and the results were regarded as inconclusive.

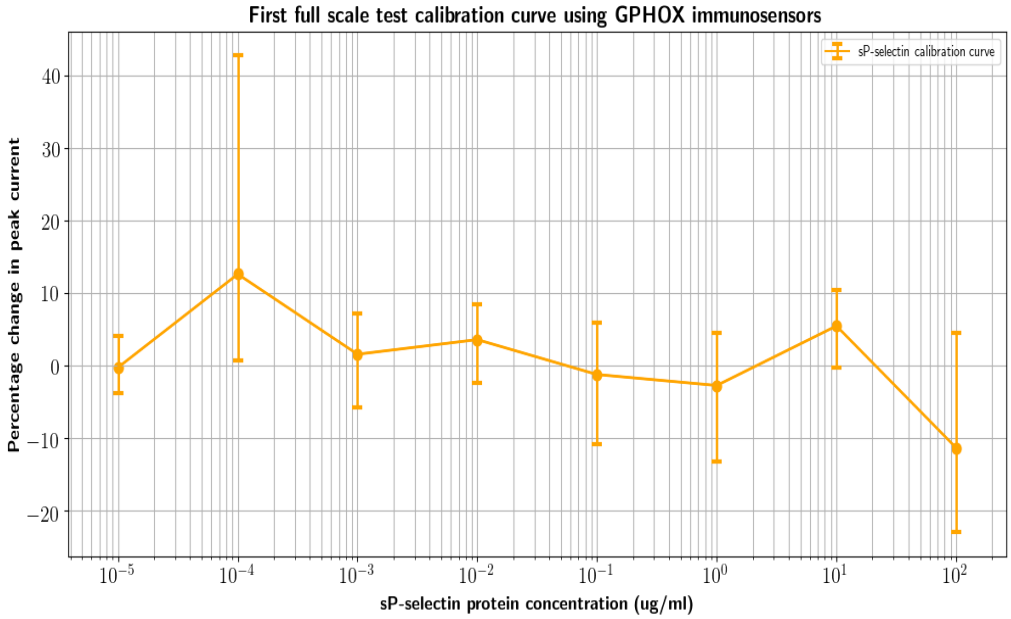

Figure 4.29: First full scale test calibration curve using the GPHOX immunosensors. The percentage change in peak current are plotted against the sP-selectin protein concentration.

Fig. 4.30 shows the calibration curve that was acquired for the second full scale test using the CNF immunosensors. All the sensors were analyzed using Method 2 of the data analysis algorithm, except for sensor 18 that did not have two inflection points. This sensor was analyzed using Method 1 and the first 40 data points were used to calculate the leading edge baseline. Again, this calibration curve showed that no linear working range could be obtained in the concentration range that was tested. Even though the error bars overlap across concentrations they are much smaller compared to the GPHOX sensors. This could be attributed to the stability and reproducibility of the CNF sensors. One interesting result was that all the sP-selectin tests showed a decrease in the peak current of about 8%, whereas the non-specific CRP test only showed a reduction of about 2%.

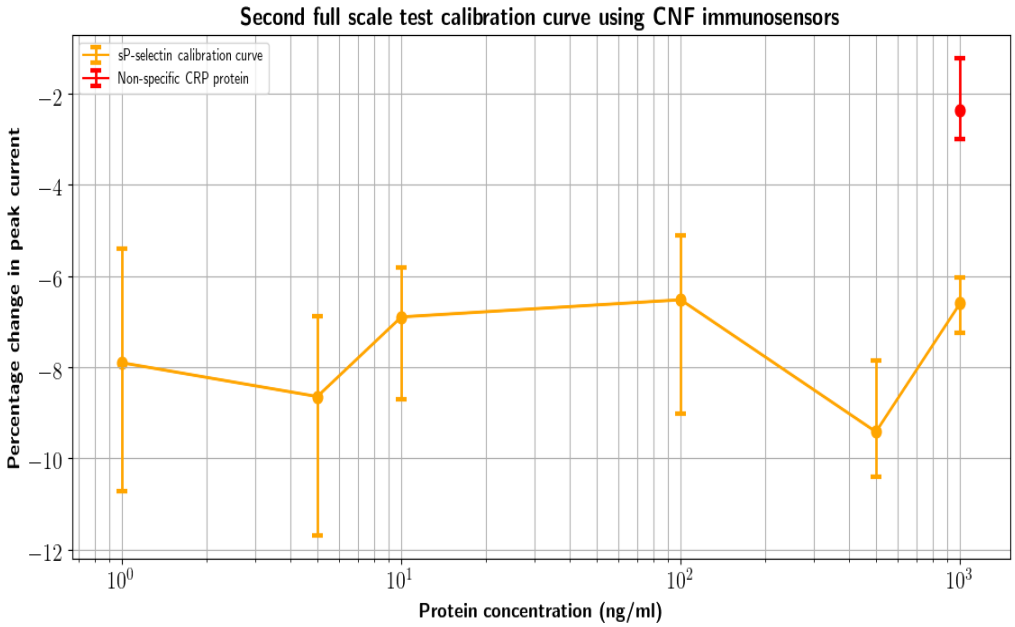

Figure 4.30: Second full scale test calibration curve using the CNF immunosensors. The percentage change in peak current is plotted against the protein concentration categories.

Fig. 4.31 shows the calibration curve that was obtained for the third full scale test. All of the peak currents were extracted using Method 2 of the data analysis algorithm. Since the pH of the redox solution was changed to 5.5 it was expected that the sP-selectin proteins would be positively charged during the tests leading to an increasing in the charge transfer efficiency, and therefore an increase in the peak current after immobilization. The calibration curve showed that there was no well defined linear region and the mean change in peak current was centered around 0%. Even the non-specific CRP test showed an overlapping response with the same concentration of sP-selectin. Since no linear range was present and there was no specificity towards sP-selectin, the results were regarded as inconclusive.

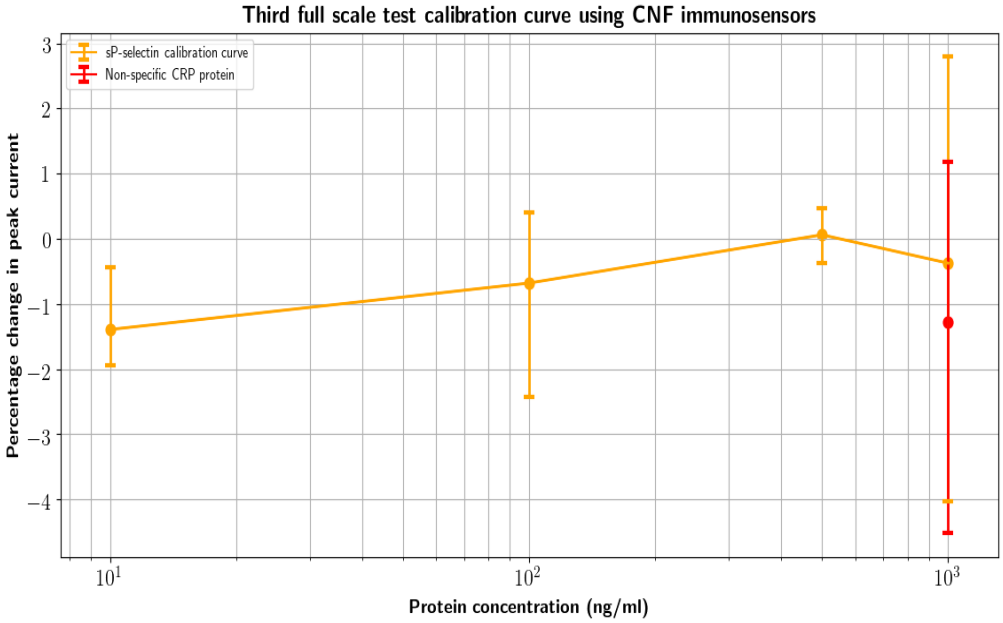

Figure 4.31: Third full scale test calibration curve using the CNF immunosensors. The percentage change in peak current is plotted versus the protein concentration that was used.

4.4.2 Immunosensor measured with the RuHex redox probe

Fig. 4.32 shows the calibration curve of the fourth full scale test with the RuHex redox probe. For this test it was expected that the percentage change in peak current would increase for increasing concentrations of the sP-selectin protein. This is because the negatively charge sP-selectin proteins could attract the positive RuHex redox probe, and therefore increase the charge transfer efficiency. Even tough it looks as though the change in peak current is higher at the high concentrations, the non-specific CRP had almost exactly the same response for the 1 μg/ml concentration. This is more indicative of proteins adsorbing to the surface of the working electrode instead of binding to the antibody. The error bars were also overlapping across the whole concentration range, which means that the different categories could not be distinguished from one another. Therefore, these test results were also inconclusive.

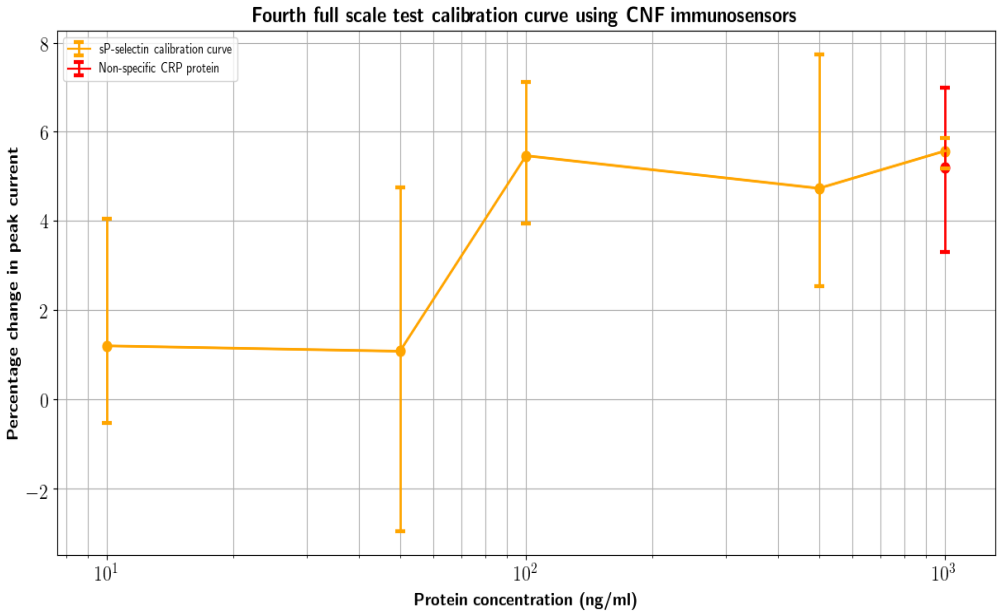

Figure 4.32: Fourth full scale test calibration curve using the CNF immunosensors. The percentage change in peak current is plotted versus the protein concentration that was used.

4.5 sP-selectin immunosensor response measured with developed potentiostat

The fifth full scale test used the developed potentiostat to perform the electrochemical measurements using the FeCN redox probe. During the baseline scans it was noted that the sensors exhibited very erratic behaviour. As an example, some of the scans are shown in Fig. 4.33. These curves were processed with the Savitzky-Golay smoothing filter, but no baseline correction was performed with the data analysis algorithm due the data that was unusable. Even though the sensors were treated with the same electrografting and antibody crosslinking protocol as previous full scale tests, it showed large variations in the peak current. The results also showed that the redox peaks were located at different positions in the scanned range. Post-processing could not be done for this full scale test, and therefore the results were deemed inconclusive. The findings are discussed in detail in Section 5.4.2.

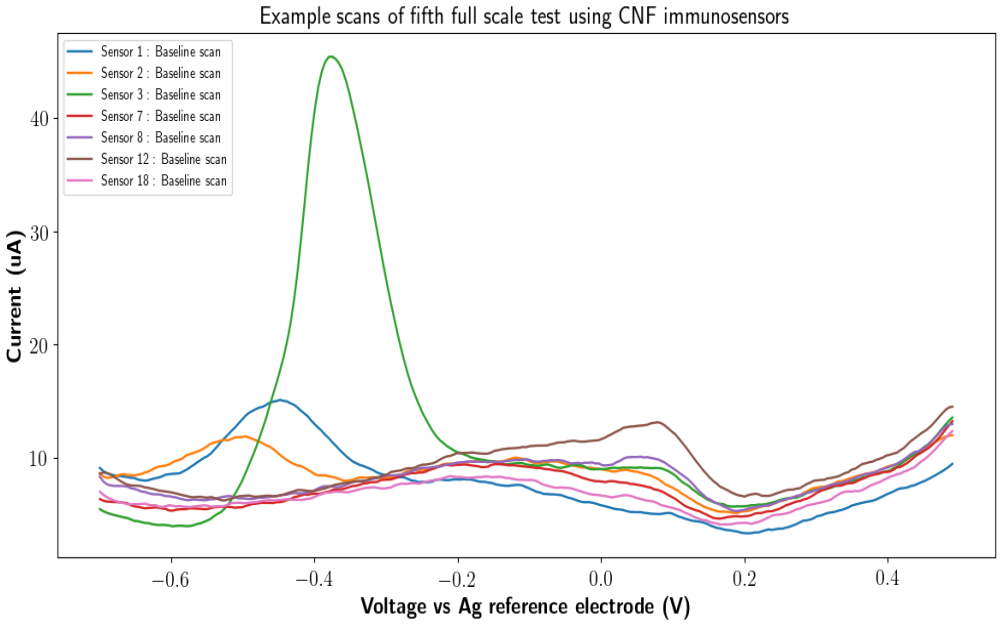

Figure 4.33: Example scans of the fifth full scale test using the CNF immunosensors.

Chapter 5

Discussion

This chapter serves as the section where the general findings of the project are discussed. It aims to discuss how well the biosensor worked and it relates the results and findings to that reported in literature. Design choices and findings that are inherent to this project, and that was not explicitly stated in literature, are also discussed. The chapter discusses the electrochemical noise reduction techniques and gives a review of the data analysis algorithm. This is followed by a discussion of the commercial sensor modification process and the development of the home-built potentiostat. Lastly, the feasibility of this biosensor is reviewed.

5.1 Electrochemical noise reduction techniques and data analysis algorithm

The main goals of the data analysis step was to reduce the amount of noise in the measurements and also to calculate the peak current relative to a baseline current. In general, that is what the data analysis of most electrochemical experiments comprise of outside of this project, and these goals can be achieved through various hardware and software implementations.

The most common hardware implementation is to use a Faraday cage for shielding of the sensor and exposed cables. This can reduce the electrical noise originating from the surrounding equipment although it is only required for low current experiments in the picoampere to nanoampere range [148]. Even though it is never a bad idea to perform experiments in a Faraday cage, it was not necessary for this project since all the sensors had currents in the low microampere range. Another hardware implementation that is recommended is the use of high quality potentiostat systems. But this noise source would only have an effect on sensors with currents lower than a few nanoampere since most industrial devices are equipped with low noise electronic components. The Gamry Interface 1000E potentiostat that was used for this project is a very robust system and therefore noise due to the device is negligible in this case.

As for any software implementations, it is suggested that a background scan is subtracted from the measurements if there are any unwanted redox peaks or background currents [148, 149]. This was not necessary for any electrochemical measurements in this work since the voltammograms only had the peaks that originated from the redox couple of interest. In this case, only a smoothing filter was used to reduce the noise in the data.

In general, it is also recommended that the peak currents are calculated from a specific baseline. The leading edge baseline correction method (Method 1) was used for some of the electrochemical measurements that were performed in this thesis. This is, however, subject to human error since the number of leading edge data points need to be chosen before the algorithm is run. Another drawback that was encountered with this method is that the same number of data points could not be used to calculate the baseline for any curve. This is because the location of the most linear data points are highly dependent on the location of the starting potential and the position of the redox peak. Each curve had to be inspected manually to make sure that only the most linear data points are used for the regression analysis that calculated the baseline. This made the data analysis step a time consuming and tedious process for cases where Method 1 had to be used. It was noted that Eissa *et al.* reported their square wave voltammetry curves (repeated in Fig. 5.1 for illustration purposes) with the inflection points of the redox peak on the zero current axis. Therefore, an algorithm that can calculate the position of the inflection points was appropriate for the data analysis of these voltammograms. Method 2 could be used without the intervention of the user, which stops human error from being introduced to the results.

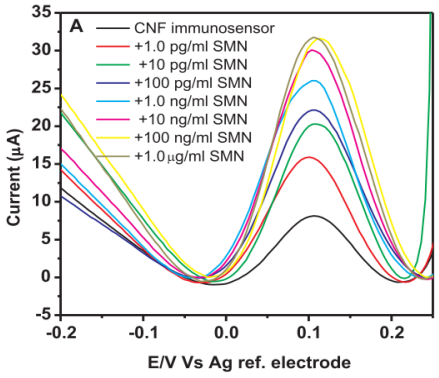

Figure 5.1: Inflection points of the square wave voltammetry curves are located on the zero current axis. [69]

Overall, the data analysis algorithm and noise reduction techniques used in this project worked well for analyzing the acquired data. The algorithm was specifically written to analyze data for this electrochemical setup which means it cannot be used as a universal script for all electrochemical measurements. Some variables, such as a range where the redox peak is located, was hard-coded into the script and it has to be changed if the setup were different. Finding the redox peak was not always as easy as looking for the maximum current since some of the curves had higher currents at the starting and ending potentials. That is why a potential range (where the redox peak is located) needed to be specified.

5.2 Biosensor development process

This section discusses all the choices and findings that were made during the sensor modification process. That includes the feasibility of the electrochemical setup, the diazonium salt electrografting, and finally the antibody crosslinking.

5.2.1 Electrochemical measurement procedures

It was important to follow the same procedures with each sensor before performing any type of electrochemical measurement or diazonium grafting modification was performed. The two techniques that were used to make sure that each sensor was treated consistently, and without contamination, was the wetting procedure and the washing step. The wetting procedure that was described in Section 3.1.1 was used to make sure that the electrode surfaces were clean of small bubbles and impurities before any measurements were done. Fig. 5.2 shows an image of an unmodified GPHOX sensor that was scanned for three consecutive cycles in the FeCN redox solution without washing the sensor or following the wetting procedure. The first scan shows almost no redox peak current and the last two scans also have very different peak currents even though there are well defined peaks present. This voltammogram shows that if the two techniques were not applied it could lead to drastically different peak currents, and thus poorly reproducible results. The figure also illustrates the importance of multiple measurements on the same sensor so that an average peak current can be acquired. The multiple scans can also be used to make sure that the sensor has a stable response before a specific curve is chosen for peak current extraction.

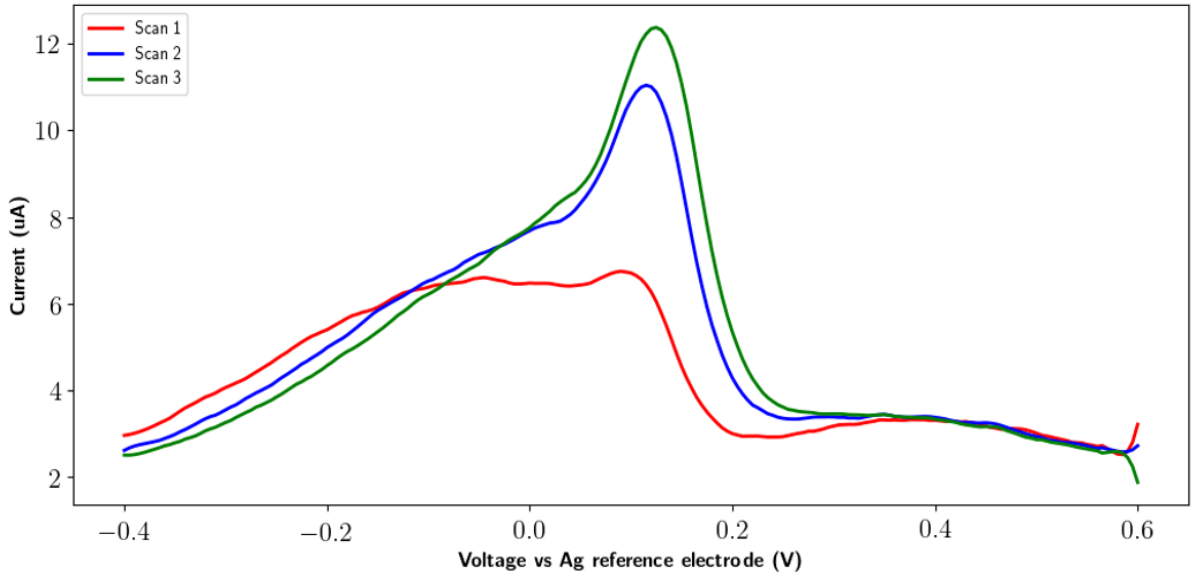

Figure 5.2: Voltammogram of a GPHOX sensor that was not subjected to the wetting procedure.

The washing and wetting procedures were also very important for sensors that had to be treated or measured in different solutions, for example, the electrochemical measurements that were taken in the redox solution after the antibody immobilization. Some of the antibody immobilized immunosensors were kept on ice with a drop of PBS on the surface of the working electrode to keep the sensor from drying out. If the PBS was not properly removed from the sensor before a baseline measurement, it could lead to changes in the redox molecule concentration since electrochemical measurements were performed in small samples of 100 μl.

5.2.2 Electrochemical window

Even though Eissa *et al.* used the same sensors, supporting electrolyte, and redox couple, it is always necessary to study the basic electrochemical behaviour of the application so that the results of any experiment can be interpreted correctly. This includes parameters such as the electrochemical potential window, electron transfer rate, and redox potentials [150]. This thesis successfully determined the electrochemical window and redox potentials of the application, but the electron transfer rate was not studied herein. The latter gives information about the current limiting factors of one-electron transfer processes, which was not of interest for this project. This would also have required more sensors which, at the time, was not available.

The goal of the electrochemical window study was mainly to determine whether the combination of the supporting electrolyte, solvent, and working electrode is compatible and electrochemically inert in the potential range where the redox couple is active. Zhou *et al.* reported that the window for glassy carbon, graphite modified glassy carbon, and chemically reduced graphene oxide electrodes in 0.1 M PBS (pH 7.0) was more or less 2.5 V [151]. The window identified for the GPHOX sensors in this work was at least 1.6 V, but the result could have been limited by the scan parameters since they were only chosen from -0.6 to 1.0 V. At the time writing, no information could be found regarding the potential window of CNFs in PBS, but the window for this application was determined to be $\sim$1.2 V. Nonetheless, both sensors had a wide enough window to accommodate the FeCN and RuHex redox probes, since only the probes contributed to the current in the potential window.

Another consideration was that of the supporting electrolyte concentration compared to the concentration of the redox molecules. The PBS had a much higher concentration of ions (0.1 M) compared to the redox probes (5 mM), which makes it statistically more likely that the supporting electrolyte ions would migrate in the cell instead of the redox probe. This was a desirable quality since the supporting electrolyte ions would migrate in the cell to balance the charge instead of the redox molecules.

Overall, these results justify the combination of the supporting electrolyte, solvent, and working electrode material, and therefore satisfy the requirements of the electrochemical cell that were mentioned in Section 2.4.1.

5.2.3 Reproducibility

The reproducibility of any biosensor is an important characteristic to be considered for the performance of the end-product. Therefore, the reproducibility of the unmodified screen printed electrodes was assessed using both redox probes before any modifications were performed. The findings showed that the CNF sensors were much more reproducible than the GPHOX sensors, since they had similar peak currents under the same experimental conditions. As such, the CNFs would make for a better sensor to be used in the biosensor development process.

5.2.4 Electrografting of 4-carboxyphenyl diazonium salt

The electrografting step proved to be a very simple way of creating carboxyl support groups on the surface of the sensors. It takes roughly 10 minutes to prepare the diazonium salt solution using a few low cost materials and a potentiostat device that can perform cyclic voltammetry. The shape of the cyclic voltammograms agreed well with that reported in literature by various groups. Fig. 5.3 shows the cyclic voltammograms from the electrochemical reduction of diazonium salt on various carbon surfaces that are reported elsewhere [69, 152, 153]. Specifically, the reduction peaks reported by *Eissa et al.* in Fig. 5.3A were also located at more or less -0.3 and -0.2 V for the GPHOX and CNF sensors, respectively. The peak reduction current of the sensors that were electrografted in this work were, however, much larger (about 50 μA).

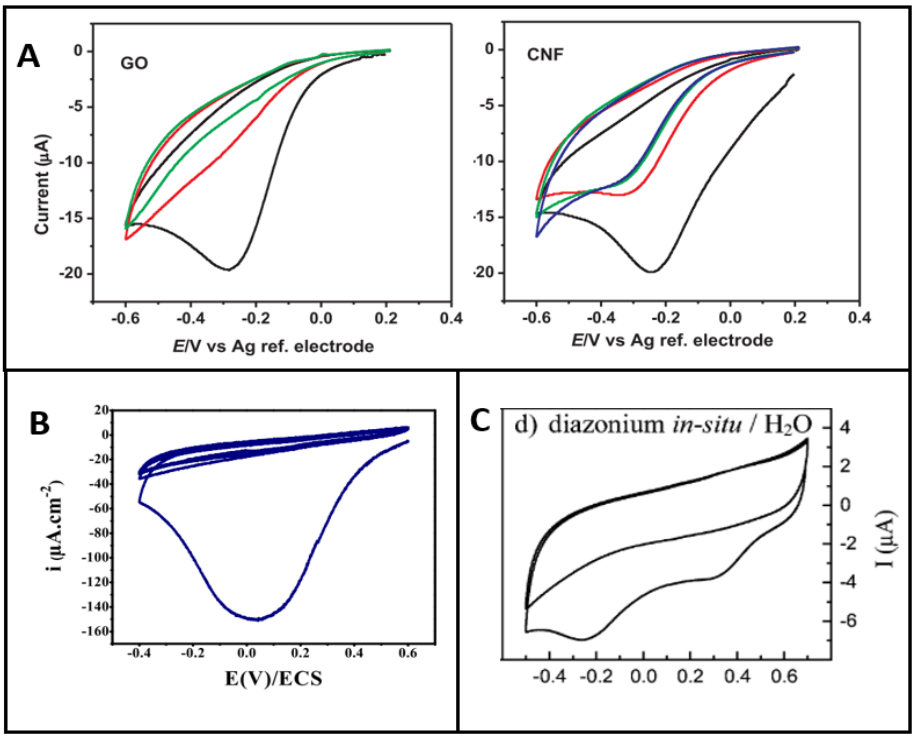

Figure 5.3: Cyclic voltammograms from the electrochemical reduction of diazonium salt on various carbon surfaces. A) Results reported by Eissa *et al.*. The black line shows the first reduction cycle and the colored lines show the subsequent cycles [69]. B) Diazonium salt reduction on a glassy carbon electrode showing that the first cycle had a large reduction peak, and subsequent cycles had no reduction peak [153]. C) Electrografting of *in-situ* prepared diazonium salt on a glassy carbon electrode [152].

Fig. 5.4A shows the square wave voltammetry results of the GPHOX and CNF sensors reported by Eissa *et al.*. It was not stated whether new sensors were used for each curve or if the same sensor was used for each grafting step. The number of cycles for each colored line was also not stated, but the general trend was that more scans lead to a smaller square wave voltammetry peak. The GPHOX sensors used in this thesis was not reproducible and therefore a similar voltammogram could not be compared to these results. Since the unmodified CNFs had a more stable peak current and higher reproducibility, the effect of the number of cycles on the square wave peak could be compared and are shown in Fig. 5.4B. The results are in agreement with literature and are likely due to the dissociated

form of the carboxyl groups that repel the negatively charged redox molecules, leading to a smaller peak current [69]. An interesting result to notice is that the CNF sensors used in this thesis had a much smaller peak current of about 40 μA compared to about 120 μA reported by Eissa *et al.*. The difference in current magnitude reported in this work and that of Eissa *et al.* might have an impact on the performance of the biosensor, and it could be due to a variety of reasons. This includes the manufacturing process of the sensors, the shipping of the sensors, or even the differences in the sampling parameters of the potentiostat devices that were used.

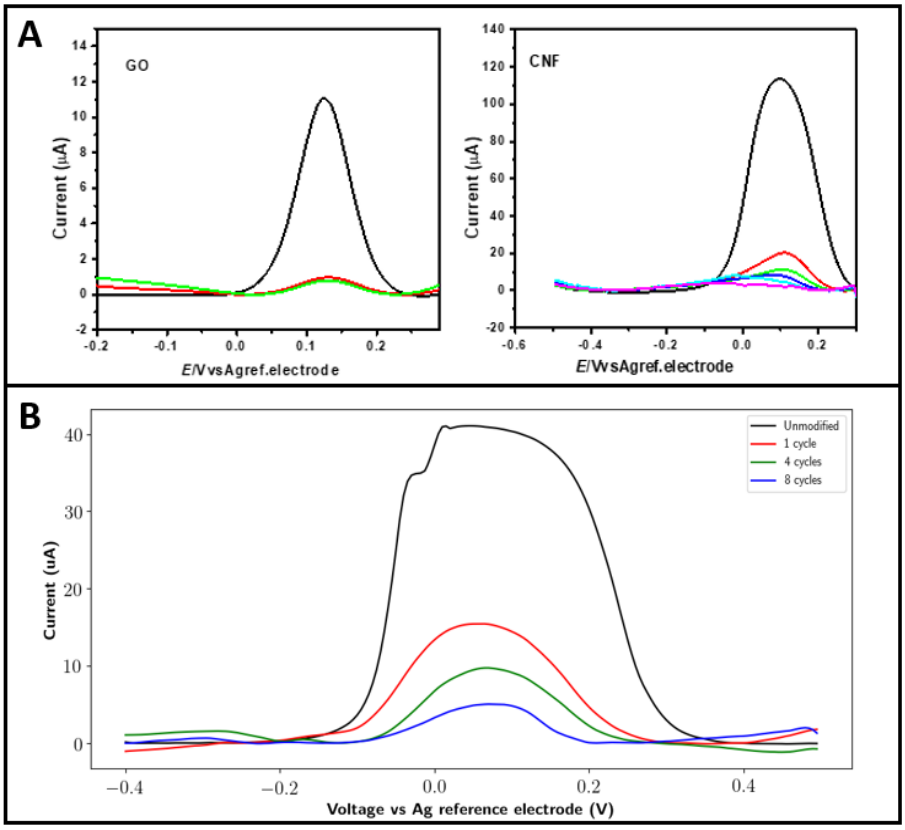

Figure 5.4: Square wave voltammetry results of the sensors in the redox couple after electrografting using a different number of cycles. The black curve shows the response of an unmodified sensor and the colored curves show the response after using more grafting cycles. A) The voltammograms for GPHOX and CNF sensors reported by Eissa *et al.* [69]. B) The voltammograms of the CNF sensors used in this thesis.

The amount of grafted carboxyl groups depend, amongst other things, on the number of cycles that are used. But more cycles also lead to a larger organic layer which could reduce the biosensor sensitivity. An important design choice thus had to be made regarding the number of cycles that are used to obtain an "optimal" coverage of the sensor surface. It is important to note that a fully optimized sensor would be outside of the project scope since that would require a large amount of materials and methods that are not easily accessible. Most notably methods such as Raman spectroscopy and X-ray photoelectron spectroscopy (XPS) that can be used to characterize the surface composition of the working electrode. Even if these methods were easily accessible, a fully optimized sensor would be dependent on a number of variables such as working electrode area, diazonium salt concentration, antibody concentration, redox molecule concentration, and pH values of various solutions. Therefore, the number of cycles were chosen somewhat arbitrarily for

each of the different full scale tests. It was noted that the unmodified GPHOX sensors already had a very low peak current response during the square wave voltammetry scans in the redox couple solution. The extra organic layer from the electrografting step further reduces this peak current which could decrease the sensor sensitivity, and therefore decrease the signal-to-noise ratio of the sensor. Thus, it was decided that only two grafting cycles would be used on the GPHOX sensors; the first cycle being the minimum necessary cycle, and the second being the cycle that is used to show that the reduction peak current decreases or completely disappears. The CNF sensors had a much larger surface area and could therefore be grafted using more cycles. Eissa *et al.* used four cycles and therefore the same number of cycles were used for all the CNF sensors.

Eissa *et al.* used two techniques (Raman spectroscopy and XPS) to confirm the presence of these surface functional groups. Specifically, XPS was used to confirm a change in the surface elemental composition of the sensors before and after the electrografting procedure. These techniques were not available during this thesis and thus similar experiments could not be used to confirm the presence of the carboxyl groups. The only way that the presence of the carboxyl groups were confirmed was through the reduction in the square wave voltammetry peaks, such as that shown in Fig. 4.10. The results of this work was inline with that reported by Eissa *et al.*.

5.2.5 Antibody crosslinking

The sP-selectin antibodies are bound to the carboxyl groups using the EDC/NHS carbodiimide crosslinking chemistry. This step could greatly affect the performance of the biosensor since it involves numerous variables such as solution pH, number of available carboxyl groups, EDC/NHS concentrations, incubation times, antibody concentration, and solution volumes. It is highly unlikely that there is a universal combination of parameters that would work for any biosensor requiring the conjugation of amine groups to carboxyl moieties. The crosslinking can, however, be perfected through trial and error with different parameters and the necessary equipment to obtain a uniform and optimal coverage of the working electrode. Since the optimization of the biosensor is not within the scope of this thesis, the parameters were chosen based on what is reported in literature.

Specifically, the EDC/NHS concentrations and incubation times were chosen to be in excess of what is reported in most literature to make sure that the carboxyl groups are activated, and that the antibody has enough time to attach to the amine reactive sulfo-NHS ester. The protocol followed for the crosslinking step was most likely not the optimal method, but the confocal fluorescent images confirmed that the antibodies were successfully immobilized on the working electrode, and this also proved that the carboxyl groups were successfully created during electrografting.

5.3 Developed potentiostat

This section discusses everything that is related to the potentiostat development process. The actual component values that were used on the PCB are given and the effect this could have had on the potentiostat is discussed. This is followed by a discussion of the noise analysis techniques that were used and ultimately the potentiostat characteristics are described.

5.3.1 Component mismatches

Table. 5.1 shows the actual values of the capacitors and resistors that were used for the developed potentiostat. All the resistors were chosen to be very close to the designed value. The feedback resistor, R1, was only about 14 Ω higher than the ideal value. This could have a decreasing effect on the current range, but the practical measurements that were performed already included this. This also had a very small effect on the current resolution that is now 121.8 nA instead of 122.07 nA according to Eq. 3.6.

Table 5.1: Actual values of the resistors and capacitors that were used for the developed potentiostat.

Resistors		
	Ideal value	**Actual value**
R1	6.6 kΩ	6.614 kΩ
R2	622 Ω	621.6 Ω
R3	17.4 kΩ	17.35 kΩ
Capacitors		
	Ideal value	**Actual value**
C3	1 nF	1.04 nF
C5	24 nF	21.6 nF
C6	2.4 nF	2.52 nF

The actual transimpedance amplifier pole (due to R1 and C3) lowered the cutoff frequency from 24.114 kHz to 23.137 kHz, according to Eq. 3.7. An LTSpice simulation of the second order Bessel filter with the actual values of R2, R3, C5, and C6 listed in the table above, showed that the new cutoff frequency shifted down to 4.65 kHz from the designed 5 kHz. This, combined with the transimpedance amplifier mismatches, could be the reason why a slightly lower cutoff frequency of 4.4 kHz was realized for the potentiostat. A simulation of the full potentiostatic circuit with the actual values showed that the cutoff frequency was located at 4.54 kHz, which was very close to the cutoff frequency that was identified with the practical measurements.

Overall, the component values were close enough to the designed values and the slight mismatches was not detrimental to the operation of the device.

5.3.2 Noise analysis

LTSpice was used to do a noise analysis in the time and frequency domain. For the time domain analysis, noise sources that are "injected" into the potentiostatic circuit were identified and modeled as arbitrary behavioural voltage sources. The simulation was used to see what effect these sources would have on the circuit, and also to identify the source that had the largest impact on the output noise at the filter stage. The frequency domain noise analysis was used to identify noise sources that originate from within the potentiostat circuit components, and to identify what the contribution of each of these sources are to the output noise at the filter stage.

The time domain noise analysis showed that the total output noise due to all the "injected" noise sources would have an RMS value of 489.3 μV. The noise injected from DAC2 contributed the most to this value, which is probably due to its large impact on the virtual ground node of the transimpedance and filter stage. This could be improved

if a voltage regulator is used to create a more noiseless virtual ground. It is worth noting that the actual measured output noise had an RMS value of 284 μV, which is much lower than LTSpice predicted. This could possibly be due to the nature of the noise sources that are used in LTSpice. Independent white noise signals are uncorrelated random processes that means it has no linear relationship with any other signals. In LTSpice, however, the arbitrary behavioural voltage sources use the same random variable to generate a time domain noise signal. The noise sources are thus correlated and it could have a superimposed effect at the output. The frequency domain analysis showed that the control amplifier stage contributed the most to the output noise, and all the resistors had a minimal effect on the thermal noise due to their small values.

Overall, the noise sources had RMS values in the same order of magnitude as the smallest possible noise value that could be measured by shorting the probe. Therefore, the whole system can be considered as a low noise system and any noise had very little effect on the accuracy of the current measurements since this was also circumvented by averaging numerous samples.

5.3.3 Potentiostat characteristics

The final potentiostatic circuit could measure currents in the range of -242.18 μA to 244.87 μA in the resolution of 121.8 nA. This current range was large enough so that any immunosensor response could be measured with a 5 mM redox species concentration without saturating the ADC readings. The potentiostat also had a voltage range of -1.65 to 1.65 V, which was large enough for the immunosensor developed in this work. For this application the pulse size, step size, and potential range could be changed by the user by setting the appropriate variables in the code and reprogramming the MCU. Only the frequency variable was fixed and could not be changed.

The home-built device employed the DMA controller from the Nucleo board to reduce processor loading that might arise when the signal is applied and sampled at the same time. This desirable characteristic was achieved with only one MCU, compared to Huang *et al.* that used dual microprocessors [128]. Even though the DStat device employed higher resolution ADCs and DACs, the 12-bit resolution of this design was sufficient to perform the desired measurements. The DStat potentiostat was designed to apply signals with high accuracy and measure currents as low as 600 fA [127]. For the purpose of this thesis, performance comparable to the DStat was not necessary since it was application specific. Therefore, the home-built potentiostat fulfilled its purpose. Since the device was also battery powered, it only required a host PC to collect the data, making it more portable than the Gamry instrument.

5.3.4 Comparison with Gamry potentiostat

During the comparison tests, the developed potentiostat showed results that were similar to that of the Gamry device. It measured a larger current than the Gamry instrument, but it still showed a linear relationship over the FeCN concentration range. The higher current could be due to a number of reasons. Firstly, even though the sampling parameters of the Gamry device are not known, they are most probably different from that of the developed potentiostat. The Gamry system might sample much closer to the end of the pulse, which means that the non-faradaic current has more time to settle and, therefore,

it is not included in the measured current. Secondly, the DAC ringing effect shown in Fig. 4.25 produced a relatively large, albeit short-lived, pulse of 75 mV that is applied to the cell at every potential step. This sudden and large change in cell voltage could charge the double-layer capacitance close to the working electrode, leading to transient current spikes in the unwanted non-faradaic current [127]. Another important characteristic is that of the redox peak location. The developed potentiostat showed that the redox peaks are located in the same potential band as the Gamry instrument indicated (64.8-98.7 mV for the home-built device vs 65.1-105.2 mV for Gamry). A very interesting trend was noted between the FeCN concentration and the location of the redox peak on both devices. The higher concentrations produced peaks that were located at more negative (reductive) potentials than the lower concentrations. This is because the reductive current is sustained for longer before it becomes diffusion limited [154]. The fact that the peaks appeared in the same potential band, shows that the control amplifier performed well in keeping the reference electrode potential stable.

The calibration curve of the different FeCN concentrations had a r^2 value of 0.999 for the developed potentiostat, which shows that the it worked excellently.

5.4 sP-selectin biosensor for detecting platelet activation

The performance of the developed immunosensor can be determined by looking at the following characteristics: selectivity, sensitivity, stability, reproducibility, and linearity [155]. Selectivity is a measure of how well the biosensor can detect the presence of a specific protein in a solution containing a mixture of proteins. Since the biosensor ultimately needs to work with blood - or at least diluted plasma samples - it has to be able to discern sP-selectin proteins from numerous non-specific proteins that are present in the sample. The sensitivity determines how well the biosensor can detect low concentrations of the protein. These two characteristics can be improved by using more robust detection techniques, such as impedance measurements, or using labels, such as gold nanoparticles, for amplification. This would require more materials and more complicated modification methods that would increase the cost of each sensor. Stability refers to the ability of the biosensor system to reject ambient disturbances in and around the transducer area. Variables such as temperature drift and degradation of the bioreceptor over a period of time could affect the stability of the sensor. The linearity is a measure of how accurate the biosensor is over a range of concentrations, and how well different concentrations can be discerned from each other. A biosensor should preferrably have a large linear detection range over the physiologically relevant concentrations of the protein. Lastly, the reproducibility refers to the ability of the biosensor to produce similar results under the same experimental conditions. Label-free immunosensors, such as the one developed in this project, use less materials and simpler methods which could make them more prone to worse performance, but also desirably inexpensive. Below follows a discussion of the performance of the biosensors in terms of the reproducibility, selectivity, sensitivity, and linearity. Testing the stability of the sensor was not within the scope of this work.

5.4.1 Measurements performed with the Gamry device

The unmodified GPHOX sensors lacked reproducibility, which could have been the reason for its poor performance. Individual sensors might have been unevenly covered by the GPHOX material, leading to the underlying carbon to be exposed to various degrees. The different working electrodes could thus have an unequal amount of functional carboxyl groups, and different amounts of exposed carbon where the diazonium salt molecule can be grafted to. Fig. 5.5 shows the peak currents of the GPHOX sensors before and after sP-selectin protein immobilization. The blue bars give the peak current of each sensor after the sP-selectin antibody attachment and BSA blocking step, and the remaining colored bars give the peak current after a specific protein concentration was immobilized. The antibody responses had largely varying peak currents ranging between 2-12 μA, which justifies why each sensor had to be compared to its own baseline current. The general trend of an increasing peak current was noticed from sensor 1 to sensor 32, which could have been due to the measurements that were performed in that order. The subsequent experiments were thus performed in an arbitrary order to remove any possibility of a time dependent variable that could influence the peak current. Overall, the GPHOX sensors had poor performance in all categories which is why it could not be used as a biosensor for sP-selectin in the way that it was used in this work.

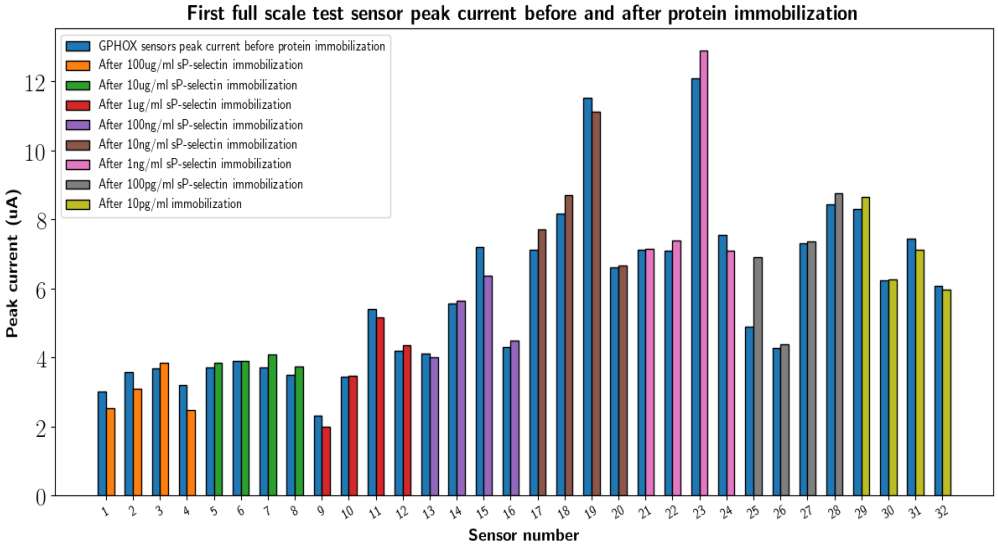

Figure 5.5: GPHOX immunosensor peak current before and after sP-selectin protein immobilization: Full scale test 1.

The unmodified CNF sensors had a slightly better reproducibility which was also evident in the baseline peak currents after antibody attachment and BSA blocking. The baseline immunosensor peak currents ranged between 9-13.75 μA for full scale test 2, and 10-18 μA for full scale test 3. These ranges were slightly lower than the GPHOX sensors, but still required each immunosensor to be compared against its own baseline.

The immunosensor used in full scale test 2 could not be analyzed in terms of sensitivity and linearity, because there was no linear working range present over the concentration range that was tested. The detection measurements, however, showed different responses for the sP-selectin and non-specific CRP. On average, the sP-selectin concentrations had

a decrease in peak current of about 8%, whereas the CRP only showed a decrease of about 2%. The isoelectric point of the sP-selectin protein is 5.83 which means that it was negatively charged in the redox solution with a pH of 7.4. An extra negatively charged layer at the surface of the working electrode could lead to the repulsion of the negatively charged FeCN molecules, and thus a lower charge transfer efficiency [69]. Therefore, the results confirmed the expectation of a smaller peak current after the sP-selectin proteins were immobilized. But the fact that the sensor could not discern between different concentrations, is troublesome. If binding took place, and the protein charge phenomenon is the reason for the decrease in current, it should have led to a much larger decrease in current for the higher sP-selectin protein concentrations. Since this was not observed, it is difficult to say with confidence whether the sensor could detect the sP-selectin protein at all. More conclusive results and other possible solutions for verifying the binding would be needed. This is discussed in Section 6.3.

The measurements of full scale test 3 had no linear working range or selectivity towards sP-selectin proteins. It is possible that the proteins did not even bind to the antibody in the pH solution of 5.5. The binding reaction between the antibody and protein is most optimal over a narrow pH range of 6.5 and 8.4. Anything outside of that range could lead to the unfolding of the protein or antibody, which inhibits the binding reaction [156]. The pH was changed so that the protein would be positively charged, but at that stage of the experiments the importance of working at a physiological pH was not recognized. Therefore, the results for test 3 were inconclusive.

The fourth full scale test was performed with the positive redox probe, RuHex. This was used to test the immunosensor response to an oppositely charged redox probe which, in theory, should be attracted to the negatively charged sP-selectin proteins. More proteins would thus increase the charge transfer efficiency leading to an increase in the peak current. Although there was an increase in the peak current for higher concentrations, it was still very small and the error bars of different categories overlapped. The non-specific CRP also had the same change in peak current as the same concentration of sP-selectin, which meant that the immunosensor was not selective towards sP-selectin. There was no linear response over the concentrations that were used, and thus the immunosensor was unsuccessful in detecting sP-selectin.

5.4.2 Measurements performed with the developed potentiostat

The immunosensor response for the fifth full scale test was highly erratic and unusual. Some curves had redox peaks outside of the normal range of 0 to 0.2 V, and some even had two peaks in the scanned range. This behaviour was not noticed for any other CNF sensor that was used in this work. Fig. 5.6 shows example curves of the CNF sensors tested in FeCN at different stages of the development process. These curves were collected during the reproducibility studies, the electrografting procedure, and full scale tests 2, 3, and 5. All sensors, except the two examples from full scale test 5, had peak locations in the potential range of 0 to 0.2 V.

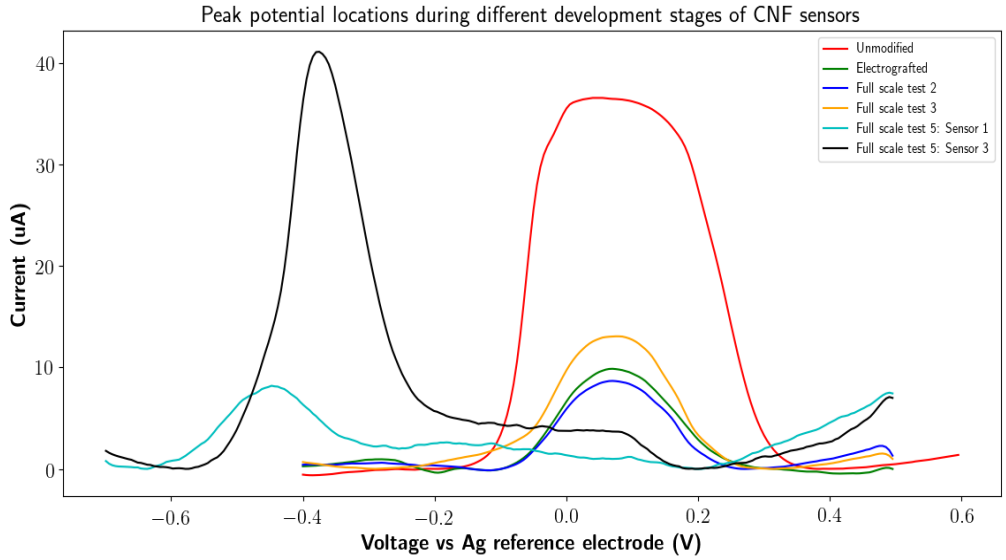

Figure 5.6: Redox peak location of various CNF sensors that were used in the development process.

Initially, it was thought that developed potentiostat failed during the experiments, but a SWV scan of an unmodified CNF sensor that was at hand showed that it was still functional. It is unclear what the exact cause of the erratic data was, but there could have been a few possibilities. One possibility could be due to the contamination of the working or reference electrodes. Especially the contamination of the reference electrode could lead to an unstable cell potential and therefore a shift in peak redox potentials [157]. In an unfortunate event, the -20°C fridge also defrosted overnight before the crosslinking chemistry procedure. Some of the products, such as the proteins, antibodies, and EDC were stored in the fridge and it could have had an effect on the activity of the solutions and chemicals. Unfortunately, there was no way of knowing whether the antibody modification procedure would work, but the electrografting was already started and the crosslinking had to be completed. Since the appropriate wetting and washing procedures were followed in the same way as the previous four full scale tests, the erratic behaviour was most probably due to the chemicals and proteins that defrosted. The final tests could not be processed by the data analysis algorithm, leading to inconclusive results.

5.5 Project objectives

The project had two main goals, namely:

1. To develop an electrochemical biosensor, based on commercial screen printed electrodes, that can detect soluble P-selectin proteins in a physiological solution;

2. To develop a portable potentiostat device that can be used to perform electrochemical measurements on the soluble P-selectin biosensor.

The first objective was not completed in such a way that the biosensor can be used to differentiate the physiologically relevant concentrations of sP-selectin proteins in a sample. Three different approaches were tried in this work, but not one succeeded in providing the performance needed to say with confidence that the methodology works well enough

to realize an sP-selectin biosensor. The three approaches were: 1) to use two different materials (GPHOX and CNF) for the sensors, 2) to change the pH of the electrochemical solution, and 3) to try two different redox probes. The first approach narrowed the choice of sensors down to the CNFs, and the last two approaches tested the working principle of the biosensor, which is the repulsion/attraction of the redox molecule due to the charged protein on the surface of the working electrode. The second approach was deemed invalid because the tests were performed in a physiologically irrelevant environment, and the third approach showed that the FeCN redox probe worked the best.

In this work, the CNF sensors and FeCN couple used in full scale test 2 provided the best result towards completing the first objective. Even though there was no linear detection range, the immunosensor had a different response for sP-selectin proteins compared to the non-specific CRP. The decrease in peak current after immobilization was in agreement with what was predicted by the working principle (i.e. the repulsion between the negatively charge protein and the negatively charged FeCN redox couple). But further experiments need to be conducted to confirm the phenomenon, and improve the sensor response.

The second objective was partly met by designing a portable potentiostat, and verifying the operation of the device by using the Gamry instrument as a benchmark. It was proved that the home-built device was more portable than the Gamry system, and it could perform electrochemical measurements on the commercial screen printed sensors. The benchmark tests showed that the developed potentiostat has performance that was comparable to the Gamry device for this specific application.

Chapter 6

Conclusions

This chapter contains a summary of the work done in this thesis. The limitations of the work are discussed followed by the recommendations for any work that builds on this thesis. Lastly, a few final conclusions are made.

6.1 Thesis summary

The goals of the project was to develop a biosensor that would be able to detect human soluble P-selectin protein in a physiological buffer, and to build the electronics that are needed to perform the measurements. This could aid in the diagnostics of platelet function and activation, as well as monitoring chronic inflammation.

The literature study was used to determine the biochemical techniques that would be needed to develop such a sensor, and also to determine what electronics would be needed to build a device that can perform the diagnostic measurements.

A carbon nanofiber and graphene oxide commercial screen printed electrode was acquired to develop the biosensor, and to establish a working proof of concept. The surface of the sensor was modified using various electrochemistry and biochemistry techniques. Firstly, it was modified with carboxyl support groups using electrochemical reduction of diazonium salt. Thereafter, human soluble P-selectin antibodies were attached to the surface using carbodiimide crosslinking chemistry. An electrochemical diagnostic technique, called square wave voltammetry, was then applied to the sensor before and after recombinant human soluble P-selectin proteins were immobilized.

To establish this proof of concept, an industrial grade Gamry potentiostat device was first used to measure the immunosensor response. Three different approaches were tried over a range of five different full scale tests. The different approaches included comparing the two sensor materials, changing the pH of the electrochemical measurement solution, and finally to test the immunosensor response with two different redox probes.

In this work, none of the five approaches succeeded in developing a biosensor that can detect soluble P-selectin. One sensor, however, had a different electrochemical response to the presence of P-selectin compared to non-specific c-reactive protein. The immunosensor was a carbon nanofiber screen printed electrode, that used the ferricyanide/ferrocyanide redox couple to perform the measurements in a label-free manner. The sensor did not

have a linear detection range, but it showed a decrease in peak current of around 8% compared to the c-reactive protein of 2%. More experiments and validation tests need to be conducted on this sensor to confidently say whether the difference was indeed due to the binding of P-selectin.

In parallel, a potentiostat device was developed so that the immunosensor could ultimately be characterized without the need of a benchtop potentiostat device. This aids in the portability of the biosensor device as a whole. The performance of the home-built potentiostat was verified by using the Gamry device as a benchmark, and the results showed that it performed well. Unfortunately, the final measurements of the immunosensor on the home-built device could not provide usable results, which was most probably due to the unknown behaviour of the defrosted chemicals and biomolecules.

6.2 Limitations of results

Even though the developed potentiostat is battery powered, it still requires a host PC to collect the scan results. The application is thus confined to any space that has a PC with Python version 3 installed. Since the device was designed to be application specific, it could only perform electrochemical measurements in the range of ± 1.65 V, and measure currents in the range of ± 242 μA in the resolution of 121.8 nA.

The sP-selectin biosensor could not detect the presence of any antigens conclusively enough to prove that the biosensor works. The sensor is not yet robust enough to be able to detect the protein in a complex mixture such as blood or even a diluted blood plasma sample.

6.3 Future recommendations

It is recommended that the basic electrochemical parameters are studied for a particular setup before any modification processes are conducted. This includes electrochemical potential window, electron transfer rates, and redox potentials. This is to make sure that the supporting electrolyte, solvent, and working electrode material are compatible and that the electrochemical energy is reserved for the redox probe in the window. This would aid in debugging strange redox behaviour downstream of the modification process.

The immunosensors are developed in a stepwise manner and, therefore, it could be helpful to confirm that each step was successful before moving on to the next modification. The type of confirmation step would depend on the modification that was performed, but common techniques such as confocal microscopy, scanning electron microscopy, Fourier transform infrared spectroscopy (FT-IR), or other forms of surface topology or composition studies would be beneficial. In this project, only voltammetric techniques and confocal microscopy was used to verify the surface modification. Square wave voltammetry was used to verify the presence of the carboxyl groups, and the confocal was used to verify the presence of the sP-selectin antibodies on the surface of the working electrode. During the project, three different FT-IR measurements were taken with three different machines to verify the presence of the carboxyl groups after the grafting procedure. All three measurements were inconclusive, which was possibly due to the small number

of carboxyl groups relative to the underlying carbon material of the working electrode. The carbon base material of the working electrode provides a very strong signal that can overshadow the signal from other oxygen containing groups, leading to inconclusive results. The confocal microscopy, however, showed that the sP-selectin antibodies are present on the working electrode which verifies both the electrografting procedure, and the EDC/NHS crosslinking chemistry. Even though this was a positive result, it is recommended that each step is verified extensively instead of only using the last verification result to confirm that all the previous modifications were successful. This would allow easier backtracking if the verification results are negative.

It is also recommended that a fluorescent sP-selectin protein is acquired to confirm that the protein binds to the antibody on the surface of the working electrode. Only an sP-selectin protein with an rho-1D4 tag was available for this specific protein during the project. The label was not verified for fluorescent microscopy imaging and, therefore, it was considered a risk to purchase the product. To make sure that the sP-selectin protein concentrations are diluted correctly, different sensors can be studied under the confocal microscope with different concentrations of a fluorescent protein. The supposedly positive results of full scale test two need to be repeated with fresh chemicals and proteins to verify the observed phenomenon. It would also be helpful if a few sensors from this same batch are studied under confocal microscopy to confirm the binding of sP-selectin proteins outside of the electrochemical measurement system. This would require either a fluorescent protein, or a secondary fluorescent antibody that can bind to the opposite side of the antigen.

One of the most time consuming steps of the data analysis was to export the data from the *.gdata* files into *.csv* files. This process can be sped up if a script is written that would automatically do this. This would most probably require the use of Gamry EchemAnalyst application programming interface functions that can open and parse the data files. The script can also be made more universal by removing hard-coded variables used in the data analysis algorithm and allowing the user to choose these values for different setups.

If needed, the hardware can be improved by using higher resolution external ADCs and DACs. Noise and circuit non-idealities can be improved by using operational amplifiers with even lower spectral noise values and lower offset voltages. The filter stage can also be designed with a lower cutoff frequency since the first 20 square wave harmonics would be enough to replicate the square wave at the ADC input. This could reduce the noise in measurements even more. To make the application more portable, a wireless module that can communicate with a smartphone device can be fitted onto the device.

6.4 Final conclusions

Even though this project was not successful in developing a sensor with a linear detection range and a low limit of detection, one sensor proved to show different characteristics when tested with a non-specific protein compared to the soluble P-selectin antigen. With the required materials and the necessary characterization methods, this sensor could be optimized to function as a label-free diagnostic tool for soluble P-selectin.

The potentiostat device that was developed in this work showed excellent performance

that is comparable to a conventional instrument. This was achieved with a few low-cost components, and an inexpensive microcontroller. If the immunosensor is perfected in future work, the home-built device can successfully be used to perform the electrochemical measurements at the point-of-need level.

Appendix A

Product datasheets

A.1 Human sP-selectin antibody

R&D SYSTEMS
a bio-techne brand

Human P-Selectin/CD62P Antibody

Monoclonal Mouse IgG_1 Clone # 9E1
Catalog Number: BBA30

DESCRIPTION

Species Reactivity	Human
Specificity	This antibody binds to CHO cells transfected with human P-Selectin but not to CHO cells transfected with either human E-Selectin or human L-Selectin.
Source	Monoclonal Mouse IgG_1 Clone # 9E1
Purification	Protein A or G purified from hybridoma culture supernatant
Immunogen	Recombinant human P-Selectin Extracellular domain
Endotoxin Level	<0.10 EU per 1 µg of the antibody by the LAL method.
Formulation	Lyophilized from a 0.2 µm filtered solution in PBS with Trehalose. See Certificate of Analysis for details.

APPLICATIONS

Please Note: *Optimal dilutions should be determined by each laboratory for each application. General Protocols are available in the Technical Information section on our website.*

	Recommended Concentration	Sample
Immunohistochemistry	8-25 µg/mL	See Below
Adhesion Blockade	The adhesion of U937 human histiocytic lymphoma cells (5 x 10^4 cells/well) to immobilized Recombinant Human P-Selectin/CD62P (Catalog # ADP3, 10 µg/mL, 100 µL/well) was maximally inhibited (80-100%) by 1 µg/mL of the antibody.	

DATA

Immunohistochemistry

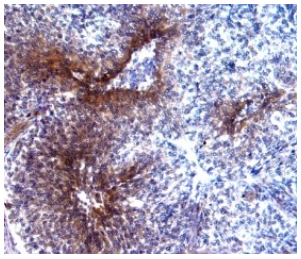

P-Selectin/CD62P in Human Breast Cancer Tissue. P-Selectin/CD62P was detected in immersion fixed paraffin-embedded sections of human breast cancer tissue using 25 µg/mL Human P-Selectin/CD62P Monoclonal Antibody (Catalog # BBA30) overnight at 4 °C. Tissue was stained with the Anti-Mouse HRP-DAB Cell & Tissue Staining Kit (brown; Catalog # CTS002) and counterstained with hematoxylin (blue). View our protocol for Chromogenic IHC Staining of Paraffin-embedded Tissue Sections.

PREPARATION AND STORAGE

Reconstitution	Sterile PBS to a final concentration of 0.5 mg/mL.
Shipping	The product is shipped at ambient temperature. Upon receipt, store it immediately at the temperature recommended below.
Stability & Storage	**Use a manual defrost freezer and avoid repeated freeze-thaw cycles.** ● 12 months from date of receipt, -20 to -70 °C as supplied. ● 1 month, 2 to 8 °C under sterile conditions after reconstitution. ● 6 months, -20 to -70 °C under sterile conditions after reconstitution.

BACKGROUND

P-Selectin, also known as GMP-140 and PADGEM, is a transmembrane glycoprotein expressed by activated platelets and endothelial cells. P-Selectin binds to PSGL-1 on myeloid cells, neutrophils, monocytes, and lymphocytes. P-Selectin plays a role in the adhesion of leukocytes and neutrophils to the endothelium.

bio-techne®
Global bio-techne.com info@bio-techne.com techsupport@bio-techne.com TEL +1 612 379 2956
USA TEL 800 343 7475 Canada TEL 855 668 8722 China TEL +86 (21) 52380373
Europe | Middle East | Africa TEL +44 (0)1235 529449

A.2 Recombinant sP-selectin protein

R&D SYSTEMS
a bio-techne brand

Recombinant Human P-Selectin/CD62P

Catalog Number: ADP3

DESCRIPTION	
Source	Chinese Hamster Ovary cell line, CHO-derived Trp42-Ala771 Accession # P16109
N-terminal Sequence Analysis	Trp42
Predicted Molecular Mass	80 kDa

SPECIFICATIONS	
SDS-PAGE	121-124 kDa, reducing conditions
Activity	Measured by the ability of the immobilized protein to support the adhesion of U937 human histiocytic lymphoma cells. When 5 x 10^4 cells/well are added to human sP-Selectin coated plates (10 µg/mL with 100 µL/well), >50% will adhere after 1 hour incubation at room temperature.
Endotoxin Level	<0.10 EU per 1 µg of the protein by the LAL method.
Purity	>97%, by SDS-PAGE visualized with Silver Staining and quantitative densitometry by Coomassie® Blue Staining.
Formulation	Lyophilized from a 0.2 µm filtered solution in PBS containing Calcium and Magnesium with Sorbitol. See Certificate of Analysis for details.

PREPARATION AND STORAGE	
Reconstitution	Reconstitute at 1 mg/mL in sterile, deionized water.
Shipping	The product is shipped at ambient temperature. Upon receipt, store it immediately at the temperature recommended below.
Stability & Storage	**Use a manual defrost freezer and avoid repeated freeze-thaw cycles.** ● 12 months from date of receipt, -20 to -70 °C as supplied. ● 1 month, 2 to 8 °C under sterile conditions after reconstitution. ● 3 months, -20 to -70 °C under sterile conditions after reconstitution.

BACKGROUND

Human P-Selectin (GMP-140, LECAM-3, PADGEM, CD62P), a member of the Selectin family, is a cell surface glycoprotein expressed by activated platelets and endothelial cells. P-Selectin is translocated to the cell surface within minutes, from alpha granules of platelets or Weibel-Palade bodies of endothelial cells, following stimulation with thrombin, histamine, PMA or peroxides. P-Selectin binds to a 106 kDa protein present on myeloid cells, neutrophils, monocytes and lymphocytes, termed PSGL-1 (P-Selectin glycoprotein ligand-1).

P-Selectin plays a role in the adhesion of leukocytes and neutrophils to the endothelium. Acting in cooperation with L Selectin,P-Selectin mediates the initial interaction of circulating leukocytes with endothelial cells that produces a characteristic 'rolling' of the leukocytes on the endothelium. This initial interaction is followed by a stronger interaction involving E-Selectin, and later ICAM-1 and VCAM-1, that leads eventually to extravasation of the white blood cell through the blood vessel wall into the extracellular matrix tissue.

ELISA techniques have shown that detectable levels of soluble P-Selectin are present in the biological fluids of apparently normal individuals. Furthermore, a number of studies have reported that levels of P-Selectin may be elevated or lowered in subjects with a variety of pathological conditions.

bio-techne®
Global bio-techne.com info@bio-techne.com techsupport@bio-techne.com TEL +1 612 379 2956
USA TEL 800 343 7475 Canada TEL 855 668 8722 China TEL +86 (21) 52380373
Europe | Middle East | Africa TEL +44 (0)1235 529449

A.3 Secondary fluorescent antibody

abcam

Product datasheet

Goat Anti-Mouse IgG H&L (Alexa Fluor® 488) ab150113

★★★★★ 2 Abreviews 17 References 4 Images

Overview

Product name	Goat Anti-Mouse IgG H&L (Alexa Fluor® 488)
Description	Goat polyclonal Secondary Antibody to Mouse IgG - H&L (Alexa Fluor® 488)
Target species	Mouse
Tested applications	**Suitable for:** IHC-Fr, ICC/IF, ELISA, Flow Cyt, IHC-P
Conjugation	Alexa Fluor® 488. Ex: 495nm, Em: 519nm

Properties

Form	Liquid
Storage instructions	Shipped at 4°C. Store at +4°C short term (1-2 weeks). Upon delivery aliquot. Store at -20°C. Avoid freeze / thaw cycle. Store In the Dark.
Storage buffer	Preservative: 0.02% Sodium azide Constituents: PBS, 30% Glycerol, 1% BSA
Purity	Immunogen affinity purified
Purification notes	This antibody was isolated by affinity chromatography using antigen coupled to agarose beads.
Clonality	Polyclonal
Isotype	IgG
General notes	Alexa Fluor® is a registered trademark of Molecular Probes, Inc, a Thermo Fisher Scientific Company. The Alexa Fluor® dye included in this product is provided under an intellectual property license from Life Technologies Corporation. As this product contains the Alexa Fluor® dye, the purchase of this product conveys to the buyer the non-transferable right to use the purchased product and components of the product only in research conducted by the buyer (whether the buyer is an academic or for-profit entity). As this product contains the Alexa Fluor® dye the sale of this product is expressly conditioned on the buyer not using the product or its components, or any materials made using the product or its components, in any activity to generate revenue, which may include, but is not limited to use of the product or its components: in manufacturing; (ii) to provide a service, information, or data in return for payment (iii) for therapeutic, diagnostic or prophylactic purposes; or (iv) for resale, regardless of whether they are sold for use in research. For information on purchasing a license to use products containing Alexa Fluor® dyes for purposes other than research, contact Life Technologies Corporation, 5791 Van Allen Way, Carlsbad, CA 92008 USA or outlicensing@lifetech.com.

Applications

A.4 STM32F446ZE chip

life.augmented

STM32F446xC/E

ARM® Cortex®-M4 32b MCU+FPU, 225DMIPS, up to 512kB Flash/128+4KB RAM, USB OTG HS/FS, 17 TIMs, 3 ADCs, 20 comm. interfaces

Datasheet - production data

Features

- Core: ARM® 32-bit Cortex®-M4 CPU with FPU, Adaptive real-time accelerator (ART Accelerator™) allowing 0-wait state execution from Fl ash memory, frequency up to 180 MHz, MPU, 225 DMIPS/1.25 DMIPS/MHz (Dhrystone 2.1), and DSP instructions
- Memories
  - 512 kB of Flash memory
  - 128 KB of SRAM
  - Flexible external memory controller with up to 16-bit data bus: SRAM,PSRAM,SDRAM/LPSDR SDRAM, Flash NOR/NAND memories
  - Dual mode Quad SPI interface
- LCD parallel interface, 8080/6800 modes
- Clock, reset and supply management
  - 1.7 V to 3.6 V application supply and I/Os
  - POR, PDR, PVD and BOR
  - 4-to-26 MHz crystal oscillator
  - Internal 16 MHz factory-trimmed RC (1% accuracy)
  - 32 kHz oscillator for RTC with calibration
  - Internal 32 kHz RC with calibration
- Low power
  - Sleep, Stop and Standby modes
  - V_{BAT} supply for RTC, 20×32 bit backup registers + optional 4 KB backup SRAM
- 3×12-bit, 2.4 MSPS ADC: up to 24 channels and 7.2 MSPS in triple interleaved mode
- 2×12-bit D/A converters
- General-purpose DMA: 16-stream DMA controller with FIFOs and burst support
- Up to 17 timers: 2x watchdog, 1x SysTick timer and up to twelve 16-bit and two 32-bit timers up to 180 MHz, each with up to 4 IC/OC/PWM or pulse counter
- Debug mode
  - SWD & JTAG interfaces
  - Cortex®-M4 Trace Macrocell™

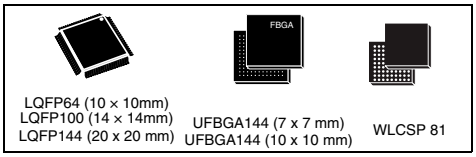

LQFP64 (10 × 10mm)
LQFP100 (14 × 14mm)
LQFP144 (20 x 20 mm)

UFBGA144 (7 x 7 mm)
UFBGA144 (10 x 10 mm)

WLCSP 81

- Up to 114 I/O ports with interrupt capability
  - Up to 111 fast I/Os up to 90 MHz
  - Up to 112 5 V-tolerant I/Os
- Up to 20 communication interfaces
  - SPDIF-Rx
  - Up to 4 × I^2C interfaces (SMBus/PMBus)
  - Up to 4 USARTs/2 UARTs (11.25 Mbit/s, ISO7816 interface, LIN, IrDA, modem control)
  - Up to 4 SPIs (45 Mbits/s), 3 with muxed I^2S for audio class accuracy via internal audio PLL or external clock
  - 2 x SAI (serial audio interface)
  - 2 × CAN (2.0B Active)
  - SDIO interface
  - Consumer electronics control (CEC) I/F
- Advanced connectivity
  - USB 2.0 full-speed device/host/OTG controller with on-chip PHY
  - USB 2.0 high-speed/full-speed device/host/OTG controller with dedicated DMA, on-chip full-speed PHY and ULPI
  - Dedicated USB power rail enabling on-chip PHYs operation throughout the entire MCU power supply range
- 8- to 14-bit parallel camera interface up to 54 Mbytes/s
- CRC calculation unit
- RTC: subsecond accuracy, hardware calendar
- 96-bit unique ID

Table 1. Device summary

Reference	Part number
STM32F446xC/E	STM32F446MC, STM32F446ME, STM32F446RC, STM32F446RE, STM32F446VC, STM32F446VE, STM32F446ZC, STM32F446ZE.

A.5 TLC2264 operational amplifier

TLC226x, TLC226xA
Advanced LinCMOS™ RAIL-TO-RAIL
OPERATIONAL AMPLIFIERS

SLOS177D – FEBRUARY 1997 – REVISED MARCH 2001

- **Output Swing includes Both Supply Rails**
- **Low Noise . . . 12 nV/√Hz Typ at f = 1 kHz**
- **Low Input Bias Current . . . 1 pA Typ**
- **Fully Specified for Both Single-Supply and Split-Supply Operation**
- **Low Power . . . 500 μA Max**
- **Common-Mode Input Voltage Range Includes Negative Rail**
- **Low Input Offset Voltage**
  950 μV Max at T_A = 25°C (TLC2262A)
- **Macromodel Included**
- **Performance Upgrade for the TS27M2/M4 and TLC27M2/M4**
- **Available in Q-Temp Automotive**
  HighRel Automotive Applications
  Configuration Control/Print Support
  Qualification to Automotive Standards

description

The TLC2262 and TLC2264 are dual and quadruple operational amplifiers from Texas Instruments. Both devices exhibit rail-to-rail output performance for increased dynamic range in single- or split-supply applications. The TLC226x family offers a compromise between the micropower TLC225x and the ac performance of the TLC227x. It has low supply current for battery-powered applications, while still having adequate ac performance for applications that demand it. The noise performance has been dramatically improved over previous generations of CMOS amplifiers. Figure 1 depicts the low level of noise voltage for this CMOS amplifier, which has only 200 μA (typ) of supply current per amplifier.

EQUIVALENT INPUT NOISE VOLTAGE
vs
FREQUENCY

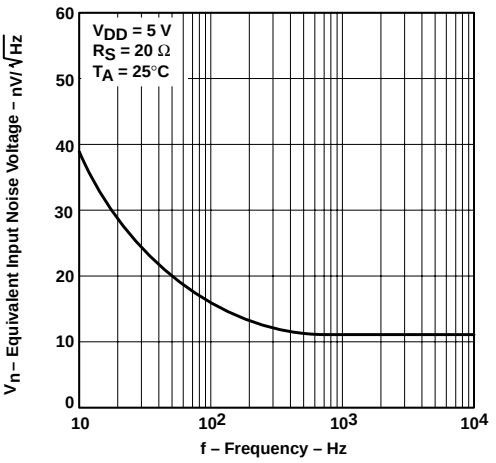

Figure 1

The TLC226x, exhibiting high input impedance and low noise, are excellent for small-signal conditioning for high-impedance sources, such as piezoelectric transducers. Because of the micropower dissipation levels, these devices work well in hand-held monitoring and remote-sensing applications. In addition, the rail-to-rail output feature with single or split supplies makes this family a great choice when interfacing with analog-to-digital converters (ADCs). For precision applications, the TLC226xA family is available and has a maximum input offset voltage of 950 μV. This family is fully characterized at 5 V and ±5 V.

The TLC2262/4 also makes great upgrades to the TLC27M2/L4 or TS27M2/L4 in standard designs. They offer increased output dynamic range, lower noise voltage and lower input offset voltage. This enhanced feature set allows them to be used in a wider range of applications. For applications that require higher output drive and wider input voltage range, see the TLV2432 and TLV2442. If your design requires single amplifiers, please see the TLV2211/21/31 family. These devices are single rail-to-rail operational amplifiers in the SOT-23 package. Their small size and low power consumption, make them ideal for high density, battery-powered equipment.

TEXAS INSTRUMENTS
POST OFFICE BOX 655303 • DALLAS, TEXAS 75265

TLC2262I operating characteristics at specified free-air temperature, $V_{DD\pm}$ = ±5 V

PARAMETER		TEST CONDITIONS		T_A†	TLC2262I			TLC2262AI			UNIT
					MIN	TYP	MAX	MIN	TYP	MAX	
I_{DD}	Supply Current	V_O = 2.5 V,	No load	25°C		425	500		425	500	
				Full range			500			500	
SR	Slew rate at unity gain	V_O = ±1.9 V, C_L = 100 pF	R_L = 50 kΩ,	25°C	0.35	0.55		0.35	0.55		V/μs
				Full range	0.25			0.25			
V_n	Equivalent input noise voltage	f = 10 Hz		25°C		43			43		nV/√Hz
		f = 1 kHz		25°C		12			12		
$V_{N(PP)}$	Peak-to-peak equivalent input noise voltage	f = 0.1 Hz to 1 Hz		25°C		0.8			0.8		μV
		f = 0.1 Hz to 10 Hz		25°C		1.3			1.3		
I_n	Equivalent input noise current			25°C		0.6			0.6		fA√Hz
THD + N	Total harmonic distortion plus noise	V_O = ±2.3 V, R_L = 50 kΩ, f = 20 kHz	A_V = 1	25°C		0.014%			0.014%		
			A_V = 10			0.024%			0.024%		
	Gain-bandwidth product	f =10 kHz, C_L = 100 pF	R_L = 50 kΩ,	25°C		0.73			0.73		MHz
B_{OM}	Maximum output-swing bandwidth	$V_{O(PP)}$ = 4.6 V, R_L = 50 kΩ,	A_V = 1, C_L = 100 pF	25°C		85			85		kHz
t_s	Settling time	A_V = −1, Step = −2.3 V to 2.3 V, R_L = 50 kΩ, C_L = 100 pF	To 0.1%	25°C		7.1			7.1		μs
			To 0.01%			16.5			16.5		
ϕ_m	Phase margin at unity gain	R_L = 50 kΩ,	C_L = 100 pF	25°C		57°			57°		
	Gain margin			25°C		11			11		dB

† Full range is −40°C to 125°C.

TLC2264I operating characteristics at specified free-air temperature, V_{DD} = 5 V

PARAMETER		TEST CONDITIONS		T_A†	TLC2264I			TLC2264AI			UNIT
					MIN	TYP	MAX	MIN	TYP	MAX	
I_{DD}	Supply current (four amplifiers)	V_O = 2.5 V,	No load	25°C		0.8	1		0.8	1	V/µs
				Full range			1			1	
SR	Slew rate at unity gain	V_O = 1.4 V to 2.6 V, C_L = 100 pF‡	R_L = 50 kΩ‡,	25°C	0.35	0.55		0.35	0.55		V/µs
				Full range	0.25			0.25			
V_n	Equivalent input noise voltage	f = 10 Hz		25°C		40			40		nV/√Hz
		f = 1 kHz		25°C		12			12		
$V_{N(PP)}$	Peak-to-peak equivalent input noise voltage	f = 0.1 Hz to 1 Hz		25°C		0.7			0.7		µV
		f = 0.1 Hz to 10 Hz		25°C		1.3			1.3		
I_n	Equivalent input noise current			25°C		0.6			0.6		fA/√Hz
THD + N	Total harmonic distortion plus noise	V_O = 0.5 V to 2.5 V, f = 20 kHz, R_L = 50 kΩ‡	A_V = 1	25°C		0.017%			0.017%		
			A_V = 10			0.03%			0.03%		
	Gain-bandwidth product	f = 50 kHz, C_L = 100 pF‡	R_L = 50 kΩ‡,	25°C		0.71			0.71		MHz
B_{OM}	Maximum output-swing bandwidth	$V_{O(PP)}$ = 2 V, R_L = 50 kΩ‡,	A_V = 1, C_L = 100 pF‡	25°C		185			185		kHz
t_s	Settling time	A_V = –1, Step = 0.5 V to 2.5 V, R_L = 50 kΩ‡, C_L = 100 pF‡	To 0.1%	25°C		6.4			6.4		µs
			To 0.01%			14.1			14.1		
ϕ_m	Phase margin at unity gain	R_L = 50 kΩ‡,	C_L = 100 pF‡	25°C		56°			56°		
	Gain margin			25°C		11			11		dB

† Full range is – 40°C to 125°C.
‡ Referenced to 2.5 V

A.6 Ultra-low on-resistance SPDT analog switch

NLAS4684

Ultra-Low Resistance Dual SPDT Analog Switch

The NLAS4684 is an advanced CMOS analog switch fabricated in Sub−micron silicon gate CMOS technology. The device is a dual Independent Single Pole Double Throw (SPDT) switch featuring Ultra−Low R_{ON} of 0.5 Ω, for the Normally Closed (NC) switch, and 0.8 Ω for the Normally Opened switch (NO) at 2.7 V.

The part also features guaranteed Break Before Make switching, assuring the switches never short the driver.

The NLAS4684 is available in a 2.0 x 1.5 mm bumped die array. The pitch of the solder bumps is 0.5 mm for easy handling.

Features

- Ultra−Low R_{ON}, $<$0.5 Ω at 2.7 V
- Threshold Adjusted to Function with 1.8 V Control at V_{CC} = 2.7−3.3 V
- Single Supply Operation from 1.8−5.5 V
- Tiny 2 x 1.5 mm Bumped Die
- Low Crosstalk, $<$ 83 dB at 100 kHz
- Full 0−V_{CC} Signal Handling Capability
- High Isolation, −65 dB at 100 kHz
- Low Standby Current, $<$50 nA
- Low Distortion, $<$0.14% THD
- R_{ON} Flatness of 0.15 Ω
- Pin for Pin Replacement for MAX4684
- High Continuous Current Capability
  ± 300 mA Through Each Switch
- Large Current Clamping Diodes at Analog Inputs
  ± 300 mA Continuous Current Capability
- Pb−Free Packages are Available

Applications

- Cell Phone
- Speaker Switching
- Power Switching
- Modems
- Automotive

ON Semiconductor®

http://onsemi.com

MARKING DIAGRAMS

A1

Microbump−10
CASE 489AA

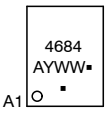

1

DFN10
CASE 485C

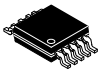

Micro10
CASE 846B

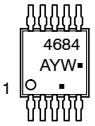

A	= Assembly Location
L	= Wafer Lot
Y	= Year
WW, W	= Work Week
▪	= Pb−Free Package

(Note: Microdot may be in either location)

FUNCTION TABLE

IN 1, 2	NO 1, 2	NC 1, 2
0	OFF	ON
1	ON	OFF

ORDERING INFORMATION

See detailed ordering and shipping information in the package dimensions section on page 11 of this data sheet.

NLAS4684

MAXIMUM RATINGS

Symbol	Parameter	Value	Unit
V_{CC}	Positive DC Supply Voltage	−0.5 to +7.0	V
V_{IS}	Analog Input Voltage (V_{NO}, V_{NC}, or V_{COM})	$-0.5 \le V_{IS} \le V_{CC} + 0.5$	V
V_{IN}	Digital Select Input Voltage	$-0.5 \le V_I \le +7.0$	V
I_{anl1}	Continuous DC Current from COM to NC/NO	±300	mA
$I_{anl-pk\ 1}$	Peak Current from COM to NC/NO, 10 duty cycle (Note 1)	±500	mA
I_{clmp}	Continuous DC Current into COM/NO/NC	±300	mA
$I_{clmp\ 1}$	Peak Current into Input Clamp Diodes at COM/NC/NO	±500	mA

Stresses exceeding Maximum Ratings may damage the device. Maximum Ratings are stress ratings only. Functional operation above the Recommended Operating Conditions is not implied. Extended exposure to stresses above the Recommended Operating Conditions may affect device reliability.
1. Defined as 10% ON, 90% off duty cycle.

RECOMMENDED OPERATING CONDITIONS

Symbol	Parameter		Min	Max	Unit
V_{CC}	DC Supply Voltage		1.8	5.5	V
V_{IN}	Digital Select Input Voltage		GND	5.5	V
V_{IS}	Analog Input Voltage (NC, NO, COM)		GND	V_{CC}	V
T_A	Operating Temperature Range		−55	+125	°C
t_r, t_f	Input Rise or Fall Time, SELECT	V_{CC} = 3.3 V ± 0.3 V V_{CC} = 5.0 V ± 0.5 V	0 0	100 20	ns/V
ESD	Human Body Model − All Pins			5	kV

DC CHARACTERISTICS − Digital Section (Voltages Referenced to GND)

Symbol	Parameter	Condition		Guaranteed Limit			Unit
			V_{CC} ±10%	−55°C to 25°C	<85°C	<125°C	
V_{IH}	Minimum High−Level Input Voltage, Select Inputs (Figure 9)		2.0 2.5 3.0 5.0	1.4 1.4 1.4 2.0	1.4 1.4 1.4 2.0	1.4 1.4 1.4 2.0	V
V_{IL}	Maximum Low−Level Input Voltage, Select Inputs (Figure 9)		2.0 2.5 3.0 5.0	0.5 0.5 0.5 0.8	0.5 0.5 0.5 0.8	0.5 0.5 0.5 0.8	V
I_{IN}	Maximum Input Leakage Current, Select Inputs	V_{IN} = 5.5 V or GND	5.5	± 1.0	± 1.0	± 1.0	μA
I_{OFF}	Power Off Leakage Current	V_{IN} = 5.5 V or GND	0	±10	±10	±10	μA
I_{CC}	Maximum Quiescent Supply Current (Note 2)	Select and V_{IS} = V_{CC} or GND	5.5	± 180	± 200	± 200	nA

2. Guaranteed by design.

DC ELECTRICAL CHARACTERISTICS – Analog Section

Symbol	Parameter	Condition	V_{CC} ±10%	Guaranteed Maximum Limit						Unit
				–55°C to 25°C		<85°C		<125°C		
				Min	Max	Min	Max	Min	Max	
R_{ON} (NC)	NC "ON" Resistance (Note 3)	$V_{IN} \le V_{IL}$ V_{IS} = GND to V_{CC} $I_{IN}I \le 100$ mA	2.5 3.0 5.0		0.6 0.5 0.4		0.7 0.5 0.4		0.8 0.5 0.5	Ω
R_{ON} (NO)	NO "ON" Resistance (Note 3)	$V_{IN} \ge V_{IH}$ V_{IS} = GND to V_{CC} $I_{IN}I \le 100$ mA	2.5 3.0 5.0		1.0 0.8 0.8		1.0 0.8 0.8		1.0 1.0 0.9	Ω
$R_{FLAT\ (NC)}$	NC_On–Resistance Flatness (Notes 3, 5)	I_{COM} = 100 mA V_{IS} = 0 to V_{CC}	2.5 3.0 5.0		0.15 0.15 0.15		0.15 0.15 0.15		0.15 0.15 0.15	Ω
$R_{FLAT\ (NO)}$	NO_On–Resistance Flatness (Notes 3, 5)	I_{COM} = 100 mA V_{IS} = 0 to V_{CC}	2.5 3.0 5.0		0.35 0.35 0.35		0.35 0.35 0.35		0.35 0.35 0.35	Ω
ΔR_{ON}	On–Resistance Match Between Channels (Notes 3 and 4)	V_{IS} = 1.3 V; I_{COM} = 100 mA V_{IS} = 1.5 V; I_{COM} = 100 mA V_{IS} = 2.8 V; I_{COM} = 100 mA	2.5 3.0 5.0		0.18 0.06 0.06		0.18 0.06 0.06		0.18 0.06 0.06	Ω
$I_{NC(OFF)}$ $I_{NO(OFF)}$	NC or NO Off Leakage Current (Figure 13) (Note 3)	$V_{IN} = V_{IL}$ or V_{IH} V_{NO} or V_{NC} = 1.0 V_{COM} = 4.5 V	5.5	–1	1	–10	10	–100	100	nA
$I_{COM(ON)}$	COM ON Leakage Current (Figure 13) (Note 3)	$V_{IN} = V_{IL}$ or V_{IH} V_{NO} 1.0 V or 4.5 V with V_{NC} floating or V_{NC} 1.0 V or 4.5 V with V_{NO} floating V_{COM} = 1.0 V or 4.5 V	5.5	–2	2	–20	20	–200	200	nA

3. Guaranteed by design. Resistance measurements do not include test circuit or package resistance.
4. $\Delta R_{ON} = R_{ON(MAX)} - R_{ON(MIN)}$ between NC1 and NC2 or between NO1 and NO2.
5. Flatness is defined as the difference between the maximum and minimum value of on–resistance as measured over the specified analog signal ranges.

A.7 DropSens sensors

DROPSENS

Graphene Oxide modified Screen-Printed Electrodes

Refs. 110GPHOX X1110GPHOX

Graphene Oxide modified
Screen-Printed Electrode
Ref. 110GPHOX

Graphene Oxide modified
Dual Screen-Printed Electrode
Ref. X1110GPHOX

These disposable Screen-Printed Carbon Electrodes (SPCEs) modified with monolayer Graphene Oxide as a carbon based nanomaterial are designed for the development of (bio)sensors with an enhanced electrochemical active area.

Ceramic substrate: L33 X W10 X H0.5 mm
Electric contacts: Silver

The electrochemical cell consists on:
Working electrode(s): GPHOX / Carbon
Counter electrode: Carbon
Reference electrode: Silver

Graphene Oxide SPCEs are commercialized in 50 units packs. Store at room temperature in a dry place.

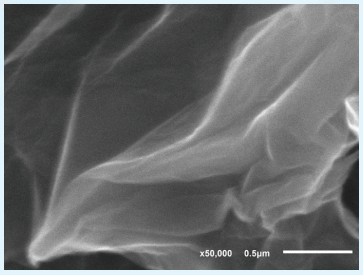

SEM image of the working electrode modified with monolayer Graphene Oxide

Also, specific connectors that act as an interface between the screen-printed electrode and any potentiostat (ref. DSC or CAC) and other accessories are available at ***DropSens***.

Related products


110GPH


DSC


CAST


FLWCL


SPELEC


STAT400

Full Catalogue

DS

Parque Tecnológico de Asturias - Edif. CEEI. 33428 LLanera (Asturias). Spain
(+34) 985 27 76 85 - info@dropsens.com - www.dropsens.com

Contact Form

DROPSENS

CSQ MED ISO 13485 CSQ ISO 9001:2008

Carbon Nanofibres modified Screen-Printed Carbon Electrodes

Refs. 110CNF
X1110CNF

Carbon Nanofibres modified Screen-Printed Carbon Electrode
Ref. 110CNF

Carbon Nanofibres modified Dual Screen-Printed Carbon Electrode
Ref. X1110CNF

These disposable **Screen-Printed Carbon Electrodes** (SPCEs) modified with **Graphitized Carbon Nanofibres (CNFs)** are designed for the development of (bio) sensors with an enhanced electrochemical active area.

Ceramic substrate: L33 x W10 x H0.5 mm
Electric contacts: Silver

The electrochemical cell consists on:
Working electrode(s): CNF / Carbon
Auxiliary electrode: Carbon
Reference electrode: Silver

CNFs SPCEs are commercialised in 50 units packs. Store at room temperature, protected from light in a dry place.

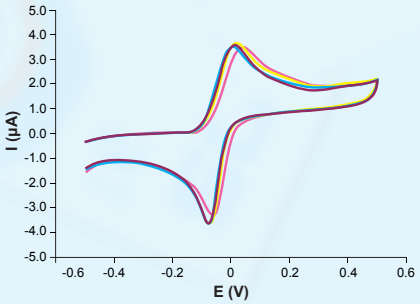

*Cyclic voltammograms of $1{\cdot}10^{-4}$ M **hydroquinone** in 0.1 M acetate buffer solution pH 5.0 at 50 mV/s. n = 5 (different CNFs SPCEs ref. DRP-110CNF) **RSD% = 4%***

Also, specific **connectors** that act as an interface between the screen-printed electrode and any potentiostat (ref. **DSC, CAC**) and other accessories are available at ***DropSens***.

Related products


110CNT


110GPH


DSC


CAC


FLWCL


STAT400

Full Catalogue

DS

Contact Form

Parque Tecnológico de Asturias - Edif. CEEI. 33428 LLanera (Asturias). Spain
(+34) 985 27 76 85 - info@dropsens.com - www.dropsens.com

A.8 Gamry Interface 1000E specifications

THE GAMRY DIFFERENCE

Gamry Instruments provides you with the complete solution to get the answers you need. We carefully consider every detail of system design. Everything from board layout, component selection, signal processing, and all the way down to the tip of our smart cell cables, is designed to deliver maximum performance. Our software is intuitive and easy to use yet powerful enough underneath to allow you to customize experiments and interfaces to suit your needs. This combination of features and capabilities give you the maximum amount of performance at incredible value.

SPECIFICATIONS

	Interface 1000T	Interface 1000B	Interface 1000A	Interface 1000E
Cell Connections	2, 3, 4			
Floating	Yes			
System				
Maximum Current	± 100 mA	±1 A		
Current Ranges	6 (1 uA - 100 mA)	9 (10 nA - 1 A)		
Current Ranges (with Gain)	8 (10 nA - 100 mA)	11 (100 pA - 1 A)		
Minimum Current Resolution	0.3 pA	3.3 fA		
Minimum Voltage Resolution	1 µV			
Maximum Applied Potential	± 5 V	± 12 V		
Rise Time	1 µs			
Noise and Ripple	<20 µV rms			
Minimum Timebase	1 ms	10 µs		
Maximum Timebase	750 s			
Minimum Potential Step	12.5 µV			
EIS Measurement				
Frequency Range	100 mHz - 20 kHz	–	–	10 µHz - 1 MHz
Impedance Accuracy	99%	–	–	See Accuracy Contour Plot
Maximum AC Amplitude	2.33 V rms	–	–	2.33 V rms
Minimum AC Amplitude	17.8 µV rms	–	–	17.8 µV rms
Control Amplifier				
Compliance Voltage	± 20 V			
Output Current	> ± 1 A			
Speed settings	3			
Unity Gain Bandwidth (typical)	980, 260, 40, 4, 0.4 kHz			
Electrometer				
Input impedance	> 10^{12} Ω			
Input current	< 20 pA			
Bandwidth (-3 dB) (typical)	> 15 MHz			
Common Mode Rejection Ratio	> 80 dB (10 kHz), > 60 dB (1 MHz)			
Applied Potential				
Accuracy	± 1 mV ± 0.2% of setting			
Resolution	12.5 µV, 50 µV, 200 µV/bit			
Potential Scan Range	± 0.4 V, ± 1.6 V , ± 6.4 V			
Measured Potential				
Accuracy	± 1 mV ± 0.3% of setting			
Resolution	400 µV, 100 µV, 10 µV, 1 µV/bit			
Applied Current				
Accuracy	± 5 pA ± 0.3% of setting			
Resolution	0.0033% full-scale/bit			
Measured Current				
Accuracy	± 5 pA ± 0.3% of setting			
Resolution	0.0033% full-scale/bit			
Bandwidth (current range dependent)	> 10 MHz (100 mA - 100 µA ranges) > 1.5 MHz (10 µA range) > 150 kHz (1 µA range)			
Stability Settings	3			
iR Compensation				
Mode	Current Interrupt			
Minimum Interrupt Time	33 µs			
Maximum Interrupt Time	715 s			
Physical Dimensions				
Weight	2 kg			
Size	24 x 6 x 27 cm (W x H x D)			
Cable	60 cm (std); 1.5 m, 3 m, 10 m			

GAMRY INSTRUMENTS 734 Louis Drive | Warminster, PA 18974 USA | +215-682-9330 | Fax: +215-682-9331 | sales@gamry.com | www.gamry.com

A.9 Tektronix TBS 1052B-Edu specifications

TBS1000B Digital Storage Oscilloscopes

Specifications

All specifications are guaranteed unless noted otherwise. All specifications apply to all models unless noted otherwise.

Model overview

	TBS1032B [2]	TBS1052B	TBS1072B	TBS1102B	TBS1152B	TBS1202B
Bandwidth	30 MHz	50 MHz	70 MHz	100 MHz	150 MHz	200 MHz
Channels	2	2	2	2	2	2
Sample rate on each channel	500 MS/s	1.0 GS/s	1.0 GS/s	2 .0 GS/s	2 .0 GS/s	2 .0 GS/s
Record length	2.5k points at all-time bases					

Vertical system – Analog channels

Vertical resolution	8 bits
Input sensitivity range	2 mV to 5 V/div on all models with calibrated fine adjustment
DC gain accuracy	±3%, from 10 mV/div to 5 V/div
Maximum input voltage	300 V_{RMS} CAT II; derated at 20 dB/decade above 100 kHz to 13 V_{p-p} AC at 3 MHz and above
Offset range	2 mV to 200 mV/div: ±1.8 V >200 mV to 5 V/div: ±45 V
Bandwidth limit	20 MHz
Input coupling	AC, DC, GND
Input impedance	1 MΩ in parallel with 20 pF
Vertical zoom	Vertically expand or compress a live or stopped waveform

Horizontal system — Analog channels

Time base range	
30 MHz model [3]	10 ns to 50 s/div
50 MHz and 70 MHz models	5 ns to 50 s/div
100MHz, 150MHz and 200MHz models	2.5 ns to 50 s/div
Time base accuracy	50 ppm
Horizontal zoom	Horizontally expand or compress a live or stopped waveform

2 Available only in North America and Europe.

3 Available only in North America and Europe.

A.10 UNI-T UT30C digital multimeter specifications

5. Resistance

Range	Resolution	Accuracy			
		UT30B	UT30C	UT30D	UT30F
200Ω	0.1Ω	±(0.8%+5)			
2000Ω(2kΩ)	1Ω	±(0.8%+2)			
20kΩ	10Ω				
200kΩ	100Ω				
2MΩ	1kΩ	----------			
20MΩ	10kΩ	±(1%+5)			

⚠ Overload Protection: All ranges are 230V(DC/ AC current).

A.11 HP 4285-A LCR meter specifications

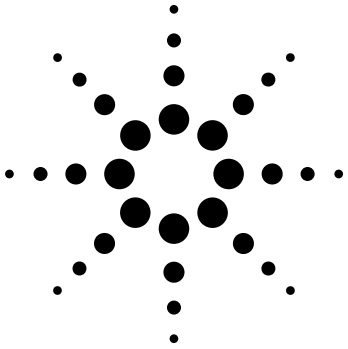

Agilent 4285A
Precision LCR Meter
Data Sheet

Specifications
The complete Agilent Technologies 4285A specifications are listed below. These specifications are the performance standards or limits against which the instrument is tested. When shipped from the factory, the 4285A meets the specifications listed in this section. The specification test procedures are covered in *Agilent 4285A Maintenance Manual* (Agilent Part Number 04285-90030).

Measurement Functions
Measurement parameters

|Z| = Absolute value of impedance
|Y| = Absolute value of admittance
L = Inductance
C = Capacitance
R = Resistance
G = Conductance
D = Dissipation factor
Q = Quality factor
R_s = Equivalent series resistance
R_p = Parallel resistance
X = Reactance
B = Suceptance
θ = Phase angle

Combinations of measurement parameters

|Z|, |Y|	L, C	R	G
θ (deg), θ (rad)	D, Q, R_s, R_p, G	X	B

Mathematical functions
The deviation and the percent of deviation of measurement values from a programmable reference value.

Equivalent measurement circuit
Parallel and series

Ranging
Auto and manual (hold/up/down)

Trigger
Internal, external, BUS (GPIB), and manual

Delay time
Programmable delay from the trigger command to the start of the measurement, 0 to 60.000 s in 1 ms steps.

Measurement terminals
Four-terminal pair

Test cable length
0 m, 1 m, and 2 m selectable

Integration time
Short, medium, and long selectable (refer to *Supplemental Performance Characteristics*, page 14, for the measurement time)

Averaging
1 to 256, programmable

Agilent Technologies

Appendix B

Reagents and dilutions

B.1 FeCN redox couple

The redox species that were used for performing electrochemical measurements were potassium ferricyanide ($K_3Fe(CN)_6$) and potassium ferrocyanide trihydrate ($K_4Fe(CN)_6 \cdot 3\,H_2O$). A fresh batch of 50 ml (5 mM in a 1:1 ratio) was made before experiments were performed. The reagents were dissolved in the supporting electrolyte, PBS(1X, pH 7.4). The solution was prepared using the following protocol:

1. Add 50 ml of PBS(1X, pH 7.4) to a falcon tube;
2. Add 82.31 mg $K_3Fe(CN)_6$ (MW = 329.24 g/mol) to the tube to get a concentration of 5 mM;
3. Add 105.6 mg $K_4Fe(CN)_6 \cdot 3\,H_2O$ (MW = 422.388 g/mol) to the tube to get a concentration of 5 mM;
4. Stir for a few minutes until the salts are properly dissolved.

B.2 RuHex redox probe

The positively charged redox probe that was used was hexaammineruthenium(III) chloride ($Ru(NH_3)_6$, RuHex). A fresh batch of 5 mM in 10 ml of PBS(1X, pH 7.4) was made before experiments were performed. The solution was prepared using the following protocol:

1. Add 10 ml of PBS(1X, pH 7.4) to a falcon tube;
2. Add 15.48 mg of $Ru(NH_3)_6$to the tube and mix until dissolved.

B.3 Dilution for potentiostat comparison tests

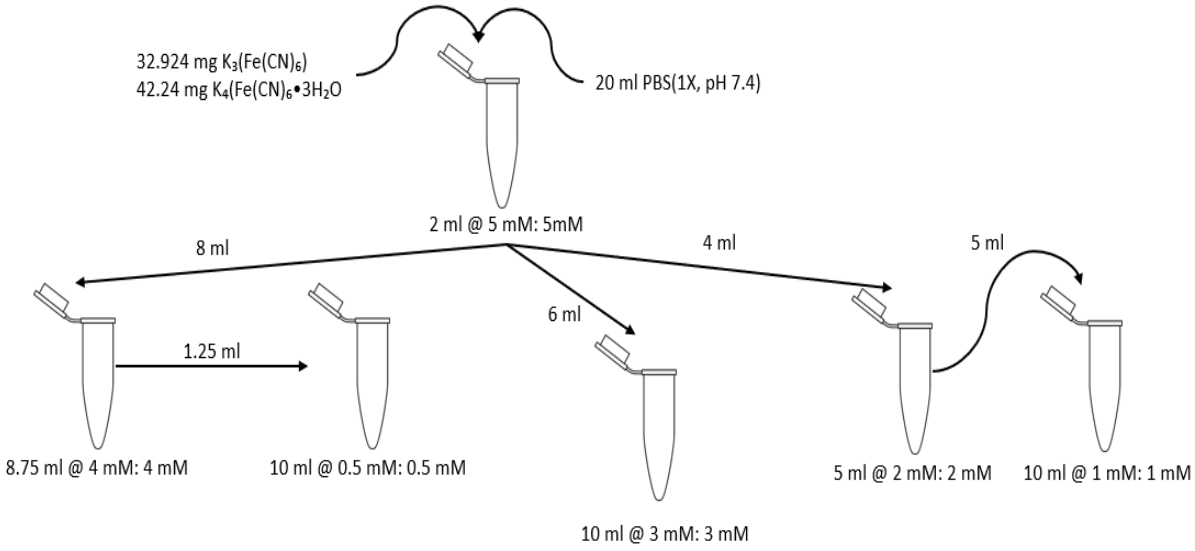

Figure B.1: Diagram illustrating how the FeCN couple was diluted for the SWV comparison tests. The volumes at the bottom indicate how much of the solution was left after performing all the dilutions.

B.4 Hydrochloric acid solution

A hydrochloric acid solution was prepared to perform the electrografting experiments. A 0.5 M HCl solution was made using the following protocol:

1. 32 % wt/wt HCl with a formula weight of 36.46 g/mol and a density of 1.1493 g/ml was acquired;
2. 24.784 ml of this stock solution was slowly added to 125 ml of deionized water;
3. The final volume was adjusted to 500 ml by slowly adding deionized water to get a 0.5 M concentration;
4. A 1 liter glass bottle was used to store this solution.

The pH of this solution was measured as 0.73 and the required volume was taken from this stock solution every time the diazonium salt mixture was made.

B.5 Diazonium salt mixture

The diazonium salt mixture in 0.5 M HCl was made every time an electrografting experiment was done. The mixture comprised of 4-aminobenzoic acid and sodium nitrite ($NaNO_2$) in equal molar concentrations of 2 mM. The typical protocol that was followed to prepare the solution is described below:

1. 25 ml of the HCl solution was added to a falcon tube;
2. 34.5 mg of $NaNO_2$ (MW = 69 g/mol) was added to this tube to obtain a concentration of 20 mM;

3. 68.57 mg of 4-aminobenzoic acid (MW = 137.14 g/mol) was added to the tube to obtain a concentration of 20 mM;
4. The solution was slowly stirred for 5 minutes at room temperature until the solids were dissolved;
5. 40.5 ml of HCl was added to a clean falcon tube;
6. 4.5 ml of the first concentrated tube was added to the new falcon tube to get a total volume of 45 ml;
7. This resulted in the dilution of the concentrated mixture to provide a 2 mM diazonium salt solution of 4-aminobenzoic acid and $NaNO_2$ in equal ratios;
8. The final solution was stirred properly before use.

The concentrated solution was made first to allow for easier weight measurements, but the 2 mM solution was used for performing electrografting experiments.

B.6 EDC/NHS activation chemistry

The EDC/NHS solution was made *in-situ* during the crosslinking chemistry step using a slightly adjusted protocol from Thermofisher Scientific:

1. 146.4 mg MES buffer (MW = 195.2 g/mol) was added to a tube with 7.5 ml distilled water to get a final concentration of 0.1 M;
2. 219.15 mg NaCl (MW = 58.44 gm/mol) was added to the same tube to get a final concentration of 0.5 M;
3. Adjust pH to 5.5 using NaOH;
4. 57.51 mg of EDC (MW = 191.7 g/mol) was added to the tube to get a concentration of 40 mM;
5. 16.285 mg of sulfo-NHS (MW = 217.13 g/mol) was added to the tube to get a concentration of 10 mM.

The final solution was 40 mM EDC and 10 mM sulfo-NHS in 0.1 M MES buffer with 0.5 M NaCl.

B.7 Antibody dilution

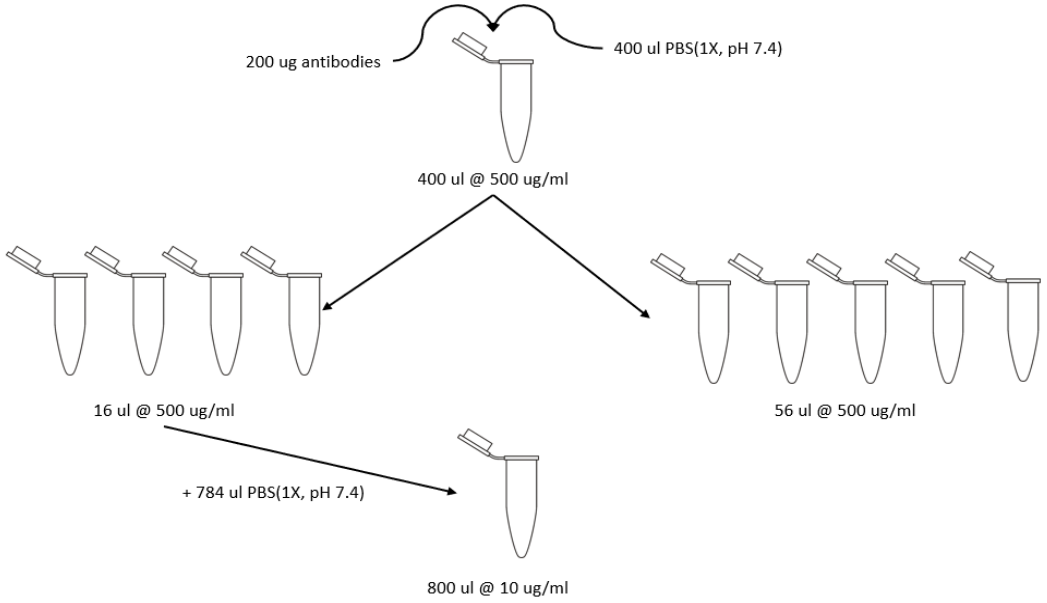

Figure B.2: Diagram illustrating how the stock antibody was made and how it was diluted. The volumes at the bottom indicate how much of the solution was left after performing all the dilutions.

B.8 Protein dilution for first full scale test

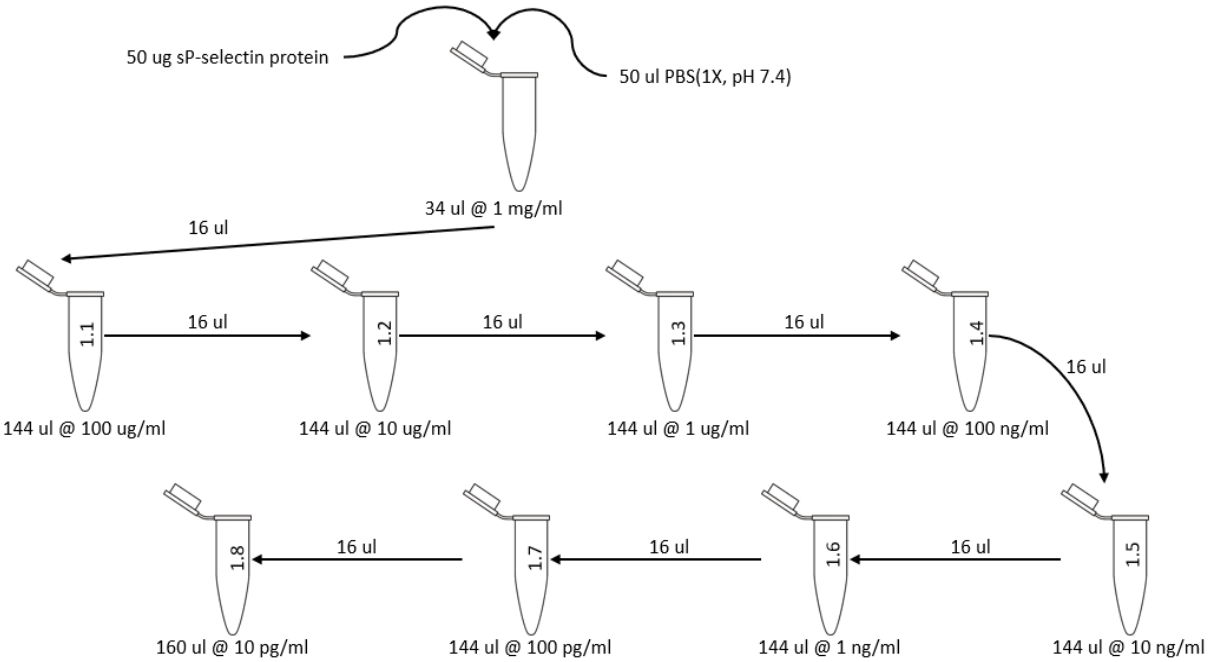

Figure B.3: Diagram illustrating how the stock protein was made and how it was diluted. The volumes at the bottom indicate how much of the solution was left after performing all the dilutions.

B.9 Protein dilution for second full scale test

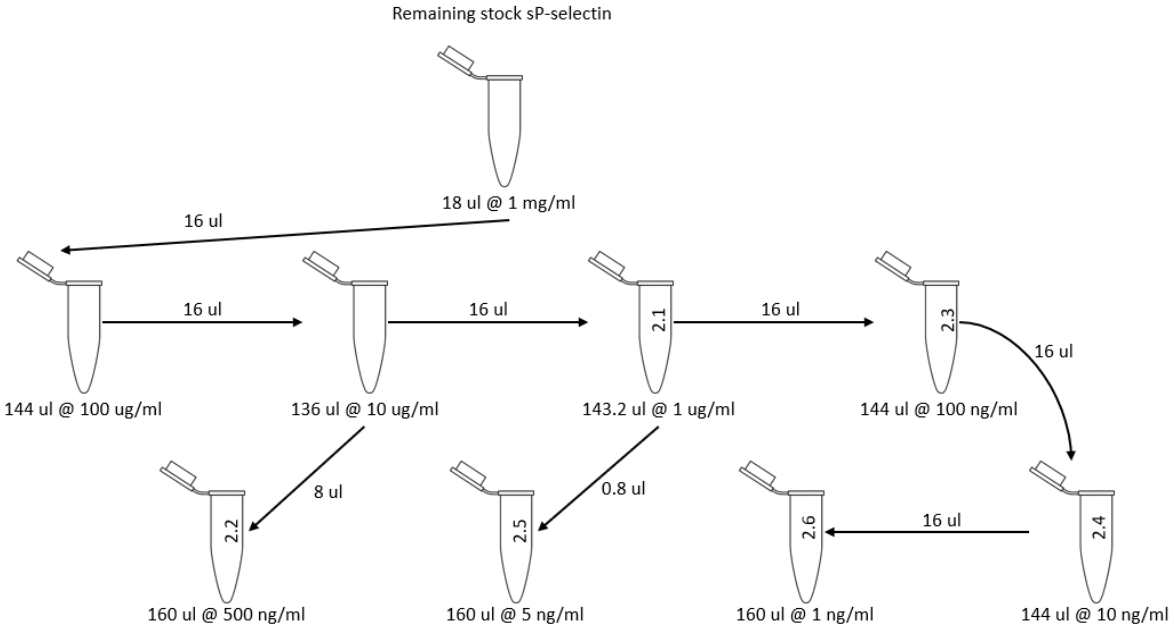

Figure B.4: Diagram illustrating how the stock protein was diluted for the second full scale test with the CNF sensors. The volumes at the bottom indicate how much of the solution was left after performing all the dilutions.

B.10 Protein dilution for third full scale test

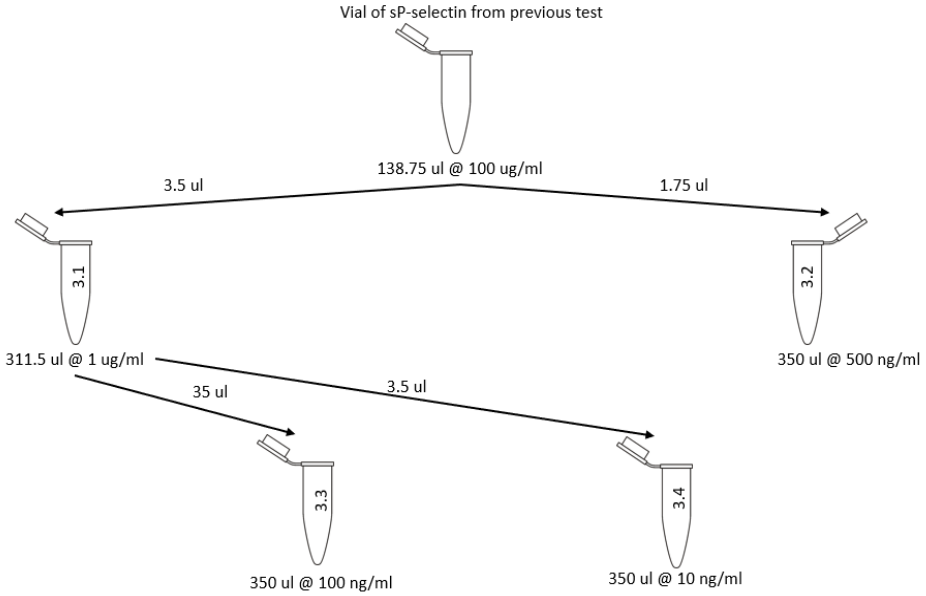

Figure B.5: Diagram illustrating how the stock protein was diluted for the third full scale test with the CNF sensors. The volumes at the bottom indicate how much of the solution was left after performing all the dilutions.

B.11 Protein dilution for fourth full scale test

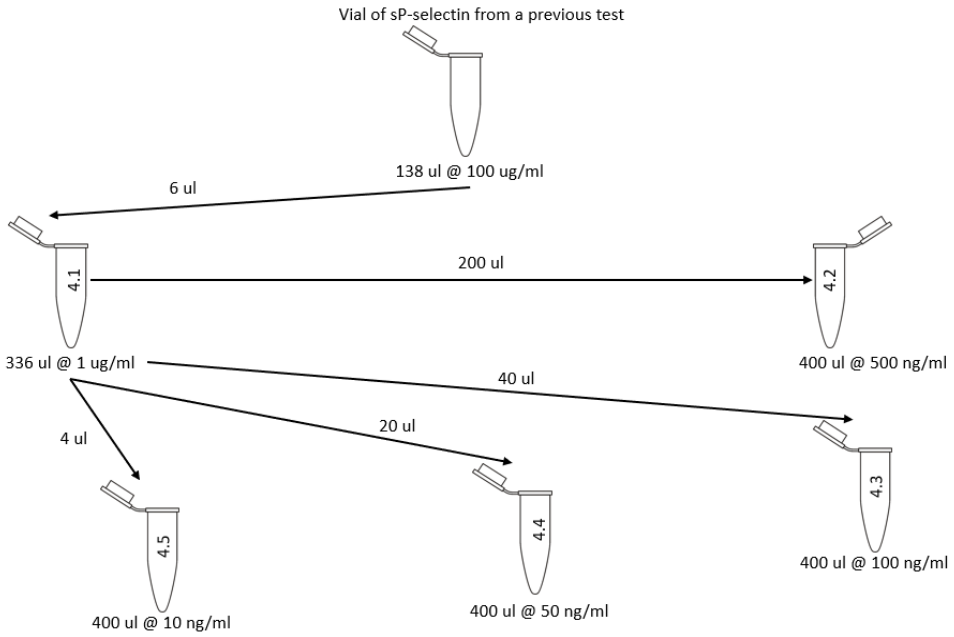

Figure B.6: Diagram illustrating how the stock protein was diluted for the fourth full scale test with the CNF sensors. The volumes at the bottom indicate how much of the solution was left after performing all the dilutions.

B.12 Protein dilution for fifth full scale test

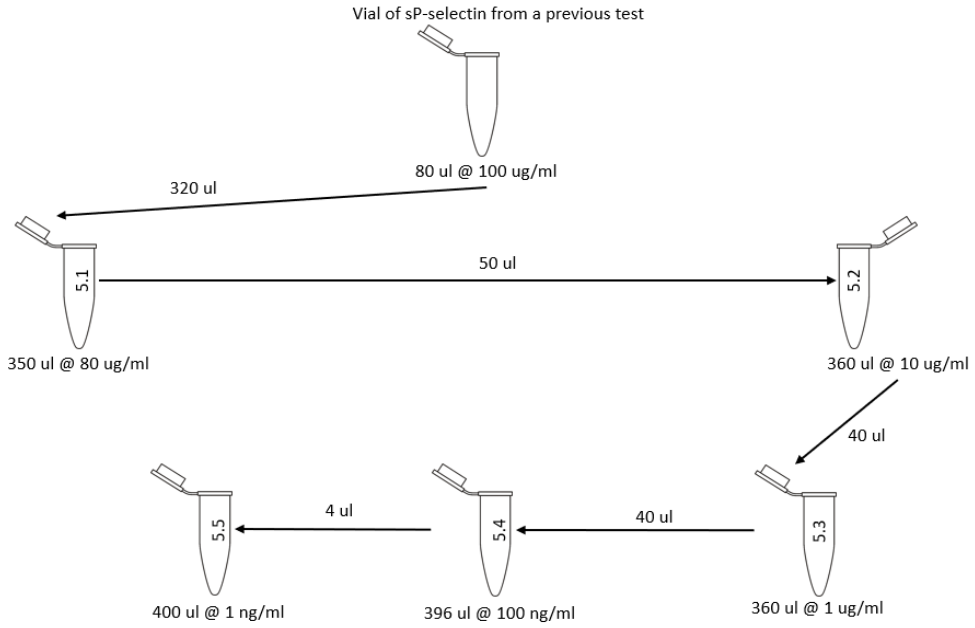

Figure B.7: Diagram illustrating how the stock protein was diluted for the fifth full scale test with the CNF sensors. The volumes at the bottom indicate how much of the solution was left after performing all the dilutions.

Appendix C

Code

C.1 Typical plotting code

```
import numpy as np
import matplotlib.pyplot as plt

filename = "Example.txt"
data = read_in_data(filename)

for key in protein_data.keys():
    x = np.asarray(protein_data[key]['x'])[1:]
    y = np.asarray(protein_data[key]['y'])[1:]
    y_filt = filter_using_savgol(y)
    baseline = get_baseline_from_inflection_points(x,
                                                   y_filt,
                                                   0.05,
                                                   0.3)
    y_final = y_filt - baseline
    peak = max(y_final)
    peaks.append(peak)
    plt.plot(x, y_final, label=key)

plt.legend()
plt.show()
```

C.2 Data algorithm code

```
from scipy.signal import savgol_filter
import numpy as np
from scipy import stats
import xlrd
import openpyxl

def save_data(filename, volt_values, avg_values):

    wbk = openpyxl.load_workbook(filename)

    try:
        sheet = wbk['AVG_UNFILTERED']
    except KeyError:
        sheet = wbk.create_sheet('AVG_UNFILTERED')

    for r in range(1, len(avg_values) + 1):
```

```
17          sheet.cell(row=r, column=1).value = volt_values[r - 1]
18          sheet.cell(row=r, column=2).value = avg_values[r - 1] * 10 ** (-6)
19
20      wbk.save(filename)
21
22  def read_in_data(filename):
23
24      wb = xlrd.open_workbook(filename)
25      sheet = wb.sheet_by_index(0)
26
27      data = {}
28      scans = []
29      for i in range(1, int(sheet.ncols/2)+1, 1):
30          sweepName = sheet.cell_value(0, (i-1)*2)
31          scans.append(sweepName)
32          data[sweepName] = {'x': [],
33                             'y': []}
34      scans.reverse()
35      for c in range(sheet.ncols):
36
37          if c%2 == 0:
38              sweepName = scans.pop()
39
40          for r in range(1,sheet.nrows):
41
42              if c % 2 == 0:
43                  data[sweepName]['x'].append(float(sheet.cell_value(r, c)))
44              else:
45                  data[sweepName]['y'].append(float(sheet.cell_value(r, c)) *
    10 ** 6)
46
47      return data
48
49  def is_number(s):
50      try:
51          float(s)
52          return True
53      except ValueError:
54          return False
55
56  def filter_using_savgol(y):
57      return savgol_filter(y, window_length=15, polyorder=4)
58
59  def get_arg_max_in_interval(x, y, x_volt_left, x_volt_right):
60
61      assert (x_volt_right > x_volt_left), "Right interval voltage value
    needs to be larger than the left interval value"
62      assert (len(x) == len(y)), "X and Y need to be the same length"
63      argstop = np.argwhere(x < x_volt_right)
64      argsbottom = np.argwhere(x > x_volt_left)
65      intersection = np.intersect1d(argstop, argsbottom)
66      ym = max(y[intersection])
67      return np.argwhere(y == ym)[0, 0]
68
69  def get_inflection_left_arg(x, y, volt_left, volt_right):
70
71      assert (len(x) == len(y)), "X and Y needs to be the same length"
72      _x = np.asarray(x)
73      _y = np.asarray(y)
```

```
74      max_arg = get_arg_max_in_interval(_x, _y, volt_left, volt_right)
75      inflection_arg = None
76
77      for i in range(max_arg, len(_y)-1, 1):
78
79          slope = (_y[i+1] - _y[i]) / (_x[i+1] - _x[i])
80
81          if slope == 0 or slope < 0:
82
83              if abs(i-max_arg) < 2:
84                  continue
85
86              inflection_arg = i
87              break
88
89      if inflection_arg is None:
90          inflection_arg = len(_y)-1
91
92      return inflection_arg
93
94  def get_inflection_right_arg(x, y, volt_left, volt_right):
95
96      assert (len(x) == len(y)), "X and Y needs to be the same length"
97      _x = np.asarray(x)
98      _y = np.asarray(y)
99
100     # find the maximum
101     max_arg = get_arg_max_in_interval(_x, _y, volt_left, volt_right)
102     inflection_arg = None
103
104     # walk to the left
105     for i in range(max_arg, 0, -1):
106
107         slope = (_y[i-1] - _y[i]) / (_x[i-1] - _x[i])
108
109         # find zero or positive slope
110         if slope == 0 or slope > 0:
111
112             if abs(i-max_arg) < 2:
113                 continue
114
115             inflection_arg = i
116             break
117
118     return inflection_arg
119
120 def get_baseline_from_inflection_points(x, y, volt_left, volt_right):
121
122     assert (len(x) == len(y)), "X and Y needs to be the same length"
123     _x = np.asarray(x)
124     _y = np.asarray(y)
125     inflect_pos_left = get_inflection_left_arg(_x, _y, volt_left,
    volt_right)
126     inflect_pos_right = get_inflection_right_arg(_x, _y, volt_left,
    volt_right)
127
128     if inflect_pos_left is not None and inflect_pos_right is not None:
129         x_infl_left = _x[inflect_pos_left]
130         y_infl_left = _y[inflect_pos_left]
```

```
        x_infl_right = _x[inflect_pos_right]
        y_infl_right = _y[inflect_pos_right]
        slope = (y_infl_right - y_infl_left) / (x_infl_right - x_infl_left)
        intercept = y_infl_left - slope * x_infl_left
        return slope * _x + intercept
    else:
        return None

def get_baseline_data_from_leading_edge(x, y):

    assert (len(x) == len(y)), "X and Y needs to be the same length"
    _x = np.asarray(x)
    _y = np.asarray((y))
    slope, intercept, r_value, p_value, std_err = stats.linregress(_x, _y)
    return slope, intercept

def get_max_current_from_baseline_using_leading_edge(x, y, full_x, full_y):

    slope, intercept = get_baseline_data_from_leading_edge(x, y)
    full_y = np.asarray(full_y)
    full_x = np.asarray(full_x)
    y_max = max(full_y)
    x_max = full_x[full_y == y_max]
    max_curr = y_max - (slope * x_max + intercept)
    return max_curr[0]

def get_max_arg_within_inflection_region(y, infl_left, infl_right):

    ym = max(y[infl_right:infl_left])
    return np.argwhere(y == ym)[0, 0]
```

C.3 Serial communication

```
import serial

ser = serial.Serial('COM5', 9600, timeout=None, parity=serial.PARITY_NONE)
numbytes = 3796

while 1:

    filename = input("Enter the filename to store the data (or type 'EXIT' to exit): ")

    if filename == "EXIT":
        break

    if filename[-4:] == ".txt":
        filename = filename[:-4]

    print("RAW data will be stored as: " + filename + "_RAW.txt " + "in the 'Output' folder")
    print("Processed data will be store as: " + filename + ".txt " + "in the 'Output' folder")
    print("Press the Blue button on the STM32F4 to perform the experiment..")
    bytes_received = ser.read(numbytes)
    print("Number of bytes received: " + str(len(bytes_received)))

```

```
    with open("Output/"+filename+"_RAW.txt", 'w+') as f:

        for line in bytes_received:
            f.write(hex(line)+"\n")

    with open("Output/"+filename+".txt", "a+") as f:
        f.write("Pulse_num,Pulse_type,Time_applied_in_ms,Staircase_val,
    Ref_adc_avg,Cvc_adc_avg\n")

    i = 0
    while i < numbytes:

        pulse_num = int((bytes_received[i] << 8) | (bytes_received[i + 1]))
        pulse_type = int(bytes_received[i + 2])
        time_applied = int((bytes_received[i + 3] << 24) |
                           (bytes_received[i + 4] << 16) |
                           (bytes_received[i + 5] << 8) |
                           (bytes_received[i + 6]))
        staircase_val = int((bytes_received[i + 7] << 8) | bytes_received[i
    + 8])
        ref_adc_avg = int((bytes_received[i + 9] << 8) | bytes_received[i +
    10])
        cvc_adc_avg = int((bytes_received[i + 11] << 8 | bytes_received[i +
    12]))
        line = str(pulse_num) + "," + \
            str(pulse_type) + "," + \
            str(time_applied) + "," + \
            str(staircase_val) + "," + \
            str(ref_adc_avg) + "," + \
            str(cvc_adc_avg) + "\n"
        i = i + 13

        with open("Output/"+filename+".txt", "a+") as f:
            f.write(line)

    print("Data has been collected\n\n")
    ser.reset_input_buffer()
```

C.4 STM32F446ZE potentiostat code

```
#include "main.h"
#include <math.h>

#define MAX_ARRAY_LENGTH 500
#define WE_ON GPIO_PIN_RESET
#define WE_OFF GPIO_PIN_SET

ADC_HandleTypeDef hadc2;
DMA_HandleTypeDef hdma_adc2;
DAC_HandleTypeDef hdac;
TIM_HandleTypeDef htim2;
TIM_HandleTypeDef htim3;
TIM_HandleTypeDef htim6;
UART_HandleTypeDef huart3;

/*************** Cell Values ***************/
const float cell_InitialPotentialVolts = 0.5;      // Vwr (working relative
    to reference)
```

```
const float cell_FinalPotentialVolts = -0.7;       // Vwr (working relative to reference)
const float cell_PotentialStepVolts = 0.005;       // 5 mV Vwr (working relative to reference)
const float cell_PulseSizeVolts = 0.020;           // 20 mV Vwr (working relative to reference)
int total_num_staircase_steps;                     // number of staircase steps
int pulse_number;                                  // number of square wave pulses = 2*total_num_steps
/*******************************************/

/******************* Working Electrode *****/
const float working_PotentialVolts = 1.65;      // 1.65 V stays constant
uint32_t working_DAC_value;                     // DAC value for working electrode = 2048
/*******************************************/

/*************** Reference Electrode ********/
float ref_InitialPotentialVolts;
float ref_FinalPotentialVolts;
uint32_t ref_IntialPotentialDACValue;
uint32_t ref_FinalPotentialDACValue;
uint32_t ref_PotentialStepDACValue;
uint32_t ref_PulseSizeDACValue;
uint32_t ref_DAC_time_applied[MAX_ARRAY_LENGTH];       // stores times that the DAC applies the voltage of each pulse
uint32_t ref_DAC_values_Stored[MAX_ARRAY_LENGTH];      // stores the DAC values that are fed to the DMA
uint32_t ref_staircase_DAC_stored[MAX_ARRAY_LENGTH];   // stores the staircase values
/*************************************/

/************** ADC Sample Variables ************/
uint32_t adc2_cvc_sample_array[64];           // DMA transfers CVC samples to this array
uint32_t forward_sample_cvc_ADC2_values[MAX_ARRAY_LENGTH]; // averaged ADC2 samples for forward current
uint32_t reverse_sample_cvc_ADC2_values[MAX_ARRAY_LENGTH]; // averaged ADC2 samples for reverse current
int reverse_pulse_sample_num;                 // counter for reverse samples
int forward_pulse_sample_num;                 // counter for forward samples
int num_adc_samples;                          // going to count up to 64 samples that need to be sampled
/*********************************************/

/****************** Time storage and flags ******************/
uint32_t time_of_cell_on;                     // time that the cell is switched on (button press time)
uint32_t time_of_first_swv_pulse_applied;     // time at start of square wave
uint32_t time_of_last_swv_pulse_applied;      // time that the cell is turned off
uint32_t time_of_adc_start_sampling;          // set by TIM3 interrupt generated after 18.6 ms after pulses are applied
uint32_t time_of_adc_stop_sampling;           // set by ADC conversion complete interrupt after 64 samples have been taken
uint32_t total_experiment_time;               // store total experiment time
uint8_t experiment_running_flag;              // flag for experiment running (0 = No, 1 = Yes)
```

```
59 uint8_t even_pulse_has_been_applied_flag;  // flag to show that the even
   pulse has just been applied
60 uint8_t odd_pulse_has_been_applied_flag;   // flag to show that the odd
   pulse has just been applied
61 uint8_t adc_start_sampling_flag;           // flag to show that the ADC
   needs to start sampling
62 uint8_t cvc_adc2_done_flag;
63 uint8_t forward_current_flag;          // flag to keep track of which
   current array should be used for summing and averaging
64 uint8_t reverse_current_flag;          // flag to keep track of which
   current array should be used for summing and averaging
65 uint8_t ignore_first_interrupt_tim3_flag;  // flag to ignore first
   interrupt of TIM3
66 int TIM3_fire_counter = 0;                 // counter for TIM3 events
67 int time_TIM3_fired[MAX_ARRAY_LENGTH];     // array to store time that TIM3
    goes off (ADC start sampling time)
68 uint8_t has_run_an_exp_flag = 0;       // special flag to see if an
   experiment has been run
69 /*****************************************/
70
71 /****************** UART and communication protocol variables **********/
72 uint8_t transmitBuf[8000];     // make buffer big enough to transmit all
   the data
73                 // in this case it is only going to use 13 x 187 x 2 =
   4862 bytes
74 /*********************************************************/
75
76 void SystemClock_Config(void);
77 static void MX_GPIO_Init(void);
78 static void MX_DMA_Init(void);
79 static void MX_DAC_Init(void);
80 static void MX_TIM2_Init(void);
81 static void MX_TIM3_Init(void);
82 static void MX_TIM6_Init(void);
83 static void MX_USART3_UART_Init(void);
84 static void MX_ADC2_Init(void);
85 void populateRefDacValues(void);
86 void resetState(void);
87 void captureEvenPulseData(void);
88 void captureOddPulseData(void);
89 uint32_t getArrayAverage(uint32_t * arr);
90 void sendDataUART(void);
91 GPIO_PinState isButtonPressed(void);
92
93 int main(void)
94 {
95   HAL_Init();
96   SystemClock_Config();
97   MX_GPIO_Init();
98   MX_DMA_Init();
99   MX_DAC_Init();
100  MX_TIM2_Init();
101  MX_TIM3_Init();
102  MX_TIM6_Init();
103  MX_USART3_UART_Init();
104  MX_ADC2_Init();
105
106  resetState();
107  HAL_GPIO_WritePin(WE_Switch_GPIO_Port, WE_Switch_Pin, WE_OFF);
```

```
108   HAL_DAC_Start(&hdac, DAC_CHANNEL_2);
109   HAL_DAC_SetValue(&hdac, DAC_CHANNEL_2, DAC_ALIGN_12B_R, working_DAC_value
        );
110   HAL_DAC_Start(&hdac, DAC_CHANNEL_1);
111   HAL_DAC_SetValue(&hdac, DAC_CHANNEL_1, DAC_ALIGN_12B_R, 0);
112
113   while (1)
114   {
115     if (!experiment_running_flag)
116     {
117       if (isButtonPressed() == GPIO_PIN_SET)
118       {
119         HAL_Delay(10);
120
121         if (isButtonPressed() == GPIO_PIN_SET)
122         {
123           experiment_running_flag = 1;
124           HAL_TIM_Base_Start_IT(&htim6);
125           HAL_GPIO_WritePin(WE_Switch_GPIO_Port, WE_Switch_Pin, WE_ON);
126           HAL_GPIO_TogglePin(LD3_GPIO_Port, LD3_Pin);
127           time_of_cell_on = HAL_GetTick();
128         }
129       }
130     }
131
132     if (even_pulse_has_been_applied_flag || odd_pulse_has_been_applied_flag
      )
133     {
134       HAL_TIM_Base_Start_IT(&htim3);
135
136       if (even_pulse_has_been_applied_flag)
137       {
138         forward_current_flag = 1;
139         reverse_current_flag = 0;
140         even_pulse_has_been_applied_flag = 0;
141       }
142       else if (odd_pulse_has_been_applied_flag)
143       {
144         forward_current_flag = 0;
145         reverse_current_flag = 1;
146         odd_pulse_has_been_applied_flag = 0;
147       }
148
149     }
150
151     if (adc_start_sampling_flag)
152     {
153       HAL_TIM_Base_Stop_IT(&htim3);
154
155       if (pulse_number == 0)
156       {
157         time_of_adc_start_sampling = HAL_GetTick();
158       }
159
160       adc_start_sampling_flag = 0;
161       HAL_TIM_Base_Start(&htim2);
162       HAL_ADC_Start_DMA(&hadc2, (uint32_t*)adc2_cvc_sample_array,
    num_adc_samples);
163
```

```
164     }
165
166     if (cvc_adc2_done_flag)
167     {
168       HAL_TIM_Base_Stop(&htim2);
169       HAL_ADC_Stop_DMA(&hadc2);
170
171       if (pulse_number == 2 * total_num_staircase_steps - 1)
172       {
173         HAL_DAC_SetValue(&hdac, DAC_CHANNEL_1, DAC_ALIGN_12B_R, 0);
174         HAL_TIM_Base_Stop_IT(&htim6);
175         HAL_GPIO_WritePin(WE_Switch_GPIO_Port, WE_Switch_Pin, WE_OFF);
176       }
177
178       cvc_adc2_done_flag = 0;
179       uint32_t cvc_avg = getArrayAverage(adc2_cvc_sample_array);
180
181       if (forward_current_flag && !reverse_current_flag)
182       {
183         forward_sample_cvc_ADC2_values[forward_pulse_sample_num] = cvc_avg;
184         forward_pulse_sample_num++;
185       }
186       else if (reverse_current_flag && !forward_current_flag)
187       {
188         reverse_sample_cvc_ADC2_values[reverse_pulse_sample_num] = cvc_avg;
189         reverse_pulse_sample_num++;
190       }
191
192       if (pulse_number == 2 * total_num_staircase_steps - 1)
193       {
194         HAL_GPIO_TogglePin(LD3_GPIO_Port, LD3_Pin);
195         total_experiment_time = HAL_GetTick() -
    time_of_first_swv_pulse_applied;
196         HAL_GPIO_TogglePin(LD2_GPIO_Port, LD2_Pin);      // shows that UART
    is transmitting
197         sendDataUART();
198         HAL_GPIO_TogglePin(LD2_GPIO_Port, LD2_Pin);
199         resetState();
200       }
201       else
202       {
203         pulse_number++;
204       }
205     }
206   }
207 }
208
209 void HAL_ADC_ConvCpltCallback(ADC_HandleTypeDef* hadc)
210 {
211   if (hadc->Instance == ADC2)
212   {
213     cvc_adc2_done_flag = 1;
214   }
215
216   if (pulse_number == 0)
217   {
218     time_of_adc_stop_sampling = HAL_GetTick();
219   }
220 }
```

```
221
222 void HAL_TIM_PeriodElapsedCallback(TIM_HandleTypeDef *htim)
223 {
224   if (htim->Instance == TIM3)
225   {
226     if (ignore_first_interrupt_tim3_flag && !has_run_an_exp_flag)
227     {
228       ignore_first_interrupt_tim3_flag = 0;
229       has_run_an_exp_flag = 1;
230     }
231     else
232     {
233       adc_start_sampling_flag = 1;
234       time_TIM3_fired[TIM3_fire_counter++] = HAL_GetTick();
235     }
236   }
237   else if (htim->Instance == TIM6)
238   {
239     HAL_DAC_SetValue(&hdac, DAC_CHANNEL_1, DAC_ALIGN_12B_R,
      ref_DAC_values_Stored[pulse_number]);
240
241     if (pulse_number % 2 == 0)
242     {
243       even_pulse_has_been_applied_flag = 1;
244     }
245     else
246     {
247       odd_pulse_has_been_applied_flag = 1;
248     }
249
250     uint32_t t = HAL_GetTick();
251     ref_DAC_time_applied[pulse_number] = t;
252
253     if (pulse_number == 0)
254     {
255       time_of_first_swv_pulse_applied = t;
256     }
257     else if (pulse_number == 2 * total_num_staircase_steps - 1)
258     {
259       time_of_last_swv_pulse_applied = t;
260     }
261   }
262 }
263
264 void resetState(void)
265 {
266   populateRefDacValues();
267   working_DAC_value = (uint32_t)(round(working_PotentialVolts / 3.3 *
      4096.0));
268   time_of_cell_on = 0;
269   time_of_first_swv_pulse_applied = 0;
270   time_of_last_swv_pulse_applied = 0;
271   time_of_adc_start_sampling = 0;
272   time_of_adc_stop_sampling = 0;
273   TIM3_fire_counter = 0;
274   total_experiment_time = 0;
275   num_adc_samples = 64;
276   forward_pulse_sample_num = 0;
277   reverse_pulse_sample_num = 0;
```

```
278
279   for (int i = 0; i < num_adc_samples; i++)
280   {
281     adc2_cvc_sample_array[i] = 0;
282   }
283
284   for (int i = 0; i < MAX_ARRAY_LENGTH; i++)
285   {
286     ref_DAC_time_applied[i] = 0;
287     forward_sample_cvc_ADC2_values[i] = 0;
288     reverse_sample_cvc_ADC2_values[i] = 0;
289     time_TIM3_fired[i] = 0;
290   }
291
292   for (int i = 0; i < 8000; i++)
293   {
294     transmitBuf[i] = 0;
295   }
296
297   experiment_running_flag = 0;
298   even_pulse_has_been_applied_flag = 0;
299   odd_pulse_has_been_applied_flag = 0;
300   adc_start_sampling_flag = 0;
301   ignore_first_interrupt_tim3_flag = 1;
302   forward_current_flag = 0;
303   reverse_current_flag = 0;
304   cvc_adc2_done_flag = 0;
305   HAL_GPIO_WritePin(GPIOB, PIN1_Pin | PIN2_Pin, GPIO_PIN_RESET);
306 }
307
308 void populateRefDacValues(void)
309 {
310   ref_InitialPotentialVolts = working_PotentialVolts -
        cell_InitialPotentialVolts;
311   ref_FinalPotentialVolts = working_PotentialVolts -
        cell_FinalPotentialVolts;
312   ref_IntialPotentialDACValue = (uint32_t)round(ref_InitialPotentialVolts /
        3.3 * 4096.0);
313   ref_FinalPotentialDACValue = (uint32_t)round(ref_FinalPotentialVolts /
        3.3 * 4096.0);
314   ref_PotentialStepDACValue = (uint32_t)round(cell_PotentialStepVolts / 3.3
        * 4096.0);
315   ref_PulseSizeDACValue = (uint32_t)round(cell_PulseSizeVolts / 3.3 *
        4096.0);
316   total_num_staircase_steps = (int)(round((float)(
        ref_FinalPotentialDACValue - ref_IntialPotentialDACValue) / (float)
        ref_PotentialStepDACValue) + 1);
317
318   for (int i = 0; i < total_num_staircase_steps; i++)
319   {
320     uint32_t stairVal = ref_IntialPotentialDACValue +
        ref_PotentialStepDACValue * i;
321     ref_staircase_DAC_stored[i * 2] = stairVal;
322     ref_staircase_DAC_stored[i * 2 + 1] = stairVal;
323
324     ref_DAC_values_Stored[i * 2] = stairVal + ref_PulseSizeDACValue;
325     ref_DAC_values_Stored[i * 2 + 1] = stairVal - ref_PulseSizeDACValue;
326   }
327   pulse_number = 0;
```

```
328 }
329
330 uint32_t getArrayAverage(uint32_t * arr)
331 {
332   uint32_t sum = 0;
333   for (int i = 0; i < num_adc_samples; i++)
334   {
335     sum += arr[i];
336     arr[i] = 0;
337   }
338   return (uint32_t)(sum >> 6);
339 }
340
341 void sendDataUART(void)
342 {
343   int byte_num = 0;
344   int ref_dac_counter = 0;
345   int forward_counter = 0;
346   int reverse_counter = 0;
347
348   for (int i = 0; i <= pulse_number; i++)
349   {
350     uint16_t pulse_num = (uint16_t)i;
351     transmitBuf[byte_num++] = (uint8_t)(pulse_num >> 8);
352     transmitBuf[byte_num++] = (uint8_t)(pulse_num & 0x00FF);
353     transmitBuf[byte_num++] = (i % 2 == 0 ? 0x0 : 0x1);
354     uint32_t time_applied = ref_DAC_time_applied[i];
355     transmitBuf[byte_num++] = (uint8_t)((time_applied & 0xFF000000) >> 24);
      // upper 8 bits
356     transmitBuf[byte_num++] = (uint8_t)((time_applied & 0x00FF0000) >> 16);
      // middle upper 8 bits
357     transmitBuf[byte_num++] = (uint8_t)((time_applied & 0x0000FF00) >> 8);
    // middle lower 8 bits
358     transmitBuf[byte_num++] = (uint8_t)(time_applied & 0x000000FF); //
    lower 8 bits
359     transmitBuf[byte_num++] = (uint8_t)(ref_staircase_DAC_stored[i] >> 8);
    // upper 8 bits
360     transmitBuf[byte_num++] = (uint8_t)(ref_staircase_DAC_stored[i] & 0
    x00FF); // lower 8 bits
361
362     if (i % 2 == 0)
363     {
364       uint16_t val = ref_DAC_values_Stored[ref_dac_counter];
365       transmitBuf[byte_num++] = (uint8_t)(val >> 8); // upper 8 bits
366       transmitBuf[byte_num++] = (uint8_t)(val & 0x00FF); // lower 8 bits
367       val = forward_sample_cvc_ADC2_values[forward_counter];
368       transmitBuf[byte_num++] = (uint8_t)(val >> 8); // upper 8 bits
369       transmitBuf[byte_num++] = (uint8_t)(val & 0x00FF); // lower 8 bits
370       forward_counter++;
371     }
372     else  // send REVERSE sample
373     {
374       uint16_t val = ref_DAC_values_Stored[ref_dac_counter];
375       transmitBuf[byte_num++] = (uint8_t)(val >> 8); // upper 8 bits
376       transmitBuf[byte_num++] = (uint8_t)(val & 0x00FF); // lower 8 bits
377       val = reverse_sample_cvc_ADC2_values[reverse_counter];
378       transmitBuf[byte_num++] = (uint8_t)(val >> 8); // upper 8 bits
379       transmitBuf[byte_num++] = (uint8_t)(val & 0x00FF); // lower 8 bits
380       reverse_counter++;
```

```
381         }
382         ref_dac_counter++;
383     }
384 
385     HAL_UART_Transmit(&huart3, transmitBuf, total_num_staircase_steps * 2 *
        13, 20000);
386 
387 }
388 
389 GPIO_PinState isButtonPressed(void)
390 {
391     return HAL_GPIO_ReadPin(USER_Btn_GPIO_Port, USER_Btn_Pin);
392 }
```

Appendix D

Printed circuit board files

D.1 Schematic

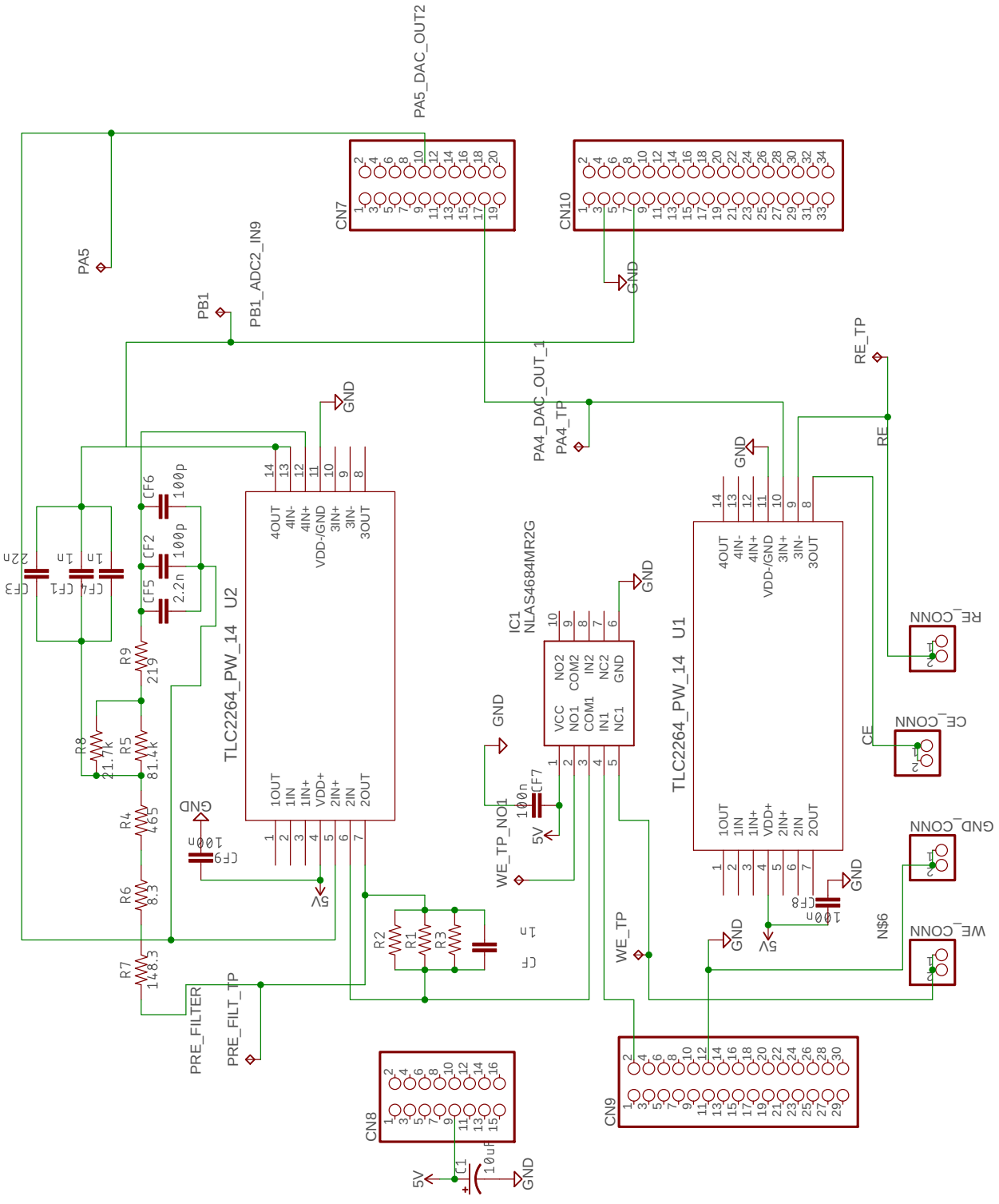

D.2 Printed circuit board layout

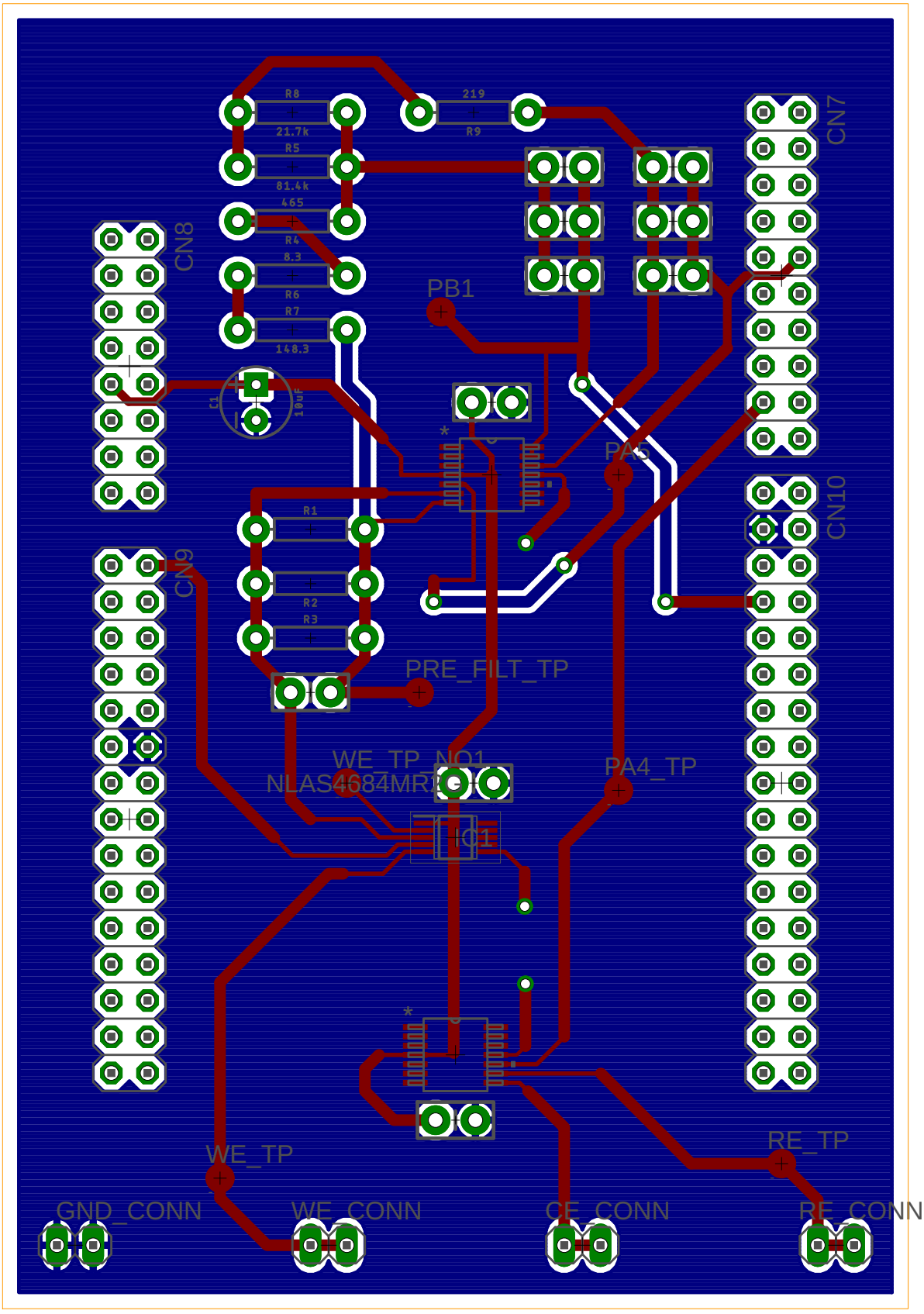

Bibliography

[1] "The top 10 causes of death." https://www.who.int/news-room/fact-sheets/detail/the-top-10-causes-of-death. Accessed: 2019-02-17.

[2] "What is cardiovascular disease?." https://www.heart.org/en/health-topics/consumer-healthcare/what-is-cardiovascular-disease. Accessed: 2019-02-17.

[3] D. Giovanni, F. Santilli, N. Vazzana, and ., "Diabetes Mellitus," in *Platelets* (A. Michelson, ed.), ch. 35, pp. 711–732, London: Elsevier, third ed., 2013.

[4] R. Cotran, *Robbins pathologic basis of disease*. Philadelphia: Saunders, 1999.

[5] C. Ling and L. Groop, "Epigenetics: A Molecular Link Between Environmental Factors and Type 2 Diabetes," *Diabetes*, vol. 58, pp. 2718–2725, dec 2009.

[6] S. Nomura, M. Suzuki, K. Katsura, G. L. Xie, Y. Miyazaki, T. Miyake, H. Kido, H. Kagawa, and S. Fukuhara, "Platelet-derived microparticles may influence the development of atherosclerosis in diabetes mellitus," *Atherosclerosis*, vol. 116, no. 2, pp. 235–240, 1995.

[7] L. M. Coussens and Z. Werb, "Inflammation and cancer.," *Nature*, vol. 420, pp. 860–7, dec 2002.

[8] S. Nomura, "Dynamic role of microparticles in type 2 diabetes mellitus.," *Current diabetes reviews*, vol. 5, pp. 245–51, nov 2009.

[9] "Put out the fire of diabetes inflammation." https://www.diabetesselfmanagement.com/blog/put-out-the-fire-of-diabetes-inflammation. Accessed: 2019-02-17.

[10] E. Golia, G. Limongelli, F. Natale, F. Fimiani, V. Maddaloni, I. Pariggiano, R. Bianchi, M. Crisci, L. D'Acierno, R. Giordano, G. Di Palma, M. Conte, P. Golino, M. G. Russo, R. Calabrò, and P. Calabrò, "Inflammation and cardiovascular disease: From pathogenesis to therapeutic target," *Current Atherosclerosis Reports*, vol. 16, no. 9, 2014.

[11] A. Natarajan, A. G. Zaman, and S. M. Marshall, "Platelet hyperactivity in type 2 diabetes: role of antiplatelet agents.," *Diabetes & vascular disease research*, vol. 5, pp. 138–44, jun 2008.

[12] E. Fuentes Q, F. Fuentes Q, V. Andrés, O. M. Pello, J. Font de Mora, and I. Palomo G, "Role of platelets as mediators that link inflammation and thrombosis in atherosclerosis.," *Platelets*, vol. 24, pp. 255–62, jun 2013.

[13] V. Evangelista and S. S. Smyth, "Interactions Between Platelets, Leukocytes and the Endothelium," *Platelets*, pp. 295–312, 2013.

[14] M. Gawaz, H. Langer, and A. E. May, "Platelets in inflammation and atherogenesis.," *The Journal of clinical investigation*, vol. 115, pp. 3378–84, dec 2005.

[15] A. V. D. Abreu, M. T. Rondina, A. S. Weyrich, and G. A. Zimmerman, "Inflammation," in *Platelets*, ch. 36, pp. 733–766, Academic Press, 2013.

[16] S.-H. Yun, E.-H. Sim, R.-Y. Goh, J.-I. Park, and J.-Y. Han, "Platelet Activation: The Mechanisms and Potential Biomarkers.," *BioMed research international*, vol. 2016, p. 9060143, 2016.

[17] "Chronic inflammation." `hhttps://www.ncbi.nlm.nih.gov/books/NBK493173`. Accessed: 2019-02-17.

[18] WHO, "Preventing chronic disease: A vital investment," tech. rep., World Health Organization, 2005.

[19] T. Bressmann, "Self-inflicted cosmetic tongue split: a case report.," *Journal (Canadian Dental Association)*, vol. 70, pp. 156–7, mar 2004.

[20] K. Hofman, "Non-communicable diseases in South Africa: A challenge to economic development," *South African Medical Journal*, vol. 104, no. 10, p. 647, 2014.

[21] World Health Organisation, "South Africa WHO Country Mortality Profile," p. 2018, 2016.

[22] South African Ministry of Health, "Strategic Plan for the Prevention and Control of Non-Communicable Diseases 2013-17," tech. rep., 2013.

[23] J. G. White, "Platelet structure," *Platelets*, pp. 45–73, 2007.

[24] R. Grozovsky, S. Giannini, H. Falet, and K. M. Hoffmeister, "Regulating billions of blood platelets: Glycans and beyond," *Blood*, vol. 126, no. 16, pp. 1877–1884, 2015.

[25] P. Harrison and D. Keeling, "Clinical Tests of Platelet Function," in *Platelets*, pp. 445–474, Elsevier, 2007.

[26] A. Michelson, *Platelets*. Amsterdam: Elsevier, third ed., 2013.

[27] N. P. Function and A. Drugs, "Normal Platelet Function and," *ACC Current Journal Review*, vol. 1458, no. February, pp. 13–16, 1999.

[28] "Coagulation cascade animation - physiology of hemostasis." `https://www.youtube.com/watch?v=cy3a__OOa2M`. Accessed: 2019-07-23.

[29] L. F. Brass, D. K. Newman, K. M. Wannermacher, L. Zhu, and T. J. Stalker, "Formation," in *Platelets* (A. Michelson, ed.), ch. 19, pp. 367–398, London: Elsevier, third ed., 2013.

[30] S. Willoughby, A. Holmes, and J. Loscalzo, "Platelets and cardiovascular disease.," *European journal of cardiovascular nursing : journal of the Working Group on Cardiovascular Nursing of the European Society of Cardiology*, vol. 1, pp. 273–88, dec 2002.

[31] M. Gawaz, "Platelets in inflammation and atherogenesis," *Journal of Clinical Investigation*, vol. 115, pp. 3378–3384, dec 2005.

[32] G. L. Reed, "Platelet secretion," in *Platelets* (A. Michelson, ed.), ch. 18, pp. 309–318, London: Elsevier, third ed., 2007.

[33] P. Ferroni, F. Martini, S. Riondino, F. La Farina, A. Magnapera, F. Ciatti, and F. Guadagni, "Soluble P-selectin as a marker of in vivo platelet activation," *Clinica Chimica Acta*, vol. 399, pp. 88–91, jan 2009.

[34] G. J. Caine and A. D. Blann, "Soluble p-selectin should be measured in citrated plasma, not in serum," *British Journal of Haematology*, vol. 121, pp. 530–532, may 2003.

[35] U. Alehagen and T. L. Lindahl, "sP-selectin is a useful biomarker for cardiovascular risk," *Cardiovascular Endocrinology*, vol. 4, pp. 22–27, mar 2015.

[36] D. Y. Xu, S. P. Zhao, and W. P. Peng, "Elevated plasma levels of soluble P-selectin in patients with acute myocardial infarction and unstable angina. An inverse link to lipoprotein(a).," *International journal of cardiology*, vol. 64, pp. 253–8, may 1998.

[37] H. Ikeda, Y. Takajo, K. Ichiki, T. Ueno, S. Maki, T. Noda, K. Sugi, and T. Imaizumi, "Increased Soluble Form of P-Selectin in Patients With Unstable Angina," *Circulation*, vol. 92, pp. 1693–1696, oct 1995.

[38] S. Sakurai, A. Inoue, C. S. Koh, M. Owa, and N. Yanagisawa, "Soluble form of selectins in blood of patients with acute myocardial infarction and coronary intervention.," *Vascular medicine (London, England)*, vol. 2, pp. 163–8, aug 1997.

[39] N. Bavbek, A. Kargili, O. Kaftan, F. Karakurt, A. Kosar, and A. Akcay, "Elevated concentrations of soluble adhesion molecules and large platelets in diabetic patients: are they markers of vascular disease and diabetic nephropathy?," *Clinical and applied thrombosis/hemostasis : official journal of the International Academy of Clinical and Applied Thrombosis/Hemostasis*, vol. 13, pp. 391–7, oct 2007.

[40] A. D. Blann and G. Y. Lip, "Hypothesis: is soluble P-selectin a new marker of platelet activation?," *Atherosclerosis*, vol. 128, pp. 135–8, feb 1997.

[41] A. D. Michelson, M. R. Barnard, H. B. Hechtman, H. MacGregor, R. J. Connolly, J. Loscalzo, and C. R. Valeri, "In vivo tracking of platelets: circulating degranulated platelets rapidly lose surface P-selectin but continue to circulate and function.," *Proceedings of the National Academy of Sciences*, vol. 93, pp. 11877–11882, oct 1996.

[42] S. R. Panicker, P. Mehta-D'souza, N. Zhang, A. G. Klopocki, B. Shao, and R. P. McEver, "Circulating soluble P-selectin must dimerize to promote inflammation and coagulation in mice," *Blood*, vol. 130, pp. 181–191, jul 2017.

[43] J. R. O. Brien, "Platelet aggregation: Part II Some results from a new method of study," *Journal of Clinical Pathology*, vol. 15, pp. 452–455, sep 1962.

[44] "Posts tagged as "aggregometer top manufacturers and uses"." `http://industrynewsblog.com/tag/aggregometer-top-manufacturers-and-uses/`. Accessed: 2019-07-23.

[45] Y. Ozaki, K. Satoh, Y. Yatomi, T. Yamamoto, Y. Shirasawa, and S. Kume, "Detection of platelet aggregates with a particle counting method using light scattering.," *Analytical biochemistry*, vol. 218, pp. 284–94, may 1994.

[46] K. Eto, S. Takeshita, M. Ochiai, Y. Ozaki, T. Sato, and T. Isshiki, "Platelet aggregation in acute coronary syndromes: use of a new aggregometer with laser light scattering to assess platelet aggregability," *Cardiovascular Research*, vol. 40, pp. 223–229, oct 1998.

[47] T. Yamamoto, Y. Egawa, Y. Shirasawa, Y. Ozaki, K. Sato, Y. Yatomi, and H. Kume, "A laser light scattering in situ system for counting aggregates in blood platelet aggregation," *Measurement Science and Technology*, vol. 6, pp. 174–180, feb 1995.

[48] P. David, A. C. Nair, V. Menon, and D. Tripathi, "Laser light scattering studies from blood platelets and their aggregates," *Colloids and Surfaces B: Biointerfaces*, vol. 6, pp. 101–114, mar 1996.

[49] "What is flow cytometry?." `https://www.news-medical.net/life-sciences/What-is-Flow-Cytometry.aspx`. Accessed: 2019-01-25.

[50] S. D. Schmidt, "A measurement by enzyme-linked immunosorbent assay.," January 2012.

[51] S. Patel, R. Nanda, S. Sahoo, and E. Mohapatra, "Biosensors in health care: The milestones achieved in their development towards lab-on-chip-analysis," *Biochemistry Research International*, vol. 2016, 2016.

[52] L. Vinet and A. Zhedanov, "Electrochemical Biosensors - Sensor Principles and Architectures," *Journal of Physics A: Mathematical and Theoretical*, vol. 44, p. 085201, feb 2011.

[53] P. Mehrotra, "Biosensors and their applications - A review," *Journal of Oral Biology and Craniofacial Research*, vol. 6, no. 2, pp. 153–159, 2016.

[54] J. Ali, J. Najeeb, M. Asim Ali, M. Farhan Aslam, and A. Raza, "Biosensors: Their Fundamentals, Designs, Types and Most Recent Impactful Applications: A Review," *Journal of Biosensors & Bioelectronics*, vol. 08, no. 01, pp. 1–9, 2017.

[55] M. M. Barsan, M. Emilia Ghica, and C. M. Brett, "Electrochemical biosensors," *Portable Biosensing of Food Toxicants and Environmental Pollutants*, pp. 33–69, 2013.

[56] T. Bhardwaj, "Review on Biosensor Technologies," *International Journal of Advanced Research in Engineering and Technology*, vol. 6, no. 2, pp. 36–62, 2015.

[57] P. Lin, F. Yan, J. Yu, H. L. W. Chan, and M. Yang, "The Application of Organic Electrochemical Transistors in Cell-Based Biosensors," *Advanced Materials*, vol. 22, pp. 3655–3660, sep 2010.

[58] M. Zhang, P. Lin, M. Yang, and F. Yan, "Fabrication of organic electrochemical transistor arrays for biosensing," *Biochimica et Biophysica Acta (BBA) - General Subjects*, vol. 1830, pp. 4402–4406, sep 2013.

[59] R. Radhakrishnan, I. I. Suni, C. S. Bever, and B. D. Hammock, "Impedance Biosensors: Applications to Sustainability and Remaining Technical Challenges," *ACS Sustainable Chemistry & Engineering*, vol. 2, pp. 1649–1655, jul 2014.

[60] R. Pruna, F. Palacio, A. Baraket, J. Bausells, A. Errachid, and M. López, "Low-Cost Impedance Measurements for Lab-on-a-Chip Architectures: Towards Potentiostat Miniaturization," *Proceedings*, vol. 1, no. 4, p. 604, 2017.

[61] R. Pruna, F. Palacio, A. Baraket, N. Zine, A. Streklas, J. Bausells, A. Errachid, and M. López, "A low-cost and miniaturized potentiostat for sensing of biomolecular species such as TNF-α by electrochemical impedance spectroscopy," *Biosensors and Bioelectronics*, vol. 100, pp. 533–540, feb 2018.

[62] Prabhakar and Thakur, "Electrochemical biosensors: fabrication and applications in biodiagnostics," in *Nanobiosensors for Personalized and Onsite Biomedical Diagnosis*, pp. 37–54, Institution of Engineering and Technology, 2016.

[63] J. Wang, "Electrochemical biosensors: towards point-of-care cancer diagnostics.," *Biosensors & bioelectronics*, vol. 21, pp. 1887–92, apr 2006.

[64] P. B. Luppa, L. J. Sokoll, and D. W. Chan, "Immunosensors–principles and applications to clinical chemistry.," *Clinica chimica acta; international journal of clinical chemistry*, vol. 314, pp. 1–26, dec 2001.

[65] J. L. Hammond, N. Formisano, P. Estrela, S. Carrara, and J. Tkac, "Electrochemical biosensors and nanobiosensors," *Essays In Biochemistry*, vol. 60, pp. 69–80, jun 2016.

[66] C. S. Kuek Lawrence, S. N. Tan, and C. Z. Floresca, "A "green" cellulose paper based glucose amperometric biosensor," *Sensors and Actuators, B: Chemical*, vol. 193, pp. 536–541, 2014.

[67] E.-H. Yoo and S.-Y. Lee, "Glucose biosensors: an overview of use in clinical practice.," *Sensors (Basel, Switzerland)*, vol. 10, pp. 4558–76, may 2010.

[68] J. Li, L. Chia, N. Goh, S. Tan, and H. Ge, "Mediated amperometric glucose sensor modified by the sol-gel method," *Sensors and Actuators B: Chemical*, vol. 40, pp. 135–141, may 1997.

[69] S. Eissa, N. Alshehri, A. M. A. Rahman, M. Dasouki, K. M. Abu-Salah, and M. Zourob, "Electrochemical immunosensors for the detection of survival motor neuron (SMN) protein using different carbon nanomaterials-modified electrodes," *Biosensors and Bioelectronics*, vol. 101, pp. 282–289, mar 2018.

[70] A. Chen and B. Shah, "Electrochemical sensing and biosensing based on square wave voltammetry," *Analytical Methods*, vol. 5, no. 9, p. 2158, 2013.

[71] L. Li, H. Zhao, Z. Chen, X. Mu, and L. Guo, "Aptamer biosensor for label-free square-wave voltammetry detection of angiogenin," *Biosensors and Bioelectronics*, vol. 30, no. 1, pp. 261–266, 2011.

[72] P. Bollella and L. Gorton, "Enzyme based amperometric biosensors," *Current Opinion in Electrochemistry*, vol. 10, pp. 157–173, 2018.

[73] K. Strimbu and J. A. Tavel, "What are biomarkers?," *Current Opinion in HIV and AIDS*, vol. 5, pp. 463–466, nov 2010.

[74] N. Duan, S. Wu, S. Dai, H. Gu, L. Hao, H. Ye, and Z. Wang, "Advances in aptasensors for the detection of food contaminants," *The Analyst*, vol. 141, no. 13, pp. 3942–3961, 2016.

[75] L. Feng, Y. Chen, J. Ren, and X. Qu, "A graphene functionalized electrochemical aptasensor for selective label-free detection of cancer cells," *Biomaterials*, vol. 32, pp. 2930–2937, apr 2011.

[76] W. Shan, Y. Pan, H. Fang, M. Guo, Z. Nie, Y. Huang, and S. Yao, "An aptamer-based quartz crystal microbalance biosensor for sensitive and selective detection of leukemia cells using silver-enhanced gold nanoparticle label," *Talanta*, vol. 126, pp. 130–135, aug 2014.

[77] Q. Xie, Y. Tan, Q. Guo, K. Wang, B. Yuan, J. Wan, and X. Zhao, "A fluorescent aptasensor for sensitive detection of human hepatocellular carcinoma SMMC-7721 cells based on graphene oxide," *Anal. Methods*, vol. 6, no. 17, pp. 6809–6814, 2014.

[78] J.-J. Zhang, T.-T. Zheng, F.-F. Cheng, J.-R. Zhang, and J.-J. Zhu, "Toward the Early Evaluation of Therapeutic Effects: An Electrochemical Platform for Ultrasensitive Detection of Apoptotic Cells," *Analytical Chemistry*, vol. 83, pp. 7902–7909, oct 2011.

[79] Ö. Satlam, B. Kizilkaya, H. Uysal, and Y. Dilgin, "Biosensing of glucose in flow injection analysis system based on glucose oxidase-quantum dot modified pencil graphite electrode," *Talanta*, vol. 147, pp. 315–321, 2016.

[80] R. Devasenathipathy, V. Mani, S. M. Chen, S. T. Huang, T. T. Huang, C. M. Lin, K. Y. Hwa, T. Y. Chen, and B. J. Chen, "Glucose biosensor based on glucose oxidase immobilized at gold nanoparticles decorated graphene-carbon nanotubes," *Enzyme and Microbial Technology*, vol. 78, pp. 40–45, 2015.

[81] P. Giménez-Gómez, M. Gutiérrez-Capitán, F. Capdevila, A. Puig-Pujol, C. Fernández-Sánchez, and C. Jiménez-Jorquera, "Monitoring of malolactic fermentation in wine using an electrochemical bienzymatic biosensor for l-lactate with long term stability," *Analytica Chimica Acta*, vol. 905, pp. 126–133, 2016.

[82] A. Umar, M. Rahman, M. Vaseem, and Y.-B. Hahn, "Ultra-sensitive cholesterol biosensor based on low-temperature grown ZnO nanoparticles," *Electrochemistry Communications*, vol. 11, pp. 118–121, jan 2009.

[83] K. Lata, V. Dhull, and V. Hooda, "Fabrication and Optimization of ChE/ChO/HRP-AuNPs/c-MWCNTs Based Silver Electrode for Determining Total Cholesterol in Serum," *Biochemistry Research International*, vol. 2016, 2016.

[84] C. Yao, C. Xie, P. Lin, F. Yan, P. Huang, and I.-M. Hsing, "Organic electrochemical transistor array for recording transepithelial ion transport of human airway epithelial cells.," *Advanced materials (Deerfield Beach, Fla.)*, vol. 25, pp. 6575–80, dec 2013.

[85] J. M. Fowler, D. K. Wong, H. B. Halsall, and W. R. Heineman, "Recent developments in electrochemical immunoassays and immunosensors," in *Electrochemical Sensors, Biosensors and their Biomedical Applications* (Academic Press, ed.), pp. 115–143, Elsevier, 2008.

[86] "Chemistry of crosslinking." `https://www.thermofisher.com/za/en/home/life-science/protein-biology/protein-biology-learning-center/protein-biology-resource-library/pierce-protein-methods/chemistry-crosslinking.html`. Accessed: 2019-07-23.

[87] S. Sharma, H. Byrne, and R. J. O'Kennedy, "Antibodies and antibody-derived analytical biosensors," *Essays In Biochemistry*, vol. 60, pp. 9–18, jun 2016.

[88] "Chemistry of crosslinking." `https://www.thermofisher.com/za/en/home/life-science/protein-biology/protein-biology-learning-center/protein-biology-resource-library/pierce-protein-methods/chemistry-crosslinking.html`. Accessed: 2019-02-08.

[89] "Carbodiimide crosslinker chemistry." `https://www.thermofisher.com/za/en/home/life-science/protein-biology/protein-biology-learning-center/protein-biology-resource-library/pierce-protein-methods/carbodiimide-crosslinker-chemistry.html`. Accessed: 2019-07-23.

[90] S. Roy, N. Soin, R. Bajpai, D. S. Misra, J. A. McLaughlin, and S. S. Roy, "Graphene oxide for electrochemical sensing applications," *Journal of Materials Chemistry*, vol. 21, no. 38, pp. 14725–14731, 2011.

[91] D. Ji, L. Liu, S. Li, C. Chen, Y. Lu, J. Wu, and Q. Liu, "Smartphone-based cyclic voltammetry system with graphene modified screen printed electrodes for glucose detection," *Biosensors and Bioelectronics*, vol. 98, pp. 449–456, dec 2017.

[92] N. F. Chiu, S. Y. Fan, C. D. Yang, and T. Y. Huang, "Carboxyl-functionalized graphene oxide composites as SPR biosensors with enhanced sensitivity for immunoaffinity detection," *Biosensors and Bioelectronics*, vol. 89, pp. 370–376, 2017.

[93] F. Salam, Y. Uludag, and I. E. Tothill, "Real-time and sensitive detection of Salmonella Typhimurium using an automated quartz crystal microbalance (QCM) instrument with nanoparticles amplification.," *Talanta*, vol. 115, pp. 761–7, oct 2013.

[94] O. Torun, I. Hakk Boyac, E. Temür, and U. Tamer, "Comparison of sensing strategies in SPR biosensor for rapid and sensitive enumeration of bacteria.," *Biosensors & bioelectronics*, vol. 37, pp. 53–60, aug 2012.

[95] T. Rattana, S. Chaiyakun, N. Witit-Anun, N. Nuntawong, P. Chindaudom, S. Oaew, C. Kedkeaw, and P. Limsuwan, "Preparation and characterization of graphene oxide nanosheets," *Procedia Engineering*, vol. 32, pp. 759–764, 2012.

[96] J. Lee, J. Kim, S. Kim, and D. H. Min, "Biosensors based on graphene oxide and its biomedical application," *Advanced Drug Delivery Reviews*, vol. 105, pp. 275–287, 2016.

[97] T. Menanteau, E. Levillain, and T. Breton, "Electrografting via Diazonium Chemistry: From Multilayer to Monolayer Using Radical Scavenger," *Chemistry of Materials*, vol. 25, pp. 2905–2909, jul 2013.

[98] A. Baraket, M. Lee, N. Zine, M. Sigaud, J. Bausells, and A. Errachid, "A fully integrated electrochemical biosensor platform fabrication process for cytokines detection," *Biosensors and Bioelectronics*, vol. 93, no. September 2016, pp. 170–175, 2017.

[99] T. M. Chinowsky, J. G. Quinn, D. U. Bartholomew, R. Kaiser, and J. L. Elkind, "Performance of the Spreeta 2000 integrated surface plasmon resonance affinity sensor," *Sensors and Actuators, B: Chemical*, vol. 91, no. 1-3, pp. 266–274, 2003.

[100] H. Baccar, M. B. Mejri, I. Hafaiedh, T. Ktari, M. Aouni, and A. Abdelghani, "Surface plasmon resonance immunosensor for bacteria detection," *Talanta*, vol. 82, no. 2, pp. 810–814, 2010.

[101] P. Damborsky, J. vitel, and J. Katrlik, "Optical biosensors," *Essays In Biochemistry*, vol. 60, no. 1, pp. 91–100, 2016.

[102] L. Kergoat, B. Piro, M. Berggren, G. Horowitz, and M.-C. Pham, "Advances in organic transistor-based biosensors: from organic electrochemical transistors to electrolyte-gated organic field-effect transistors," *Analytical and Bioanalytical Chemistry*, vol. 402, pp. 1813–1826, feb 2012.

[103] C. Liao and F. Yan, "Organic Semiconductors in Organic Thin-Film Transistor-Based Chemical and Biological Sensors," *Polymer Reviews*, vol. 53, pp. 352–406, jul 2013.

[104] S. Sinn, L. Müller, H. Drechsel, M. Wandel, H. Northoff, G. Ziemer, H. P. Wendel, and F. K. Gehring, "Platelet aggregation monitoring with a newly developed quartz crystal microbalance system as an alternative to optical platelet aggregometry," *The Analyst*, vol. 135, no. 11, p. 2930, 2010.

[105] X. Jiang, R. Wang, Y. Wang, X. Su, Y. Ying, J. Wang, and Y. Li, "Evaluation of different micro/nanobeads used as amplifiers in QCM immunosensor for more sensitive detection of E. coli O157:H7.," *Biosensors & bioelectronics*, vol. 29, pp. 23–8, nov 2011.

[106] Y. Wang, J. Ping, Z. Ye, J. Wu, and Y. Ying, "Impedimetric immunosensor based on gold nanoparticles modified graphene paper for label-free detection of Escherichia coli O157:H7," *Biosensors and Bioelectronics*, vol. 49, pp. 492–498, nov 2013.

[107] "Graphene oxide." `https://www.acsmaterial.com/blog/index/view/id/14`. Accessed: 2019-09-09.

[108] A. Azadbakht, A. R. Abbasi, Z. Derikvand, and Z. Karimi, "Preparation of the carboxylic acid-functionalized graphene oxide/gold nanoparticles/5-amino-2-hydroxybenzoic acid as a novel electrochemical sensing platform," *Monatshefte fur Chemie*, vol. 147, no. 4, pp. 705–717, 2016.

[109] W. Sun, Y. Zhang, X. Ju, G. Li, H. Gao, and Z. Sun, "Electrochemical deoxyribonucleic acid biosensor based on carboxyl functionalized graphene oxide and poly-l-lysine modified electrode for the detection of tlh gene sequence related to vibrio parahaemolyticus," *Analytica Chimica Acta*, vol. 752, pp. 39–44, 2012.

[110] L. Guadagno, M. Raimondo, V. Vittoria, L. Vertuccio, K. Lafdi, B. De Vivo, P. Lamberti, G. Spinelli, and V. Tucci, "The role of carbon nanofiber defects on the electrical and mechanical properties of CNF-based resins," *Nanotechnology*, vol. 24, p. 305704, aug 2013.

[111] "Metrohm: Screen printed electrode." `http://www.dropsens.com/en/screen_printed_electrodes_pag.html`. Accessed: 2019-07-23.

[112] J. Kailashiya, N. Singh, S. K. Singh, V. Agrawal, and D. Dash, "Graphene oxide-based biosensor for detection of platelet-derived microparticles: A potential tool for thrombus risk identification," *Biosensors and Bioelectronics*, vol. 65, pp. 274–280, mar 2015.

[113] R. Lacroix, C. Dubois, A. S. Leroyer, F. Sabatier, and F. Dignat-George, "Revisited role of microparticles in arterial and venous thrombosis," *Journal of Thrombosis and Haemostasis*, vol. 11, pp. 24–35, jun 2013.

[114] M. L. Rand, R. Leung, and M. A. Packham, "Platelet function assays," *Transfusion and Apheresis Science*, vol. 28, pp. 307–317, jun 2003.

[115] P. Singh, S. Srivastava, P. Chakrabarti, and S. K. Singh, "Nanosilica based electrochemical biosensor: A novel approach for the detection of platelet-derived microparticles," *Sensors and Actuators B: Chemical*, vol. 240, pp. 322–329, mar 2017.

[116] H. Yao, N. Li, S. Xu, J.-Z. Xu, J.-J. Zhu, and H.-Y. Chen, "Electrochemical study of a new methylene blue/silicon oxide nanocomposition mediator and its application for stable biosensor of hydrogen peroxide.," *Biosensors & bioelectronics*, vol. 21, pp. 372–7, aug 2005.

[117] S. ROBERT, P. PONCELET, R. LACROIX, L. ARNAUD, L. GIRAUDO, A. HAUCHARD, J. SAMPOL, and F. DIGNAT-GEORGE, "Standardization of platelet-derived microparticle counting using calibrated beads and a Cytomics FC500 routine flow cytometer: a first step towards multicenter studies?," *Journal of Thrombosis and Haemostasis*, vol. 7, pp. 190–197, jan 2009.

[118] R. Van Kruchten, J. M. E. M. Cosemans, and J. W. M. Heemskerk, "Measurement of whole blood thrombus formation using parallel-plate flow chambers a practical guide," *Platelets*, vol. 23, no. 3, pp. 229–242, 2012.

[119] C. Godino, A. G. Pavon, A. Mangieri, G. M. Viani, S. Galaverna, M. Spartera, A. Chieffo, A. Cappelletti, A. Margonato, and A. Colombo, "PlaCor PRT measurement of shear-activated platelet aggregate formation in stable patients treated with single and dual antiplatelet therapy," *Platelets*, vol. 25, pp. 337–342, aug 2014.

[120] E. Ergezen, M. Appel, P. Shah, J. Kresh, R. Lec, and D. Wootton, "Real-time monitoring of adhesion and aggregation of platelets using thickness shear mode (TSM) sensor," *Biosensors and Bioelectronics*, vol. 23, pp. 575–582, nov 2007.

[121] Santos-Martinez, I. Inkielewicz-Stepniak, C. Medina, K. Rahme, D. D'Arcy, D. Fox, J. Holmes, H. Zhang, and M. W. Radomski, "The use of quartz crystal microbalance with dissipation (QCM-D) for studying nanoparticle-induced platelet aggregation," *International Journal of Nanomedicine*, p. 243, jan 2012.

[122] A. Sun, A. G. Venkatesh, and D. A. Hall, "A Multi-Technique Reconfigurable Electrochemical Biosensor: Enabling Personal Health Monitoring in Mobile Devices," *IEEE Transactions on Biomedical Circuits and Systems*, vol. 10, no. 5, pp. 945–954, 2016.

[123] N. Elgrishi, K. J. Rountree, B. D. McCarthy, E. S. Rountree, T. T. Eisenhart, and J. L. Dempsey, "A Practical Beginner's Guide to Cyclic Voltammetry," *Journal of Chemical Education*, vol. 95, pp. 197–206, feb 2018.

[124] "Cyclic voltammetry." `https://chem.libretexts.org/Bookshelves/Analytical_Chemistry/Supplemental_Modules_(Analytical_Chemistry)/Instrumental_Analysis/Cyclic_Voltammetry`, June 2019. Accessed: 2019-09-09.

[125] A. J. Bard, *Electrochemical methods : fundamentals and applications*. New York: Wiley, 2nd ed. ed., 2001.

[126] "Chemistry libretexts: Cyclic voltammetry." `https://chem.libretexts.org/Bookshelves/Analytical_Chemistry/Supplemental_Modules_(Analytical_Chemistry)/Instrumental_Analysis/Cyclic_Voltammetry`. Accessed: 2019-07-26.

[127] M. D. Dryden and A. R. Wheeler, "DStat: A versatile, open-source potentiostat for electroanalysis and integration," *PLoS ONE*, vol. 10, p. e0140349, oct 2015.

[128] C.-y. Huang, "Design of a Portable Potentiostat with Dual-microprocessors for Electrochemical Biosensors," *Universal Journal of Electrical and Electronic Engineering*, vol. 3, pp. 159–164, nov 2015.

[129] A. Ainla, M. P. S. Mousavi, M.-N. Tsaloglou, J. Redston, J. G. Bell, M. T. Fernández-Abedul, and G. M. Whitesides, "Open-Source Potentiostat for Wireless Electrochemical Detection with Smartphones," *Analytical Chemistry*, vol. 90, pp. 6240–6246, may 2018.

[130] AANEC08, "Basic overview of the working principle of a potentiostat/galvanostat (pgstat) electrochemical cell setup," tech. rep., Metrohm Autolab, Herisau, Switzerland, 12 2011.

[131] Gamry, "Understanding ir compensation," tech. rep., Gamry Instruments, 734 Louis Drive, Warminster, PA 18974, United States of America, 01 2018.

[132] G. N. Meloni, "Building a microcontroller based potentiostat: A inexpensive and versatile platform for teaching electrochemistry and instrumentation," *Journal of Chemical Education*, vol. 93, no. 7, pp. 1320–1322, 2016.

[133] E. Ghodsevali, S. Morneau-Gamache, J. Mathault, H. Landari, É. Boisselier, M. Boukadoum, B. Gosselin, and A. Miled, "Miniaturized FDDA and CMOS based potentiostat for bio-applications," *Sensors (Switzerland)*, vol. 17, no. 4, 2017.

[134] A. A. Rowe, A. J. Bonham, R. J. White, M. P. Zimmer, R. J. Yadgar, T. M. Hobza, J. W. Honea, I. Ben-Yaacov, and K. W. Plaxco, "CheapStat: An Open-Source, Do-It-Yourself Potentiostat for Analytical and Educational Applications," *PLoS ONE*, vol. 6, p. e23783, sep 2011.

[135] A. Nemiroski, D. C. Christodouleas, J. W. Hennek, A. A. Kumar, E. J. Maxwell, M. T. Fernandez-Abedul, and G. M. Whitesides, "Universal mobile electrochemical detector designed for use in resource-limited applications," *Proceedings of the National Academy of Sciences*, vol. 111, no. 33, pp. 11984–11989, 2014.

[136] M. F. Diouani, O. Ouerghi, A. Refai, K. Belgacem, C. Tlili, D. Laouini, and M. Essafi, "Detection of ESAT-6 by a label free miniature immuno-electrochemical biosensor as a diagnostic tool for tuberculosis," *Materials Science and Engineering C*, vol. 74, pp. 465–470, 2017.

[137] "Pearson - the biology place." `http://www.phschool.com/science/biology_place/biocoach/biokit/carboxyl.html`. Accessed: 2019-08-28.

[138] D. Kinnamon, S. Muthukumar, A. Panneer Selvam, and S. Prasad, "Portable Chronic Alcohol Consumption Monitor in Human Sweat through Square-Wave Voltammetry," *SLAS Technology*, vol. 23, no. 2, pp. 144–153, 2018.

[139] G. Ertürk, M. Hedström, M. A. Tümer, A. Denizli, and B. Mattiasson, "Real-time prostate-specific antigen detection with prostate-specific antigen imprinted capacitive biosensors," *Analytica Chimica Acta*, vol. 891, pp. 120–129, 2015.

[140] T. Scientific, *MAN0017125: Procedure for Two-step Coupling of Proteins Using EDC and NHS or Sulfo-NHS*. Thermo Scientific, Pierce Biotechnology, 3747 Meridian Road, Rockford, IL 61105, USA, a.0 ed., 2017.

[141] J. P. Gosling, *Immunoassays : A Practical Approach*. Practical approach series ; 228, Oxford: Oxford University Press, 2000.

[142] "Molecular weight and isoelectric point of various animal immunoglobulins." `https://www.agrisera.com/en/info/molecular-weight-and-isoelectric-point-of-various-immunoglobulins.html`. Accessed: 2019-07-12.

[143] "Ruthenium hexamine reversible cyclic voltagram - io rodeo documentation for cheapstat." `http://stuff.iorodeo.com/docs/cheapstat/ruthenium.html`. Accessed: 2019-08-27.

[144] P. A. Research, *Application Note: Square Wave Voltammetry*. Princeton Applied Research, Princeton Applied Research, 801 S. Illinois Avenue, Oak Ridge, TN 37830, application note s-7 ed., 2019.

[145] J.-a. A. Ho, A. F.-j. Jou, L.-c. Wu, and S.-L. Hsu, "Development of an immunopredictor for the evaluation of the risk of cardiovascular diseases based on the level of soluble P-selectin," *Methods*, vol. 56, pp. 223–229, feb 2012.

[146] "Uniprotkb - p16109." `https://www.uniprot.org/uniprot/P16109#sequences`. Accessed: 2019-07-26.

[147] "Expasy." `https://web.expasy.org/protparam/`. Accessed: 2019-07-26.

[148] J. Ketter, "What is the best way to do data analysis on electrochemical biosensors based on square wave voltammetry?." Online Forum: `https://www.researchgate.net/post/What_is_the_best_way_to_do_data_analysis_on_electrochemical_biosensors_based_on_square_wave_voltammetry`, March 2019. Accessed: 2019-08-25.

[149] M. Jakubowska, "Signal Processing in Electrochemistry," *Electroanalysis*, vol. 23, no. 3, pp. 553–572, 2011.

[150] Y. Shao, J. Wang, H. Wu, J. Liu, I. A. Aksay, and Y. Lin, "Graphene based electrochemical sensors and biosensors: A review," *Electroanalysis*, vol. 22, no. 10, pp. 1027–1036, 2010.

[151] M. Zhou, Y. Zhai, and S. Dong, "Electrochemical sensing and biosensing platform based on chemically reduced graphene oxide," *Analytical Chemistry*, vol. 81, no. 14, pp. 5603–5613, 2009.

[152] D. Bélanger and S. Baranton, "Electrochemical Derivatization of Carbon Surface by Reduction of in Situ Generated," *Journal of Physical Chemistry B*, vol. 109, pp. 24401–24410, 2005.

[153] M. Bourourou, H. Barhoumi, A. Maaref, and N. Jaffrezic-Renault, "Electrochemical Study of Modified Glassy Carbon Electrode with Carboxyphenyl Diazonium Salt in Aqueous Solutions," *Sensors & Transducers*, vol. 27, no. May, pp. 22–28, 2014.

[154] R. Baskaran, "Why reduction peak shifts to negative potential?." Online Forum: `https://www.researchgate.net/post/Why_reduction_peak_shifts_to_negative_potential`, 10 2017. Accessed: 2019-09-10.

[155] N. Bhalla, P. Jolly, N. Formisano, and P. Estrela, "Introduction to biosensors," *Essays in Biochemistry*, vol. 60, no. 1, pp. 1–8, 2016.

[156] "An introduction to antibodies: Antibody-antigen interaction." `https://www.sigmaaldrich.com/technical-documents/articles/biology/antibody-antigen-interaction.html`. Accessed: 2019-08-22.

[157] C. Tlili, "What normally cause sharp peak and voltage shifting issue from swv(squarewave voltammetry)?." Online Forum: `https://www.researchgate.net/post/What_normally_cause_sharp_peak_and_voltage_shifting_issue_from_SWVsquarewave_voltammetry`, June 2018. Accessed: 2019-09-10.